Extremely thin absorber "eta" solar cells with nanostructured II-VI absorber Materials and Properties

Raul Salazar

UNIVERSITÉ DE GRENOBLE

THÈSE

Pour obtenir le grade de

DOCTEUR DE L'UNIVERSITÉ DE GRENOBLE

Spécialité : **Matériaux, Mécanique, Génie Civil, Electrochimie**

Arrêté ministériel : 7 août 2006

Présentée par

Raúl SALAZAR

Thèse dirigée par **Valentina IVANOVA** et
codirigée par **Henri MARIETTE**

préparée au sein du **Laboratoire :** CEA-LETI, MINATEC Campus
dans **l'École Doctorale I-MEP2** : Ingénierie - Matériaux, Mécanique, Environnement, Energétique, Procédés, Production

Cellules solaires avec un absorbeur II-VI nanostructuré
Matériaux et Propriétés

Thèse soutenue publiquement le **19/11/2012**,
devant le jury composé de :

M. Daniel BELLET
Professeur à l'INP Grenoble, Président
M. Daniel LINCOT
Directeur de Recherche CNRS (IRDEP, Chatou), Rapporteur
M. Arnaud ETCHEBERRY
Directeur de Recherche CNRS (Institut Lavoisier, Versailles), Rapporteur
Mme. Valentina IVANOVA
Expert au CEA Grenoble, Directrice de thèse
M. Henri MARIETTE
Directeur de Recherche CNRS (Institut Néel, Grenoble), Co-directeur de thèse
M. Patrik SCHMUKI
Professeur à l'Université d'Erlangen-Nuremberg (Allemagne), Membre
Mme. Claude LEVY-CLEMENT
Directrice de recherche CNRS (ICMPE, Thiais), Membre
M. Dmitry ALDAKOV
Chercheur CNRS au CEA/INAC, Membre

UNIVERSITÉ DE GRENOBLE

THÈSE

Pour obtenir le grade de

DOCTEUR DE L'UNIVERSITÉ DE GRENOBLE

Spécialité : **Matériaux, Mécanique, Génie Civil, Electrochimie**

Arrêté ministériel : 7 août 2006

Présentée par

Raúl SALAZAR

Thèse dirigée par **Valentina IVANOVA** et
codirigée par **Henri MARIETTE**

préparée au sein du **Laboratoire :** CEA-LETI, MINATEC Campus
dans **l'École Doctorale I-MEP2** : Ingénierie - Matériaux, Mécanique, Environnement, Energétique, Procédés, Production

Extremely thin absorber "*eta*" solar cells with nanostructured II-VI absorber

Materials and Properties

Thèse soutenue publiquement le **19/11/2012**,
devant le jury composé de :

M. Daniel BELLET
Professeur à l'INP Grenoble, Président
M. Daniel LINCOT
Directeur de Recherche CNRS (IRDEP, Chatou), Rapporteur
M. Arnaud ETCHEBERRY
Directeur de Recherche CNRS (Institut Lavoisier, Versailles), Rapporteur
Mme. Valentina IVANOVA
Expert au CEA Grenoble, Directrice de thèse
M. Henri MARIETTE
Directeur de Recherche CNRS (Institut Néel, Grenoble), Co-directeur de thèse
M. Patrik SCHMUKI
Professeur à l'Université d'Erlangen-Nuremberg (Allemagne), Membre
Mme. Claude LEVY-CLEMENT
Directrice de recherche CNRS (ICMPE, Thiais), Membre
M. Dmitry ALDAKOV
Chercheur CNRS au CEA/INAC, Membre

Abstract

The development of semiconducting materials for the extremely thin absorber (*eta*) solar cell using cheap and scalable methods was the main objective of this work. The *eta*-solar cell is composed of all inorganic materials consisting of an extremely thin layer of absorbing material (1.1 <Eg< 1.8 eV) sandwiched between nanostructured transparent electron and hole conductors (Eg ≥ 3.3 eV). Compact and defect free ZnO thin film and nanowires (NWs) were prepared galvanostatically. The ZnO nanowire dimensions were controlled with the ZnO seed layer or the applied current density. The photosensitization of the ZnO nanowires with conformal layers of CdS, CdSe and CdTe prepared by Successive Ionic Layer Adsorption and Reaction (SILAR) was studied. The improvement of the absorber structural and optical properties by annealing and chemical treatment was achieved. The Close Spaced Sublimation (CSS) and Quantum Dot (QD) sensitization were also used for CdTe thin shell deposition, while the first method produced low coverage, the second resulted in better coverage but with not optimal optical features. The ZnO NW/absorber heterostructure was completed with a hole conducting CuSCN layer. The influence of the CuSCN layer (prepared by three methods) morphology on the *eta*-solar cell performance is discussed. Electrodeposited and SILAR prepared films exhibited rougher surfaces than that by the Impregnation technique (which affects the electrical conductivity). The ZnO/absorber core/shell heterostructures were also tested in a photoelectrochemical cell. The recorded efficiencies (up to 2 %) for the case of CdS and CdSe photosensitizers demonstrated an improvement of the ZnO/absorber interfaces and the material quality achieved by the modified-SILAR technique. These results let us to consider that today a Renascence of the SILAR method is happening.

Résumé

L'objectif de ce travail est d'élaborer des méthodes peu chères pour produire des matériaux semi-conducteurs pouvant entrer dans la fabrication de cellules solaires de type "*eta*" (extremely thin absorber). Ces cellules sont constituées d'une couche extrêmement fine d'un adsorbeur inorganique dont la bande interdite est situé entre 1.1 et 1.8 eV placée entre deux nanostructures transparentes l'une de type n et l'autre de type p et dont les bandes interdites doivent être supérieurs à 3.3 eV. Une couche compacte et des nanofils de ZnO ont été préparés en mode galvanostatique. Les dimensions des nanofils ont été contrôlées à l'aide de la couche compacte et de la densité du courant appliqué. La photosensibilisation des nanofils par des couches uniformes de CdS, CdSe et CdTe préparée par la méthode SILAR (Successive Ionic Layer Adsorption and Reaction) a été étudiée. Les propriétés de ces couches ont été améliorées par recuit et traitement chimique. En ce qui concerne les fines coquilles de CdTe deux autres méthodes de sensibilisation ont été également étudiées : la CSS (Close Spaced Sublimation) et les QDs (Quantum Dots). La première méthode conduit à un faible recouvrement alors que la seconde produit un matériau mal défini optiquement. Les hétérostructures formées sur les nanofils ont été complétées par une couche de CuSCN, un semi-conducteur de type p, préparée par trois méthodes différentes. L'influence de la morphologie de ces couches sur les propriétés des cellules *eta* a été étudiée. Les films préparés par électrodéposition et SILAR sont plus rugueux que ceux obtenus par imprégnation et leur conductivité est moins bonne. Les hétérostructures (avec CdS et CdSe comme absorbeurs) ont été testées dans une cellule photoélectrochimique et les rendements obtenus (jusque 2%) montrent une amélioration certaine des propriétés de ces matériaux préparée par SILAR-modifiée ainsi que des interfaces ZnO/absorbeur. La qualité des matériaux obtenus par SILAR montre qu'aujourd'hui on peut s'attendre à une Renaissance de cette technique.

Acknowledgements

I wish to express my profound gratitude to my thesis supervisor Prof. Valentina Ivanova and co-supervisor Prof. Henri Mariette for the immense guidance and supervision.

I would like to thank the Nanosciences Foundation and CONACYT-México for the financial support. Especially to the former director Prof. Roland Hérino, actual director Prof. Alain Fontaine and of all the staff of the Nanosciences Foundation: Marie-Anne Carré, Stéphanie Monfront and Fériel Kouiten for their invaluable assistance. To Rocío Moreno Canales, Samuel Manterola Martínez and Georgina Méndez Reyes from CONACYT-México (Jefe de Departamento de Gestion de Becas en el Extranjero, Subdirector de Becas en el Extranjero, y Enlace de Seguimiento del Desempeño Académico, respectivamente).

My thanks also go to all the personnel from the "Service de Depôt" (SDEP) from the "Commissariat à l'Énergie Atomique et aux énergies alternatives" - "Laboratoire d'Electronique et de Technologies de l'Information" (CEA-LETI) specially to the head of Service (SDEP) Laurent Vandroux and the head of the Laboratory (LDJ) Sylvain Maitrejean for all the support. Also many thanks to the secretaries for all the invaluable help. I would like to extend my thanks to the former colleagues from the laboratory of L2MA.

I would like to thank all the partner laboratories involved in the project "*New Concepts Solar Cells with II-VI Semiconductor Nanostructures*:

- CEA Grenoble/LETI/DOPT (Department d'Optoelectronique): Alain Million, Sergio Bernardi, Muriel Jolliot, Joelle Bonaime, Pierre Ferret, Guy Feuillet, Carole Granier, Ivan-Christophe Robin.
- CEA Grenoble/INAC (Institut Nanosciences et Cryogénie)/SP2M: Joël Bleuse, Régis André.

Also to other partner laboratories that facilitate the work done in this thesis:

- CEA Grenoble/INAC/SPRAM: Peter Reiss and Dmitry Aldakov.
- Grenoble INP/Laboratoire des Matériaux et du Génie Physique (LMGP) Daniel Bellet, Vincent Consonni, Etienne Puyoo, Laurent Terrier.

I am deeply grateful also to all technical support from the “Plateforme des caracterisation”: Brigitte Florin, Jean-Marc Fabbri, Hugo Dansas. And the director of the XRD at INAC: Stephanie Pouget.

Je remercie le Directeur: Denis Favier et l’Assistante: Augustine Alessio de l’école doctoral I-MEP2 (Ingénierie-Matériaux Mécanique Energétique Environnement Procédés Production).

Finally, I would to thank all my colleagues and friends: Sylvia Sanchez, Alexandru Delamoreanu, Cyril Chappaz and Hervé Muguerra.

Table of Contents

List of abbreviations and symbols

PV	Photovoltaics
eta	Extremely Thin Absorber
NWs	Nanowires
ZnO	Zinc Oxide
CdS	Cadmium Sulphide
CdSe	Cadmium Selenide
CdTe	Cadmium Telluride
CuSCN	Copper Thiocyanate
ECD	Electrochemical Deposition
SILAR	Successive Ionic Layer Adsorption and Reaction
CSS	Close Spaced Sublimation
2D	Two-dimensional
AM	Air Mass
DSSC	Dye-sensitized Solar Cell
E_g	Bandgap
CB	Conduction Band
VB	Valence Band
TCO	Transparent Conductive Oxide
FF	Fill Factor
$CdCl_2$	Cadmium chloride
LbL	Layer-by-layer
PDDA	Poly-(diallyldimethylammonium)
SCE	Saturate Calomel Electrode
TGA	Thioglycolic acid
TGH	Triacylglycerol hydrolase
GSH	Glutathione
SEM	Scanning-electron microscope
XRD	X-ray diffraction
EDX	Energy-dispersive X-ray spectroscopy
STEM	Scanning transmission electron microscope

FWHM	Full Width at Half Maximum
J-V	Current-Voltage
V_{oc}	Open-circuit voltage
J_{sc}	Short-circuit current density
P_{max}	Maximum power
η (%)	Solar cell efficiency
QDs	Quantum Dots
PL	Photoluminescence

Introduction

The Sun provides daily unlimited energy that should be used to meet the global energy demands. Researchers around the world are trying to find the ultimate technology that would allow the large-scale harvesting of sunshine.

Photovoltaics (PV) has been regarded as a good choice to produce low cost and clean energy for the society. Until recently, investments in PV research have been driven by the imminent shortages of fossil fuels and problems related to climate changes, health hazards and political problems.

The efficiencies of commercialized solar cell have increased at a slow pace and the high production costs are a disadvantage when compared to well established energy systems.

Considerable progress in PV technology is therefore required in order to face the growing energy problems. The new solar cell must not only be highly efficient but also cheap.

Among some of the innovations, the third generation solar cell based on nanomaterials seems to hold the answer to overcome the hurdles of high production costs. Although not being highly efficient, their cost-efficiency balance is estimated as a good alternative to push PV to large scale commercialization.

The motivation behind this thesis is to contribute to the progress of PV technology using more cost-effective processes. The all-inorganic Extremely Thin Absorber (*eta*) Solar Cell seems a good choice among the nanostructures-based solar cells. In this work we exploit low cost deposition methods for the preparation of high quality materials for the *eta*-solar cell.

With this purpose, the electrodeposited ZnO thin films and nanowires (NWs) are extensively studied since they play a fundamental role as nanostructured electrodes. Also, wet chemical room temperature deposition methods for the preparation of light absorbing materials (CdS, CdSe and CdTe) and the wide bandgap hole conductor (CuSCN) are investigated.

The present manuscript is divided in five chapters:

The first chapter presents the objectives of this thesis where a brief introduction to photovoltaics, the third generation nanostructured solar cells with emphasis on the *eta*-solar cell is presented. The properties of the materials used in this study are also described.

The second chapter details the experimental conditions and characterization techniques employed to carry out this work. In the first part, the material preparation is described. The different characterization techniques used for the analysis of the material properties and solar cell performance are included in the second part.

The third chapter is devoted to the results on the electrochemical preparation of ZnO thin layers and nanowire arrays. The influence of deposition parameters on the structural and optical properties of the galvanostatically prepared ZnO films is studied. The effect of these layers (as seed) on the dimensions and density of consequently electrochemically grown ZnO nanowires is covered. The galvanostatic deposition of ZnO nanowires is also briefly discussed. And interesting findings on the preparation of ZnO nanowalls by electrochemical deposition is demonstrated.

The fourth chapter explains the obtained results on the photosensitization of ZnO NW arrays with extremely thin light absorbing layers of CdS, CdSe and CdTe. These semiconductors are prepared by classical and modified Successive Ionic Layer Adsorption and Reaction (SILAR) method. The improvements of photosensitizing layer properties upon modified-SILAR technique are explained. For the case of CdTe, three different approaches for its deposition are used: SILAR, Close Spaced Sublimation (CSS) and Quantum Dot (QD) functionalization.

Finally, the preparation and characterization of complete *eta*-solar cell are introduced in the chapter five. Three deposition methods for the hole conducting layer (CuSCN) are compared: Electrochemical deposition (ECD), SILAR and Impregnation. The quality of the ZnO/absorber interfaces and photosensitizing shells are analyzed using the photoelectrochemical *eta*-solar cell.

The conclusion summarizes the overall results obtained during this work and proposes future investigations that may contribute for the development of efficient *eta*-solar cells.

CHAPTER I : Extremely Thin Absorber Solar Cells

This chapter presents the objectives of this thesis. The first part is an introduction to solar cells and the development of the photovoltaic technology; a special section is dedicated to the third generation solar cells since this thesis deals with a newly proposed type of nanostructured solar cell.

In a second part, the extremely thin absorber solar cell is introduced. Its potential to solve the nowadays problems related to the need of clean energy sources is highlighted. The problematic related with high production cost of existent solar cells is addressed by the implementation of easy processing and cheap deposition methods, as well as with the reduction of the use of materials. The literature review aims to immerse the reader into this type of solar cell, the role of each component and its effect on the cell performance.

Finally, the materials studied in this thesis, their properties and preparation methods are introduced. Special emphasis is drawn on the electrochemical deposition of ZnO 2D layer and nanowires since they are the backbone of the proposed solar cell. The choice of the photosensitizing materials is justified by the proposition of low cost and large-scalable deposition methods.

1 PHOTOVOLTAICS

Solar energy represents a promising widespread primary energy source. The energy from sunlight that reaches the Earth in 1 hour surpasses that of all of the energy consumed by humans in the entire year. Therefore, its capture, conversion and storage are crucial for the production of sustainable energy. According to international Energy Associations and Institutes, the solar energy exceeds all other renewable and fossil energy resources [1, 2]. Figure I.1 shows a representation of the solar irradiation versus established energy resources.

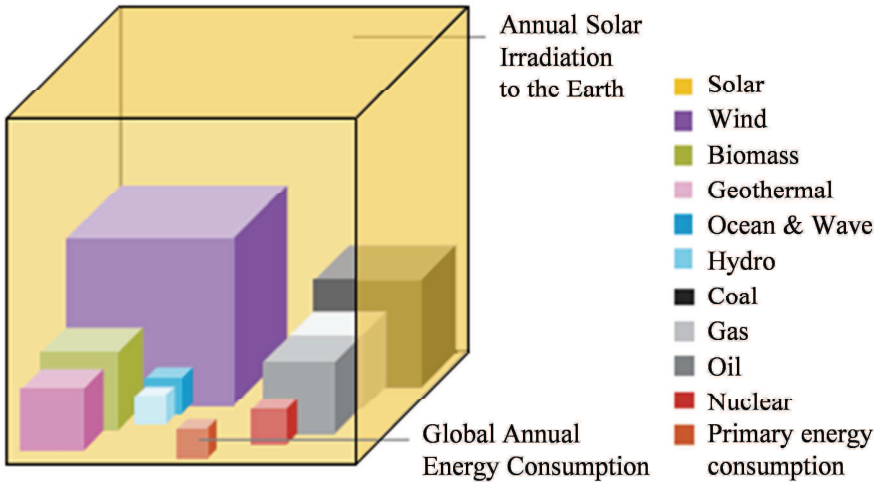

Figure I.1. Solar irradiation versus established energy resources. For the fossil fuels the total reserves are represented while for renewable energies their yearly potential is shown [2].

The photovoltaic (PV) technology is based on the capture and conversion of the solar light into electricity. The basic principle lies on the generation of electron-hole pairs in semiconductors upon light absorption, and on the separation of electrons and holes by an internal electric field. The collected charge carriers give rise to a photocurrent when the electrode contacts are connected to a load (Figure I.2). In the ideal case, the generated current should be proportional to the light intensity power, however fundamental losses occur that limit the overall cell efficiency (Figure I.3) [3].

The research on PV started with the discovery of the photovoltaic effect by the French scientist Alexandre Edmond Becquerel in 1839. But it was truly born with the demonstration of the first silicon solar cell (with an efficiency of 4%) at the Bell Telephone Laboratories in 1954. After such milestone, the historical development of PV technology has been followed by important research discoveries in materials, novel approaches and cell designs [4].

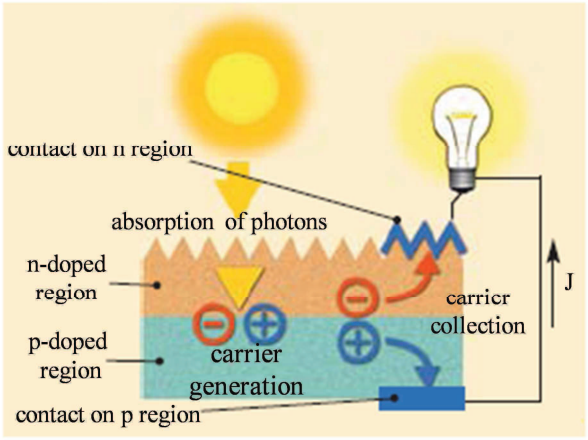

Figure I.2. The Photovoltaic Effect in a Solar Cell [1].

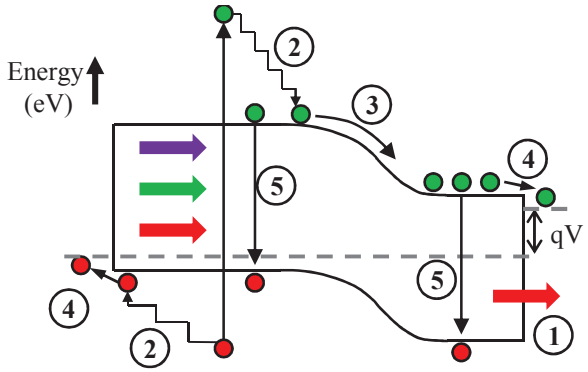

Figure I.3. Diagram of the primary loss processes in a standard solar cell: (1) non absorption of photons with energies below the bandgap; (2) lattice thermalization loss; (3) and (4) junction and contact voltage losses; (5) recombination losses (radiative and non radiative recombination of electrons and holes with electronic states within the bandgap due to defects or impurity atoms) [5, 6].

Three generations of solar cells have been identified in relation to the impact on the evolution of PV technology:

i) The First-generation (crystalline silicon technology) represents the classical single bandgap (p-n junction) solar cell. Despite their high manufacturing costs, these monocrystalline silicon-based solar cells have a mature market.

ii) The Second-generation or "thin film" solar cells are characterized by lower production costs: material wise and manufacturing processes in compared to the crystalline technology. Only few-micrometers-thick layers of CdTe, GaAs, amorphous silicon (a-Si), Copper Indium Sulfide (Selenide) (CIS(e)), Copper Indium Gallium Sulfide (CIGS) and multijunction cells of a-Si/m-Si are developed. Although their efficiencies remain lower than those of the first-

generation, this type of cells prompted the development of light weight and flexible panels at relatively lower cost.

iii) Third-generation solar cells, still in research phase, include multi-layer systems (a-Si, GaAs and others), p-i-n junctions, the use of plastic lenses or mirrors to concentrate sunlight, and other cutting edge innovations such as polymer, nanocrystalline and dye-sensitized solar cells. Some of these systems do not require the p-n junction like in traditional semiconductor based solar cells and therefore could potentially overcome the Shockley-Queisser limit of 31% power efficiency for single bandgap solar cells [7]. Some of these new concepts will be discussed later in this chapter.

In Table I.1 are listed the highest independently confirmed efficiencies for solar cells as of January 2012.

Table I.1 Confirmed terrestrial cell efficiencies measured under the global AM1.5 spectrum (1000W/m^2) at 25°C [8].

Status on Solar Cell Efficiencies in (%)					
First generation silicon		*Second generation Thin film*		*Third generation*	
c-Si	25.0 ± 0.5	GaAs	28.3 ± 0.8	DSSC	11.0 ± 0.3
mc-Si	20.4 ± 0.5	CIGS	19.6 ± 0.6	Organic	10.0 ± 0.3
		CdTe	16.7 ± 0.5	GaInP/GaInAs/Ge	34.1 ± 1.2
		a-Si	10.1 ± 0.3	a-Si/nc-Si	12.3 ± 0.3
		CZTSSe *	10.1 ± 0.2	GaInP/GaAs/GaInAs *	36.9 ± 1.5

* 'notable exceptions'. Not recognized as a class record but with notable characteristics that will be of interest for the photovoltaic community. Results from concentrator cells are not included which could increase up to 43.5 ±2.6% for the case of a GaInP/GaAs/GaInAs multijunction solar cell. Copper-zinc-tin-sulfide-(Selenide) (CZTSSe).

1.1. Third Generation Solar Cells

The contribution of the second generation solar cells to the progress of PV technology goes beyond is based in the introduction of new materials, also deposition methods and new concepts were developed. The need to improve efficiencies and to minimize factors that detriment the performance of the cells became main focus of research.

The Shockley-Queisser limit was raised to about 41% with the use of concentrators of light, and thermalization losses and inefficient light absorption were tackled with the implementation of hot-carrier and tandem solar cells (multijunction) [5, 6]. Regardless of the high efficiencies obtained in concentrator solar cells, a photovoltaic device that is cost-effective and globally scalable is the ultimate goal for both research and industry.

New developments in nanotechnology, materials and even biotechnology may hold the formula that would enable the widespread to sustainable energy production. The goal of such new third generation photovoltaics (PVs) is to reduce the cost of solar energy below the current level of around $1/Watt (second generation PV) to less than $0.20/Watt (Figure I.4) [9].

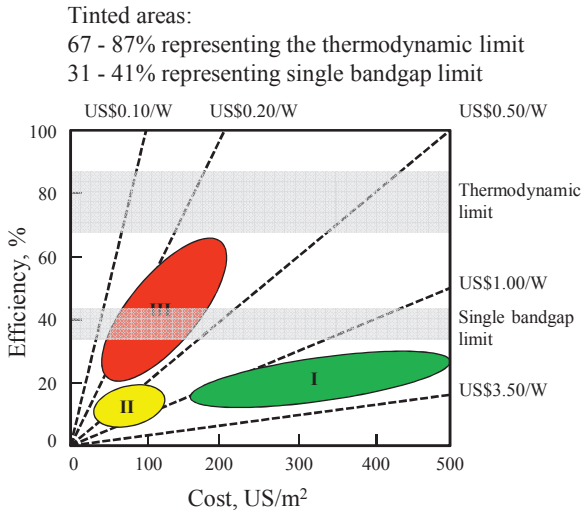

Figure I.4. Efficiency and cost projections for first- (I), second- (II), and third generation (III) PV technologies (wafer-based, thin films, and advanced thin films, respectively) [9].

A large variety of nanomaterials are being actively studied due to their potentially low-cost production and possibility of higher performance than current PV technologies. For example:

i) Semiconducting quantum wells and quantum dots could be absorbers with a highly quantized band structure, that are capable to generate multiple excitons from a single

absorbed photon with energy greater than the bandgap of the material [10–13].

ii) Materials with intermediate bands or mini-bands having one or more energy levels within the bandgap such that they could absorb photons in parallel with the normal operation of a single-bandgap cell [14].

iii) Organic dyes and bulk heterojunctions of polymers have permitted the development of low cost, flexible solar cells that are capable to perform in dim and variable light conditions [15, 16].

iv) Nanowires, nanotubes and nanoparticles among other nanostructures have allowed the development of more robust all inorganic solid-state nanostructured solar cells. Light trapping effects, increased surface area, improved charge separation and collection are among some advantages [17, 18].

2 THE EXTREMELY THIN ABSORBER SOLAR CELL (eta)

In the imperative quest to find cheap, stable and clean sources of energy substitutes, nanostructured solar cells represent an innovative and promising alternative to reduce the high cost and massive use of materials of their single-crystalline and thin film counterparts. The concepts relay in the separation of photogenerated electrons and holes locally to distances larger than the overlap of their wave functions, aiming to reduce the recombination probability.

Nanostructured electrodes were first introduced in the Dye Sensitized Solar Cell (DSSC) by Grätzel et al. in 1991 [15], Figure I.5. Ever since, nanoparticle, nanoporous or nanowire based electrodes have been extensively investigated in different third generation nanostructured solar cells (DSSC, hybrid organic-inorganic, eta solar cells). The nanostructured semiconductor must fulfill certain requirements in order to be considered for the construction of efficient photoelectrodes: wide bandgap (>3.3 eV), high charge carrier mobility (from 0.01 to 10 $cm^2\ V^{-1}\ s^{-1}$ in the case of TiO_2), and the possibility to be synthesized with a high surface area. Other optical effects like light trapping and more direct path for the collection of charge carriers are desired [19].

Layers formed by interconnected TiO_2 nanoparticles have been the choice of material due to the thought ultrafast electron injection from the dye into the conduction band of the TiO_2 nanoparticles [20, 21]. ZnO is n-type wide bandgap semiconductor with similar properties like TiO_2. Moreover, it could be grown in monocrystalline nanowire form. ZnO NWs have the advantage of easy synthesis and control over the morphology of the nanostructures and the charge carrier mobility is higher (>10 $cm^2\ V^{-1}\ s^{-1}$) than that of nanocrystalline TiO2. Additionally problems related to scarcity or price of Ti could also be solved if ZnO is used as electrode material instead TiO_2.

In a same trend, the implementation of core/shell nanorod architecture (single crystalline nanorod cores covered with a continuous nanocrystalline layer) appears as an interesting option in the third generation solar cells research. The aligned one-dimensional nanostructures promise superior electrical performances over the porous versions due to better charge transport by the oriented geometrical structure of the nanorods. Charge recombinations in randomly packed nanoparticle networks could be therefore avoided [21, 22].

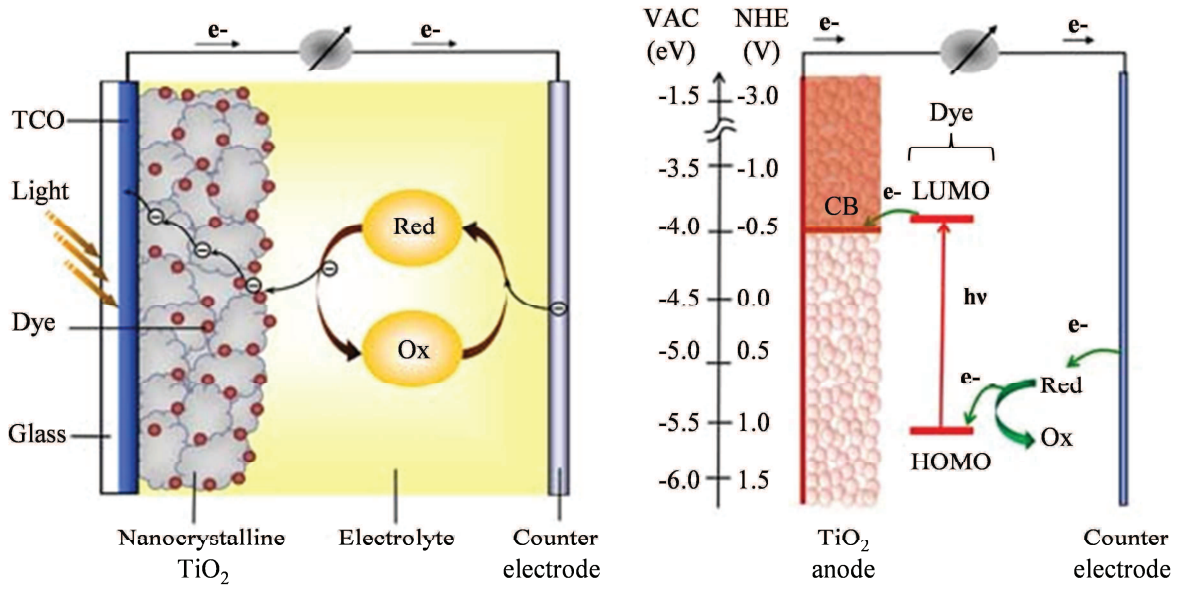

Figure I.5. (a) Structure of a Grätzel Solar Cell: A mesoporous TiO_2 nanoscaffolding houses small dye molecules, which harvest light and generate excitons (a quasi-particle which can be seen as an electron-hole pair bound by Coulomb forces). Electrons flow through the TiO_2 to an anode mounted on glass substrate, and the dye's electrons are regenerated by the cathode via a redox couple such as I^-/I^-_3, (b) Typical energy diagram of the DSSC: electrons are excited from dye HOMO to LUMO, where they transfer to the conduction band (CB) of the TiO_2 nanostructure, and to the anode. Meanwhile, holes left in dye LUMO travel up in energy through the redox couple, and then up to the cathode. The maximum attainable voltage is believed to be approximately determined by the energy difference between the Fermi energy of illuminated electrons in the semiconductor and the redox energy of the hole transport layer [15, 16].

Among the innovative nanostructured solar cell configurations, the all-inorganic extremely thin absorber (*eta*) solar cell appears as a potential choice to develop long-lasting and more robust devices (Figure I.6).

The *eta*-solar cell consists of an extremely thin layer of absorbing material (direct bandgap (Eg) between 1.1 and 1.8 eV) sandwiched between nanostructured transparent electron and hole conductors ($Eg \geq 3.3$ eV) (Figure I.6 b). The highly structured electrode allows the reduction of the absorber thickness while ensuring maximal absorption of light due to light scattering effects [23].

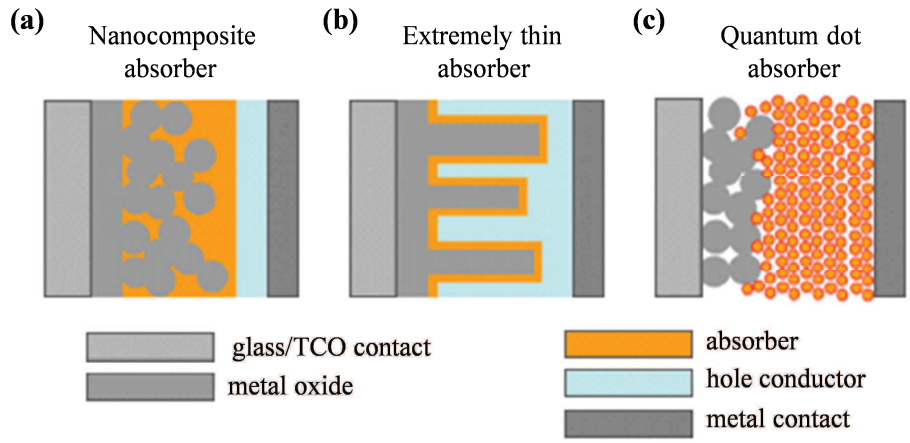

Figure I.6. Schematic cross sections of inorganic solid-state nanostructured solar cells with: (a) ultra-thin nanocomposite absorber; (b) extremely thin absorber and (c) quantum dot absorber. For the three cases, the charge separation occurs at the absorber-metal oxide interface. In (a and b) the collection efficiency of photogenerated charge carriers is enhanced by drift in the electric field of the p-i-n structure ("i" standing for intrinsic or undoped absorber). And the third one (c) relays on the depleted region between the QD layer and the transparent substrate for field-driven charge transport and separation [18].

The working principle resembles closely to that of a dye-sensitized solar cell (Figure I.5). The charge separation occurs at the interface between the light absorbing element (molecular dye in DSSC and inorganic layer in *eta*) and the wide bandgap window material [15]. Photogenerated electrons in the absorbing layer is injected into the conduction band (E_c) of the electron conductor, while the holes are transferred into the valence band (E_v) of the hole conductor. The efficient separation of charges is favored by suitable offsets between the respective bands of the absorbing layer and wide bandgap electron and hole conductors (Figure I.7).

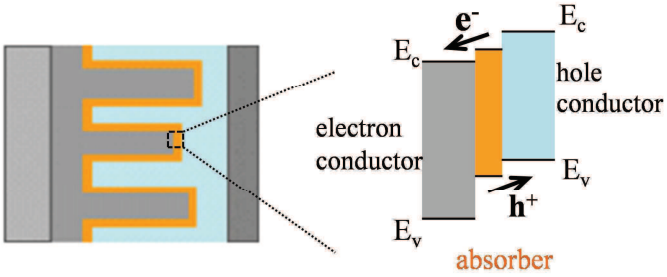

Figure I.7. Schema of the electron energy level diagram of an ideal *eta*-solar cell (type-II or staggered energy band lineup: the conduction band of the smaller bandgap material lies above that of the larger bandgap material or its valence band lies below that of the larger bandgap material).

The historical development and progress of the *eta*-solar cell can be summarized as follows:

- 1996: introduction of the concept by Könenkamp et al using a heterojunction formed by PbS quantum dots [24];
- 1997: Siebentritt et al. reported the fully-inorganic heterojunction solar cells [25];
- 1998: Tennakone, et al demonstrated 0.13% of efficiency with the n-TiO_2/Se/p-CuSCN structure [26];
- 2001: Kaiser et al explored $CuInS_2$ as the absorber material in a TiO_2/$CuInS_2$/CuSCN cell [27]. Similarly Ernst et al presented the TiO_2/CdTe based *eta*-solar cell [28];
- In 2005, the group of Claude Lévy-Clément published pioneering works on *eta*-solar cells based on ZnO NWs. Efficiencies of 2.3% were achieved when CdSe absorbing material and CuSCN hole conductor were used [29]. To date, the research on *eta*-solar cells has been focused mainly on the implementation of new absorber materials. Nanoporous TiO_2 and ZnO NW arrays remain as commonly used n-type materials and ZnTe, CuSCN and PEDOT:PSS as p-type hole conductors [30–32]. Table I.2 summarizes the obtained *eta*-solar cell efficiencies to date.

Table I.2. Timeline of the *eta*-solar cell efficiencies [33].

Year	Cell	Efficiency (%)
1998	TiO_2/Se/CuSCN	0.13
2002	TiO_2/PbS/Spiro-OMeTAD	0.49
2004	TiO_2/In_2S_3/ $CuInS_2$/Au	4.00 [34]
2005	ZnO/CdSe/CuSCN TiO_2/$In_x(OH)_y$/ $CuInS_2$/graphite	2.3 5.00 [35]
2006	TiO_2/CdS/CuSCN TiO_2/$In(OH)_x$ S_y/PbS/PEDOT:PSS/Au	1.3 0.83 [36]
2007	TiO_2/Sb_2S_3/CuSCN * Si NWs	3.4 3.4 [37]
2008	ZnO/In_2S_3/CuSCN	3.4
2009	TiO_2/Sb_2S_3/CuSCN ZnO/In_2S_3/ CuSCN/Au TiO_2/$In_x(OH)_y$ S_2/Sb_2S_3/CuSCN/Au * GaAs NWs	3.4 3.20 [38] 3.37 [39] 4.50 [40]
2010	TiO_2/Sb_2S_3/CuSCN TiO_2/Sb_2S_3/Spiro-OMeTAD TiO_2/Sb_2S_3/P3HT ZnO/In_2S_3/ $CuInS_2$	3.7 3.1 5.1 4.17 [41]

	* Si NWs	5.00 [42]
2011	ZnO:Al/CdSe/Cu_2O	3.16 [43]
2012	* n-GaAs/InGaP/p-GaAs	4.70 [44]

* Not *eta*-solar cell but notable contributions on the nanowire-based solar cells.

2.1. The Nanowire-Version of the Eta-Solar Cell

This thesis is focused on the eta-solar cell based on ZnO NWs as previously introduced by the group of Claude Lévy-Clément. This configuration requires only a few-tens-of-nanometer-thick layer of absorbing material to fully absorb the available solar energy radiation. As a consequence of the thinner absorber and the advantageous electrical and optical properties of the nanostructured electrodes, the photogenerated carries can be efficiently collected and transported through the nanowire channels (Figure I.8). Moreover, the NW-array electrode represents the most viable choice as n-type window material in the eta-solar cell. A template made out of NWs, different from that formed by nanoparticles or porous material, offers a direct path for the transport of electrons and the radial p-i-n junction could be easily controlled [45].

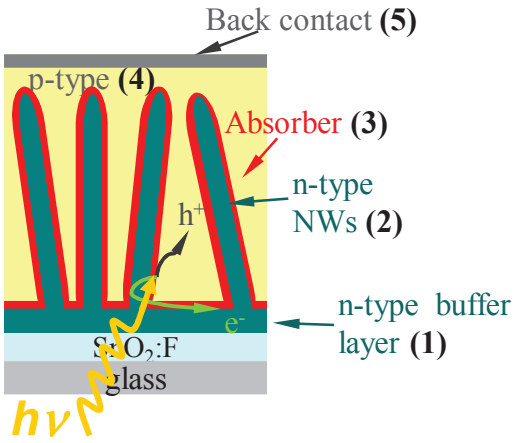

Figure I.8. Schematic diagram of the nanowire-version *eta* solar cell [23].

The proposed nanowire version of the *eta*-solar cell consists of the following elements:

(1) n-type ZnO buffer layer (Eg ≥ 3.3 eV) that serves as insulating layer between the transparent conducting oxide (TCO) and the rest of the components. Shunts are avoided in this way.

(2) n-type ZnO NW array that serves as nanostructured electrode. The surface enlargement by the highly structured electrode is about 100 times relative to planar thin films. Enhanced photon absorption is promoted due to light-trapping effects [30, 46].

(3) An extremely thin (20-40 nm) absorber layer (1.1 <Eg< 1.8 eV) conformally deposited on the NW surface. The reduction in local thickness leads to an improved charge collection probability. In our work CdS, CdSe and CdTe preparation is studied.

(4) Void-filling with hole transporting p-type semiconductor (CuSCN), also wide bandgap ($Eg \geq 3.3$ eV).

(5) Metallic back contact.

2.2. The Extremely Thin Absorber Layer

The extremely reduced thickness of the absorber layer is the main advantage of the *eta*-solar cell. This allows the reduction of required absorber material for full absorption, opens up the opportunity to use materials with low diffusion length, thus being promising to lower production costs.

Theoretically, efficiencies up to 15% could be achieved for an absorber thickness of 15-20 nm (for CdTe and $CuInS_2$, respectively) [47, 48], while similar efficiencies are nowadays obtained with 1.5-6 μm thick layers in in thin film solar cells. The theoretical model refers to an ideal case where each component of the *eta*-solar cell performs at its best. In the real scenario, the absorber deposition presents several constrains in terms of the obtained crystalline quality and morphology on the nanowire surface. Figure I.9 depicts the possible photovoltaic phenomena for different sensitizing shell properties and Table I.3 summarizes the effects of the absorber layer properties on the performance of the *eta*-solar cell.

Suitable deposition techniques should be used to ensure uniform coverage of the ZnO NWs, allowing to control the layer thickness and properties. The absorber layer in a nutshell must fulfill the following requirements [18]:

(a) It has to be thick enough to guarantee maximum absorbance of photons and to prevent tunneling currents at the p-i-n junction (Figure I.9 b).

(b) It has to be thin enough to ensure the collection of photogenerated carriers which might be limited due to low diffusion lengths (intrinsic property of the absorbing material and crystalline quality) (Figure I.9 c).

(c) It should uniformly cover the entire nanowire surface as to guarantee good charge separation at the heterostructure. The depletion layer at the ZnO/absorber interfaces could be affected by the discontinuous and too thin sensitizing layer (Figure I.9 d).

(d) Its crystalline quality has to be good in order to avoid charge recombination within the layer. The lifetime of photogenerated electrons should be higher than the diffusion time to reach the ZnO nanowire. Potential barriers at the interfaces due to poor quality of the materials might also hinder the charge separation (Figure I.9 e) [49].

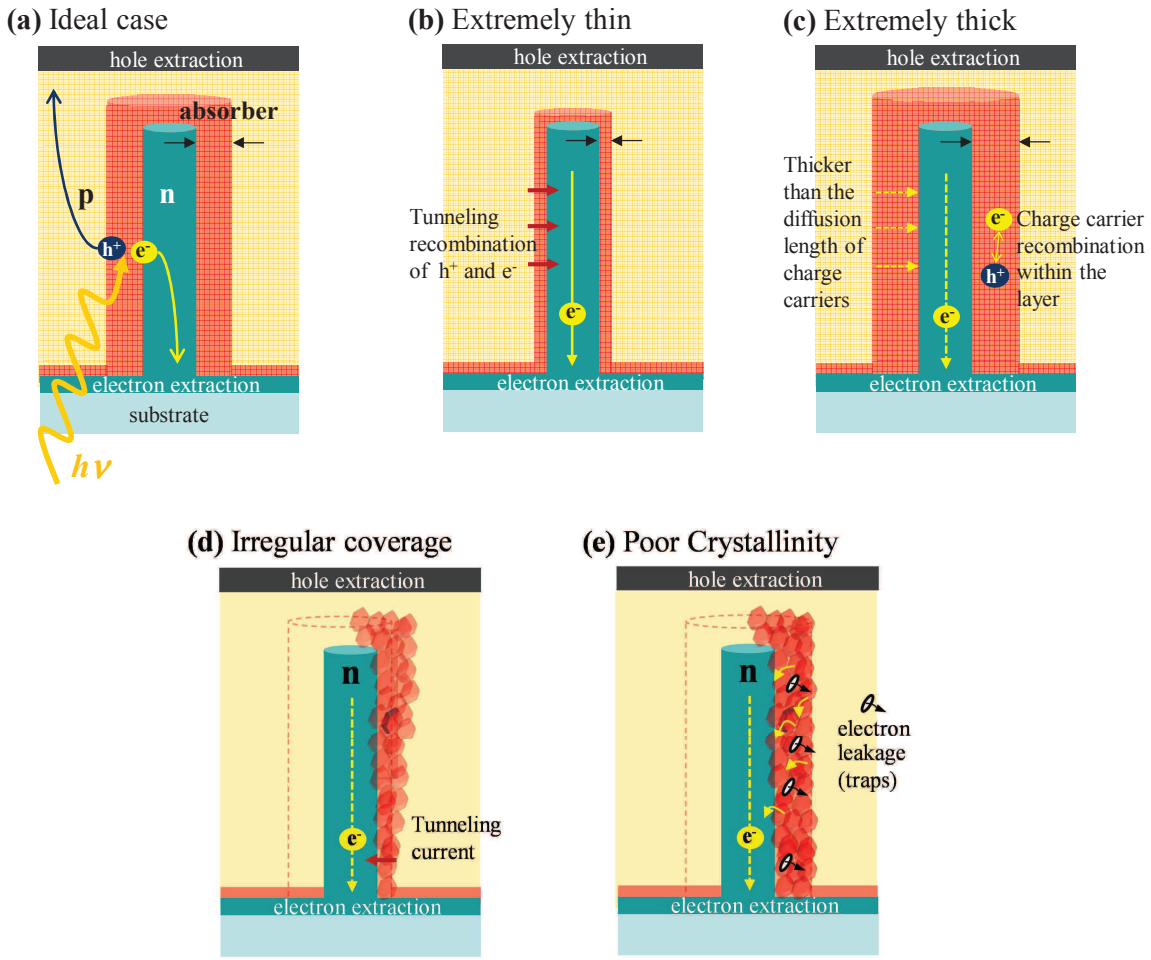

Figure I.9. (a) Scheme of the cross section of a single p/absorber/n heterostructure in the *eta*-solar cell; Effects of the absorber layer: (b) extremely thin layer might present tunneling currents; (c) Extremely thick layer could hinder the electron collection due to low diffusion length of photogenerated carriers; (d) Non uniform layer might present shunts in uncovered areas and inefficient charge separation and (e) poor crystalline layer might present losses due to recombinations at grain boundaries.

Table I.3 Dependence of the *eta*-solar cell performance on the absorber layer properties.

Layer property	**Effects**	**Influence in cell performance**
Small thickness	High Tunneling current Low shunt resistance	high J_{sc}, low V_{oc} low FF
Large thickness	High shunt resistance High series resistance	high V_{oc}, low J_{sc} low FF
Defects in the absorber layer	Shunts by tunneling Low optical absorption	high J_{sc} low V_{oc}, low FF
Fluctuations of thickness	Shunts by tunneling Low optical absorption Poor interface (p-i-n) (deficient charge separation)	high J_{sc} low V_{oc}, low FF

2.3. The P-Type Hole Transporting Semiconductor

The DSSC is the best example of the potential of nanostructures for the development of low-cost photovoltaic devices [15]. However technical complications on the sealing of the cell have limited its industrialization. As a consequence, the development of a solid-state version of this cell has received considerable interest.

Spiro-OMeTAD [50, 51], poly(3-hexylthiophene) (P3HT) [52], Cu_2O [43], ZnTe [53], PEDOT:PSS [36] and CuSCN [32, 38, 46] have been used as solid hole-transporting materials aiming to avoid the use of liquid electrolytes.

Modeling and analysis of all-solid semiconductor sensitized solar cells have reported that two processes take place in the hole transporting material [54, 55]:

i) An additional series resistance intrinsic of the material, reducing the fill factor (FF) and
ii) The recombination at the absorber interface limiting the open circuit potential V_{oc}.

Investigation on deposition methods that allow the control of the material properties would be crucial to overcome such limiting factors and would allow to finally exploit the advantages offered by the all-inorganic nanostructured solar cells.

3 THE MATERIALS FOR THE eta-SOLAR CELL

3.1. Zinc Oxide (ZnO)

ZnO is a technologically valuable semiconductor. Research on ZnO goes back to the 1960s, even earlier, and it has already found numerous industrial applications.

Recent technological progress in electronics and optoelectronics requires the development of novel multifunctional devices. Apart from the required material properties, cost effectiveness and simplicity of design are among the concerns related to the materials selection. ZnO is a potential candidate not only due to its unique properties but also due to the facility to prepare it in wide range of morphologies using variety of techniques.

ZnO possesses probably the richest family of nanostructures with a vast variety in shapes and in properties. For example, ZnO nanostructures such as nanocombs, nanorings, nanohelixes, nanosprings, nanobelts, nanowires and nanocages have been synthesized by both physical and chemical methods. The resulting morphology depends on the deposition technique and growth conditions. The rich family of morphologies of ZnO stems from the differences between the energies of ZnO surfaces. Under thermodynamic equilibrium conditions, the highest growth rate is along the c-axis (in the more stable wurtzite structure). Therefore, the control of growth kinetics makes it possible to change the growth behavior and thus the morphology of ZnO nanostructures. Figure I.10 shows the typical growth morphologies of one-dimensional ZnO nanostructures, and Table I.4 summarizes the most used deposition methods along with the obtained ZnO structures.

Besides of the multiple structures in which ZnO can be synthesized, ZnO is a versatile functional material. Optical properties like wide direct bandgap (3.3 eV at room temperature), large exciton binding energy (60 meV at 300K) make it suitable for applications in lighting, lasing or photovoltaics. Its piezoelectric and pyroelectric nature (granted by large electromechanical coupling and the lack of centre of symmetry in wurtzite) allow the creation of mechanical actuators, piezoelectronic sensors and nanogenerators. Its chemical composition, electrical and photosensitive characteristics make it a viable candidate to develop gas sensors, photodetectors and to be used in photocatalysis. Additionally, doping of ZnO (with aluminium-AZO, indium-IZO or gallium GZO) is of great interest to replace the more commonly used indium tin oxide (ITO) as transparent conducting electrodes. Although ZnO is foreseen for many industrial applications, optoelectronic devices entirely based on it

so far cannot be produced due to the inability to change its conductivity (p-type ZnO) [56]. Nevertheless, ZnO remains a good candidate as electron conductor in solar cells. Properties of ZnO and devices using ZnO are listed in Table I.5.

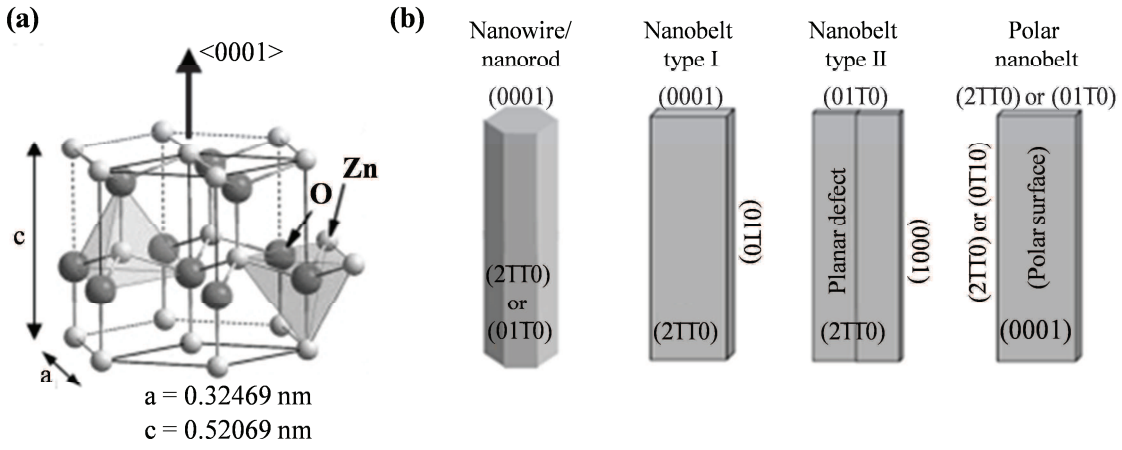

Figure I.10. (a) ZnO hexagonal wurtzite crystal structure (arrow indicates the growth direction). (b) Typical growth morphologies of one-dimensional ZnO nanostructures and the corresponding facets. The Polar surfaces arise from the alternating planes of tetrahedrally coordinated O^{2-} and Zn^{2+} ions stacked along the c-axis in the wurtzite structure [56].

Table I.4 Summary of deposition methods and nanostructures of ZnO.

Methods	**Obtained nanostructures**	**Temp in °C***	**Ref**
Vapor phase			
*Chemical Vapor Deposition (CVD)***	Nanowires, dendritic side-branched/comb-like structures, nanosheets, nanobelts, nanorings, nanoribbons, nanohelices, thin films.	800 (VLS) 1150-1400 (VS)850 (VSS)	[57–60]
Metal-organic CVD (MOCVD)	nanorods	500	[61]
Assisted Pulsed Laser Deposition (PLD)	nanorods	700	[62]
Solution routes			
Chemical Bath Deposition (CBD)	Nanowires, microtubes, nanoplates, flower-like	95	[63, 64]
Electrodeposition	Nanowires, thin films, porous films, hollow urchin-like	80	[65–67]
Hydrothermal	Nanoparticles, powder, Nanowires	90-200	[68]
Spray pyrolysis	Thin films	400	[69]

* The highest temperature is given. It could be the substrate temperature or the temperature at which the source material was heated.

** Vapor-liquid-solid (VLS), vapor-solid (VS) and vapor-solid-solid (VSS) processes.

Table I.5 ZnO nanostructure properties and applications

Properties	**Value**	**Applications**	**Ref**
Optical			
Direct bandgap *Exciton binding energy* *Refractive index* *Transparency to visible light*	3.37 eV (380 nm) 60 meV 1.96 at 1064 nm	Lasing, optical cavities, waveguides, light emitting diodes (homojunctions and p-n junctions), solar cells, photocatalysis, and photodetectors.	[70–74]
Electrical			
Carrier concentration: - *bulk* - *single NW* - *NW array* *Conductance* [75]: - *single NW* *Mobility:* - *bulk (300K)* - *single NW:*	 <10^6 cm^{-3} 4.0 x 10^7 cm^{-3} 6.2 x10^{19} cm^{-3} ~1.6 x 10^{-7} S μ_e=100-200 cm^2/Vs μ_h=5-50 cm^2/Vs Up to μ_e=80 cm^2/Vs	Field effect transistors, sensors, DSSC, hybrid and *eta*-solar cells.	[56] [76–79]
Piezoelectric			
Piezoelectric coefficient: [80] - *bulk* - *nanobelt*	 d_{33}=10pm/V d_{33}=26.3 pm/V	Nano electromechanical systems, piezoelectric sensors, mechanical energy conversion.	[81] [82]

3.1.1. ZnO Electrodeposition (ECD)

ZnO and especially ZnO nanowires have attracted the attention of the research community. Their interesting properties that arise from their dimensions in the nanorange have prompted the development of innovative devices, especially solar cells. As can be seen in Table I.4 most common methods for ZnO nanowires growth require high temperatures.

Electrochemical method has shown to be an advantageous technique for the deposition of ZnO 2D layers and NWs. It is a low temperature deposition technique that does not require complex procedures, advanced equipment and delicate experimental conditions [83]. Furthermore, working at lower temperature prevents damages of the substrate and the active

materials, which makes electrochemical deposition (ECD) well suited for the deposition on flexible substrates.

One of the main goals of this thesis is to show that semiconducting material with required properties could be prepared by low cost techniques In this way, a balanced cost-efficiency relation would contribute to the progress of the photovoltaic industry. Due to this reason, we choose the electrochemical deposition method for the growth ZnO 2D and NW arrays. Furthermore, we explore the galvanostatic deposition mode due to the fact that it has a higher potential for industrialization compared to the potentiostatic one.

Electrochemical Deposition Principle of ZnO

Generally the deposition of ZnO thin layers is based on the nitrate reduction method [84–86] because it allows the fast deposition of thick films. An alternative method to form ZnO electrochemically is based on the reduction of molecular oxygen O_2 [65, 87–93] or hydrogen peroxide, H_2O_2 [94, 95]. The last precursor shows strong limitation in its use, due to poor electrochemical kinetics. The reduction of dissolved O_2 exhibits favorable kinetics and does not produce unwanted reaction products.

We chose to use O_2 as precursor due to the above mentioned advantages. This method, when aqueous solution with zinc chloride as zinc precursor is used, was proposed by Peulon and Lincot [65]. The O_2 reduction method is especially well suited for the fabrication of nanowire arrays [45, 96] whose dimensions can be easily monitored by controlling the electrodeposition parameters: concentration of precursors, deposition temperature, applied current density or deposition potential, and total passed charge density [89, 97]. Moreover the limited solubility of O_2 in hot water and thus the lower rate of the electrodeposition process could be turned in advantage for the preparation of ZnO thin films than thick ones.

The principle of the ZnO electrodeposition using O_2 as precursor is depicted in Figure I.11: OH^- generation occurs upon application of a potential or a current (mixed two and four-electron pathway according to Equation I.1 and Equation I.2 [93]), the accumulation of OH^- causes a rise of the pH at the vicinity of the electrode and the formation of $Zn(OH)_2$ is prompted by the presence of Zn^{2+} in the solution. Subsequent transformation of $Zn(OH)_2$ into ZnO (Equation I.3) is influenced by the bath temperature (room temperature favoring $Zn(OH)_2$ stabilization [90]).

$O_2 + 2H_2O + 2e^- \rightarrow H_2O_2 + 2OH^-$ $E°= -0.065\ V\ (NHE)$ **Equation I.1**

$O_2 + 2H_2O + 4e^- \rightarrow 4OH^-$ $E°= 0.401\ V\ (NHE)$ **Equation I.2**

The overall reaction for zinc oxide formation is:

$Zn^{2+} + ½\ O_2 + 2e^- \rightarrow Zn(OH)_2 \rightarrow ZnO + H_2O$ $E°= 0.93\ V\ (NHE)$ **Equation I.3**

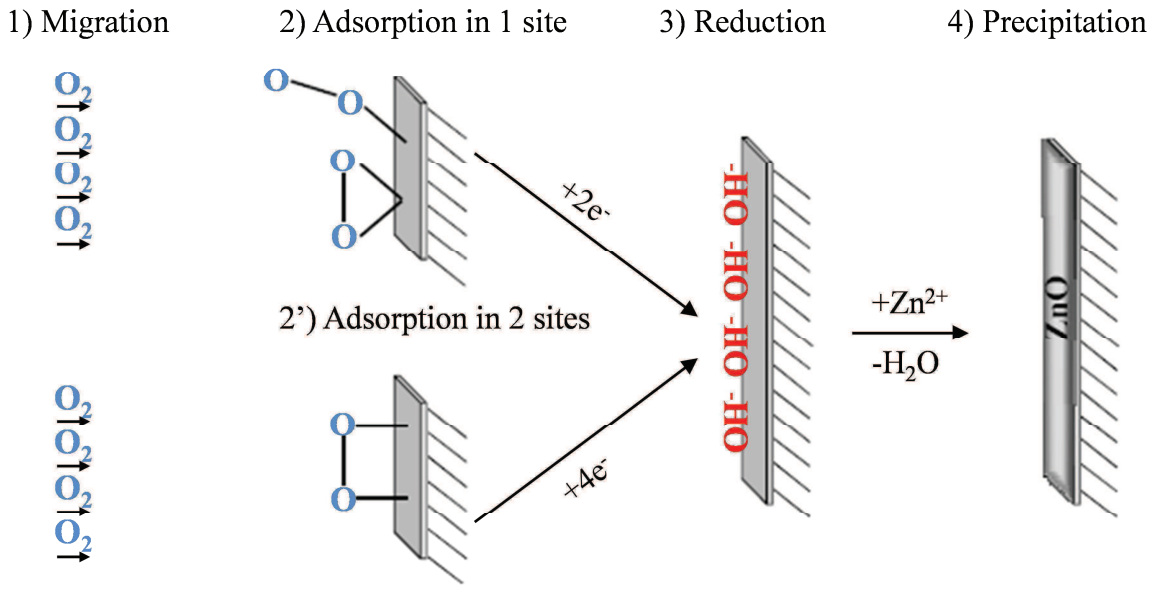

Figure I.11. Schema of the ZnO electrodeposition from O_2 reduction [98].

3.2. The Photosensitizing Semiconductors (CdS, CdSe and CdTe)

The development of the nanostructured solar cells has been in great extent due to excellent properties of semiconductors such as ZnO and TiO_2. In particular, the richness of the obtainable morphologies, the n-type conductivity and well-developed synthesis methods of ZnO make it suitable as main component in the nanostructured solar cells. However, ZnO can only absorb light in the UV region due to its wide bandgap (3.3 eV). Among the promising choices to increase its light harvesting capabilities in the visible region (400-800 nm) is the sensitization with narrow bandgap materials.

The thin film solar cells have shown to be both efficient and cheap relative to the single-crystalline Si counterparts. Conversion efficiencies of 19.9 and 16.5% have been achieved using $Cu(InGa)Se_2$ [99] and CdTe [100] as absorbing materials. However, drawbacks concerning scarcity of tellurium and indium are among the main constrains for the further industrial development of thin film solar cells based on such materials.

Recently, several semiconductors have been compared with respect to their extraction cost and the annual electricity production potential. The so-called "highly strategic potential" materials are proposed as a solution to the energy related problems [101]. Pyrite (FeS_2), copper sulfide (Cu_2S), copper oxide (CuO), a-Si:H and lead sulfide (PbS) were found to be among the front runners. FeS_2 for example is a highly absorbing material (0.95 eV) that can be produced from abundant and non-toxic materials at relatively low cost [49].

The Choice of Materials

Despite the encouraging results on other novel earth-abundant materials such as $Cu_2ZnSn(Se, S)_4$ [102], and the attractiveness of the above mentioned materials, appropriate deposition techniques must be found to take advantage of their properties. Moreover materials combinations for contacts or heterojunction formation must be carefully designed.

To date CdTe [32], CdSe [29, 46], In_2S_3 [103], $CuInS_2$ [41, 104] conformal coatings on ZnO nanorods were prepared for the fabrication of *eta*-solar cells. Despite the pioneer efforts, the achieved efficiencies (up to 4.17 % with $CuInS_2$ [41]) remain low to be considered for industrialization. Moreover, some of the preparation methods required expensive equipment and complex procedures that impede the control over the layer properties and thickness.

*In this thesis CdS, CdSe and CdTe were chosen as photosensitizers due to the extensive knowledge on synthesis methods and properties of these materials. Industrially-wise, the production lines and recycling methods are well established for CdTe modules, for instance. The development of a cost-efficient CdTe-based nanostructured solar cell could boost the solar energy production without significant changes in technology or equipments. Moreover, low cost chemical deposition methods like SILAR or QD sensitization could tackle the problems related to the scarcity of Te. Additionally, the band alignment between the studied materials and ZnO follows the type-II which is required in the eta-solar cells (*Figure I.12*).*

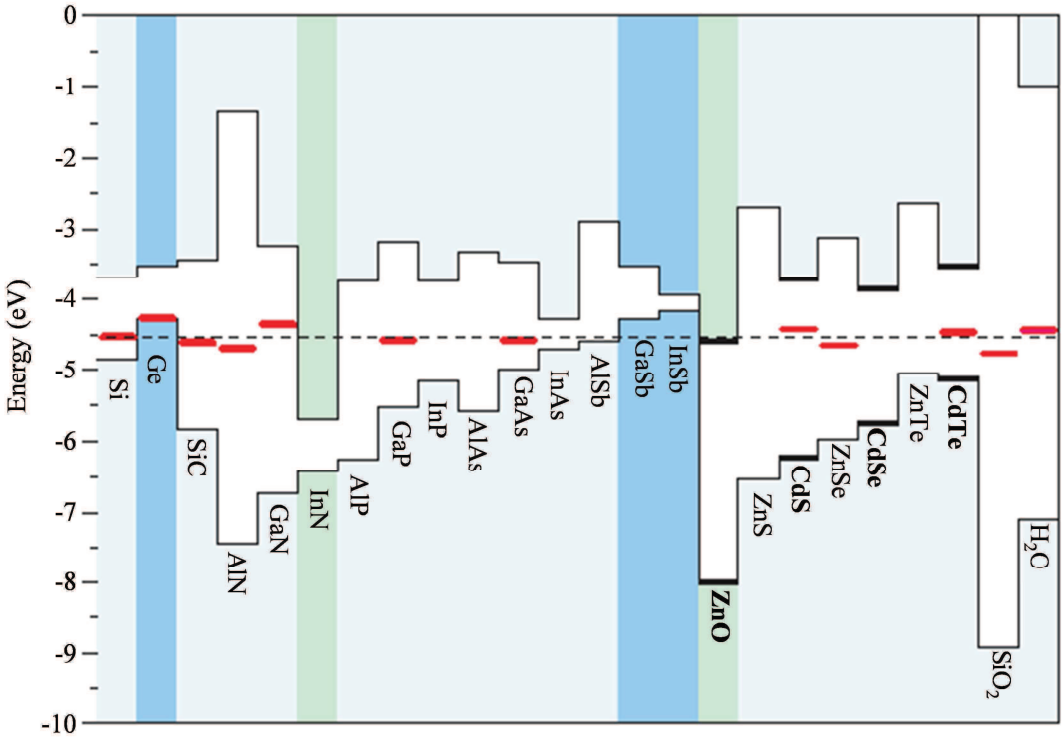

Figure I.12. Relative positions of the conduction band minimum and valence band maximum for a number of semiconductors and insulators [105].

3.2.1. Cadmium Sulfide (CdS)

Cadmium Sulfide (CdS) is a II-VI direct bandgap semiconductor material extensively studied in the past decades. Its interesting properties and easy-synthetic methods have allowed its integration in a wide range of applications from sensing to water splitting systems and other optoelectronic applications (Table I.6) [106, 107].

In photovoltaics, interfacing of n-type CdS layer has improved the performance of thin-film solar cells. Important optical and electrical effects were identified in the CdS layers used as window material and high efficiencies have been achieved for CdTe, $CuInGaSe_2$ (CIGS) and InP/CdS/ZnO thin film solar cells [108, 109].

In the third generation solar cells realm, CdS shares a good presence despite the toxicity of *Cd*. Novel architectures and encouraging solar cell efficiencies have been demonstrated using CdS [110, 111]. ZnO/CdS core/shell heterostructures have been previously demonstrated using Hydrothermal, MOCVD, and CBD methods [112–114]. However, the studies are focused only on the synthesis and paid no attention to the control of the thickness, morphology, and coverage of CdS shell. Other works on SILAR deposition of the CdS absorber showed interesting results for photovoltaics but the results of their efficiencies were not reported [115–119]. Moreover, CdS by SILAR has not yet proposed to be used in the *eta*-solar cell.

The core/shell architecture in *eta*-solar cells using ZnO NWs as core and CdS as the sensitizing shell appears as a good choice. Their application could permit to take advantage of both guided charge collection by the ZnO nanowires as a highway for the electron transport, and exploiting the properties of CdS as sensitizer. Briefly, the use of CdS as sensitizer in the *eta*-solar cell seems promising due to the following arguments:

(a) Wider bandgap of CdS (2.4 eV) increases the absorption of bare ZnO structures in the solar spectrum region.
(b) The type-II band structure of the ZnO/CdS heterostructure and the energy difference between the conduction band edges of CdS and ZnO (positioned at -4.1 and -4.3 eV respect to vacuum for CdS and ZnO respectively) promotes charge separation.
(c) CdS is a potential candidate as an interfacial layer between ZnO and other narrow bandgap materials such as CdSe, CdTe, $CuInS(e)_2$, among others.

The photovoltaic mechanism of the ZnO nanowire/CdS core/shell heterostructure obeys the following principle (Figure I.13): photogenerated charge carriers in the CdS absorber layer are separated due to the type-II band structure. The position of the conduction band edges produces the required driving force for the transfer of excited electrons from CdS towards ZnO [119]. The higher electronegativity of CdS compared to CdSe or CdTe could further reduce the rate of recombination between electron-hole pairs.

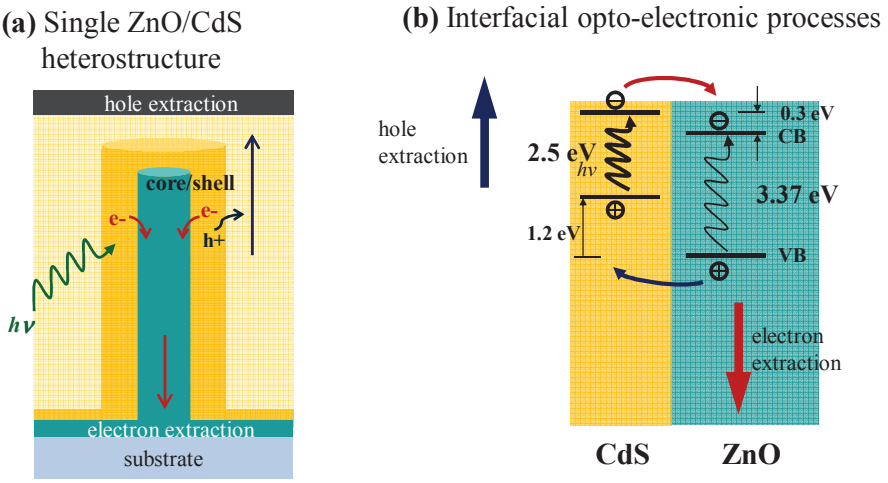

Figure I.13. (a) Scheme of a single ZnO/CdS core/shell heterostructure for the *eta*-solar cell. (b) Schematic illustration of the type-II bandgap alignment: interfacial charge generation, separation and transfer between ZnO and CdS in the nanostructure are shown [112].

CdS Deposition Method

In this thesis, the electrochemically grown ZnO nanowire arrays were sensitized with CdS thin layers via a classical Successive Ionic Layer Adsorption and Reaction (SILAR) technique. By this method, developed at CEA-LETI by Y. Nicolau et al. in 1984 [120–125]*, CdS layers were prepared in a reproducible and controllable way. The semiconducting absorber was deposited by sequential immersions of the ZnO NW arrays in solutions containing corresponding* Cd^{2+} *cations and* S^{2-} *anions. Further experimental details and the SILAR deposition method can be found in chapter II.*

CdS Properties

Cadmium sulfide is an inorganic compound that occurs in nature with two different crystal structures: hexagonal wurtzite (more stable) and the cubic zinc blende (Figure I.14 a). In both forms, the cadmium and sulfur atoms are four coordinated. Table I.6 lists the most common deposition methods, properties and applications of CdS.

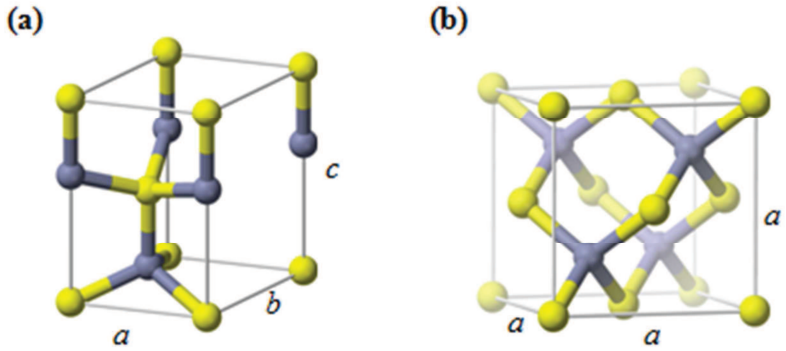

Figure I.14 (a) Wurtzite and (b) zinc blende unit cells [126].

Table I.6 Summary of the deposition methods, properties and applications of CdS

Methods	**Properties**	**Applications**	**Ref**
Chemical Bath Deposition (CBD), *Metal Organic Chemical Vapor Deposition (MOCVD),* *Sol gel,* *Sputtering,* *Electrodeposition,* *SILAR,* *Molecular Beam Epitaxy (MBE)*	n-type semiconductor, Direct bandgap: 2.42 eV, Melting point: 1750 °C, Refractive index: 2.529, Unit cell hexagonal: a=4.12, b=4.12 c=6.72 (Å) α =β=90, γ=120 (°)	Laser diodes, n-type material in solar cells (thin film layer, nanowires or extremely thin sensitizing layer), photoresistors, thin film transistors.	[126]

3.2.2. Cadmium Selenide (CdSe)

The use of CdS as sensitizer in the *eta*-solar cell and other nanostructured solar cell seems a good alternative. However, the bandgap of CdS is not optimum to capture the available solar spectrum and photons with energies below its bandgap (2.4 eV) would not be harvested.

Lower bandgap sensitizers CdSe, CdTe, CIS, CIGS and CZTS seem to be good choices to further enhance the capture of solar radiation. Among the available sensitizing materials, CdSe represents a viable option to be used in the *eta*-solar cell: its bandgap (1.7 eV) will extend the light absorption up to 700 nm, its conduction band edge is energetically more negative than that of CdS (Figure I.15) and the extensive research in synthetic routes and material properties would permit to have more control over desired characteristics in the nanoregime [127–130].

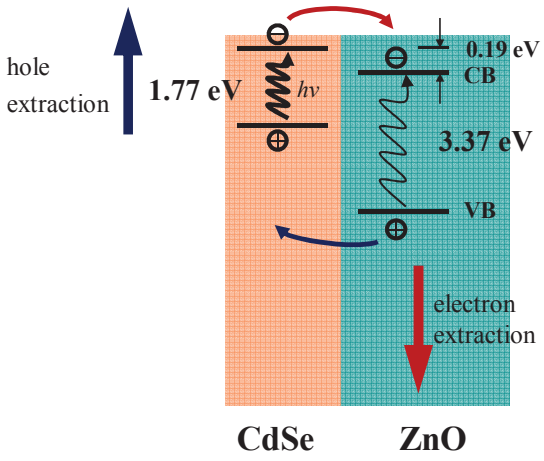

Figure I.15. Energy-band alignment and charge-transfer mechanism between ZnO and CdSe extremely thin sensitizer [131].

Eta-solar cells using CdSe as sensitizer have been previously published. The coverage of the ZnO nanowires was carried out mainly by electrochemical routes, magnetron sputtering and vapor phase deposition. Although the reported results are encouraging, the use of a solution-base technique for the fabrication of photoanodes to be applied in the *eta*-solar cell seems rather attractive. In one hand, the some electrolytes for the electrodeposition are not ZnO friendly (pH acidic or basic), and also, the high temperatures in vapor phase methods

limit the use of substrates and higher growth rates make difficult to control the shell thickness. [29, 30, 43, 132–135].

CdSe Deposition Method

In this work, the fabrication of ZnO/CdSe nanowires was carried out by SILAR technique. The expertise gained in the synthesis of CdS by the same method is applied for the deposition of CdSe conformal layers. Ionic solutions containing Cd^{2+} and Se^{2-} in ethanol were used as sources and the shell thickness was controlled by the number of SILAR cycles. The deposition was performed at room temperature. Approaches for the improvement of material crystalline quality and interfaces were also proposed.

CdSe Properties

Cadmium selenide is a direct bandgap II-VI semiconductor which has been applied in a wide variety of applications but it is mostly used for biomedical imaging in the form of nanoparticles. Three crystalline forms are known: wurtzite, sphalerite and rock-salt, but wurtzite is the most stable. Table I.7 lists the most common deposition methods, properties and applications of CdSe [136].

Table I.7 Summary of the deposition methods, properties and applications of CdSe

Methods	**Properties**	**Applications**	**ref**
Chemical Bath Deposition (CBD), *Electrodeposition,* *SILAR* *Molecular Beam Epitaxy (MBE)*	n-type semiconductor, Direct bandgap: 1.74 eV, Melting point: 1268 °C, Refractive index: 2.5 Unit cell hexagonal: a =4.2, b=4.2, c=7 (Å) α =β=90, γ=120 (°)	Laser diodes, nanosensing, biomedical imaging, sensitizer in *eta* and QDs solar cells solar cells, thin film transistors	[136–142]

3.2.3. Cadmium Telluride (CdTe)

CdTe is a II-VI semiconductor with a high optical absorption coefficient (>10^4) and narrower bandgap (1.5 eV) than CdS and CdSe. This makes CdTe a better candidate for the development of solar cells [45, 143]. Modules based on polycrystalline thin-film CdS/CdTe solar cells have already made the transition from laboratory research to large manufacturing scales. The obtained efficiencies (up to 11 % in modules, [8]), close to that of traditional Si technologies, are due to the unique physical properties of CdTe. The use of only about 1 % of CdTe, amount compared to the one required for Si, remains among one of the advantages of choosing CdTe in photovoltaic technology [144].

In the *eta*-solar cell, various sensitizers have been explored for the development of more efficient photoanodes. PbS [145], In_2S_3 [38] and CdTe [45, 143]. Among them, CdTe seems the most promising due to the extensive research in synthetic methods and the vast understanding of the material properties. Despite the scarcity problems related to Te and toxicity of Cd, the synthetic methods for CdTe layer and nanocrystals are fully developed and matured. Moreover the band alignment between ZnO and CdTe follows the type-II configuration which warranties the charge separation and transfer in the heterostructure (Figure I.16).

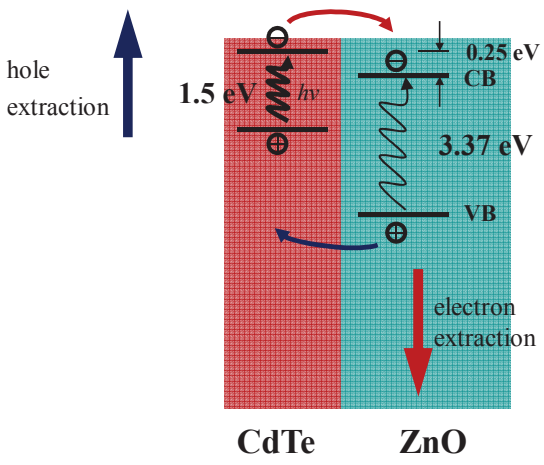

Figure I.16. Energy-band alignment and charge-transfer mechanism between ZnO and CdTe extremely thin sensitizer [146].

CdTe Deposition Methods

In this thesis, the explored preparation methods for the deposition of CdTe extremely thin layer on ZnO NWs were SILAR, QDs functionalization and Close Spaced Sublimation (CSS).

- *The sensitization of the ZnO NW array by SILAR was carried out in ethanolic solutions at room temperature. Ionic solutions containing Cd^{2+} and Te^{2-} were used as sources and the shell thickness was controlled by the number of SILAR cycles. Annealing and chemical treatment ($CdCl_2$) were also performed as in the case of CdSe.*
- *The sensitization of ZnO NW arrays with CdTe QDs was performed by a layer-by-layer (LbL) deposition method. The CdTe shell on the ZnO NWs was formed by alternate layers of water-soluble CdTe nanoparticles (with a negative surface charge) and a polymer (polyelectrolyte) with positive charge centres (poly-(diallyldimethylammonium), PDDA) using a layer-by-layer (LbL) method* [147, 148]. *The sensitization with CdTe QDs was part of collaboration with Dr. Peter Reiss, Dr. Dmitry Aldakov from CEA/INAC and Prof. Marco A. Schiavon from Universidade Federal de São João del-Rei, Brasil.*
- *CdTe films by CSS were prepared at 580 and 480 °C (source and substrate temperature respectively). Both CdTe source and substrate are supported by graphite blocks, which are heated independently by quartz lamps. The CSS deposition was performed in homemade CSS equipment at the Optoelectronic Department of CEA-Leti (DEOPT) in the frame of the project "New Concepts Solar Cells with II-VI Semiconductor Nanostructures" supported by the Nanosciences Foundation of Grenoble.*

CdTe properties

Despite concerns related to toxicity of *Cd* and scarcity of *Te*, CdTe represents the second most utilized solar cell material in the world. Its most stable crystalline form is the cubic zinc blende. Table I.8 lists the most common deposition methods, properties and applications of CdTe [149, 150].

Table I.8 Summary of the deposition methods, properties and applications of CdTe

Methods	**Properties**	**Applications**	**Ref**
Chemical Bath Deposition (CBD), Electrodeposition, SILAR Molecular Beam Epitaxy (MBE)	p-type semiconductor, Direct bandgap: 1.44 eV, Melting point: 1092 °C, Refractive index (600 nm): ~3, Absorption coefficient: 6×10^4/cm Unit cell cubic: a =b=c=6.48 (Å) α =β=γ=90 (°)	Thin film solar cells, sensitizer in *eta* and QDs solar cells solar cells, infrared detectors (HgCdTe), X-ray detectors (CdZnTe)	[149], [150]

3.3. Copper Thiocyanate (CuSCN)

CuSCN is a wide bandgap p-type semiconductor that has found various applications in optoelectronic devices such as transparent transistors, light emitting diodes and solar cells [151]. CuSCN has shown to serve as transparent hole conductor in DSSC [152–155] and other solid state solar cells [26, 156]. Although the penetration into nanoporous TiO_2 or ZnO-NW arrays seem to be an important issue that deserves to be studied [157], in eta solar cells, the highest energy conversion efficiencies have been obtained when using CuSCN.

The p-type character of CuSCN is thought to be due to copper vacancies [158, 159]. Two structures of CuSCN have been identified: 1) the hexagonal or rhombohedral β-phase [160, 161] and 2) orthorhombic α-phase [162]. Although in both the Cu atoms are tetrahedrally coordinated (by one N atom and three S atoms), the difference between phases stems from the fact that: i) the N-Cu bonds are collinear in the β-phase whereas there is a slight tilt bend at the N atom in the α-phase, and ii) the SCN units are parallel to each other along the c-axis in the β-phase, while they are canted in an alternating in the α-phase. Table I.9 lists the most common deposition methods, properties and applications of CuSCN.

CuSCN Deposition Methods

In this thesis, the preparation of CuSCN by three methods is studied: Impregnation ECD and SILAR.

The deposition by Impregnation was carried out from a CuSCN-saturated n-propyl sulphide solution [163].

SILAR as for the case of the photosensitizers, seems an attractive technique due to the fact that good infiltration of the material could be achieved. CuSCN was deposited from aqueous ionic solutions containing Cu^{+} *and SCN- ions as sources* [164].

The ECD deposition technique was explored since it represents a good choice for industrialization. CuSCN was deposited from aqueous electrolyte solution containing Cu^{2+}, SCN^{-} *and triethanolamine (TEA,* $N(CH_2CH_2OH)_3$*) to chelate with* Cu^{2+} *cations* [165].

Table I.9. Summary of the deposition methods, properties and applications of CuSCN.

Methods	Properties	Applications	Ref
Electrodeposition, *Impregnation,* *SILAR*	p-type semiconductor, Bandgap: 3.6 eV, Conductivity at 30°C = 1.92 10^{-4} mhos cm^{-1} Unit cell hexagonal: a =b= 3.85, c= 10.93 (Å) α =β=90, γ=120 (°) Unit cell rhombohedral: a =b= 3.85, c= 16.44 (Å) α =β=90, γ=120 (°)	Transistors, light emitting diodes and nanostructured solar cells	[154] [163] [151]

CHAPTER II : Experimental and Characterization Techniques

This chapter describes the experimental conditions and characterization techniques used in this thesis.

In the first part the different deposition methods and detailed conditions for the preparation of the used materials are given. Chemical, electrochemical and vapor phase techniques were employed. The fabrication of the all-inorganic and photoelectrochemical *eta*-solar cells is also explained.

In the second part the different characterization techniques used for the analysis of the morphology, structural and optical properties of the prepared materials are described. The solar cells characterization technique is also included.

1 DEPOSITION METHODS

1.1. Electrodeposition

Electrochemical deposition is a process by which a film of solid metal or semiconductor is deposited from a solution of ions onto an electrically conducting surface. The deposited film could have dimensions ranging from nanometers to several micrometers. This method allows variety of nanostructures to be obtained when the deposition conditions are carefully controlled.

1.1.1. Electrochemical Deposition of ZnO Layers and Nanowires

In this work the electrochemical deposition of ZnO 2D layers and NWs was carried out using molecular oxygen (O_2) reduction by the method proposed by the group of D. Lincot [65]. The principle of ZnO electrodeposition by molecular oxygen reduction involves the following processes: i) generation of OH^- anions during the electrochemical reduction of O_2 which could be four or two electron reaction as shown by Equation II.1 and ii) ZnO formation after chemical precipitation of $Zn(OH)_2$ (Equation II.2):

i. Electrochemical reduction of O_2:

$$O_2 + 2H_2O + 4e^- \rightarrow 4OH^-$$

$$O_2 + 2H_2O + 2e^- \rightarrow H_2O_2 + 2OH^- \qquad \textbf{Equation II.1}$$

ii. Chemical precipitation and ZnO formation

$$Zn^{2+} + 2OH^- \rightarrow Zn(OH)_2 \rightarrow ZnO + H_2O \qquad \textbf{Equation II.2}$$

ZnO deposition conditions and chemicals [166]:

- ***Zinc oxide thin films*** were deposited from an aqueous solution containing 5 10^{-3} M $ZnCl_2$ and 0.1 or 1 M KCl. They were prepared galvanostatically at varied current densities between -0.08 and -0.16 mA cm^{-2} or potentiostatically at -1.0 V vs saturated calomel electrode (SCE). The deposition temperature was varied from 25 to 70 °C.

- ***ZnO nanowires*** were grown potentiostatically at -1.0 V vs SCE onto ZnO 2D layers from an aqueous electrolyte containing 5 10^{-4} M $ZnCl_2$ and 1 M *KCl*. The deposition temperature was fixed at 80 °C. For their galvanostatic deposition from the same electrolyte, the following current densities were applied: -0.08, -0.13, -0.18 and -0.23 mA cm^{-2}.

All chemicals were from Fluka ($ZnCl_2$, 97.0 % and *KCl*, 99.5 %) analytical reagent grade and were used without further purification. Prior to the deposition, molecular oxygen was bubbled through the bath till saturation (30 minutes at 0.25 Pa) and it was maintained at a lower pressure during the deposition process. The electrolyte was stirred during deposition using a magnetic stirrer at 300 rotations per minute (rpm).

The deposition was done using a conventional three electrode electrochemical cell (Figure II.1). Electrochemical measurements were performed using potentiostat-galvanostat PARSTAT 2273 (Princeton Applied Research) monitored by the POWERSUITE software. The Table II.1 contains the list of the different substrates used as working electrodes. A helical platinum wire and a saturated calomel electrode were employed as counter and reference electrodes, respectively. 1 cm^2 active area of the working electrode was masked to perform depositions on it.

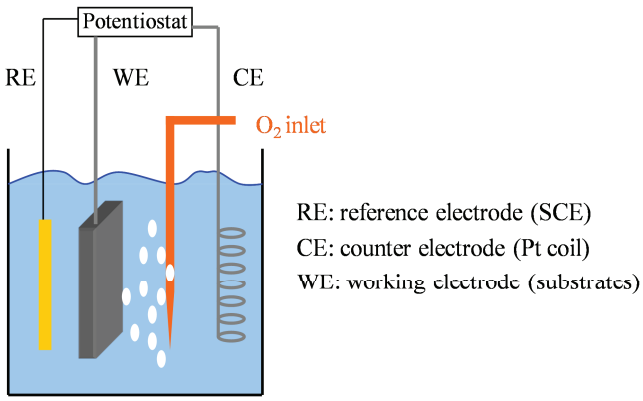

Figure II.1. Three-electrode electrochemical cell used for the deposition of ZnO.

Substrate cleaning procedure:

The substrates were ultrasonically cleaned consequently in acetone, ethanol and isopropanol for 15 min in each solvent, with rinsing steps with hot MiliQ water in-between.

In the case when the Saphire/ZnO 2D layer was used as working electrode, a metallization process by radio frequency sputtering for 6 minutes was carried out after the cleaning procedure with the aim to deposit small gold (Au) nanoparticles (to improve the substrate conductivity).

Table II.1 List of substrates used as working electrodes for the deposition of ZnO layers and nanowires.

Substrate	Properties	Provider
1. Glass substrate covered with transparent conductive oxide ((TCO), fluorine-doped tin oxide ($SnO_2:F$))	resistance of 10 Ω/square (900 nm thickness)	AGC Fabritech Co., Ltd. Japan
2. Bulk c-plane ZnO layer prepared By MOCVD, annealed at 1050 °C.	n-type semiconductor (1.5 μm thickness) Highly resistive	Partner: CEA-LETI/DEOPT
3. Bulk c-plane ZnO layer prepared by MOCVD As deposited at 450 °C	n-type semiconductor (1.5 μm thickness)	Partner CEA-LETI/DEOPT
4. Al_2O_3/c-plane ZnO layer prepared by MOCVD, annealed at 1050 °C.	n-type semiconductor (1.5 μm thickness) Highly resistive	Partner CEA-LETI/DEOPT
5. SiO_2/ TiN(100 nm)/Au (100 nm)	metal	Partner CEA-LETI/DTSI
6. Al_2O_3/c-plane ZnO layer by MOCVD, annealed at 1050 °C, layer of Au QDs by RF sputtering (6 minutes deposition)	metal	Partner CEA-LETI/DEOPT

1.1.2. Electrochemical Deposition of CuSCN

The electrochemical deposition of CuSCN is carried out in a conventional three electrode electrochemical cell (Figure II.1). For this case, the ZnO/absorber heterostructure arrays were used as working electrode. The CuSCN filling material was deposited from an aqueous solution containing 12 mM $CuSO_4\ 5H_2O$ (Sigma-Aldrich 99.995% purity), 60 mM *KSCN* (Sigma-Aldrich) and 120 mM triethanolamine (*TEA*, Sigma-Aldrich). The layers were deposited at -0.5 and -0.4 V vs SCE. The total passed charge was 0.45 C cm^{-2} [165].

For the deposition of CuSCN nanowires electrodeposition, see Appendix A [167].

1.2. Successive Ionic Layer Adsorption and Reaction

The Successive Ionic Layer Adsorption and Reaction (SILAR) is an ionic layer-by-layer deposition process. It is based on the successive surface adsorption and reaction of cations and anions. In the ideal case, a single ionic monolayer is formed during the first adsorption step which reacts with the subsequently adsorbed monolayer of the counter ions and thus a monolayer of the desired compound is formed. In these ideal conditions the thickness of the film should increase linearly with the number of SILAR cycles. Such cycle-dependent layer-by-layer growth is analogous to vapor-phase atomic layer deposition (ALD). Figure II.2 is a schematic drawing of the steps consisting one deposition SILAR cycle.

A complete SILAR growth cycle involves four steps: (i) immersion of a substrate into cationic solution, (ii) rinsing of the substrate to remove loosely bonded M^{n+}, (iii) immersion of the substrate into the anionic precursor, in this manner cations and anions react, and (iv) the substrate is again rinsed with deionized water to remove unadsorbed and unreacted anions from the substrate. The immersions and rinsing times can be varied to control the desired layer morphology. The thickness, structural and optical properties of the as prepared compound were controlled with the number of deposition cycles [120, 123].

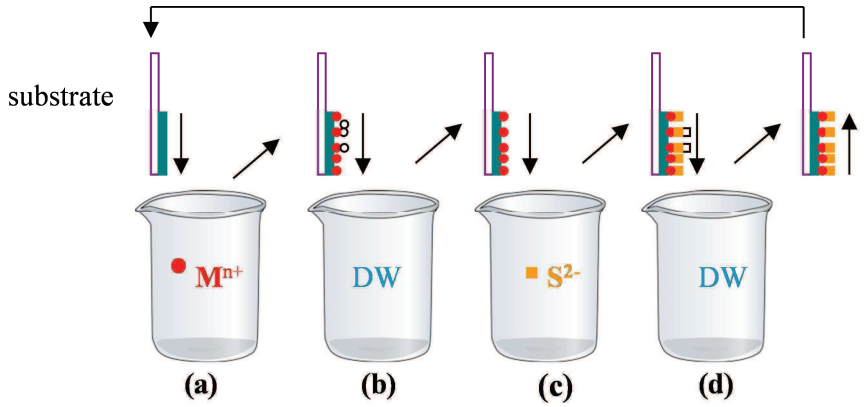

Figure II.2. Schematic drawing of the steps of one SILAR cycle, including: (a) cations adsorption, (b) rinsing, (c) anions adsorption and reaction and (d) rinsing.

CdS, CdSe and CdTe extremely thin absorber layers were prepared by this deposition technique for the photosensitization of electrodeposited ZnO NW arrays thus forming the core/shell nanostructure of the *eta*-solar cell [123, 141, 168].

CuSCN layer as pore filling *p*-type material was also deposited by SILAR method on the core/shell nanostructure to complete the *eta*-solar cell [169, 170].

1.2.1. Cadmium Sulfide Deposition

For the deposition of CdS thin layers, Cd^{2+} and S^{2-} aqueous solutions were prepared. The deposition was performed at room temperature. The immersion and rinsing times were fixed at 20 seconds each. The CdS preparation by SILAR was carried out up to 120 cycles.

***Cd^{2+}* solution preparation:** Cadmium nitrate tetrahydrate (ACROS organics $Cd(NO_3)_2 \cdot 4H_2O$) was used to prepare 50 mM Cd^{2+} cationic aqueous solution (pH =5).

***S^{2-}* solution preparation:** Sodium sulfide monohydrate (SIGMA-ALDRICH $Na_2S \cdot 9H_2O$ ACS reagent >= 98%) 50 mM aqueous solution was used as S^{2-} anionic-source. All chemicals were analytical reagent grade and were used without further purification (pH = 12).

1.2.2. Cadmium Selenide Deposition

For CdSe deposition, two different solutions containing cadmium (Cd^{2+}) and sodium selenide (Na_2Se) ions in ethanol were prepared. The immersion and rinsing step times were fixed at 20 seconds each. This SILAR cycle was repeated up to 20 times.

***Cd^{2+}* solution preparation:** cadmium nitrate tetrahydrate was used to prepare 50 mM Cd^{2+} cationic solution. The chemical was purchased from ACROS organics $Cd(NO_3)_2 \cdot 4H_2O$, purity 99+%.

***Na_2Se* solution preparation:** Sodium selenide (Na_2Se) was prepared by mixing of 60 mM $NaBH_4$ and 0.050 M SeO_2 in ethanol while the container was purged with *Ar*. In this way SeO_2 is reduced by $NaBH_4$ according to Equation II.3. Figure II.3 shows the evolution of the color of the solution with the reaction time till Na_2Se is prepared. After 1 hour Ar-purging and stirring, the solution became clear (with yellowish color) and homogenous. As prepared volume of Na_2Se solution was separated in different flasks to be used for further CdSe SILAR deposition. Na_2Se solution was kept under *Ar* atmosphere to avoid the oxidation. The employed chemicals were from SIGMA-ALDRICH: SeO_2, (purity 99.995%) and $NaBH_4$ (powder, purity 98+ %).

$$SeO_2 + 2NaBH_4 + 6C_2H_5OH \rightarrow Se^{2-} + 2Na^+ + 2B(OC_2H_5)_3 + 5H_2 + 2H_2O$$

Equation II.3

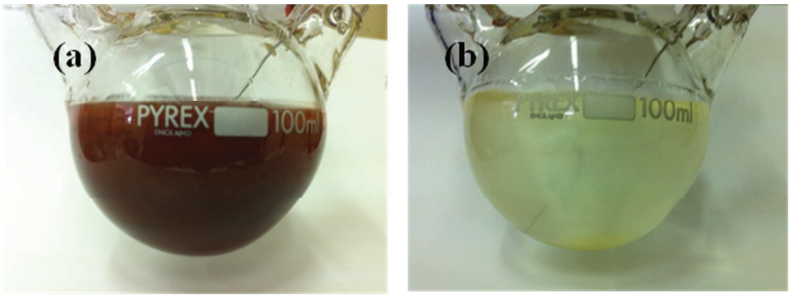

Figure II.3. Evolution of the solution color during the reaction between SeO_2 and $NaBH_4$ with the time: (a) at the beginning of the reaction and (b) after full reduction of SeO_2 to Na_2Se.

1.2.3. Cadmium Telluride Deposition

For the deposition of CdTe sensitizing layer ionic solutions were prepared in similar way as in the case of CdSe.

***Cd^{2+}* solution preparation:** cadmium nitrate tetrahydrate was used to prepare 50 mM Cd^{2+} cationic solution in ethanol. The same chemical was used as for CdSe preparation.

***Te^{2-}* solution preparation:** Te^{2-} was prepared by adding of 1 M $NaBH_4$ to 0.050 M TeO_2 in ethanol while the container was purged with Ar. Figure II.4 shows the evolution of the color of the Te^{2-} solution with the reaction time. After 1 hour *Ar*-purging and stirring the solution color changed from dark grey to clear-pink with dark precipitates. Here we have to note that for the preparation of Te^{2-} solution: the amount of $NaBH_4$ was almost doubled, and the decantation of the solution was required in order to avoid the contamination by Tellurium (*Te*). The decanted pink solution was placed in a different flask for further SILAR deposition of CdTe. This solution is less stable due to the low solubility of Te^{2-}. SIGMA-ALDRICH TeO_2 (purity 99.995%) and $NaBH_4$ (powder, purity 98+ %) were used.

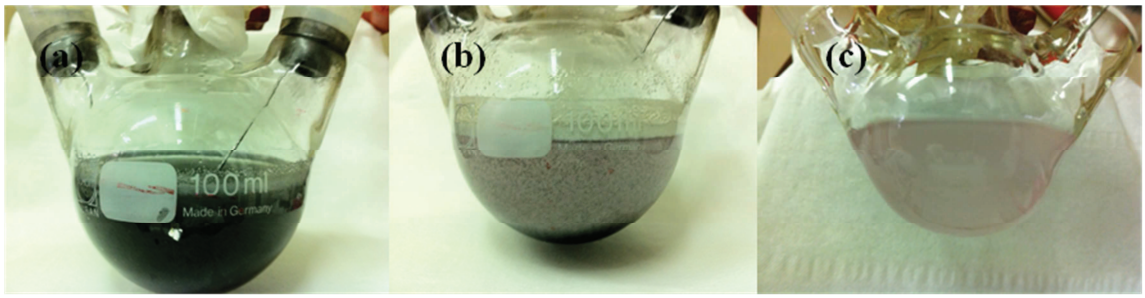

Figure II.4. Pictures showing the color change during the reaction between TeO_2 and $NaBH_4$ with time: (a) initial mixture of the chemicals, (b) after 1 hour purging and stirring and (c) decanted Te^{2-} solution ready to be used for SILAR deposition of CdTe.

1.2.4. Copper Thiocyanate Deposition

CuSCN was deposited on the ZnO NW/absorber heterostructures as pore filling p-type material to complete the *eta*-solar cell. The molar concentration ratio of [$S_2O_3^{2-}/Cu^{2+}$] was varied in order to control the stability of the cationic precursor (Cu^+). The film quality and the deposition rate were influenced by the [SCN^-/Cu^+] molar concentration ratio and the immersion and rinsing times. The used chemicals were from Sigma-Aldrich, analytical reagent grade copper sulphate ($CuSO_4.5H_2O$), sodium thiosulphate ($Na_2S_2O_3$) and potassium thiocyanate (*KSCN*).

Preparation of extremely thin layers of CuSCN: low concentration of ions and short immersion times are applied. 20 seconds immersion and rinsing steps were performed. The number of cycles was up to 30.

***Cu^+* solution preparation:** 30 mM of $CuSO_4.5H_2O$ and 10-60 mM of $Na_2S_2O_3$ were dissolved in deionized water to produce aqueous solution containing Cu^{2+} ions. Cu^+ ions were generated according to Equation II.4.

$$[Cu(S_2O_3)]^- \rightarrow Cu^+ + S_2O_3^{2-} \qquad \textbf{Equation II.4}$$

Based on the heterogeneous precipitation theory of insoluble solid in aqueous solution, CuSCN crystallites are formed and precipitate on the substrate. The stability of Cu^+ ions is determinant from the concentration ratio of [$S_2O_3^{2-}/Cu^{2+}$] in the preparation solution. Below we show the evolution of the solution stability at three molar ratios. In the first case when 10:30 (mM) ratio is tested the solution is opaque with white color due to the CuSCN formation in the bulk solution. In the intermediate case 30:30 (mM), a deposit of CuSCN on the beaker walls is observed. Finally, for the 60:30 (mM) ratio no CuSCN formation was observed; neither in the bulk solution nor on the beaker walls. Figure II.5 shows these effects. Therefore the intermediate molar concentration ratio was chosen as cationic source solution for CuSCN SILAR deposition.

***SCN^-* solution preparation:** The anion precursor was aqueous potassium thiocyanate (*KSCN*) solution with a concentration 30 mM.

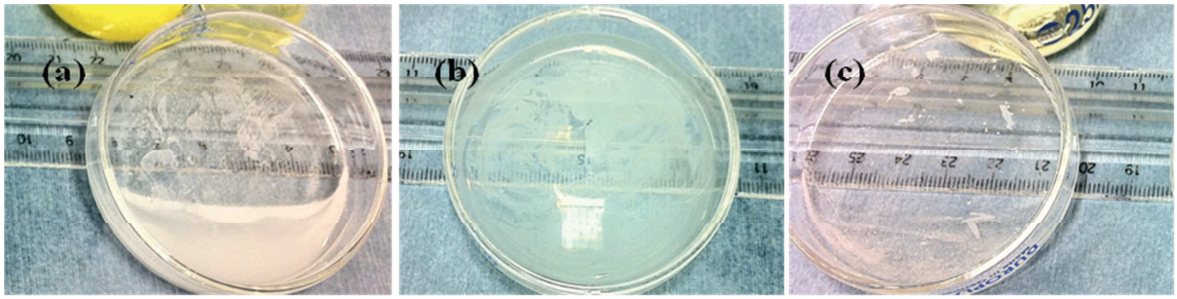

Figure II.5. Concentration ratio effects of [$S_2O_3^{2-}$:Cu^{2+}] on the obtained CuSCN deposit: (a) for 10:30 (mM) the CuSCN formation occurs in the bulk solution, (b) with 30:30 (mM) a white thin film is uniformly covering the beaker walls, and (c) for a ratio of 60:30 (mM) no deposit is observed.

CuSCN as p-type pore filling material for the eta-solar cell: higher ion concentrations and longer reaction times were optimal for the filling of the nanostructures. The immersion times were 40 seconds while the rinsing steps were only 10 seconds. The number of cycles was up to 40.

Cu^+ solution preparation: 50 mM of $CuSO_4.5H_2O$ and 50 mM of $Na_2S_2O_3$ were used to prepare the cationic solution.

SCN **solution preparation:** The anion precursor was aqueous potassium thiocyanate (*KSCN*) solution with a concentration 50 mM.

1.3. Close Spaced Sublimation

The Close Spaced Sublimation (CSS) technique involves the sublimation of a CdTe source which is separated from the substrate by a small distance, usually, millimeters. The kind of source used in this technique strongly affects the control of the deposition parameters, especially the deposition rate. When depositing CdTe thin films by CSS, the most common CdTe sources are: single-crystal or polycrystalline wafers, powders, or pellets. A thick CdTe film deposited onto glass or molybdenum substrate (CdTe source-plate) and then sintered in this work, CdTe thin films were deposited by CSS technique using a CdTe paste as source [171].

CdTe films were deposited on the ZnO thin layers and NW arrays in homemade CSS equipment at the Optoelectronic Department of CEA-Leti. Figure II.6 shows a schema of this deposition set-up. Source and substrate are separated by quartz spacers. Both CdTe source and substrate are supported by graphite blocks, which are heated independently by quartz lamps. This assembly is inserted in a quartz tube, which is vacuum sealed. In this work, the source-substrate distance was fixed to be 2.5 mm. The films were deposited under argon atmosphere using the following deposition parameters: source temperature of 580 °C, substrate temperature of 480 °C, and pressure at 1 Torr. The deposition rates were calculated from the ratio between the film thickness and the deposition time. A paste made of CdTe (5N 99.999% from Sichuan Western Minmetals Co., Ltd) and propylene glycol was used as source.

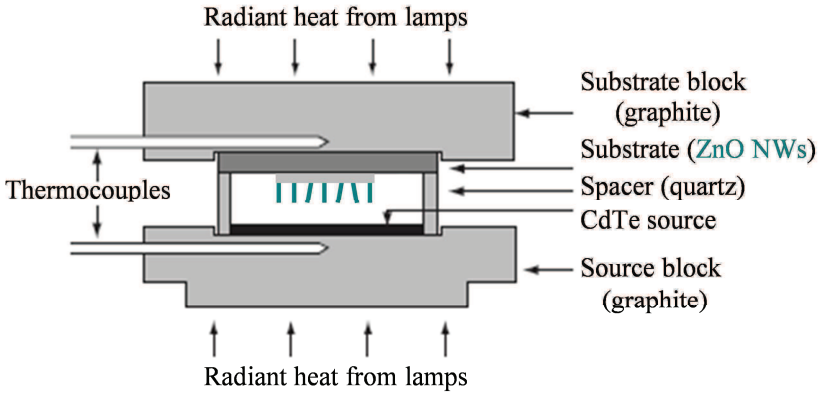

Figure II.6. CSS deposition system [171].

1.4. Quantum Dots Functionalization

CdTe quantum dots (QDs) were prepared by solvo-thermal method by Prof. Marco A. SCHIAVON from Universidade Federal de São João del-Rei, Brasil. The CdTe QDs were capped with different stabilizing molecules (*thioglycolic acid* (*TGA*), *triacylglycerol hydrolase* (*TGH*) and *glutathione* (*GSH*)).

The sensitization of ZnO NWs arrays with CdTe QDs was carried out by a layer-by-layer (LbL) method (Figure II.7). The CdTe shell on the ZnO NWs was prepared by alternate layers of water-soluble CdTe nanoparticles with a negative surface charge, and a polymer (polyelectrolyte) with positive charge centers (*poly-(diallyldimethylammonium)*, *PDDA*) using a layer-by-layer (LbL) method [147, 148].

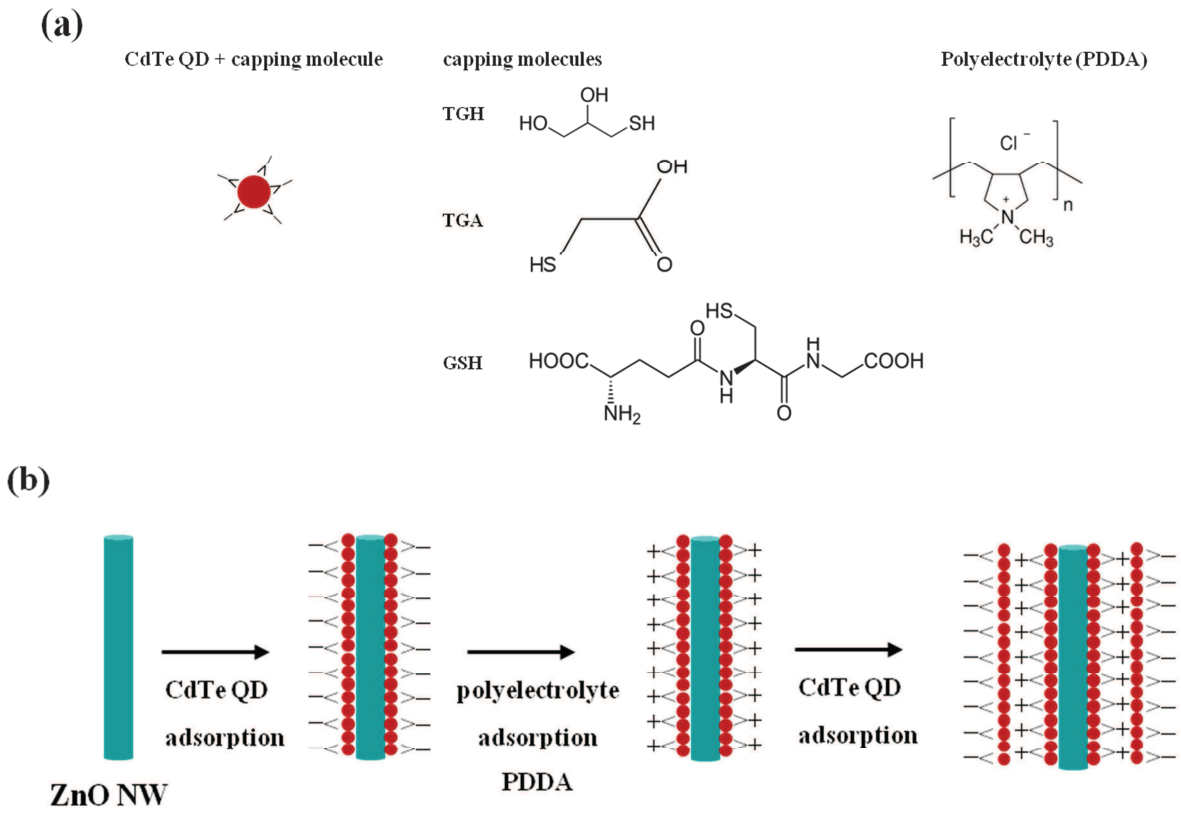

Figure II.7. (a) Components for the sensitization of ZnO NWs with CdTe QDs, and (b) scheme of the LbL QD sensitization process.

The QDs functionalization was carried out in a Microprocessor controlled SILAR deposition system (Figure II.8). The ZnO NW arrays were dipped and withdrawn at 1.0 mm/sec by a robotic arm into the aqueous *PDDA* solution. Then they were rinsed in deionized

water, followed by the immersion in CdTe QDs water solution. Finally, a second rinsing step finishes the cycle and prepares the substrate to start the next deposition cycle.

The immersion times were fixed at 20 seconds and between 10 and 30 bilayers were deposited.

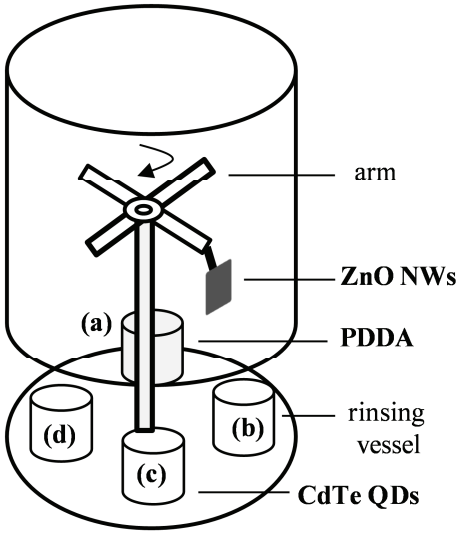

Figure II.8. Computer-controlled LbL deposition system: (a) *PDDA* polymer solution, (b) beaker for rinsing with deionized water, (c) CdTe QDs solution and (d) beaker for rinsing with deionized water.

1.5. CuSCN Deposition by Impregnation

In order to complete the *eta*-solar cell, the free space between ZnO/absorber heterostructures was filled with the p-type CuSCN. The third method used in this work for its preparation was the impregnation technique [155, 172]. 5.75 10^{-2} M of *CuSCN* (Aldrich, purity ~ 99 %) was dissolved in propyl sulphide ($(CH_3CH_2CH_2)_2S$, Aldrich, purity ~ 97 %)) and stirred for six hours. The solution was spread repeatedly over the pre-heated sample. The substrate was heated at 100 °C on a hot plate to evaporate the solvent. Figure II.9 shows the scheme of the deposition setup.

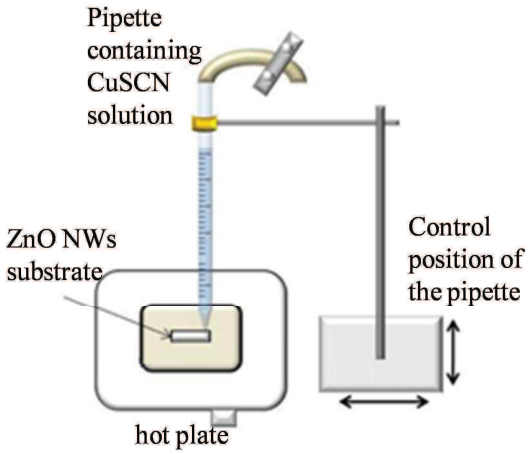

Figure II.9. Scheme of the setup for the deposition of CuSCN by impregnation technique.

The solution casting was repeated several times until the desired volume of solution is deposited (from 0.06 to 0.1 ml cm^{-2}). The study done by the group of Lévy-Clément proposed a formula that correlates the deposited volume and the thickness of the CuSCN layer (Equation II.5) [173]:

$$V_{CuSCN} = 0.027(L) + 0.035(E_{CuSCN}) \qquad \textbf{Equation II.5}$$

Where V_{CuSCN} is the volume of the CuSCN solution (in $ml\ cm^{-2}$), L is the length of the nanowires (in μm) and E_{CuSCN} is the thickness of the CuSCN layer measured from the top of the nanowires (in μm).

1.6. Eta-Solar Cell Fabrication

What follows is a short description of the *eta*-solar cell fabrication steps (Figure II.10):

(1) Electrodeposition of a ZnO buffer layer on TCO substrates (SnO_2:F). The role of this layer is to prevent the contact of the other components of the cell and the conducting substrate, in this way short-circuits are avoided. Another important function is to serve as a seed layer for the consequent growth of ZnO NWs which permits to tailor their density and dimensions. The thickness and morphology of the layer can be easily controlled by the temperature and the total passed charge density.

(2) Electrodeposition of ZnO nanowires for the formation of the nanostructured electrode. High surface area, direct path for the transport of electrons, and other optical effects like light scattering and trapping are granted by the nanostructures. The density, length and diameter of the nanowires can be additionally controlled by the electrolyte concentration, the substrate morphology, and the total passed charge density during the deposition.

(3) Nanowire array sensitization with extremely thin layer of light absorbing material (CdS, CdSe or CdTe) prepared by SILAR, CSS and QDs functionalization.

(4) Pore filling with the p-type semiconductor prepared by electrodeposition, SILAR or impregnation techniques.

(5) Finally, the cells are completed by adding 100 nm thick gold contact by thermal evaporation in vacuum.

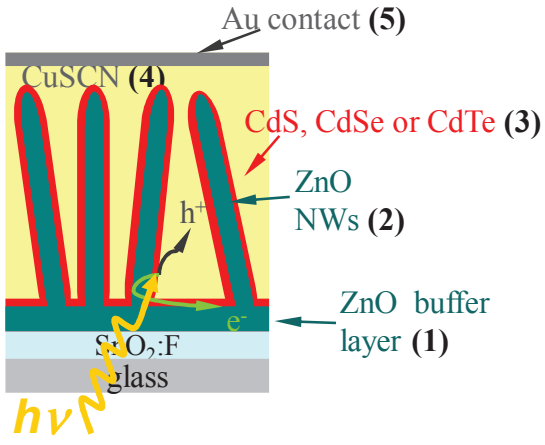

Figure II.10. Schematic illustration of the *eta*- solar cell.

1.7. The Photoelectrochemical Eta-Solar Cell Fabrication

Figure II.11 shows the photoelectrochemical *eta*-solar cell. What follows is a short description solar cell fabrication steps [174]:

(1) The TCO/ZnO/absorber (core/shell ZnO/CdS or ZnO/CdSe) heterostructures is used as nanostructured cathode (working area of 0.25 cm^{-2} delimited with a metallic mask).
(2) A platinum (Pt) coated plate is placed on top the nanostructured electrode to complete the cell.
(3) Finally the $3I^-/I^-_3$ redox electrolyte is added between both electrodes completing the circuit as in a standard DSSC.

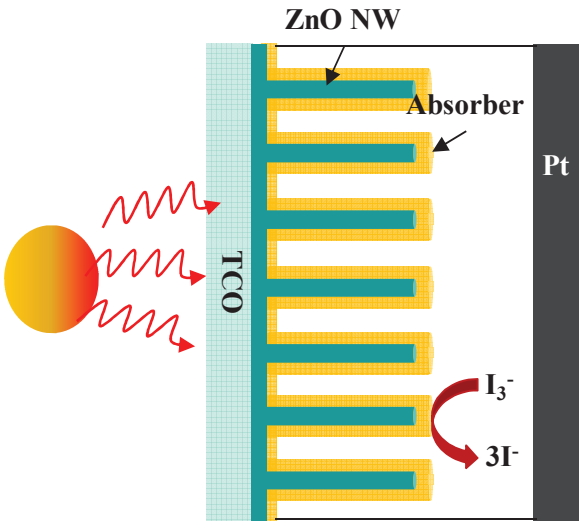

Figure II.11. Schematic illustration of the photoelectrochemical *eta*-solar cell.

2 CHARACTERIZATION TECHNIQUES

The following equipments were used to analyze the material properties:

- Scanning electron microscopy (SEM) - Hitachi S-4100 and Zeiss 5000 apparatus were used for the investigation of surface morphology.
- X-ray diffractometer (Philips PW-1710) with the Co K_α radiation (λ = 1.7889 Å) and X'Pert, PANalytical B.V., Almelo, The Netherlands with $CuK_\alpha 1$ (λ = 1.5406 Å) were used for structural characterization.
- Hitachi U-4100 and λ950 Perkin Elmer spectrophotometers were used to measure the optical transmission and absorbance properties in the visible–near-infrared (NIR) wavelength region.
- The chemical composition of the different ZnO thin films and absorbing layers was determined by Energy Dispersive X-ray (EDX) with the help of a Hitachi S-5500 scanning electron microscope.
- Photoluminescence measurements were carried out on a homemade PL setup with a He-Cd laser as excitation at room temperature.

The solar cells were characterized on:

- Newport SP94023A (AM 1.5) solar simulator using a Keithley 2400 station in the dark and under illumination.

The next sections describe the principles of each characterization technique.

2.1. Scanning Electron Microscopy

A scanning electron microscope (SEM) is a type of electron microscope that images a sample by scanning it with a beam of electrons in a raster scan pattern. The electrons interact with the atoms that make the sample producing signals that contain information about the sample's surface topography, composition, and other properties such as electrical conductivity. The electron beam, which typically has an energy ranging from 0.2 keV to 40 keV, is focused and scans in a raster fashion over a rectangular area of the sample surface. The interactions between the electron beam and the sample, the signal types, and the interaction volume are depicted in Figure II.12 [175, 176].

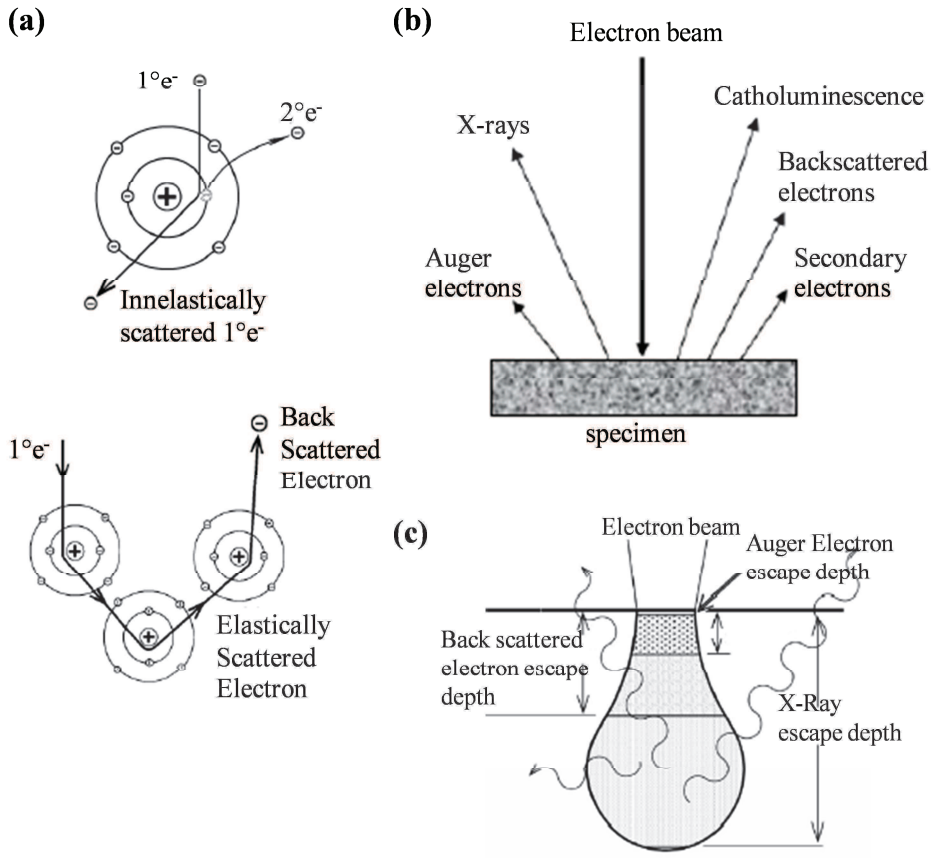

Figure II.12. (a) Inelastic and elastic interactions between beam electrons and the sample, (b) types of produced signals and (c) the interaction volume.

Inelastic interactions occur when a beam electron interacts with the electric field of the specimen atom electron. This results in a transfer of energy to the atom specimen and an expulsion of an electron from that atom as a secondary electron. If the vacancy due to the creation of a secondary electron is filled from a higher level orbital, an X-Ray characteristic of that energy transition is produced. (Figure II.12a)

The beam electrons can interact with the coulomb (electric charge) field of both the specimen nucleus and electrons. These interactions are responsible for a multitude of signal types: backscattered electrons, secondary electrons, X-Rays, Auger electrons, cathodoluminescence (Figure II.12b)

The interaction volume extends from less than 100 nm to around 5 µm into the surface. The size of the interaction volume depends on the electron's landing energy, the atomic number of the specimen and the specimen's density (Figure II.12c).

2.2. Scanning Transmission Electron Microscopy

A scanning transmission electron microscope (STEM) is a type of transmission electron microscope (TEM). The electrons pass through a sufficiently thin specimen. However, in STEM the focused electron beam is scanned over the sample in a raster.

The rastering of the beam across the sample makes these microscopes suitable for analyzing techniques such as mapping by energy dispersive X-ray spectroscopy (EDX), electron energy loss spectroscopy (EELS) and annular dark-field imaging (ADF). These signals can be obtained simultaneously, allowing direct correlation of the image and the quantitative data.

By using a STEM and a high-angle detector, it is possible to form atomic resolution images where the contrast is directly related to the atomic number (z-contrast image). Usually STEM is a conventional transmission electron microscope equipped with additional scanning coils, detectors and needed circuitry [177].

2.3. Energy-Dispersive X-Ray Spectroscopy

Energy-dispersive X-ray spectroscopy (EDS or EDX) is an analytical technique used for the elemental analysis or chemical characterization of a sample. Its characterization capabilities are due to the fundamental principle that each element has a unique atomic structure allowing unique set of peaks on its X-ray spectrum. To stimulate the emission of characteristic X-rays from a specimen, a high-energy beam of charged particles such as electrons is focused into the sample being studied. At rest, an atom within the sample contains ground state electrons in discrete energy levels or electron shells bound to the nucleus. The incident beam may excite an electron in an inner shell, ejecting it from the shell while creating a hole where the electron was. An electron from an outer, higher-energy shell then fills the hole, and the difference in energy between the higher-energy shell and the lower energy shell may be released in the form of an X-ray. The number and energy of the X-rays emitted from a specimen can be measured by an energy-dispersive spectrometer. As the energy of the X-rays is characteristic of the difference in energy between the two shells, and of the atomic structure of the element from which they were emitted, this allows the elemental composition of the specimen to be measured (Figure II.13a) [176, 178].

The central component of an EDS system is a solid-state detector, consisting of a semiconductor. As each X-ray photon hits the detector, a very small current is produced by knocking out electrons from the semiconductor. Each electron ejected from a silicon electron shell consumes about 3.8 eV of energy from the X-ray. Therefore an X-ray photon starting with 7.471 eV of energy (Ni Kα) will produce an amount of about 1.966 electrons. By measuring the produced current by each X-ray photon, the original energy of the X-ray can be calculated. An EDS spectrum is essentially a histogram of the number of X-rays measured at each energy. (Figure II.13b)

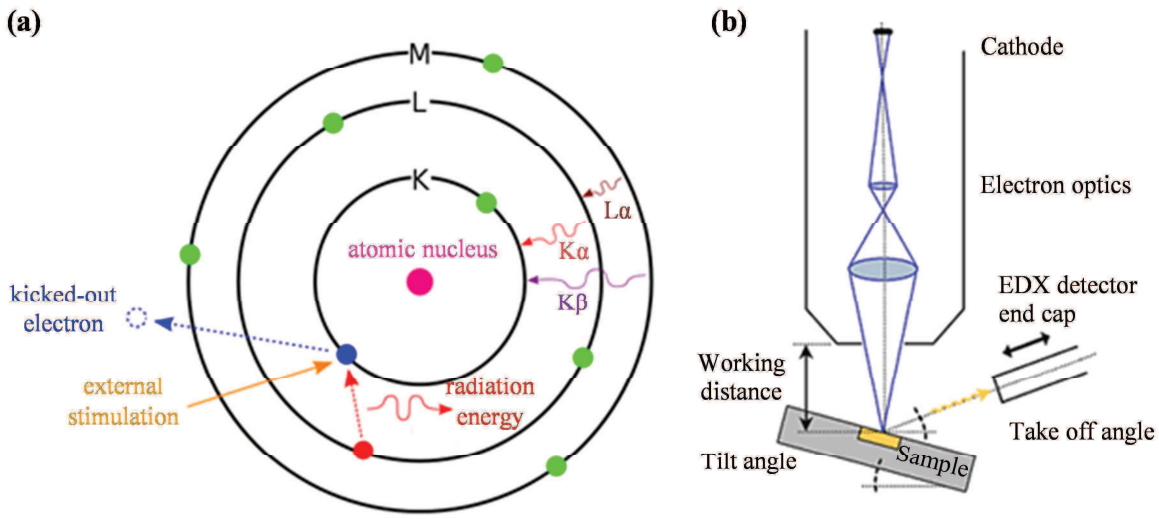

Figure II.13. (a) Principle of EDS and (b) schema of an SEM equipped with an EDX detector.

2.4. X-Ray Diffraction

X-ray diffraction (XRD) is non-destructive technique that reveals information about the chemical composition and crystallographic structure of materials [179].

X-rays are electromagnetic radiation with short wavelength. In an X-ray tube, a high voltage draws electrons toward a metal target (the anode: copper or cobalt). The sample is irradiated by the monochromatic X-ray radiation impinging at a certain angle with respect to the sample surface (incident angle). The incident X-rays radiation excites the crystal atoms (electron cloud) which then relax, emitting spherical radiation waves. When the sample presents a crystalline structure, there is diffraction when the waves associated to X-ray are in phase (constructive interference when the Bragg condition is verified (Equation II.6). Because

each crystalline material has a characteristic atomic structure, it will diffract X-rays in a unique characteristic pattern.

$$Sin\theta = \frac{n\lambda}{2d_{(h,k,l)}}$$ **Equation II.6**

Were $d_{(h,k,l)}$ is the distance between the reticular plans (hkl) of the crystalline lattice, θ is the incidence angle of X-ray with respect to the sample surface, λ is the wave length of the incident beam and n is an integer which represents the order of the diffraction mode.

θ-2θ Mode. X-ray measurement can be performed in different geometrical configurations, depending on the expected information. In our case we use the *θ-2θ Mode*, which principle is to fix the X-ray source and to turn the counter of an angle 2θ when the goniometric that carries the sample turns of an angle θ (Figure II.14). When an angle corresponding to a family of planes (h,k,l), the Bragg condition is achieved and the counter records an increase of the diffracted intensity. Thus, the peak position in a diagram of the diffracted intensity as a function of the incidence angle θ is characteristic of the crystalline lattice.

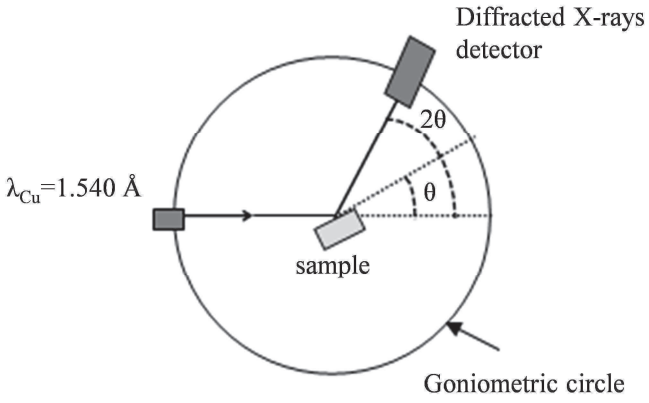

Figure II.14. Scheme of an X-ray diffractometer.

- A database (ICDD PDF-4+: International Centre for Diffraction Data, Powder Diffraction File-4+) gathers the spectra of X diffraction of powder reference samples, which allow the identification of the analysed material as well as the crystalline orientation and other useful information [180].

- Crystallite size were estimated by Scherrer's formula (Equation II.7) assuming a spherical geometry [181]:

$$D = \frac{K\lambda}{\beta \cos\theta}$$ **Equation II.7**

Where D is the crystallite size, K is a dimensionless number (1.075 for spherical crystallites), λ is the X-ray wavelength, β is the FWHM (Full Width at Half Maxima) of the diffraction peak, and θ is the Bragg diffraction angle.

- Strain (ε) calculations were performed using the **Equation II.8** [182]:

$$\beta \cos\theta = \frac{K\lambda}{D} + 4\varepsilon \sin\theta$$ **Equation II.8**

Where D is the crystallite size, K is a dimensionless number (1.075 for spherical crystallites), λ is the X-ray wavelength, β is the FWHM (Full Width at Half Maxima) of the diffraction peak, θ_B is the Bragg diffraction angle and ε is the microstrain.

And the texture coefficients Tc_{hkl} were estimated following the

- Equation II.9 [183]:

$$Tc_{hkl} = \frac{I_{hkl} / I_{0,hkl}}{\frac{1}{N}\sum_{N} I_{hkl} / I_{0,hkl}}$$ **Equation II.9**

where I_{hkl} and $I_{0,hkl}$ are the integrated intensities of the <hkl> crystallographic direction from the sample and the PDF reference file, respectively, N corresponds to the number of considered peaks.

2.5. UV-Vis Spectroscopy

UV/Vis spectroscopy is routinely used in analytical chemistry for the quantitative determination of different analytes, such as transition metal ions, highly conjugated organic compounds, and biological macromolecules. Spectroscopic analysis is commonly carried out in solutions but solids and gases may also be studied.

This technique is complementary to fluorescence spectroscopy, which deals with transitions from the excited state to the ground state, while absorption measures transitions from the ground state to the excited state.

The instrument used in ultraviolet-visible spectroscopy is called a UV/Vis spectrophotometer. It measures the intensity of light passing through a sample (I), and compares it to the intensity of light before it passes through the sample (I_0). The ratio (I/I_0) is called the transmittance, and is usually expressed as a percentage ($\%T$). The absorbance (A) is based on the transmittance as described by Equation II.10:

$$A = log(\%T/100\%) \qquad \textbf{Equation II.10}$$

The UV-visible spectrophotometer can also be configured to measure reflectance. In this case, the spectrophotometer measures the intensity of light reflected from a sample (I), and compares it to the intensity of light reflected from a reference material (I_0) (such as a white tile). In this case the ratio (I/I_0) is called the reflectance, and is usually expressed as a percentage ($\%R$).

The basic parts of a spectrophotometer are a light source, a holder for the sample, a diffraction grating in a monochromator or a prism to separate the different wavelengths of light, and a detector. In our case, the spectrometer was equipped with an integrating sphere for the diffuse light since we are working with nanostructures and light scattering effects are expected (Figure II.15). The radiation source is often a tungsten filament (300 - 2500 nm), a deuterium arc lamp, which is continuous over the ultraviolet region (190 - 400 nm), Xenon arc lamp, which is continuous from 160-2000 nm; or more recently, light emitting diodes (LED) for the visible wavelengths. The detector is typically a photomultiplier tube, a photodiode, a photodiode array or a charge-coupled device (CCD). Single photodiode detectors and photomultiplier tubes are used with scanning monochromators, which filter the light so that only light of a single wavelength reaches the detector at one time. The scanning monochromator moves the diffraction grating to "step-through" each wavelength so that its intensity may be measured as a function of wavelength. Fixed monochromators are used with CCDs and photodiode arrays. As both of these devices consist of many detectors grouped into one or two dimensional arrays, they are able to collect light of different wavelengths on different pixels or groups of pixels simultaneously [184].

The bandgap of the materials can be estimated from the direct optical transition using Equation II.11, where λ_e is the wavelength at the observed transition [185].

$$E_g\,(eV) = 1240/\lambda_e\,(nm) \qquad \textbf{Equation II.11}$$

Or it could be more accurately determined from Tauc relation (Equation II.12) [186]:

$$\alpha h\nu = A(h\nu - E_g)^n \qquad \textbf{Equation II.12}$$

where E_g is energy bandgap, A is a constant, α is the absorption coefficient, $(h\nu)$ is the photon energy and n is an index which assumes the values *1/2*, *3/2*, *2* and *3* depending on the nature of the electronic transition (*1/2* is for direct transitions for instance).

In this method the extrapolation of the linear portion of the curve $((\alpha h\nu)^2$ versus the photon energy, $h\nu$) to absorption equal to zero gives the value of the direct bandgap.

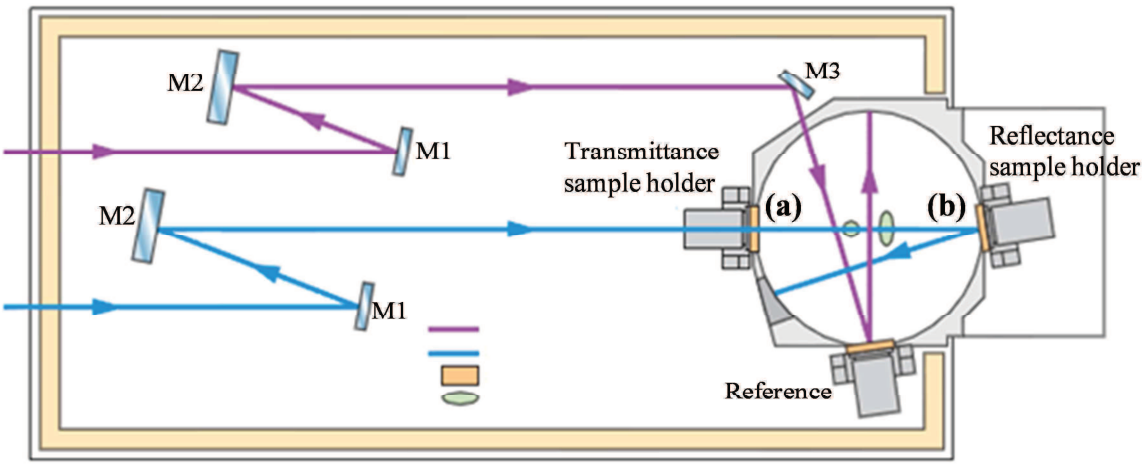

Figure II.15. Scheme of the UV-Vis spectrometer setup. For transmission and reflectivity measurements the sample is placed in the (a) and (b) positions, respectively.

2.6. Photoluminescence

Photoluminescence (PL) is the spontaneous emission of light from a material under optical excitation. The excitation energy and intensity are chosen to probe different regions and excitation concentrations in the sample [187].

PL spectroscopy is a selective and extremely sensitive probe of discrete electronic states. Features of the emission spectrum can be used to identify surface, interface, and

impurity levels and to gauge alloy disorder and interface roughness. The intensity of the PL signal provides information on the quality of surfaces and interfaces. Under pulsed excitation, the transient PL intensity yields the lifetime of nonequilibrium interface and bulk states. Variation of the PL intensity under an applied bias can be used to map the electric field at the surface of a sample. In addition, thermally activated processes cause changes in PL intensity with temperature.

PL analysis is a nondestructive method. In addition, time-resolved PL can be very fast, making it useful for characterizing the most rapid processes in a material. The fundamental limitation of PL analysis is its reliance on radiative events. Materials with poor radiative efficiency, such as low-quality indirect bandgap semiconductors, are difficult to study via ordinary PL. Similarly, identification of impurity and defect states depends on their optical activity. Although PL is a very sensitive probe of radiative levels, one must rely on secondary evidence to study states that couple weakly with light. Figure II.16a shows a typical PL set-up. The instrumentation includes: an optical source and an optical power meter or spectrophotometer.

In the bulk of a crystalline material, translational symmetry leads to the formation of electronic energy bands. Defects and impurities break the periodicity of the lattice and perturb the band structure locally. The perturbation usually can be characterized by a discrete energy level that lies within the bandgap. Depending on the defect or impurity, the state acts as a donor or acceptor of excess electrons in the crystal. Figure II.16b depicts the possible the radiative and nonradiative recombination processes.

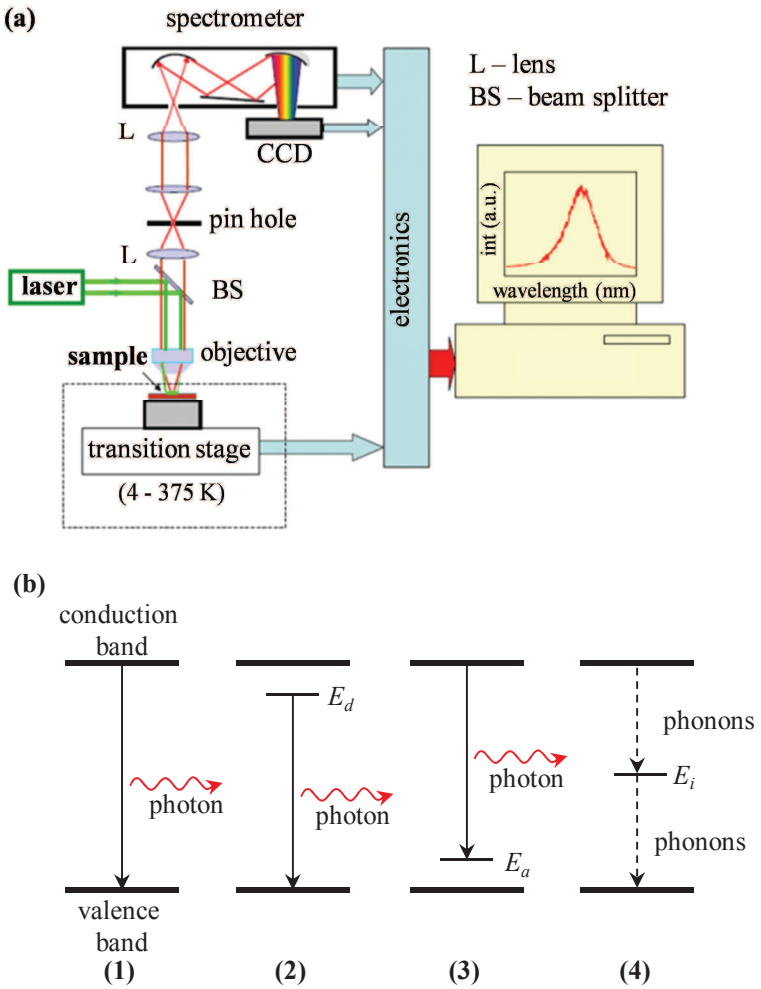

Figure II.16. (a) Typical experimental set-up for PL measurements. (b) Radiative recombination paths: (1) band-to-band, (2) donor (E_d) to valence band, (3) conduction band to acceptor (E_a); and nonradiative recombination (4) via an intermediate state (E_i) [188].

2.7. Solar Cell Efficiency Characterization

The need for performance comparisons of different photovoltaic (PV) devices has given rise to efficiency measurements. The photovoltaic conversion efficiency (PCE), determined from the current versus voltage (J-V) characteristics of an illuminated solar cell, is typically measured with respect to a standard solar spectrum at a given intensity (100 mW cm^{-2}) [189].

The short circuit current, (J_{sc}), flows with zero external resistance ($V=0$) and is the maximum current density delivered by the solar cell at given illumination level. Similarly, the open circuit voltage, (V_{oc}), is the potential that develops at the ends of the solar cell when the

external load resistance is very large (Figure II.17). The power delivered to the load reaches a maximum (P_{max}) at a finite load resistance value. The fill factor, (FF), is another number that characterizes the solar cell and is defined as the ratio of P_{max} to the area of the rectangle formed by V_{oc} and J_{sc} (Equation II.13).

$$FF = \frac{P_{max}}{(V_{oc})(J_{sc})}$$ **Equation II.13**

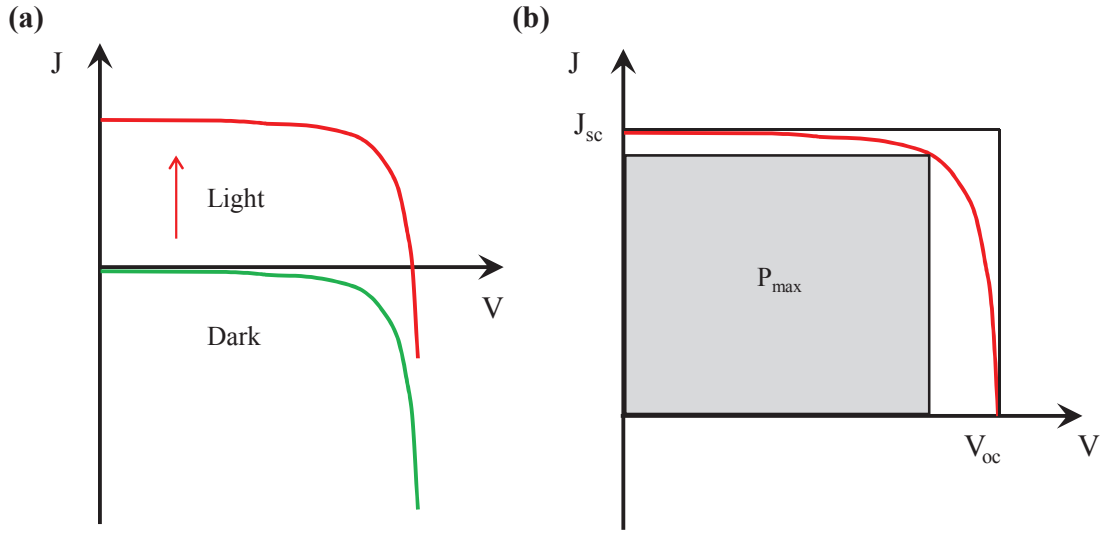

Figure II.17. (a) Progression of the solar cell I-V curve as the incident light increases and (b) maximum power delivered by the solar cell, P_{max} (area of the largest rectangle under the J-V curve).

The efficiency of the solar cell is the ratio of P_{max} and the optical power incident on the cell (Equation II.14):

$$\eta = \left(\frac{Maximum\ Electrical\ Power}{Area\ \text{x}\ Irradiance}\right) \text{x } 100 = \frac{P_{max}}{A\ \text{x}\ E_{STD}}\ x\ 100$$

Equation II.14

Where A is the total area, P_{max} is the maximum power and E_{STD} is the irradiance of the standard spectrum normalized to some total irradiance (100 mW cm^{-2}).

The efficiency of a PV device is normally measured in a solar simulator using the reference cell method where the simulator intensity is adjusted so that the measured short-circuit current of the reference cell is equal to its calibrated value at the standard test intensity (100 mW cm^{-2}). Figure II.18 shows a basic setup for measuring the PV device efficiency. The standards for cell testing are: i) Air mass 1.5 spectrum (AM1.5) for terrestrial cells and Air

Mass 0 (AM0) for space cells; ii) Intensity of 100 mW cm^{-2} (1 kW m^{-2}, one-sun of illumination) and iii) Cell temperature of 25 °C.

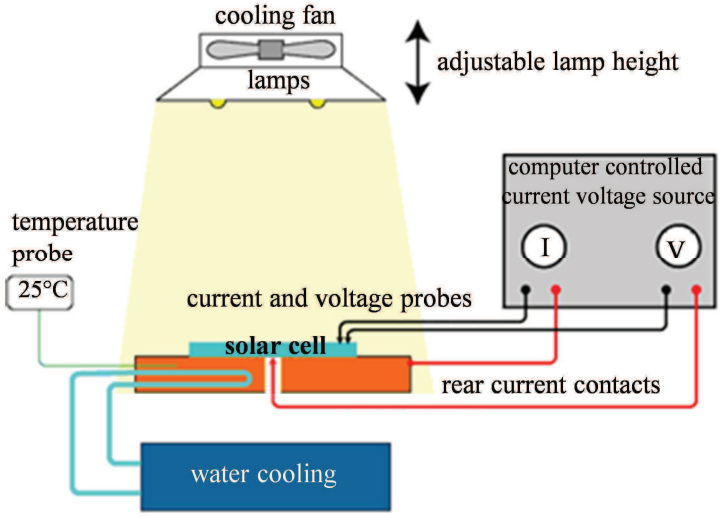

Figure II.18. Basic setup to measure the performance of a solar cell [190].

In this chapter the preparation methods for each component of the *eta*-solar cell were presented. The used characterization techniques were also described and the procedure for the fabrication of the solar cells was also introduced.

CHAPTER III : ZnO Electrodeposition

In this chapter, the results on the deposition of ZnO thin films and nanowires by electrochemical method will be discussed.

In the first part, the effect of deposition parameters when galvanostatic mode is used on the structural and optical properties of the films will be individually addressed.

The second part is especially dedicated to the growth of ZnO nanowires. The effect of the galvanostatically deposited ZnO seed layer on the nanowire dimensions and density is covered. A small paragraph discusses the galvanostatic deposition of ZnO nanowires;

Further, some novelties about electrodeposition of ZnO nanowires and other nanostructures on polar ZnO surfaces are presented.

1 ZnO THIN FILMS (Influence of Deposition Parameters)

In this section, the results on the electrochemical deposition by galvanostatic mode of ZnO thin films, called "buffer layers" in the *eta*-solar cell are presented. Regardless of the efforts which have been done to master the galvanostatic preparation of ZnO layers, to our knowledge, till now the deposition of uniform ZnO 2D thin films by this method has not been achieved. Here we show that defect free compact ZnO thin layers could be prepared by galvanostatic deposition and demonstrate that these films could be further used as seed layers for growth of ZnO nanowires with a large diameter. To perform this investigation an aqueous solution containing $ZnCl_2$ and KCl as a Zn^{2+} precursor and supporting electrolyte, respectively, was used. This solution is very appropriate since depending on the $ZnCl_2$ concentration compact thin films or nanowires could be grown. The influence of various deposition parameters (bath temperature, supporting electrolyte (KCl) concentration and current density) on the film morphology and optical properties has been systematically studied (fixed stirring speed of 300 rpm). We believe that this work could contribute towards the development of cheap and scalable method for electrochemical deposition of well controlled polycrystalline ZnO thin films.

1.1. Role of Bath Temperature and Molecular Oxygen Concentration

The influence of temperature on the potentiostatic deposition of zinc oxide films from the aqueous Zn-Cl-H_2O system was investigated [90] and among other conclusions, it was found that high quality compact thin films were only obtained at temperature equal or above 70 °C.

In this study we fixed the current density at -0.13 mA cm^{-2} (previously used to deposit at 25 °C ZnO composed of nanograins [89]) and varied only the bath temperature. Figure III.1 shows the chronopotentiograms obtained for ZnO deposition at temperatures between 25 and 70 °C. The close inspection of the curves obtained at temperatures equal or above 50 °C shows that three regions could be distinguished: (i) a sudden potential decrease towards more negative values shortly after the current application. It could be attributed to a rise of the surface resistivity due to a passivation effect in the first stage of ZnO formation, i.e., generation of OH^- ions; (ii) a tendency of the potential to increase, believed to be produced by

a completed nucleation process and initial growth stage (progressive reaction of Zn^{2+} with the OH^- ions and early formation of ZnO) suggesting that the layer becomes more conductive with time; (iii) a plateau representing the reaction stabilization and ZnO steady growth favoring the deposition of good quality layer. In this sense, the potential minimum observed in the first region could be regarded as an indicator of the nucleation and initial growth stages. Affected from the deposition temperature it could also indicate the stabilization in ZnO formation (see the inset of Figure III.1). It is seen that the potential minimum value becomes less negative with temperature increase (from 50 to 70 °C). This effect could be attributed to faster reaction kinetics of the chemical reaction (Equation I.3) and thus enhanced transformation of the initial amorphous-resistive layer into a more conductive one.

Although obeying the same deposition behavior, the chronopotentiogram obtained at 25 °C is significantly different from those obtained at higher studied temperatures. According to [191], the concentration of molecular oxygen at saturation at 25, 50, 60 and 70 °C is expected to be 1.28, 1.00, 0.925 and 0.9 mM, respectively. Assuming the concentration of molecular oxygen as the main parameter responsible for the observed deposition potential behaviour, then the chronopotentiogram at 25 °C could be explained as follows: i) the considerably reached negative potential value can be attributed to the large amount of produced OH^- due to the high molecular oxygen concentration close to the electrode surface; ii) the potential plateaus (reached at -1.17 V and around -1.0 V) could be related with the same phenomenon observed at higher temperatures, i.e. a tendency towards the deposition stabilization. The potential variation evidences the non-optimal reaction conditions and thus the plateaus could be considered only as structural or morphological transitions of the film (slow formation of ZnO or thickness changes). Therefore, although reported to be an important parameter for the ZnO layer deposition at room temperature [96], in the present case, the electrolyte saturation with molecular oxygen is not sufficient to obtain compact highly crystalline ZnO thin films.

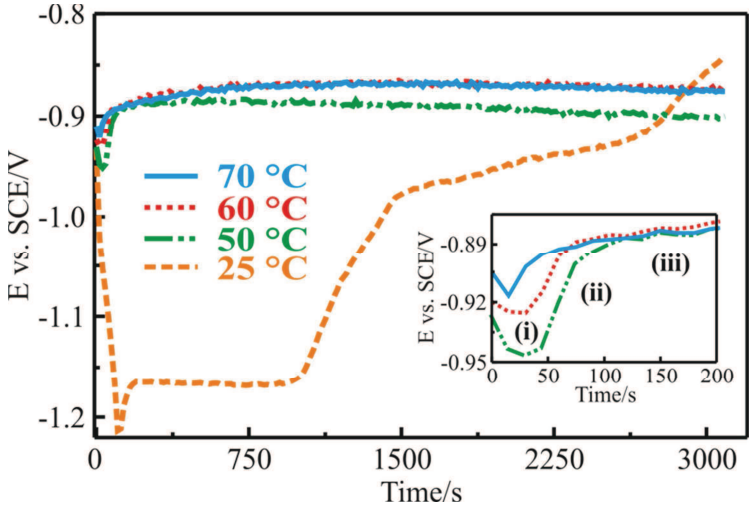

Figure III.1. Chronopotentiograms obtained during deposition of ZnO 2D layers at j = -0.13 mA cm^{-2} from an electrolyte containing 5 mM *$ZnCl_2$* and: 0.1 M *KCl* at 25, 50, 60 and 70 °C. The inset shows an enlarged view of the potential onset of curves recorded 50, 60 and 70 °C. All curves were recorded for a total passed charge density Q = 0.4 C cm^{-2}. Prior to all depositions the electrolyte was bubbled 30 min with oxygen.

Figure III.2 shows the SEM images of galvanostatically deposited ZnO films at different bath temperatures. At 25 °C (Figure III.2 a) the layer has a granular appearance and an open structure that at some extent leaves the TCO substrate uncovered (small areas of pyramidal-like structure). For comparison in the inset of the figure 2a the morphology of the bare substrate is shown. This film is formed of small grains as previously reported [89]. The non-optimal thermodynamic conditions might be the cause of why the grains do not coalesce and thus some regions of the TCO substrate are not covered. The exploration of large surface area (Figure III.2 b) shows relatively large sheet-like crystals also forming part of the film. Formerly attributed to the deposition mode [96], we found that the origin of the inhomogeneous layer is mainly caused by disproportionate concentrations of Zn^{2+} and Cl^- ions. After several sample preparations using the same electrolyte, the density of sheet-like crystals on the surface is increased. This phenomenon is discussed later with the role of the *KCl* concentration. A possible explanation of why the galvanostatic mode is more sensitive to produce such structures could be: (i) the low OH^- generation rate and (ii) the negative potential values reached at 25 °C. It should be noted that the deposition current density under same condition but using potentiostatic mode (E = -1V vs SCE [192]) reaches values that are five times higher than the used current density in this case (-0.13 mA cm^{-2}). Therefore, the small amount of produced OH^- ions is not enough to match the predominant concentration of Zn^{2+} ions at 25 °C [90] and thus creating unbalanced concentration gradients.

After increasing the deposition temperature to 50 °C (Figure III.2 c) a transition to a more compact ZnO layer is seen, the substrate is fully covered. The big sheet-like crystals still remain (like in Figure III.2 b) evidencing the not sufficiently improved conditions with temperature deposition. The morphology of ZnO layer deposited at 70 °C is shown on Figure III.2 d. The same results are obtained at 60 °C. The obtained films are compact and homogeneous on the entire surface demonstrating the important role of bath temperature. Besides the expected enhancement of the electrochemical reaction kinetics, precipitation and dehydration processes as reported in [90], the temperature influences the solution species repartition, being $ZnCl^{+}$ predominant at 70 °C (Fig. 8a). The only difference between the films deposited at 60 and 70 °C is their thickness, which is 300 and 330 nm, respectively, for 0.4 C cm^{-2} passed charge density (Figure III.3). It shows that the deposition process at 70 °C is more efficient.

X-ray diffraction analyses were performed on samples prepared at -0.13 mA cm^{-2} applied current density and at various bath temperatures. The XRD patterns (Figure III.4) of all samples present peaks corresponding to ZnO powder and their intensities tend to increment with the deposition temperature increase. The different full width at half maximum (FWHM) of the (002) diffraction peak compared to the other peaks confirms the strongly oriented growth of ZnO along the c-axis at higher temperatures. These results indicate that the layers obtained at 60 and 70 °C (curves 3 and 4, Figure III.4) are the most c-axis oriented whereas the films obtained at 25 and 50 °C (curve 1 and 2, Figure III.4) do not exhibit preferential orientation.

Estimated mean crystallite sizes, from Scherrer's formula using the FWHM of the (100) and the (101) diffraction peaks and taking into the account the strain involved in the ZnO layer [182], were 65, 312, 385 and 441 nm for temperatures 25, 50, 60 and 70°C, respectively. In Table III.1 is shown the evolution of the strain with the deposition temperature, using Equation III.**1**, where β is the FWHM (corrected for instrumental broadening), θ is the peak position, λ= 1.7889, K is a constant close to unity, D is the crystallite size and ε is the microstrain.

$$\beta\cos\theta = \frac{K\lambda}{D} + 4\varepsilon\sin\theta \qquad \textbf{Equation III.1}$$

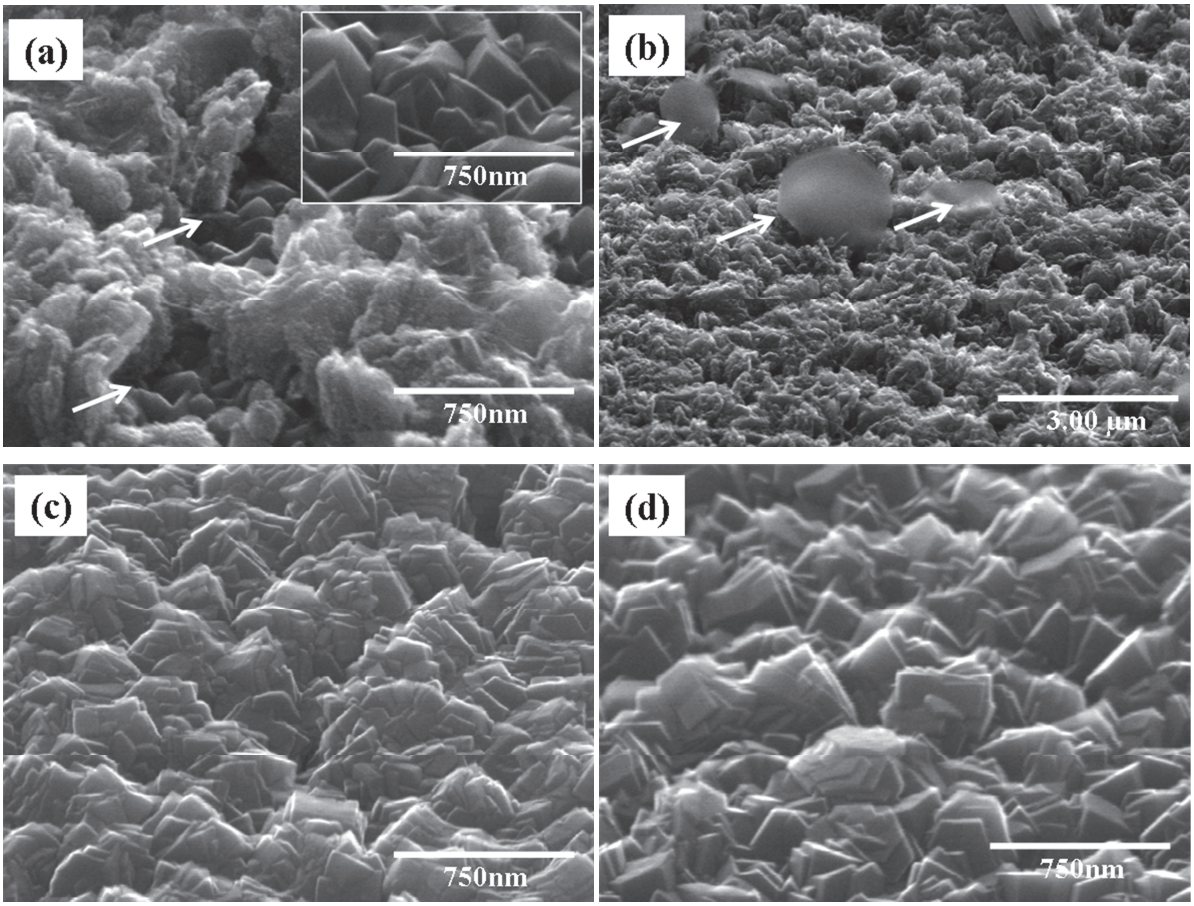

Figure III.2. SEM images (tilted view, 45°) of ZnO layers deposited at j = -0.13 mA cm^{-2} from an aqueous solution containing 5 mM *$ZnCl_2$* and 0.1 M *KCl* at: (a) 25 °C (arrows point the areas of bare TCO substrate). Inset shows the surface morphology of the bare SnO_2:F substrate used in this study; (b) same conditions as (a), larger view (arrows indicate the sheet-like crystals); (c) 50 °C and (d) 70 °C. The passed charge density was fixed at Q = 0.4 C cm^{-2}.

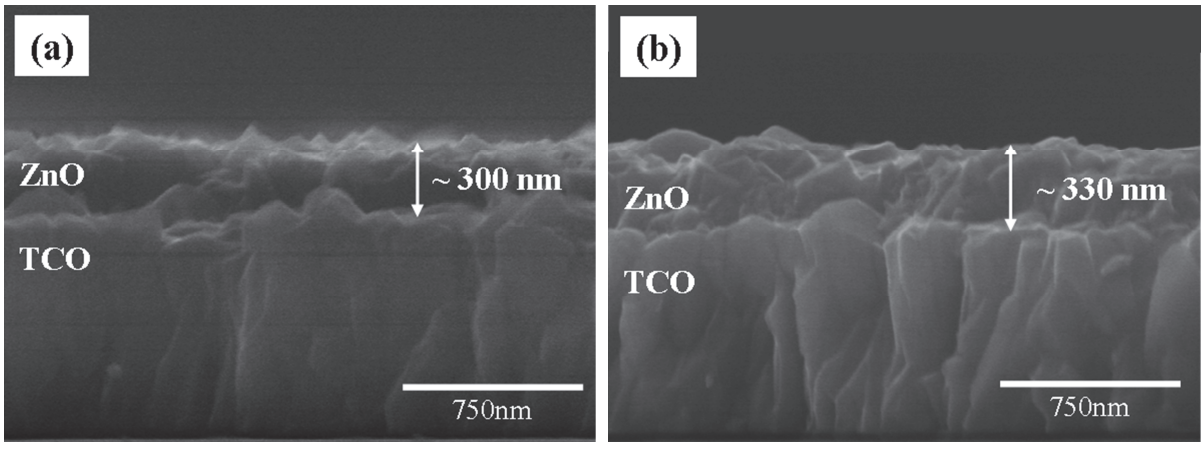

Figure III.3. Cross-sectional view of ZnO thin films deposited from a solution containing 5 mM *$ZnCl_2$* and 0.1 M *KCl* at -13 mA cm^{-2}, at: (a) 60 °C and (b) 70 °C. The total passed charge was fixed at Q = 0.4 C cm^{-2}.

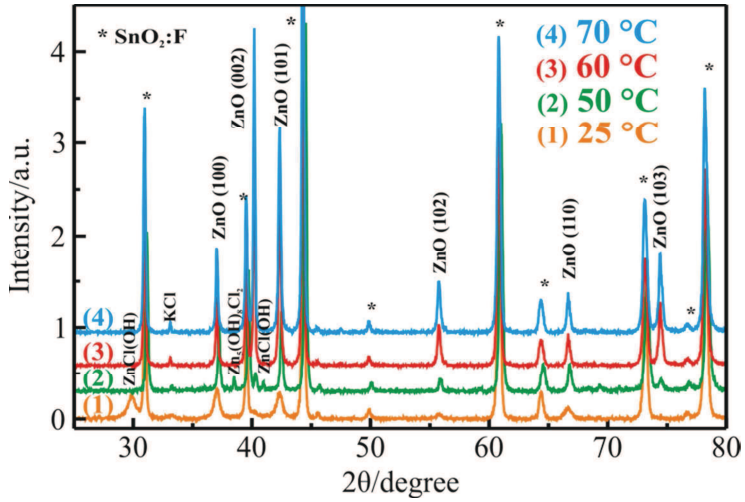

Figure III.4. X-ray diffraction patterns of ZnO layers deposited at j = -0.13 mA cm^{-2} from an electrolyte containing 5 mM *$ZnCl_2$* and 0.1 M *KCl* at: 25 °C (curve 1), 50 °C (curve 2), 60 °C (curve 3) and 70 °C (curve 4). The diffraction peaks of *SnO_2:F* substrate are marked with stars (*).

Table III.1 Strain values of electrodeposited ZnO thin films at different temperatures, calculated from Equation III.1. Strain values were estimated using the Williamson–Hall approach.

Temperature, °C	Strain (ε)
25	2.73 10^{-3}
50	0.68 10^{-3}
60	0.39 10^{-3}
70	0.23 10^{-3}

Although presenting the same ZnO structure the diffraction peaks intensity differences for the films deposited at lower (25°C) and higher (70°C) temperatures could be related to the level of preferred orientation of the grains forming the layer. The texture coefficients Tc (hkl) were estimated following the

Equation III.2, where Ihkl and I0,hkl are the integrated intensities of the <hkl> crystallographic direction from the sample and the reference file (PDF 4+ 04-001-7297), respectively. *N* corresponds to the number of considered peaks. Figure III.5 shows the texture coefficients of the <100> and <002> crystallographic directions for layers grown at j = -0.13 mA cm^{-2}, Q = 0.4 C cm^{-2} and at various temperatures. Texture coefficients for a sample grown at j = -0.08 mA cm^{-2} and 70°C are also given. For a randomly oriented sample the texture coefficient is *Tc (hkl)* = 1 whereas for a textured sample it is *Tc (hkl)* = 6. Figure 4 shows the preferential growth along the <002> for samples grown at 70 °C.

$$Tc_{hkl} = \frac{I_{hkl} / I_{0,hkl}}{\frac{1}{N}\sum_{N} I_{hkl} / I_{0,hkl}}$$

Equation III.2

The texture coefficients from the layer grown at -0.08 mA cm^{-2} evidence the extent of the influence on the deposition rate on the preferential growth along the <002> direction.

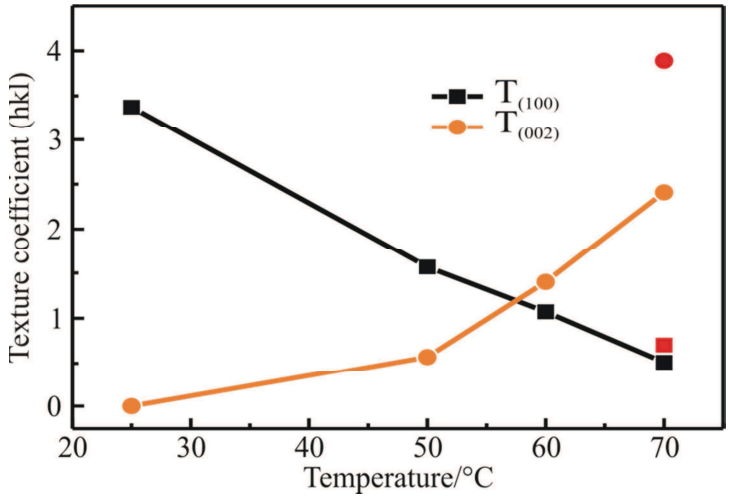

Figure III.5. Dependence of the texture coefficient of <100> and <002> crystallographic directions on the deposition temperature. ZnO layers were deposited at j = -0.13 mA cm^{-2}, Q = 0.4 C cm^{-2} and at the indicated temperatures. Symbols in red are the texture coefficients for a sample grown at j = -0.08 mA $cm^{-2}$and 70 °C.

The optical UV–Vis transmission spectra of the layers grown at different temperatures can be seen on Figure III.6a. The layers deposited at 25 °C exhibit poor transmissions features probably due to scattering effects produced by the big sheet-like defects and the highly porous morphology of the layer. An improved film transparency is observed for the films obtained at temperatures ≥ 50 °C due to their better crystallinity. The bandgap of these layers was estimated from the absorption spectra and the results are shown on Figure III.6b. Bandgap values are close to the ones reported in the literature for bulk ZnO (i.e., 3.37 eV). However a small variation from 3.25 to 3.45 eV is observed, depending on the deposition temperature. Among various possibilities to explain the variation of the bandgap, the chlorine doping concentration into ZnO might be considered [193]. In a recent paper, Rousset et al. investigated the influence of chlorine doping into ZnO by adding $ZnCl_2$ (Cl^- ions) in the $Zn(ClO_4)_2$ electrolyte [193]. The deposition was made potentiostatically at 70 °C and -1V.

They show that the increase of [$ZnCl_2$] increases the chlorine doping concentration and decreases the bandgap.

The composition of the deposited ZnO thin films was analysed by EDX. In Table III.2 are given the chlorine concentrations for deposits prepared at j = -0.13 mA cm^{-2} and at different temperatures. It is seen that the amount of chlorine (~1%) is smaller in the layers grown at the higher temperatures. A comparison with our results and paper ref [193] let think that the chlorine doping might be the reason of the bandgap variation. There is a noticeable relation between the chlorine content and the variation of the bandgap (Table III.2). The bandgaps of 3.45 and 3.25 eV observed for thin films grown at 50 and 70 °C, suggest that ZnO layers grown at lower temperatures might be higher chlorine doped than those grown at 60 and 70°C with carrier concentrations of 3.10^{19} cm^{-3} and 7.10^{17} cm^{-3}, respectively. To confirm this hypothesis further investigation is necessary.

The temperature-dependent photoluminescence (PL) properties of the ZnO thin films are displayed in Figure III.7. The layers exhibit low UV emission at about 3.33 eV (372 nm) and intense green emissions centred at about 2.23 eV (550 nm) under UV excitation (325 nm He-Cd laser). The room temperature PL spectrum of ZnO usually shows two important peaks: one near band-edge UV emission at 380 nm, and other visible emission in the green or red region (Figure III.8 [194]). From Figure III.7 it can be seen that the near band-edge emission (372 nm) increases whereas the defect related emission (550 nm) decreases at higher deposition temperature. This confirms that at higher temperature ZnO layers with better crystalline quality and bigger grain size are deposited. However, the broad emissions are a signal that these films could consist of grains with different sizes. Strain and chlorine doping effects should be also taken into account.

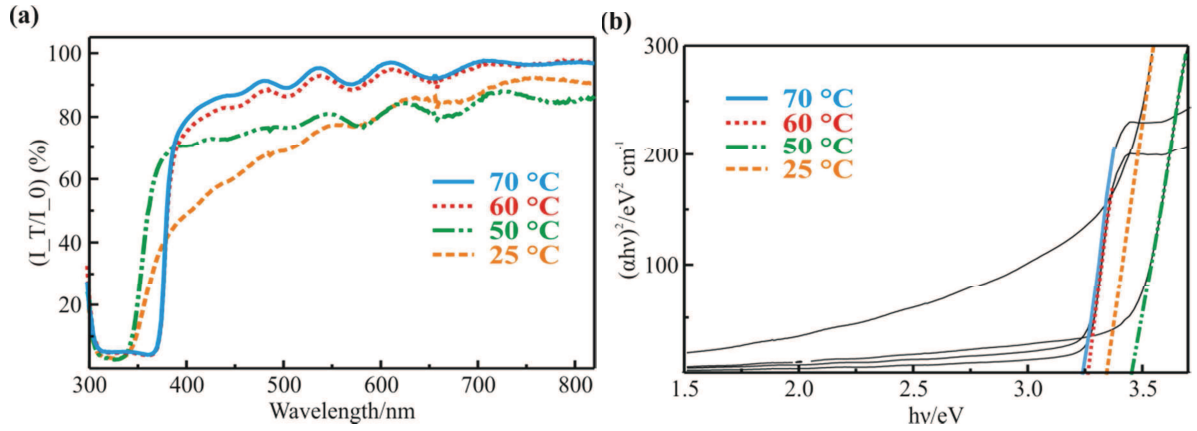

Figure III.6. (a) Optical transmission spectra of ZnO layers deposited at 25, 50, 60 and 70 °C, j = -0.13 mA cm^{-2} and Q = 0.4 C cm^{-2}, from an electrolyte containing 5 mM $ZnCl_2$ and 0.1 M KCl. (b) Dependence of $(\alpha h\nu)^2$ versus $h\nu$ for ZnO layers obtained from (a).

Table III.2. Relationship between chlorine content, band gap and carrier concentration of the ZnO layers grown at different temperatures. *the carrier concentration is taken from reference [193].

Deposition Temperature, °C	Chlorine Concentration, %	Band gap, eV	Carrier Concentration*, cm^{-3}
70	0.77 (+/- 0.03)	3.25	7.10^{17}
60	0.63 (+/- 0.03)	3.25	
50	1.37 (+/- 0.04)	3.45	3.10^{19}
25	0.96 (+/- 0.03)	3.35	

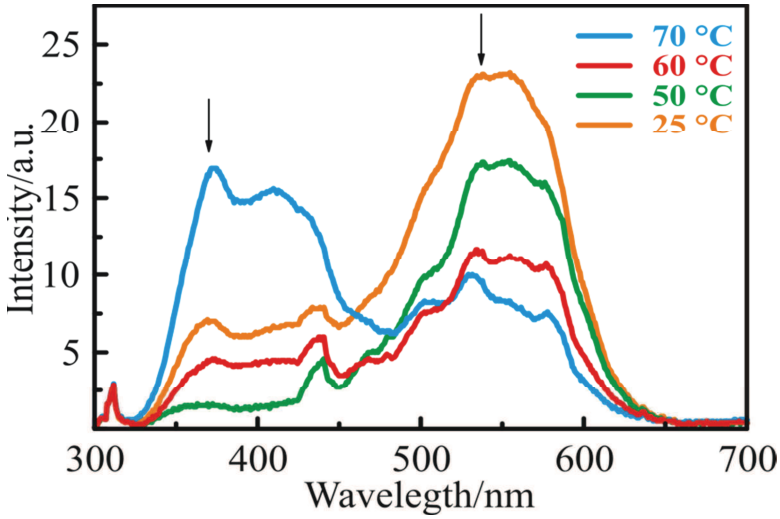

Figure III.7. Room temperature PL spectra of the ZnO thin films deposited at 25, 50, 60 and 70 °C, j = -0.13 mA cm^{-2} and Q = 0.4 C cm^{-2}, from an electrolyte containing 5 mM $ZnCl_2$ and 0.1 M *KCl*.

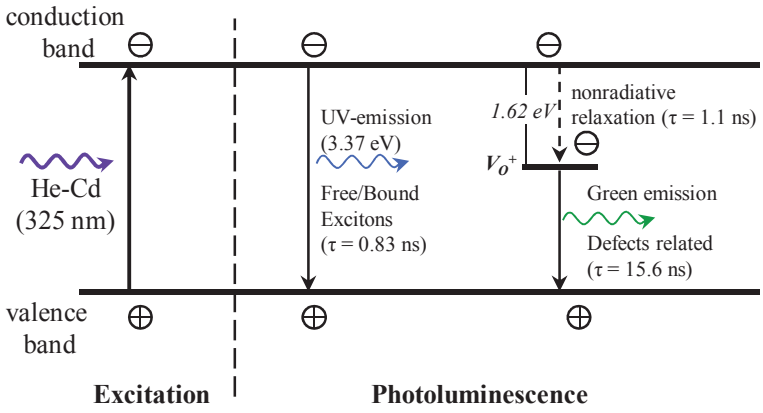

Figure III.8. Scheme of the UV/visible excitation and emission processes in ZnO [194].

1.2. Role of the Supporting Electrolyte Concentration

The concentration of the supporting electrolyte has long been known to influence the reaction rates in solutions. The effects generally arise from medium polarity changes by ionic species. The effect of supporting electrolyte on the ZnO electrodeposition from aqueous zinc chloride system using molecular oxygen precursor was the object of several studies. The chemical nature of the anions and [*KCl*] on the ZnO nanowires dimensions and optical properties [195, 196] and growth mechanism of ZnO layers [88, 197] have been discussed. Depending on the application, until now, the influence of the supporting electrolyte concentration has been granted a positive connotation, and has been regarded as a way to enhance the deposition processes [198] or tune the optoelectronic properties of ZnO nanowires [195, 197, 198]. Here we report on the role of *KCl* concentration on ZnO compact thin films galvanostatic deposition. The $ZnCl_2$ concentration was fixed to 5 mM and that of *KCl* was 0.2 and 1 M. Chronopotentiograms obtained with the studied [*KCl*] at 25 and 70°C are depicted on Figure III.9. Regardless of the temperature, the deposition potential for 1 M *KCl*, shows a behavior completely different to those obtained with 0.2 M *KCl* or 0.1 M *KCl* (Figure III.1). A slow but steady tendency towards more negative potentials clearly evidences the effect of *KCl* concentration on the reduction of O_2 and thus generation of OH^-. Similar effects exposed in [197], were attributed to the strong adsorption of chloride anions (Cl^-) providing the electrode surface passivation. Besides the already blocked reaction sites by the adsorbed Cl^- ions on the surface, an additional capping effect [199] due to the preferential adsorption onto the (0001) surfaces, would also block the newly formed ZnO grains or certain faces thus hindering O_2 reduction and increasing the substrate resistivity. Onsets of what appear to be stabilizing plateaus, develop after certain deposition time, occur sooner with temperature increase.

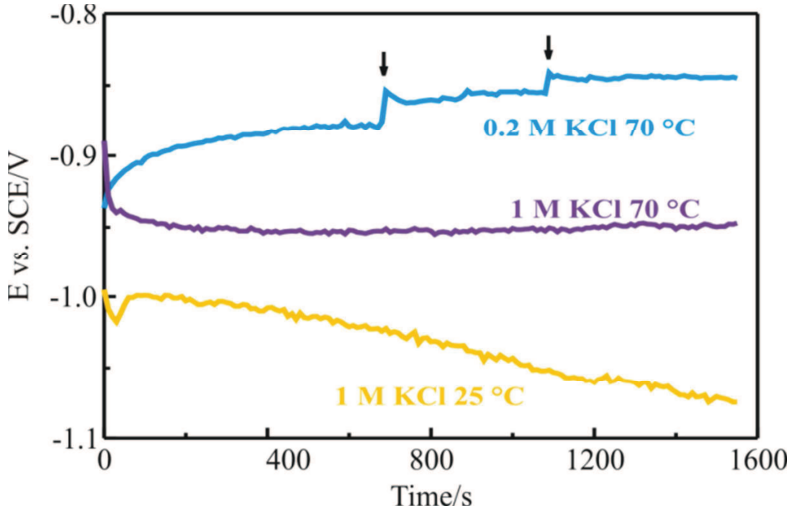

Figure III.9. Chronopotentiograms obtained during deposition of ZnO 2D layers at j = -0.13 mA cm^{-2} from an electrolyte containing 5 mM *$ZnCl_2$* and 0.2 and 1 M *KCl* at 70 °C, and 1M *KCl* at 25 °C. All curves were recorded for a total passed charge density Q = 0.4 C cm^{-2}. Prior to all depositions the electrolyte was bubbled 30 min with oxygen.

SEM image of ZnO layer morphology obtained with 1.0 M *KCl* at 25 °C with an applied current density of -0.13 mA cm^{-2} is shown in Figure III.10a. It is clearly visible that the surface of the film prepared at 25 °C is formed by coalesced big platelet-like structures with considerable dimensions in the micrometer range (see the close view image in the inset). The large amount of non-conducting matter on the electrode surface could be the reason for the considerably negative potential values reached at higher [*KCl*] (Figure III.9). A noticeable difference in the morphology for the layers deposited at temperatures between 25 and 70 °C with 1 M *KCl* is observed (Figure III.10b). At high temperature the density of platelet-like sheets is very low and underneath the bare TCO substrate is seen (inset of Figure III.10b), in contrary to the observation done in the previous section that compact ZnO 2D layers could be prepared with [*KCl*] equal to 0.1 M at 70 °C. As expected doubling [*KCl*] to 0.2 M has an effect on the deposition potential. Although following the same deposition regime as with 0.1 M *KCl*, two small destabilizations (at 700 and 1100 seconds, Figure III.9), probably related with layer morphology changes, are observed. This was confirmed by SEM observation (Figure III.10c), which showed that this film is composed of smaller number of previously found sheet-like crystals and a compact ZnO layer underneath. Thus the presence of big crystals can explain why the deposition potential behaves as in the case with 0.1 M *KCl* in the early deposition stage and then destabilizes.

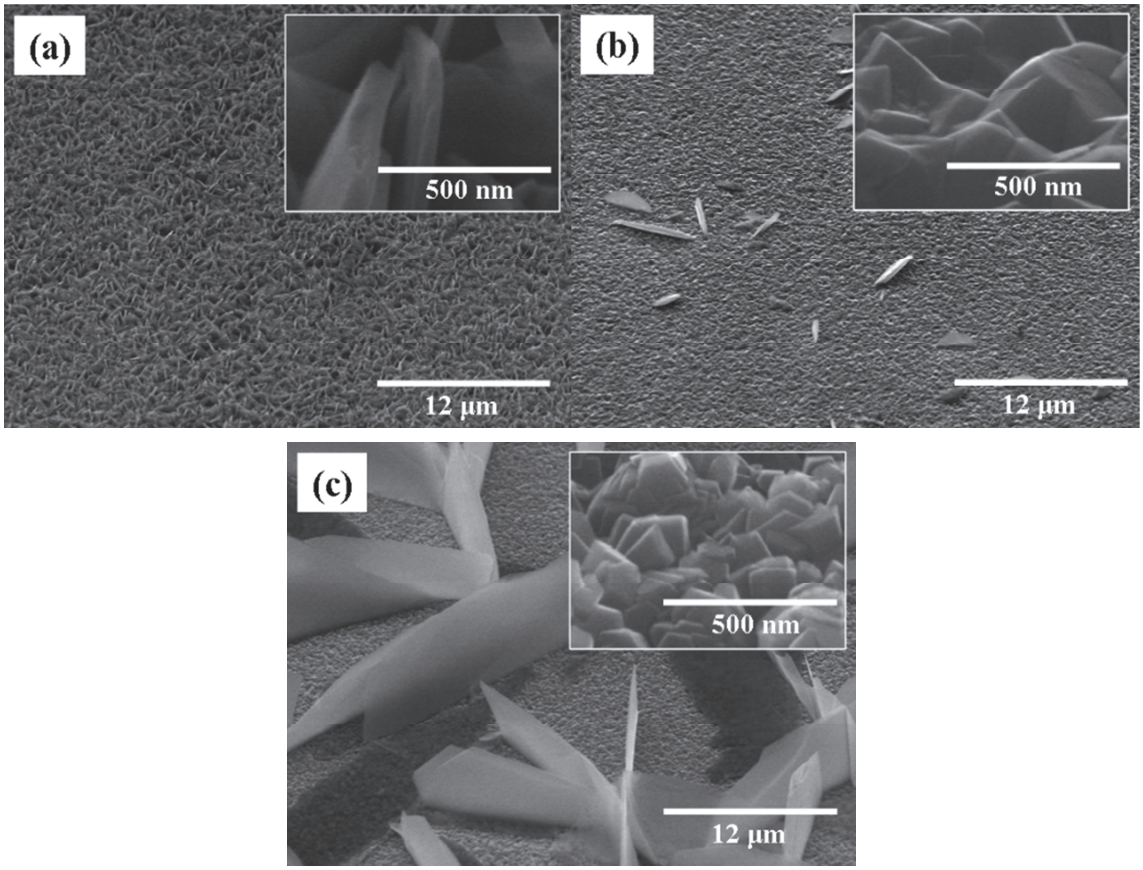

Figure III.10. SEM images (tilted view, 45°) of ZnO 2D films deposited at j= -0.13 mA cm^{-2}, Q = 0.4 C cm^{-2} from an electrolyte containing 5 mM *$ZnCl_2$* and: (a) 1 M *KCl* at 25 °C. The inset is an enlarged view of the big sheet-like crystals.; (b) 1 M *KCl* at 70°C (the inset shows the bare TCO substrate underneath the big crystals); and (c) 0.2 M *KCl* at 70°C. The inset is an enlarged view of the ZnO compact layer seen underneath.

The increased [*KCl*] influences the species complexation in the solution. Species repartition diagrams of electrolytes containing 5 mM $ZnCl_2$ and 0.1 or 1 M *KCl* at 70 °C are depicted in Figure III.11 (a) and (b), respectively. When the *KCl* concentration in the solution is 0.1 M, Zn^{2+} ions are in higher amount in the acidic region, whereas for a concentration of 1 M, their percentage in the solution is 10 times lower. The $ZnCl^{+}$ species are predominant in the both electrolytes and therefore once the O_2 reduction starts the shift to higher pH values is promoted. The formation of $Zn(OH)^{+}$ and $Zn(OH)_3^{-}$ is chemically favorable when Zn^{2+} ions are available in the complexed form of $ZnCl^{+}$. From these diagrams is also seen that the solution with higher [*KCl*] contains $ZnCl_2$ in high quantity. The higher O_2 and Zn^{2+} diffusion at such temperatures insures their availability close to the electrode surface. Although not being significant the complexation of Zn^{2+} ions when the *KCl* concentration is increased to 0.2 M, it would lead to decrease of Zn^{2+} quantity in the solution (from 36 to 19 %). In this sense, the small amount of uncomplexed Zn^{2+} would be sufficient for the formation of the

first ZnO layer. Once the concentration of Zn^{2+} reaches a limit, the formation of ZnO might follow another chemical reaction path [90]:

$$ZnCl^{+} + 2OH^{-} \rightarrow ZnO + H_2O + Cl^{-} \qquad \textbf{Equation III.3}$$

Although it is difficult to tell if both reactions are responsible for the big sheet-like crystals formation, to a certain extent the one expressed by Equation III.3 is rather probable at higher *KCl* concentrations. Therefore it is possible to express their formation in terms of Zn^{2+} ions availability close to the electrode, being impeded either by the complexation with Cl^{-} or a lower diffusion at 25 °C.

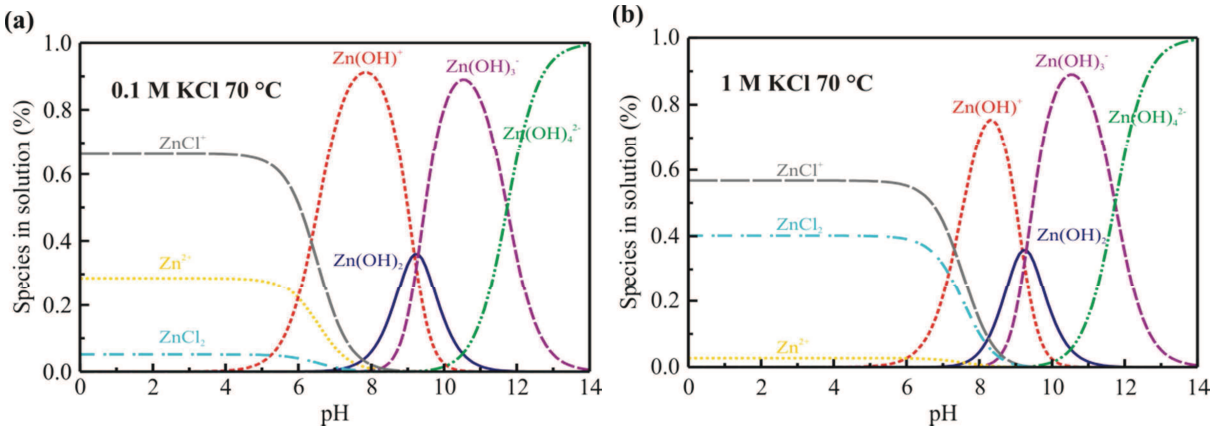

Figure III.11. Species distribution diagrams in solution at 70 °C as a function of pH for electrolytes containing 5 mM $ZnCl_2$ and (a) 0.1 M KCl or (b) 1 M *KCl*.

Figure III.12 shows XRD patterns of the ZnO layers deposited with different [*KCl*]. Additional peaks to those assigned to ZnO planes appear when doubling the concentration from 0.1 to 0.2 M of *KCl* at 70 °C (curve 3, Figure III.12). The peaks corresponding to ZnO structure are coming from the thin film observed underneath the big sheets (inset Figure III.10c). The relatively low intensity of the peaks confirms the thinness of the layer and the smaller grain dimensions. The appearance of the peaks coming from several ZnO planes evidences the random layer orientation. Strikingly, although on the SEM image (inset in Figure III.10) it is possible to see that for the small hexagonal shaped grains the peak from the (002) plane is not present. It has been previously reported that high *KCl* concentrations hinder the crystal growth along the c-axis of ZnO due to the strong adsorption of Cl^{-} ions onto the (0001) plane [195]. The rest of the peaks have been indexed to correspond to the zinc hydroxychloride compounds: $Zn_5(OH)_8Cl_2$ (PDF4+ 00-072-1444) or ZnCl(OH) (PDF4+ 04-

009-6259). Their formation is promoted when high concentrations of $ZnCl_2$ are used and follows the reaction [87]:

$$5Zn^{2+} + 2O_2 + 4H_2O + 2Cl^- + 8e^- \rightarrow Zn_5(OH)_8Cl_2 \qquad \textbf{Equation III.4}$$

Although it is unclear which reaction occurs, from the species repartition diagrams it is possible to see the changes in their amount due to the [*KCl*] variation, being $ZnCl^+$ the species involved in the formation of *ZnCl(OH)* and $ZnCl_2$ in that of $Zn_5(OH)_8Cl_2$ respectively [87]. Some traces of Zn and KCl were found in the layer prepared with 1M *KCl* at 25 °C (curve 1, Figure III.12). At high overpotential Zn deposition and Equation III.4 is favored due to the large amount of available electrons, being in agreement with the potential values obtained in the chonopotentiogram (Figure III.9). The relatively high intensities from $Zn_5(OH)_8Cl_2$ and *ZnCl(OH)* compounds might also find its origin in the fact that with such high *KCl* concentrations, the amount of $Zn(OH)_3^-$ species is rather high and at low deposition temperature the water removal process is not that efficient. For the layer deposited at 70 °C from the electrolyte containing 1M *KCl* the small amount of big crystals was not possible to be detected and only peak belonging to the bare TCO substrates are observed (curve 2, Figure III.12).

From the results presented above we can infer that an optimal *KCl* concentration (0.1 M *KCl*) is required for the deposition of defect-free, compact good quality ZnO films.

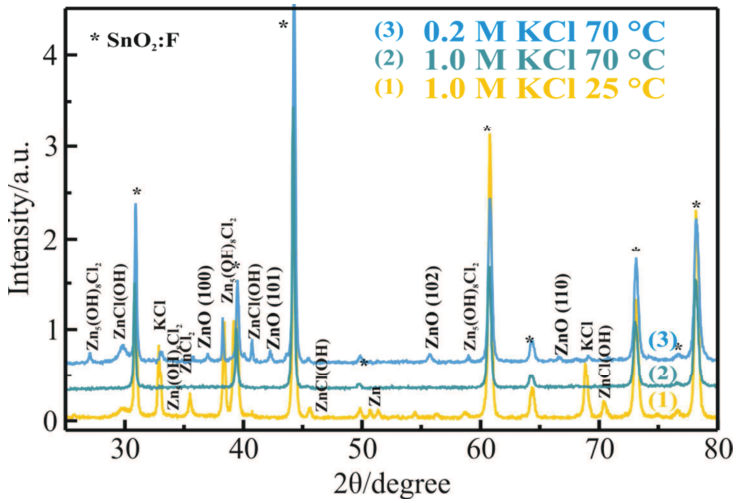

Figure III.12. X-ray diffraction patterns of ZnO layers deposited at j = -0.13 mA cm^{-2} from electrolyte containing 5 mM *$ZnCl_2$* and 1 M *KCl* at 25 °C (curve 1); 5 mM *$ZnCl_2$* and 1 M *KCl* at 70 °C (curve 2) and 5 mM *$ZnCl_2$* and 0.2 M *KCl* at 70 °C (curve 3). The diffraction peaks of *SnO_2:F* substrate are marked with stars (*).

1.3. Role of the Applied Current Density

Aiming to better understand the role of the key parameters in the deposition mechanism of ZnO layers, as well as to acquire the knowledge on how to control its morphologies and properties, a supplementary study on the role of the applied current density was also performed. The deposition time or applied charge density also influences the surface morphology and thickness. In this study we used an electrolyte containing 5 mM $ZnCl_2$ and 0.1 M *KCl* and the thin films were deposited at 70 °C. For low charge densities (0.2 C cm^{-2}), the layer appears to be formed by small grains and is 170 nm thick, while for larger deposition periods (0.4 C cm^{-2}), the grains are bigger and the film is more flat with a 330 nm thickness. The current density-dependent morphology evolution is shown in Figure III.13. The ZnO layer deposited at -0.08 mA cm^{-2} (Figure III.13a) is formed of quite large and well-faceted hexagonal grains with the c-axis perpendicular to the substrate, characteristic for the ZnO growth. The cross-sectional view depicted in the inset of Figure III.13a shows that the film has columnar structure. The slight change of the deposition current density to -0.10 mA cm^{-2} leads to smaller dimension hexagonal grains which are more randomly arranged (Figure III.13b). At higher deposition current densities (i.e. -0.13 mA cm^{-2} and -0.16 mA cm^{-2}) the resulted film surface becomes denser, flatter and smoother (Figure III.13c).

If the deposition follows the growth mechanism discussed in the beginning of this chapter, and the potential minimum is taken as a nucleation indication, in the initial deposition stage at higher current densities a larger nuclei number will be generated. Then the randomly oriented nuclei are expected to grow along the c-axis due to the higher surface energy of the polar (0001) plane. Although the preferential growth is energetically favoured, and the (0001) oriented nuclei are expected to grow at a higher rate, other electrochemical effects must be taken into account. It is well known that the ZnO electrodeposition happens under quasi-equilibrium conditions [87], meaning a constant generation and consumption of OH^- ions. In this case the rate of OH^- production is proportional to the deposition current density, therefore higher OH^- production due to the high current densities values (-0.13 mA cm^{-2} and -0.16 mA cm^{-2}) might induce considerable excess of OH^- close to the electrode surface, affecting the growth direction and mechanism. At current densities -0.08 mA cm^{-2} and -0.10 mA cm^{-2} the deposition potential shows very stable behaviour (Figure III.14), this could be regarded as balanced generation and consumption of *OH-* ions. Due to the small rate of OH^- formation at these lower studied current densities, the polarity of the layer of electrogenerated OH^- ions

does not exert a strong enough force over the nuclei, allowing a preferential c-axis growth. Although not comparable due to the use of different deposition conditions (i.e. NO_3^-) our findings on the morphology dependence from applied current density present rather different results [86, 194]. It was reported an enhancement of the growth velocity along the c-axis for higher deposition currents (-1.5 compared to -1.1 mA cm^{-2}).

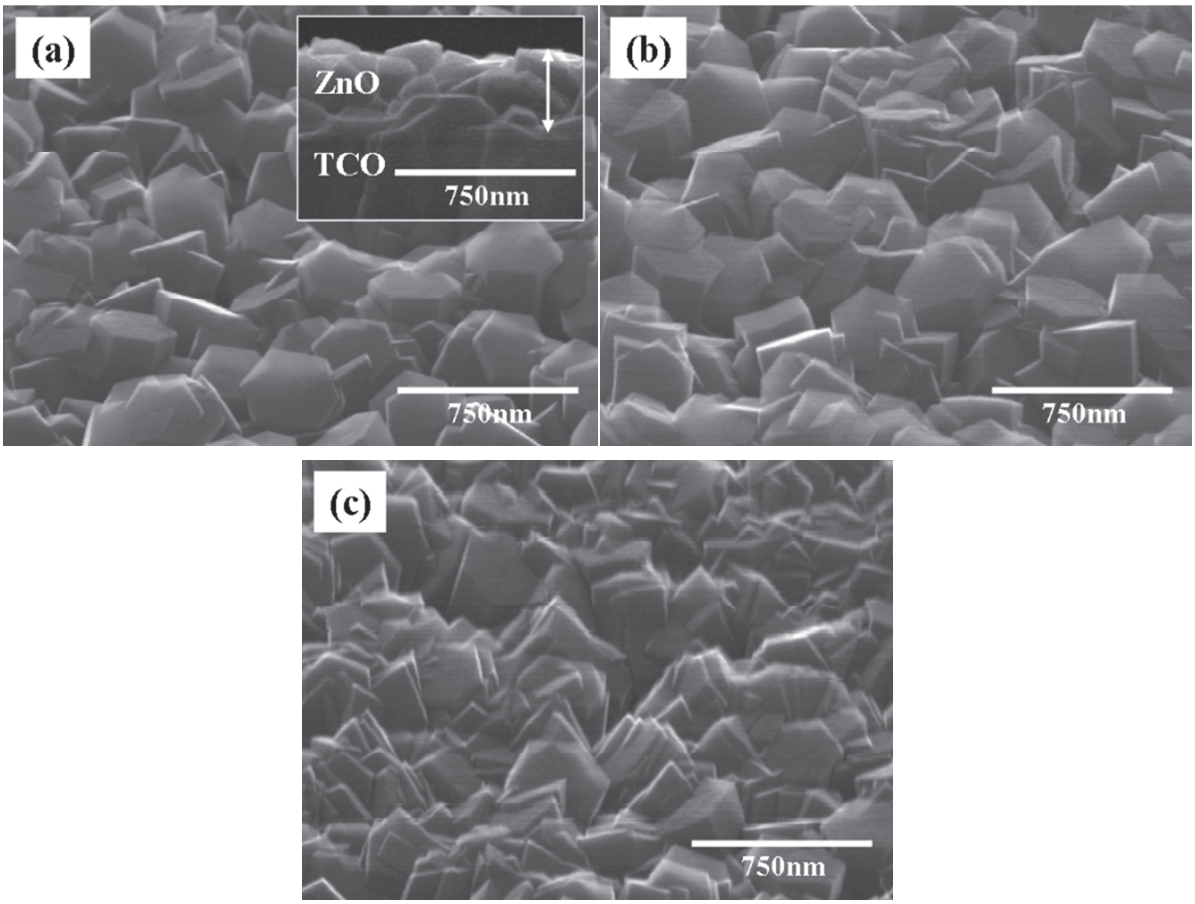

Figure III.13. SEM images (tilted view, 45°) of ZnO 2D films deposited from 5 mM $ZnCl_2$ and 0.1 M KCl, at 70 °C, Q = 0.4 C cm^{-2} and at following current densities: (a) -0.08 mA cm^{-2}. The inset represents a cross-sectional view of the layer; (b) -0.10 mA cm^{-2} and (c) -0.16 mA cm^{-2}.

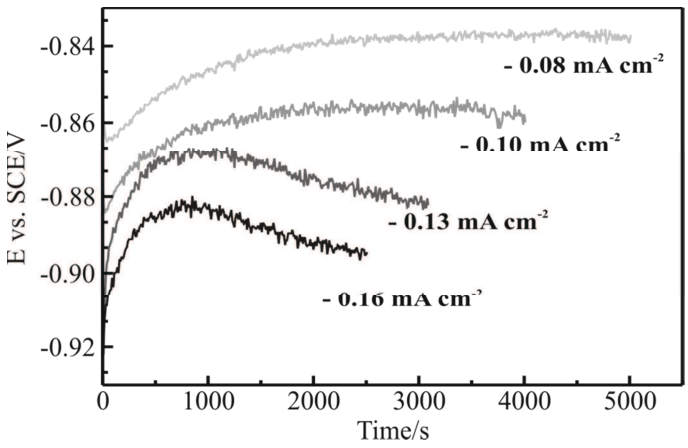

Figure III.14. Chronopotentiograms obtained during deposition of ZnO 2D layers at different current densities: -0.08; -0.10; -0.13 and -0.16 mA cm^{-2} from an electrolyte containing 5 mM *$ZnCl_2$* and 0.1 M *KCl* at 70 °C. All curves were recorded for a total passed charge density Q = 0.4 C cm^{-2}. Prior to all depositions the electrolyte was bubbled 30 min with oxygen.

The XRD analysis of the ZnO thin films deposited at -0.08 and -0.13 mA cm^{-2} shows that the films exhibit all ZnO diffraction peaks (Figure III.15). The ratio between peak intensities of (002) and other planes is higher for the films deposited at -0.08 mA cm^{-2}, whereas it is lower for those prepared at -0.13 mA cm^{-2}. This fact confirms the highly c-axis oriented crystallites in contrast to the nearly random oriented structure at higher deposition current densities. The annealing process (rapid thermal annealing and in conventional furnace at 500 °C) performed on the films deposited at these studied current densities showed only an increase of the diffraction peaks intensity without any other changes. The layers prepared at the studied different current densities also exhibit good optical transparency.

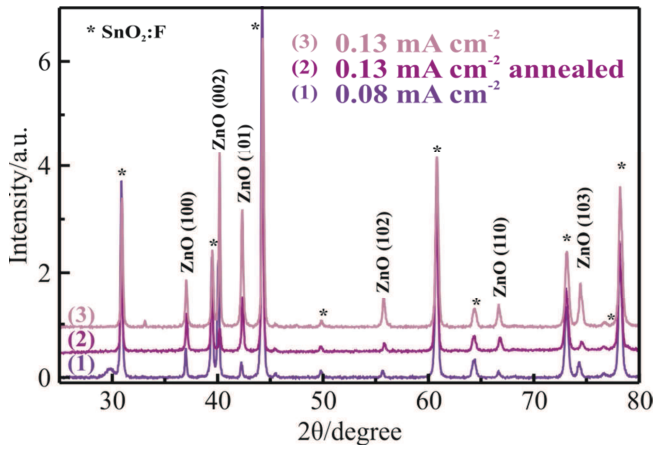

Figure III.15. X-ray diffraction patterns of ZnO layers deposited from a solution containing 5 mM *$ZnCl_2$* and 0.1 M *KCl* at 70 °C and current density of: -0.08 mA cm^{-2} (curve 1) and -0.13 mA cm^{-2} (curve 2 and 3 after annealing and without annealing, respectively). The diffraction peaks of *SnO_2:F* substrate are marked with stars (*).

In summary of this section we can say that by varying the deposition current density ZnO thin films with different morphologies (from small grains to larger hexagonal grains) could be prepared.

2 ZnO NANOWIRES (Tailoring the Nanowire Dimensions)

In this section, the control over the dimensions and density of electrodeposited ZnO nanowires is demonstrated. The influence of different parameters is studied:

i) The morphology and thickness of the galvanostatically deposited ZnO seed layers.
ii) The deposition current density when the nanowires are grown using the galvanostatic mode.
iii) The polarity of ZnO substrates.

2.1. Tailoring of the NW Dimensions by the Electrodeposited Seed Layer

One potential application of ZnO thin films is their integration as an electronic buffer layer in nanostructured (*eta* and dye sensitized) or electron transporting layer in organic solar cells. It has been reported that the morphology of ZnO thin films plays a role on the diameter and the density of electrodeposited ZnO NWs grown on them [89]. In that study electrodeposited and sprayed ZnO buffer layers were used. It was found that the density of ZnO NWs was double on the electrodeposited layer compared with the sprayed layers.

In this thesis, the realization of ZnO NW arrays on galvanostatically deposited ZnO seed layers with control dimensions was one of the primary objectives.

2.1.1. The Role of the Layer Morphology

Figure III.16 shows the SEM images of ZnO NWs arrays deposited potentiostatically (at -1 V vs SCE) on the 2D ZnO layers grown at 70 °C at different current densities (-0.10 and -0.16 mA cm^{-2}) and with the same passed charge density -0.4 C cm^{-2}. As discussed in the previous section these seed layers exhibit different morphologies depending on the applied current density. The 2D layer prepared at lower current density (-0.10 mA cm^{-2}, Figure III.13b) is composed of hexagonal grains with size about 350-400 nm, whereas that deposited at higher current density is flatter with larger grains (-0.16 mA cm^{-2}, Figure III.13c). As could be expected the ZnO NWs electrodeposition on the seed layer composed of hexagonal grains follows the epitaxial growth mechanism and the resulted NWs are large with the same ~ 400 nm diameter as the nucleus (Figure III.16a and cross-section image in the inset). The length of these NWs is around 1.5 μm. A very thick and densely packed ZnO NWs array is deposited

on the flatter 2D films (Figure III.16b). The large grain size and the flat substrate are the reason for the ZnO NWs array to exhibit a very closely packed structure, due to the lower density of nucleation centres. These ZnO NWs are so close in the arrays that they are forming almost a compact film due to their coalescing. In the inset of Figure III.16b it is seen that single NWs could be distinguished although the structure is close packed. In that case for the same passed charge density (15 C cm^{-2}) the ZnO NWs are twice longer (~ 3 μm).

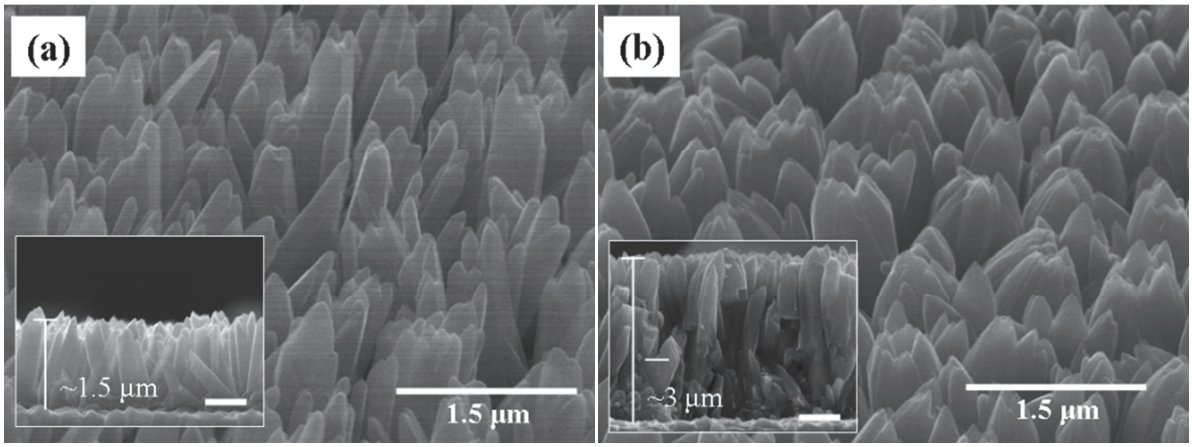

Figure III.16. SEM images (tilted view, 45°) of ZnO nanowire arrays deposited on seed layers prepared at 70 °C (a) -0.10 mA cm^{-2} and (b) -0.16 mA cm^{-2}. The ZnO nanowire array were deposited from 0.5 mM $ZnCl_2$ and 1 M *KCl*, at 80 °C, Q = 15 C cm^{-2}. The insets represent cross-sectional views of the nanowires (scale is 750 nm).

2.1.2. The Role of the Layer Thickness

A way to electrodeposit nanowires with smaller diameter was to vary the thickness of the galvanostatically prepared seed layer. Indeed, when using a thinner layer as seed layer (about 170 nm, grown with a charge density of 0.2 C cm^{-2} and j = -0.13 mA cm^{-2}) the ZnO NWs are thinner (about 150 nm in diameter) and oriented in different directions (Figure III.17). Whereas on thicker layer (350 nm, and prepared under the same conditions but with higher passed charge density (0.4 C cm^{-2})) the nanowires are thick and closely packed as those shown in Figure III.16b. It was also observed that the ZnO NWs grow faster on the seed layer composed of hexagonal grains probably due to its better crystalline quality.

The possibility to control the density and dimensions of the electrodeposited nanowires could also come from the fact that ZnO is a polar crystal with positively Zn-terminated (0001) and negatively O-terminated ($000\bar{1}$) surfaces. Therefore, the surface energies of the polar {0001} planes are higher than those of nonpolar $\{01\bar{1}0\}$ and $\{11\bar{2}0\}$ (Table III.3) [200]. In this way,

the preferential growth along the c-axis or [0001] direction is energetically favourable and therefore ZnO would grow faster on this plane (Figure III.18).

Table III.3. Calculated surface energies of ZnO surfaces [200–202].

Surface orientation	Surface energy (γ), J/m^2
$(10\bar{1}0)$	1.12
$(11\bar{2}0)$	1.06
* Zn-(0001)	2.15
* O-$(000\bar{1})$	1.7

* For the Zn-(0001) and O-(0001) surfaces, half of the surface cleaving energy is listed as an approximate value.

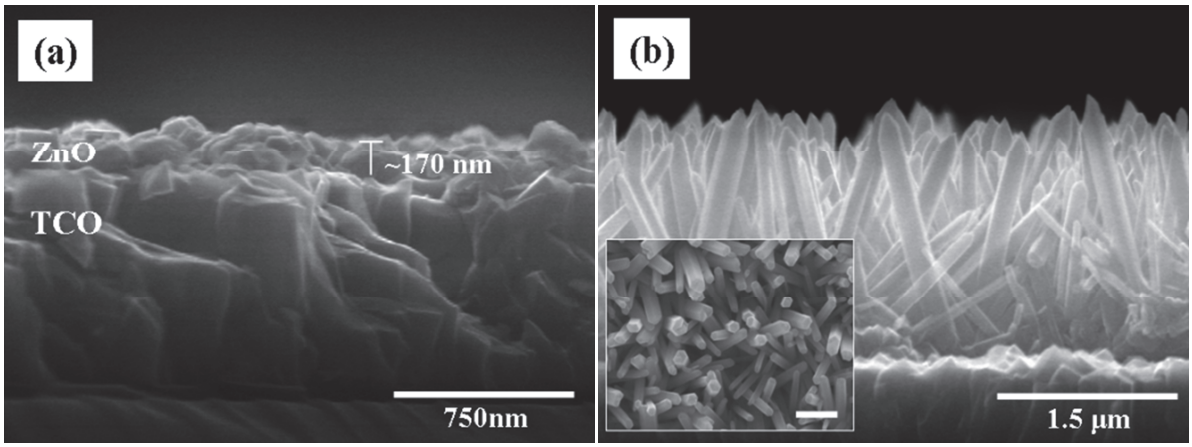

Figure III.17. SEM images (cross-sectional view) of: (a) ZnO 2D film deposited from 5 mM $ZnCl_2$ and 0.1 M *KCl*, at 70 °C, Q = 0.2 C cm^{-2}, at -0.13 mA cm^{-2} and (b) the ZnO nanowires grown on the layer from 0.5 mM $ZnCl_2$ and 1 M *KCl*, at 80 °C, Q = 15 C cm^{-2}. The inset represents a top-view of the nanowire array (scale is 750 nm).

Figure III.19 shows the PL spectra form a ZnO 2D layer and ZnO NW array. For the case of the NWs, it can be seen that the near band-edge emission (372 nm) is sharper and more intense than the defect related emission (550 nm). This indicates that the as-grown nanowires are with fewer defects than the 2D layer.

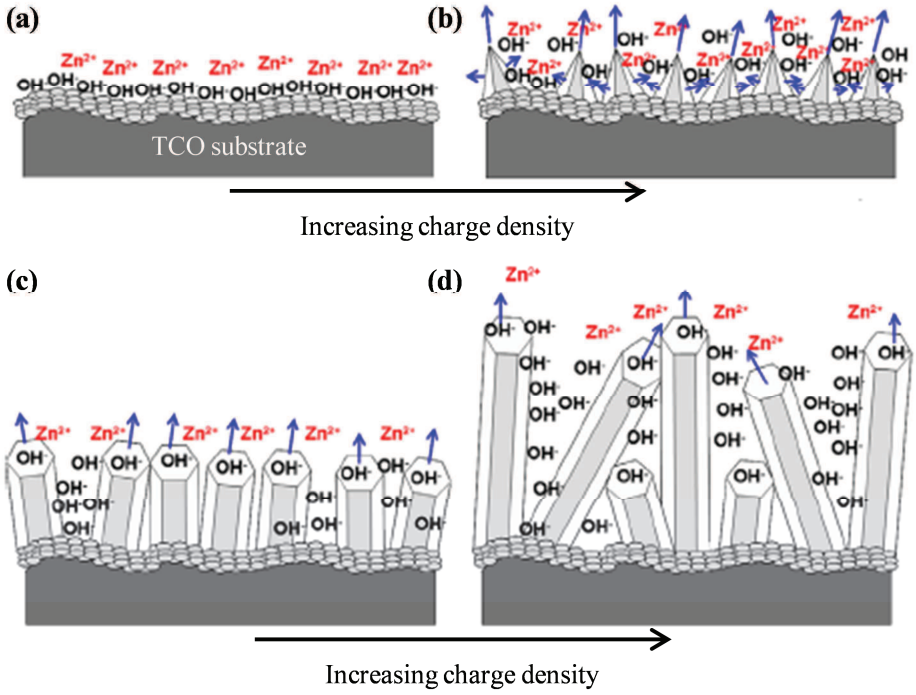

Figure III.18. Scheme of the growth mechanism of ZnO nanowires: (a) ZnO buffer layer electrodeposited on top of the TCO substrate. The blue arrows indicate the preferential growth along the [0001] (the length of the arrows is proportional to the growth rate, showing that the longitudinal growth is faster than the lateral one), the charge density increases from (a) to (b), (c) and (d) images, respectively [196].

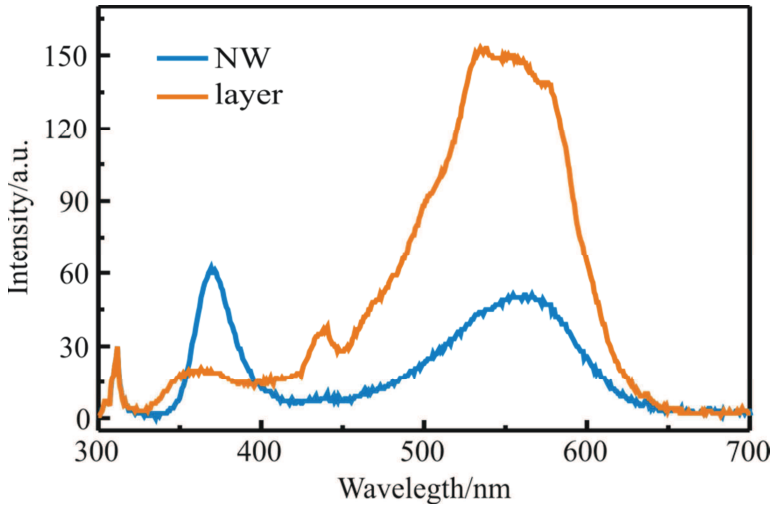

Figure III.19. Room temperature PL spectra a ZnO film (deposited at 25 °C, j = -0.13 mA cm^{-2} and Q = 0.4 C cm^{-2}, from an electrolyte containing 5 mM *$ZnCl_2$* and 0.1 M *KCl*) and ZnO NW array grown on the galvanostatically deposited layer (deposited at 80 °C, E = -1 V vs SCE and Q = 15 C cm^{-2}, from an electrolyte containing 5 mM *$ZnCl_2$* and 0.1 M *KCl*).

In summary, in this section is shown that ZnO nanowires with controlled dimensions could be grown using different types of electrodeposited ZnO seed layers. In this way, ZnO nanowires with diameters between 150 nm to 400 nm are prepared.

2.2. Tailoring of the Nanowire Dimensions by the Applied Current Density

Here, ZnO nanowires deposition by galvanostatic mode and the effect of the applied current density on their density and dimensions are presented.

The amount of electrochemically produced OH^- is crucial for the formation of ZnO [65, 87] (Equation II 1 and 2) and therefore the applied current density is an important parameter influencing the rate of electrochemical reactions, e.g., the amount of reduced O_2. For instance, in the section ***1.3*** has been shown that at higher current densities a more compact and randomly oriented ZnO 2D layer is deposited (Figure III.13c). In the contrary, at lower applied current densities, the layer is formed by larger hexagonal grains (Figure III.13a). This result is related from one side with OH^- ions generation and from the other side with available active surface states.

In a similar way we have found that the applied current density influences the growth of ZnO NW arrays. It has been shown that the lowering of the $ZnCl_2$ concentration leads to the formation of nanowires [65]. That is why we use the same electrolyte as for 2D layer preparation but the concentration of $ZnCl_2$ is ten times lower. Figure III.20 shows SEM images of NW arrays deposited at different current densities. From these images it is seen that:

i) The density of NWs increases with the applied current density.

ii) The diameter of NWs decreases with the increase of the applied current density. In this case the larger amount of generated OH^- occupies all nucleation sites in the initial growth stage thus forming later a denser array of nanowires with smaller diameters. In Table III.4 is summarized this observation for the NW diameter dependence for all studied current densities.

iii) The length of the nanowires does not follow a linear change with the increase of the deposition current density. For a same passed charge density (Q = -0.8 C cm^{-2}), NWs prepared at j = -0.13 and -0.18 mA cm^{-2} are 750 nm and they are longer than those deposited at the other studied current densities. These results could be explained with an equilibrated production and consumption of OH^-.

iv) The tip morphology of the NWs changes from a flat (at j = -0.08 mA cm^{-2}) to a rounder/sharper shape (at j = -0.23 mA cm^{-2}), which is similarly to that of the potentiostatically grown nanowires (Figure III.21). The slow growth rate at

j = -0.08 mA cm^{-2} causes balanced production of OH^- and consumption of Zn^{2+} thus resulting in flatter nanowire tips (Figure III.22) [166].

Although it is hard to estimate the efficiency of the deposition process due to the fact that the ZnO electrodeposition is not a pure electrochemical process, a correlation between the total passed charge density (Q = 0.8 C cm^{-2}) and the total amount of deposited matter reflects on the ZnO NWs dimensions (Table III.4).

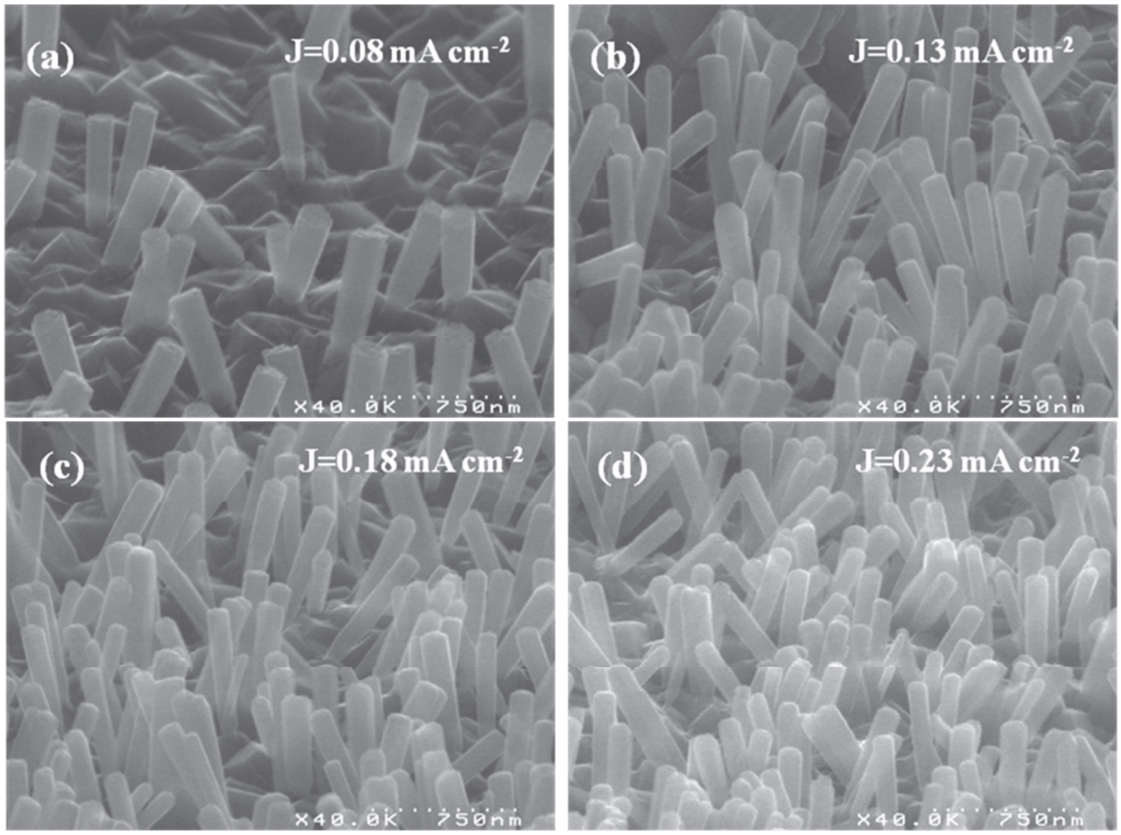

Figure III.20. Tilted view (45°) SEM images of ZnO NW arrays deposited on TCO from electrolyte containing 0.5 mM $ZnCl_2$ and 1 M KCl at -0.08 mA cm^{-2} (a), -0.13 mA cm^{-2} (c) and -0.18 mA cm^{-2} (c) and -0.23 mA cm^{-2}. The temperature of the bath was 80 °C and total passed charge Q = 0.8 C cm^{-2}.

Table III.4 ZnO NW average dimensions and densities obtained under different current densities.

Deposition current density (mA cm^{-2})	length(nm)	Diameter (nm)	Density (NWs/cm^2)
-0.08	580	170	~ 4.4 x 10^8
-0.13	680	120	~ 1.5 x 10^9
-0.18	600	100	~ 2.0 x 10^9
-0.23	480	100	~ 3.0 x 10^9

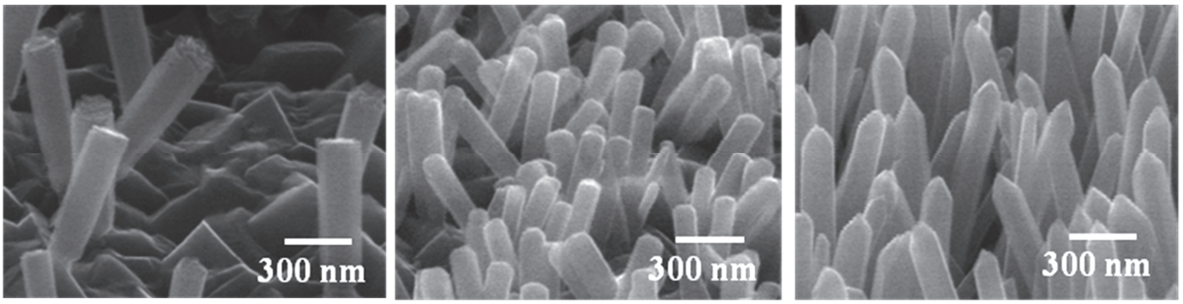

Figure III.21. Tilted view (45°) SEM images of ZnO NW arrays deposited on TCO from an electrolyte containing 0.5 mM $ZnCl_2$ and 1 M *KCl* at (a) -0.08 mA cm^{-2}, (b) 0.23 mA cm^{-2} and (c) in potentiostatic mode at E = -1.0 V vs SCE. The temperature of the bath was 80 °C, Q = 0.8 C cm^{-2} for (a) and (b) and 10 C cm^{-2} for (c).

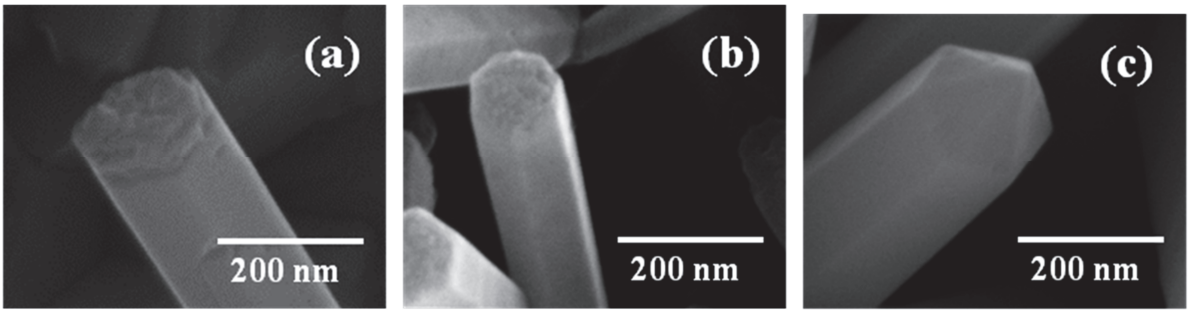

Figure III.22. Magnified SEM images of the ZnO NW arrays from Figure III.21

In summary, here we have shown the dependence of the ZnO NW dimensions on the applied current density.

2.3. Substrate Polarity Effects on ZnO Nanowire Electrodeposition

In this section, the effects of ZnO substrate surface polarity on the electrochemical growth of ZnO nanowires are discussed. Although it is not directly related with the objective of this thesis we have some interesting findings that would like to present.

The electrochemical growth of ZnO nanowires was carried out in two different configurations: (A) O-polar surface facing the counter electrode in the electrochemical cell, and (B) Zn-polar surface facing the counter electrode (Figure III.24). For these experiments, the bifacial substrates (Zn- and O-polar Figure III.23) were delivered from the Optoelectronic Department of LETI. Here it should be noted that the surface polarity could be confirmed by etching experiments.

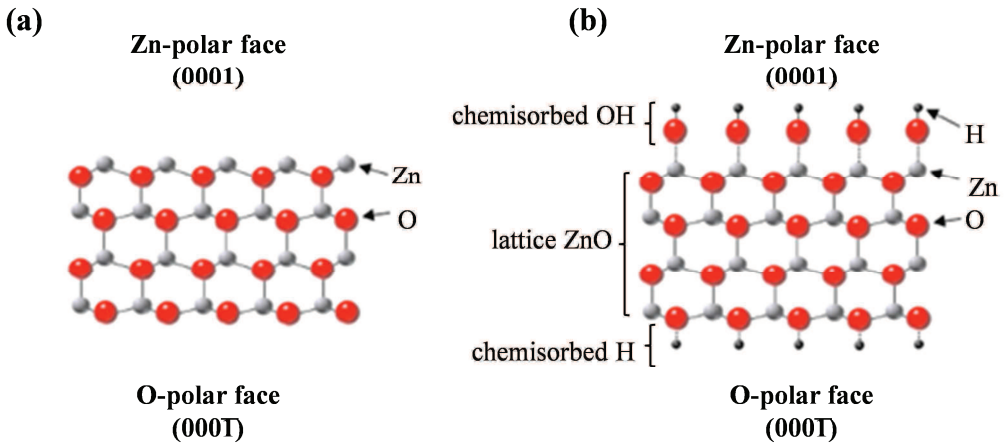

Figure III.23. (a) Ball model (side view) of the wurtzite ZnO structure along with its Zn-polar (0001) and O-polar (000$\bar{1}$) faces. (b) Ball model depicting the affinity towards OH^- and H adsorption [203].

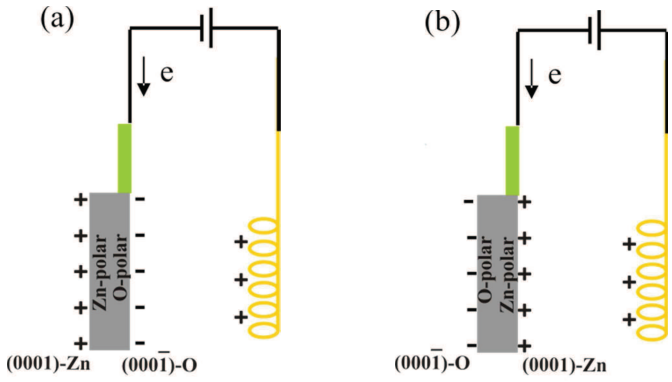

Figure III.24. Scheme of the used configurations for ZnO nanowires electrodeposition on: (a) O-polar ZnO surface facing the Pt counter electrode (CE) and (b) Zn-polar ZnO substrate facing the CE.

2.3.1. Electrochemical Deposition on O-Polar ZnO Surfaces

Figure III.25 shows the SEM images of electrodeposited ZnO nanowires when configuration (A) was used. Contrary to the tilted NWs grown on TCO substrates or ZnO seed layers (Figure III.17), here well aligned and perpendicular to the substrate plane ZnO NWs on O-terminated surface are prepared (Figure III.25a). This demonstrates once again that ECD is a technique to grow highly ordered ZnO NWs with desired dimensions.

No grow of NWs is observed on the Zn-terminated face (back side). In this case a thin layer of ZnO is formed with pyramidal-shaped grains together with few scattered bundles of NW (Figure III.25b). Simulations in crystal growth propose a reduced migration of Zn adatoms on Zn-polar surface while the contrary holds for the O-polar surface [204]. Therefore, the growth of the compact ZnO layer on Zn-polar surfaces might be the result of the reduced mobility of Zn^{2+} ions adsorbed on the surface.

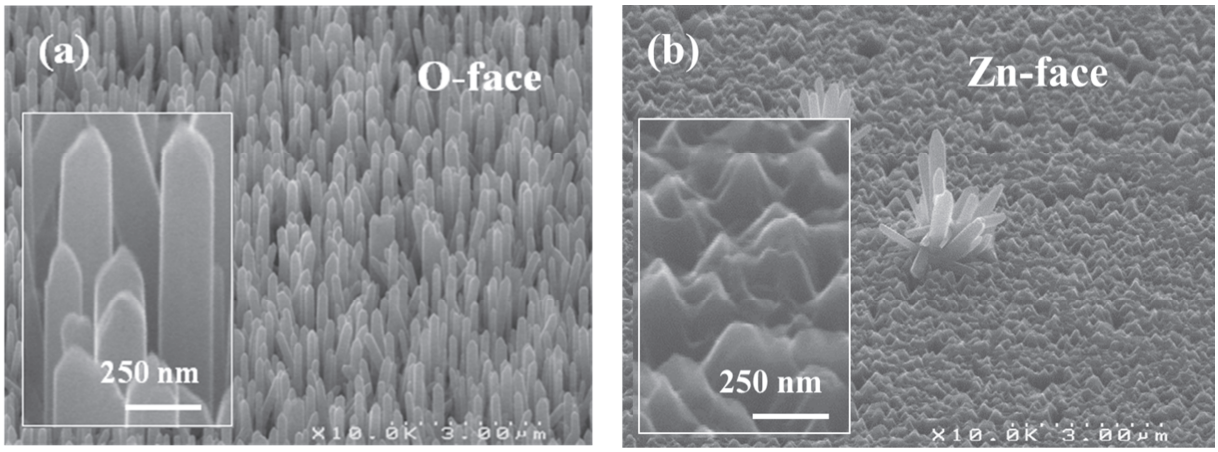

Figure III.25. SEM images tilted view (45 °) of the ZnO nanowires grown by ECD on polar ZnO substrates (O-polar surface facing the counter electrode). (a) ZnO NWs observed in the O-polar (0001) surface and (b) compact ZnO layer on the Zn-polar (0001) surface. Deposition conditions: E = -1V vs SCE, 80°C, total passed charge density Q = 20 C cm^{-2} and electrolyte composed of 0.5 mM $ZnCl_2$ + 1 M *KCl*.

2.3.2. Electrochemical Deposition on Zn-Polar ZnO Surfaces

Strikingly different ZnO nanostructures are grown when the Zn-polar surface faces the Pt counter electrode (electrochemical deposition in the B configuration). Slightly tilted nanowires are deposited on the O-polar surface (Figure III.26a), whereas well defined hexagonal patterns formed by ZnO nanowalls among small NWs are grown on the Zn-

terminated surface (Figure III.26b). Here we have to note that this kind of novel ZnO nanostructure formation is only observed when the electrodeposition method is used. In vapor-phase deposition techniques, ZnO NWs do not grow on Zn-terminated surface [205]. The observed phenomena were attributed to a consequence of minimization of surface energy due to the spontaneous polarization along the {0001} direction [206].

In the present study, the main objective was to grow ZnO NWs by electrochemical deposition on its polar phases. However, there are important implications that should be taken into account when using the electrochemical deposition: i) for instance, simultaneous redox reactions could be observed on bipolar electrodes when subjected to an electric field; ii) the potential difference between the two extremities could cause oxidation and reduction reactions at opposite surfaces [207]. Although not ruled out, it is difficult to identify possible bipolar electrochemical processes in the present case due to the large thickness of the used electrode (500 μm).

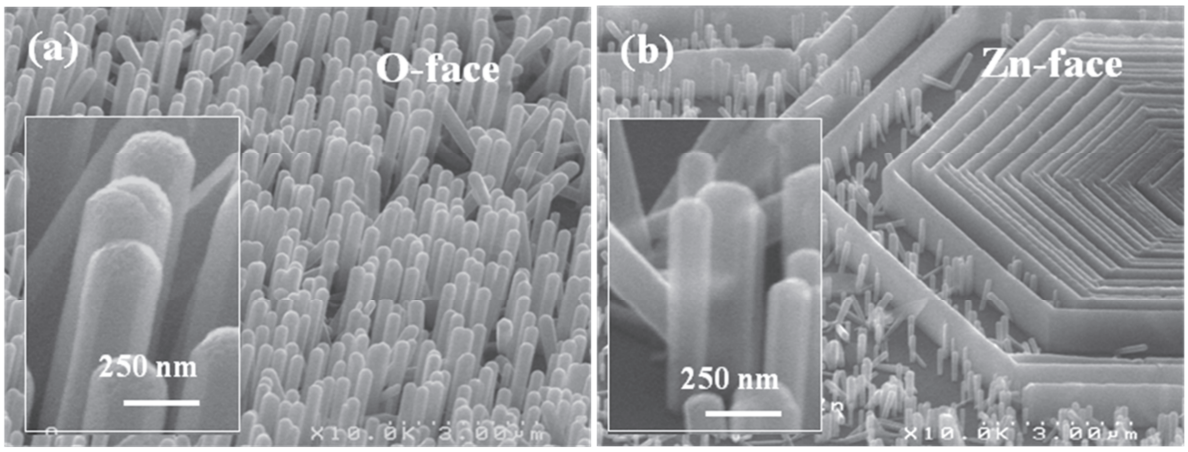

Figure III.26. SEM images (45°) of the ZnO nanowires grown by ECD on polar ZnO substrates (Zn-polar surface facing the counter electrode). (a) ZnO NWs observed in the O-polar (0001) surface and (b) ZnO nanowalls and NWs on the Zn-polar (0001) surface. Deposition conditions: E = -1V vs SCE, 80 °C, total passed charge density Q = 20 C cm^{-2} and electrolyte composed of 0.5 mM $ZnCl_2$ + 1 M *KCl*.

The observed results are treated separately as concerning two different surfaces whose polarities inherit to them different conducting properties, reactivity and growth behaviour.

Chemical and Electrochemical phenomena. The reactivity towards O_2 reduction and ZnO formation is changed upon direct electrical connection:

i) For the O-terminated face, the density of carriers at the surface, due to the dangling bonds of *O* atoms, is enhanced upon injection of current and therefore

the O_2 reduction is accelerated. The production of OH^- in excess explains the sharp NWs tips (Figure III.25a-inset) when the deposition is carried out in the A configuration [208]. The observed round tips of the NWs are result of lower current density due to recombination and scattering effects when the electrons travel to the opposite surface (in configuration B) (Figure III.25b-inset).

ii) For the case of the Zn-terminated surface, the injected electrons compensate the positive ionic charges of the Zn atoms at the surface. The electrons excess over the positive ionic charges cancels out the low diffusion effects of Zn^{2+} and thus promote the growth of ZnO nanowires although less efficient than on the O-surface.

Physical phenomena. The control over the growth kinetics of the ±(0001) facets in ZnO has been used to prepare piezoelectric nanobelts into diverse structures by vapor-phase methods [206]. Here, employing an electrochemical deposition, the effect of induced polarization due to the applied potential might also be accounted on the observed results:

i) The polarity of the O-terminated surface is affine to the positively charged Pt counter electrode (configuration A). The electric field lines evenly promote the transport of ions towards the substrate due to the accumulation of negative charges on the O-polar surface (Figure III.27a). This could explain the orientation of the NWs perpendicular to the substrate (Figure III.25a).

ii) For the case of the Zn-(0001) polar face, the positively charged surface is not in accordance with standard electrochemical processes. In the configuration B, the applied electric field inversely polarizes the surface thus influencing the surface effects (Figure III.27). The resulting electric field lines (Figure III.27b), cause NWs growth at certain angle to the substrate surface (Figure III.28e) [209]. Moreover, the substrate reactivity towards OH^- ions is also influenced and growth of NWs is permitted [205].

iii) The ZnO nanowalls formation is mostly probable due to dislocations produced during the mechanical cutting of the substrates (Figure III.28a and c). Polishing experiments showed that the O-surface was more rapidly cleaved than the Zn-polar surface, revealing different fracture resistance between the polar faces [210]. The dislocation density produced during the cutting process and the

configuration used during the electrochemical deposition are the key parameters for the growth of such ZnO nanowalls.

The highly oriented nanowalls perpendicular to the substrate (Figure III.28b and d), different from the tilted NWs (Figure III.28e), confirm that the O-terminated dislocations served as nucleation sites. The inverted polarity of the hexagonal patterns formed by oxygen atoms are affine to the positively charged Pt counter electrode, the perpendicular alignment of the nanowalls is the result of the electric field lines as previously discussed.

The difference in the length between NWs and nanowalls is another indication of their growth on different surface polarities (NWs are ~720 nm height, nanowalls are 1 μm) [211].

In summary, here we have shown that different ZnO nanostructures could be obtained when exploiting the polarity of ZnO substrates. Patterned ZnO surfaces (chemically or physically performed) in combination with electrochemical deposition could be an attractive method for the development of innovative optoelectronic devices.

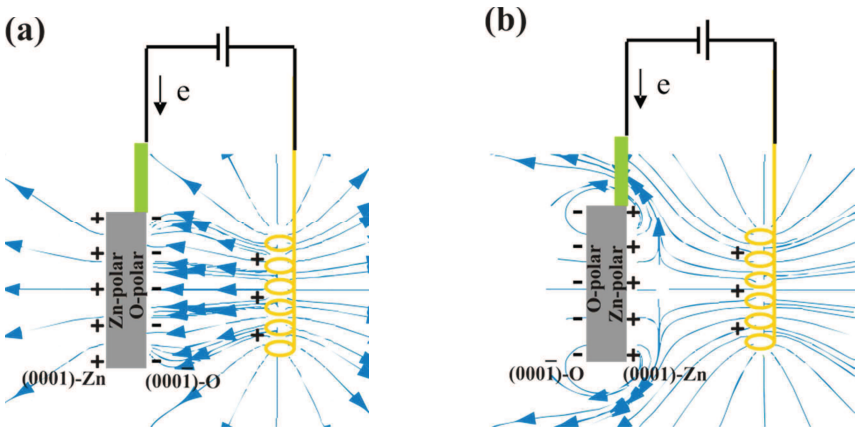

Figure III.27. Simulated mapping of the electric field during the electrochemical processes: (a) O-surface facing the Pt counter electrode. (b) Zn-surface facing the Pt counter electrode. Arrows in the field lines show the directions of the force between the Pt counter electrode and the Zn- and O-polar faces.

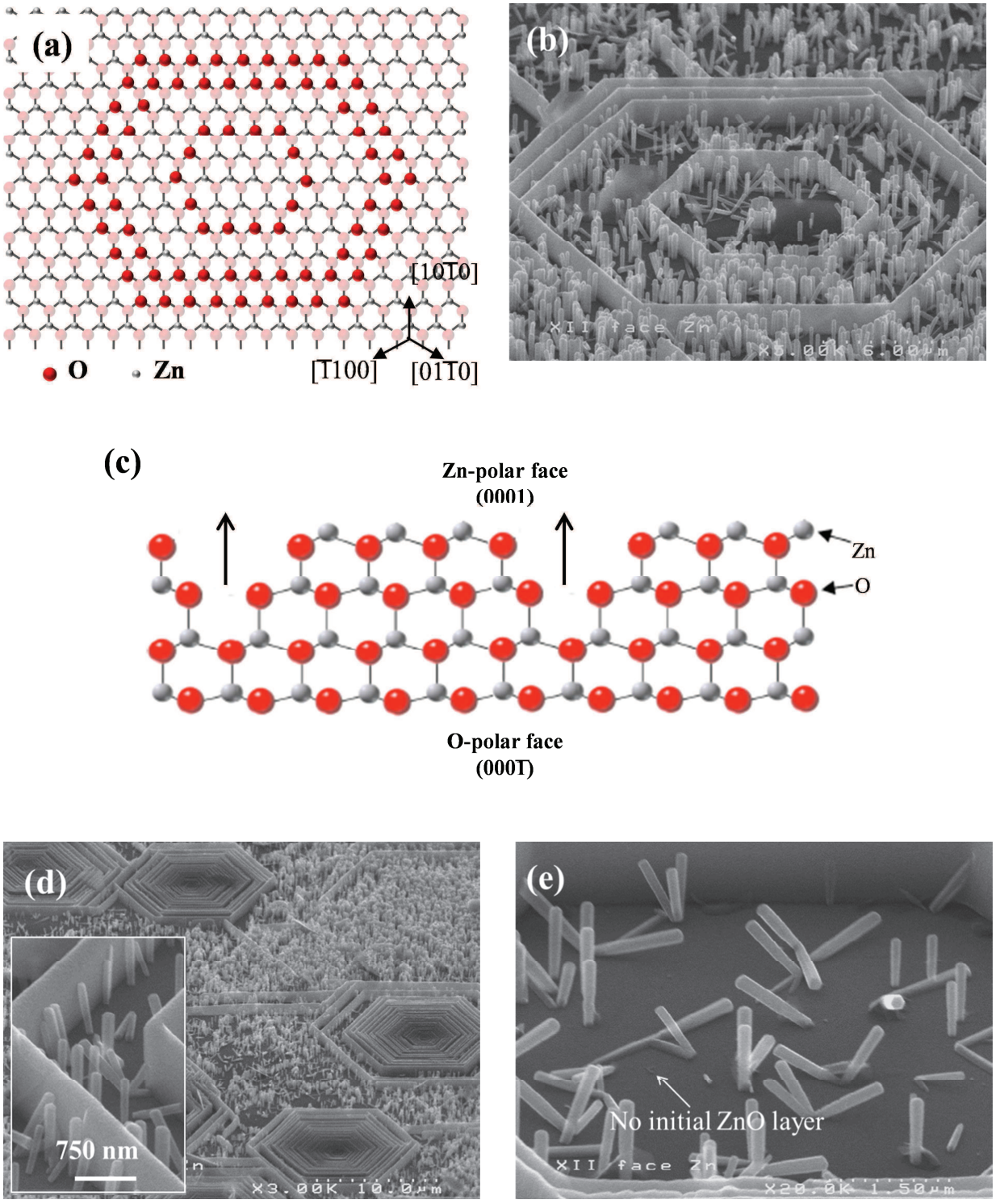

Figure III.28. (a) Top and (c) side view schema of surface dislocations on the Zn-(0001) face produced during sample preparation. (b and d) hexagonal patterns formed after electrochemical deposition of ZnO on Zn-polar surface and (e) scattered NWs grown between nanowalls.

3 CONCLUSION

In this chapter, we have presented the preparation of ZnO 2D compact layers by galvanostatic deposition using O_2, reduction. Aiming to better understand the deposition mechanism and to control the morphology and properties of these thin films, the influence of bath temperature, supporting electrolyte concentration and applied current densities have been studied.

Equally, the tailoring of electrodeposited nanowire dimensions and density was demonstrated. The galvanostatically deposited ZnO 2D layers were used as seed for ZnO NWs deposition. The polarity of ZnO substrates showed remarkably to influence the nanowire growth.

The obtained results seem attractive for future optoelectronic and photovoltaic applications.

CHAPTER IV : ZnO NW Photosensitization

In this chapter, the photosensitization of ZnO NW arrays with extremely thin light absorbing layers of CdS, CdSe and CdTe will be discussed.

A modified SILAR technique consisting of intermediate annealing procedure for improving the film properties will be introduced.

A chemical treatment is implemented for additional improvement of CdSe and CdTe material properties

CdTe is prepared by three different approaches: SILAR, CSS and QDs functionalization. Advantages and drawbacks for each deposition technique are emphasized.

As prepared materials exhibit optical and crystalline properties suitable to be further used in nanostructured solar cells.

1 PREPARATION OF ZnO/CdS CORE/SHELL HETEROSTRUCTURES

The first part of this section discusses the photosensitization of electrochemically grown ZnO NW arrays with CdS thin layers by classical SILAR process.

In the second part, an intermediate annealing procedure to improve the CdS properties and interfaces is introduced.

1.1. CdS Layer Deposition by Classical SILAR Technique

CdS absorber layer was deposited on the surface of the ZnO nanowires by sequential immersions of ZnO NW arrays in solutions containing corresponding Cd^{2+} cations and S^{2-} anions (refer to CHAPTER II for more experimental details). The growth of the CdS layers was monitored by UV-visible absorption spectra and controlled by the number of deposition cycles.

1.1.1. Structural and Optical Properties of the ZnO/CdS Core/Shell Heterostructures (Classical SILAR)

Figure IV.1 shows the SEM images of the ZnO/CdS heterostructures obtained under standard deposition conditions proposed by Nicolau et al. [122, 124]. It can be observed that the smooth surfaces of the ZnO nanowires became rough after the deposition of 20 SILAR cycles (Figure IV.1b). Enlarged SEM images reveal that the layer is formed by loosely bound nanoparticles or clusters of CdS (Figure IV.1b inset). The estimated thickness of the layer is about 15-25 nm. The maintained hexagonal shape of the nanowires after SILAR deposition shows that the pH of the solutions for CdS deposition (pH = 5 and 12 for Cd^{2+} and S^{2-} solutions, respectively) is friendly towards ZnO.

Figure IV.1b also reveals an accumulation of CdS nanoparticles at the top of the nanowires. In the SILAR method the homogeneous supply of ions at the nanowire surface plays an important role in the grow rate. The aggregation of nanoparticles at the tips could be explained by the fact that they are the first part from the sample which gets in contact with the solution. The ions diffuse through the space between nanowires and after successive ionic adsorption and reaction form the material. In Figure IV.1c SEM images of the inhomogeneous

coverage of the nanowire tips are shown. Regardless of the looseness of the outer part of the layer, it can be seen that CdS grows only on the nanowires and not in the bulk solution. This is very important when a uniform thin film is desired to be deposited on more complex structures. Alternative methods such as Chemical Bath Deposition (CBD) might result in the complete filling of the space between nanowires due to uncontrolled reaction in the bulk solution.

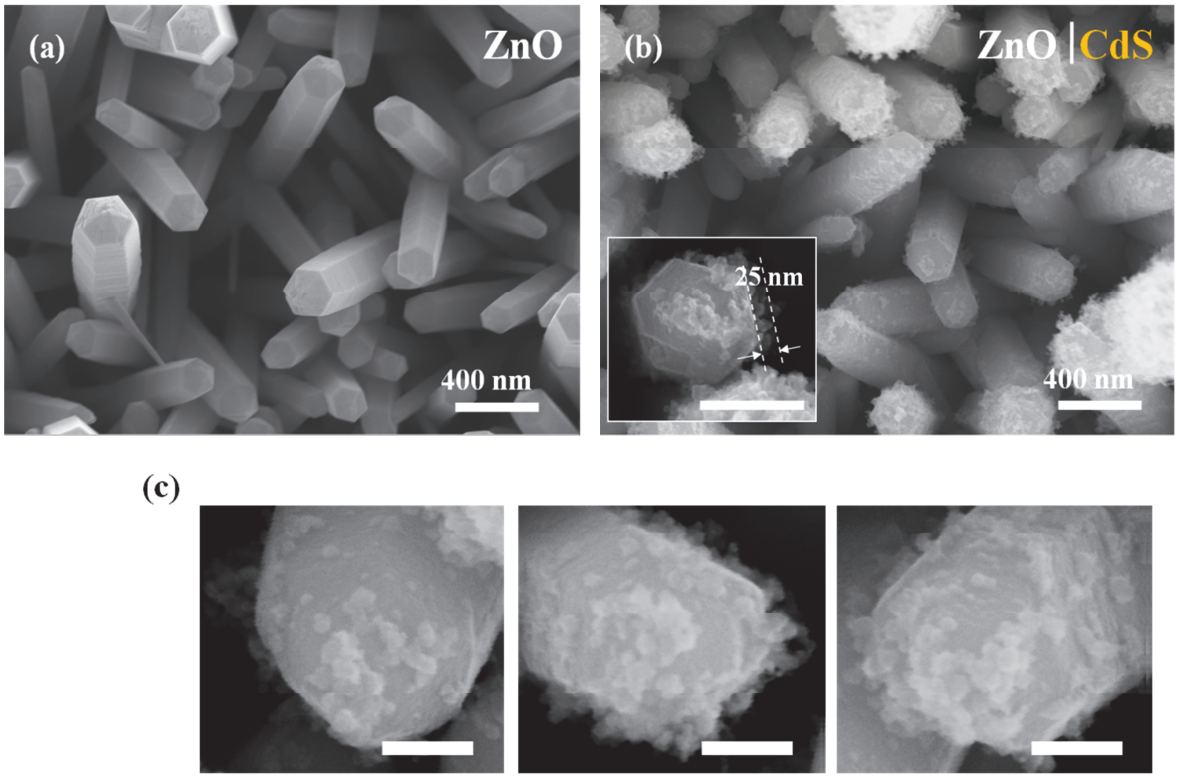

Figure IV.1. SEM images (top view) of CdS-coated ZnO nanowires. (a) bare ZnO nanowire array and (b) after 20 SILAR cycles CdS deposition. The inset shows a high magnification SEM image of single ZnO/CdS heterostructure (the scale bar is 200 nm). (c) High-magnification images showing variations in the coverage and density of CdS nanoparticles (scale bar is 100 nm).

Accumulation of CdS nanoparticles at the top of the nanowires raised concerns about the possibility to uniformly cover of the entire nanowire by the proposed SILAR method. Figure IV.2 shows cross-sectional SEM images of the ZnO/CdS nanowire array. It can be seen that the CdS layer is continuously deposited from the bottom to the top of the nanostructure and the accumulation of CdS nanoparticles is only on the NW tip. This uneven coverage of the structure might pose complications when optimizing the deposition of the p-type conductor. Thickness inhomogeneity could provoke different electro-optic phenomena:

the diffusion length of photogenerated carriers and charge separation mechanism might be different in thicker and thinner areas of the layer

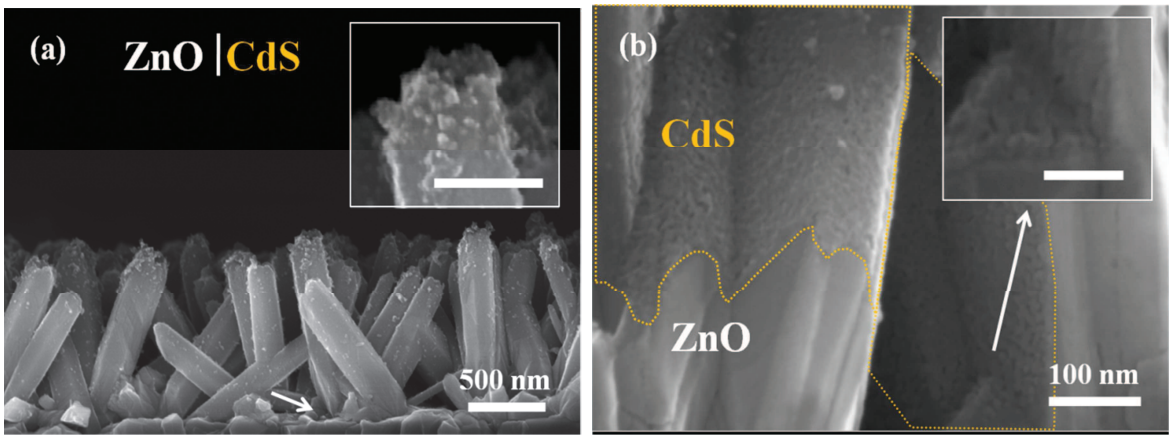

Figure IV.2. (a) Cross-sectional SEM images of CdS-coated ZnO NW array after 40 cycles of deposition; the inset shows the accumulation of CdS material at the top of the nanostructures; (b) magnified image at the bottom of the nanowires (indicated by the arrow in (a)) Scale bars in inset in (a) is 200 nm and in inset in (b) is 50 nm.

Figure IV.3 shows the XRD spectra from the ZnO/CdS nanostructures. Although the FWHM are fairly wide, the formation of CdS is confirmed by the presence of the diffraction peaks characteristic for its hexagonal phase (PDF 4+ 04-008-2191). The large values of FWHM (0.9238, 0.7954 and 1.03, at 25, 28.3 and 43.9°, respectively) are the result of the small grains forming the layer. The grain size of about ~10 nm was calculated from the (0100), (0101) and (0110) diffraction peaks (when CdS layer was deposited after 120 cycles).

In the ideal case, the material formation by SILAR method happens after the reaction between the successively adsorbed single ionic layers (analog to the vapor phase Atomic Layer Deposition, ALD) (Figure IV.4a). The broad distribution of CdS nanoparticles size and the looseness of the layer (close to an amorphous appearance) give an idea about the possible growth mechanism:

i) It could be possible that a localized CBD process takes place during the layer growth. The rinsing procedure, applied for the elimination of the loosely bound ions, seems to be inefficient due to the developed surface area by the ZnO NWs. Cd^{2+} or S^{2-} ions remain in a water layer and react upon the consequent immersion in the counter-ion solution thus forming a cloud of CdS nanoparticles at the nanowire walls (Figure

IV.4b). These dispersed CdS nanoparticles subsequently attach to the surface of the ZnO NWs as the deposition continues.

ii) No surface effects seemed to be present and the nanoparticles grow in all directions within the water layer. This could explain why most of the diffraction peaks belonging to CdS are observed in the XRD pattern, which is normally challenging to be detected when analyzing nanometer-thick films.

iii) The polarity of the solvent could play an important role in the SILAR deposition process. Since deposition of CdS is carried out in aqueous medium, the highly polar water molecules, compared to organic solvents, could cancel out nanowire surface effects. The effects regarding the polarity of the solvent will be discussed in the following section.

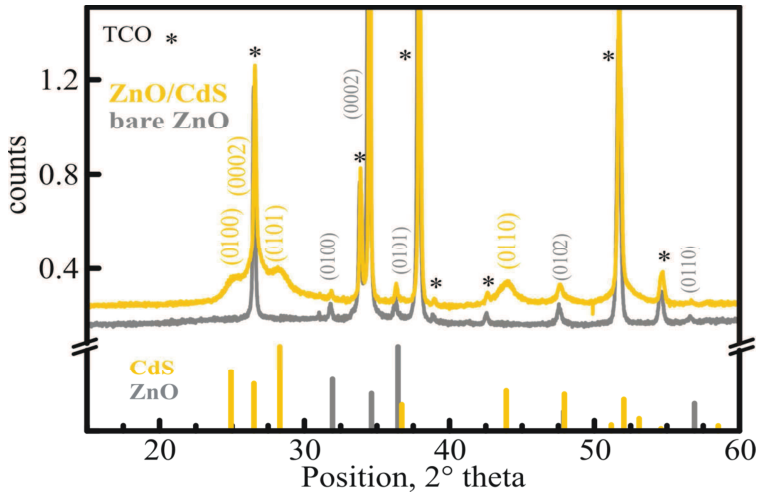

Figure IV.3. XRD patterns of the ZnO/CdS nanowire array and the reference diffraction peaks for the hexagonal phases of ZnO and CdS. The stars indicate the peaks from the SnO_2:F substrate.

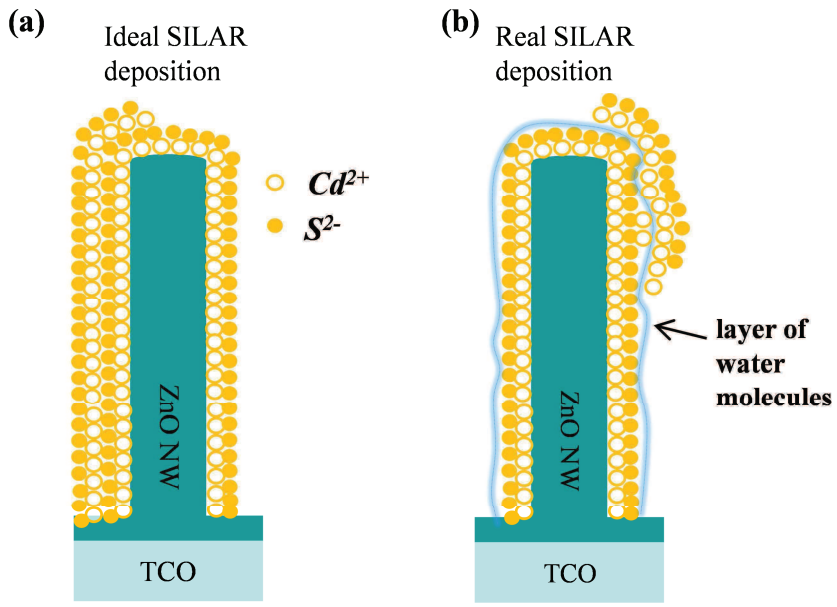

Figure IV.4. (a) Schema of an ideal monolayer formation during ionic layer-by-layer SILAR deposition. (b) Diagram of the CdS nanoparticle formation at the ZnO nanowire tip due to water and ions accumulation.

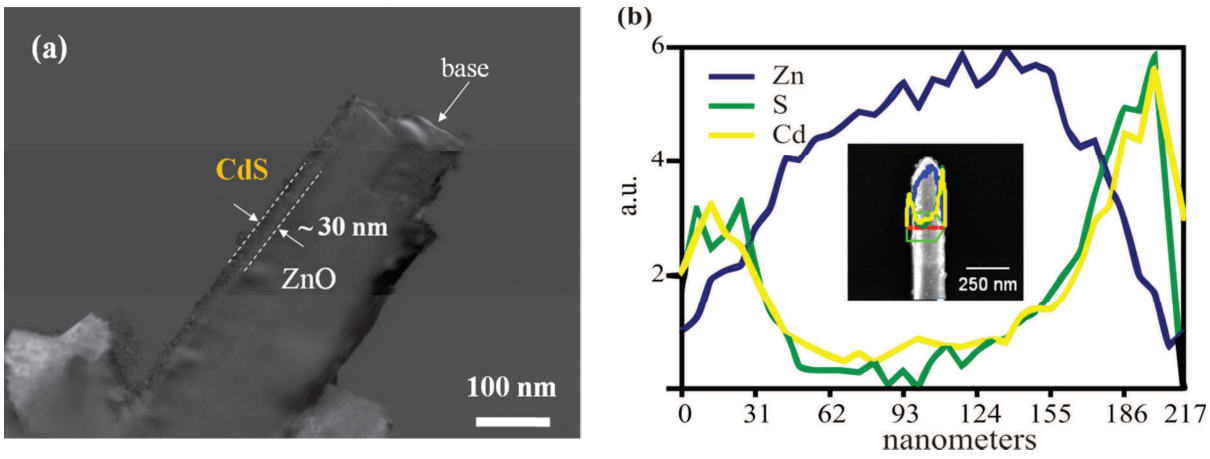

Figure IV.5. (a) Dark field (DF) STEM image of a single ZnO/CdS core/shell heterostructure obtained after 40 SILAR cycles for CdS deposition (the arrow points towards the bottom of the nanowire detached from the substrate while sample preparation). (b) EDX line-scan across the nanostructure as indicated in the inset (SEM image of the heretostructure).

Microstructure details and the chemical composition of the ZnO/CdS nanostructures are shown in Figure IV.5. STEM and EDX analysis confirm the presence of the CdS layer around the ZnO nanowire.

The STEM image of a single ZnO/CdS core/shell nanowire shows that the thickness of the CdS layer is about 30 nm after 40 SILAR cycles, while the ZnO core is around 180 nm. It can

be seen that the surface of the ZnO nanowire is uniformly covered from the bottom to the top (Figure IV.5a). The thickness of the CdS shell could be controlled by increasing the number of SILAR cycles.

The elemental composition of the single ZnO/CdS heterostructure is shown in Figure IV.5b. The signals belonging to *Zn*, *Cd* and *S* are clearly detected and the spatial distribution demonstrates the core/shell composition. While *Zn* and *O* signals are observed at center (core area), the signatures from *Cd* and *S* are found in the shell. The sharp decrease in intensity of *Cd* and *S* around ~30 nm confirms the STEM observations about the shell thickness. The line-scan reveals the formation of the shell with a composition ratio of *S*/*Cd* close to one.

Optical Properties of the ZnO/CdS Core/Shell Heterostructures Prepared by Classical SILAR

The ZnO nanowire sensitization was followed by sequential color changes with the number of SILAR cycles. The white-colored bare ZnO NW array turned yellow with increasing the number SILAR cycles (Figure IV.6a).

UV-visible spectra reveal the progressive increase of the absorbance (Figure IV.6b). It can be seen that the absorbance increases with the deposition cycles, which is related with the thickness of the deposited CdS layer. The onset of the absorption gradually moves to the bandgap energies characteristic for CdS bulk material (2.4 eV, ~516 nm) and the absorbance saturation is reached after 40 SILAR cycles. The blue shift in the CdS absorption edge observed after 5 and 10 cycles could be due to quantum confinement effects (crystallite size smaller than Bohr diameter of bulk CdS ~8nm) or due to the contribution of ZnO substrate [212].

Generally, the growth of light absorbing nanostructures (QDs for example) shows a monotonic increase of absorbance due to more controlled growth conditions at high temperatures (100 - 200 °C) [141, 213]. For the case of SILAR technique, the low deposition temperature results in a broader distribution of CdS nanoparticles size and the increase of absorbance is less gradual (Figure IV.6b).

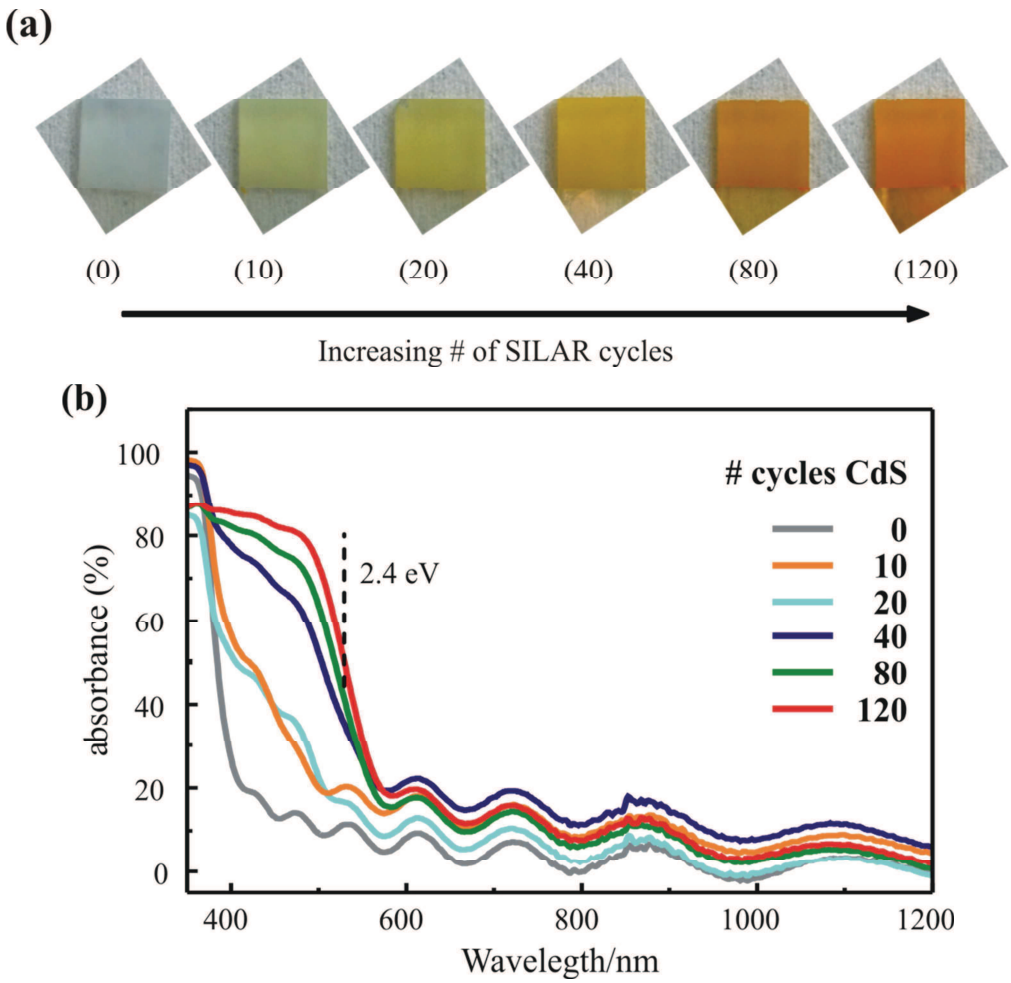

Figure IV.6. (a) Pictures of ZnO NW arrays before and after their photosensitization by indicated SILAR cycles. (b) UV-visible absorbance spectra of the CdS sensitized ZnO NWs arrays. Bang gap of bulk CdS is indicated

The disappearance of the ZnO band edge with increasing number of SILAR cycles is clearly visible for samples prepared with more than 80 cycles. Possible indirect transitions might be present due to the type-II band alignment as the quality of the CdS layer and interfaces improve with deposition cycles. Photogenerated holes and electrons migrate from ZnO to CdS and from CdS to ZnO, respectively, due to the position of the energy levels. The interfacial charge transfer, as the layer of CdS becomes thicker, affects the direct transition probability from the conduction to the valence band of ZnO [127].

The calculated bandgaps between 2.35 and 2.4 eV (Figure IV.7) are in accordance with reported values for CdS bulk (2.4 eV) [126, 214]. The shift towards longer wavelengths indicates that the CdS formed after 40 SILAR cycles reaches the properties of bulk material. In the present case, the determination of the bandgaps was challenging due to the broad

absorption edges close to 500 nm. Nevertheless, sharper transitions in the curves above 40 deposition cycles confirm the good optical properties of the CdS shell.

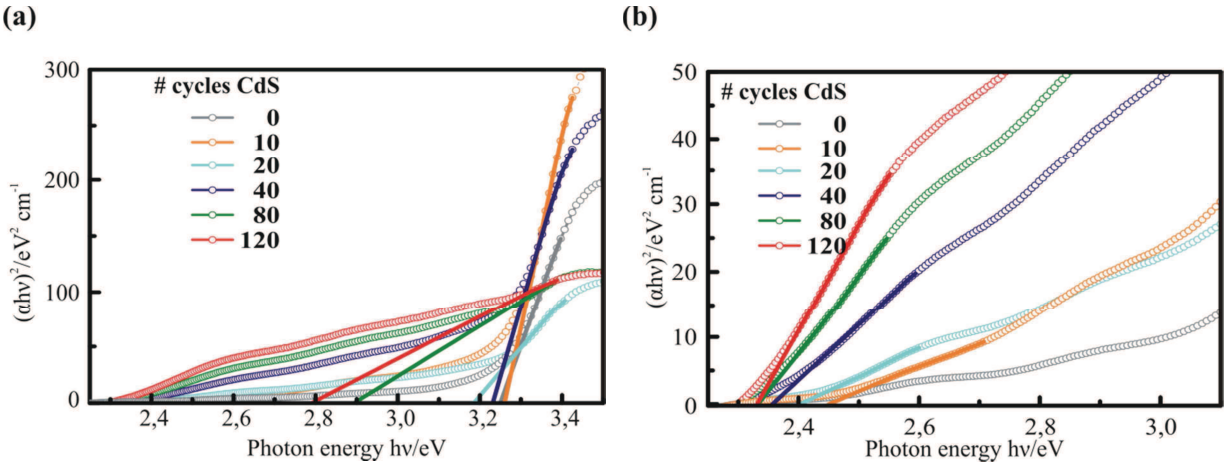

Figure IV.7. (a) Optical bandgap evolution of the ZnO/CdS heterostructures versus the number of SILAR cycles, and (b) same Tauc plots highlighting the spectrum region for the expected optical transition of CdS.

1.2. CdS Layer Deposition by Modified SILAR Technique

The results discussed in the previous section seem promising for the sensitization of the ZnO nanowires. Nevertheless, an optimization of the interfaces and an improvement of the deposition method must be further explored in order to ensure good solar cell performance. As stated previously, control over the shell properties is an important issue since they strongly affect the electrical and optical properties of the core/shell heterostructures [215].

The present section discusses the improvement of ZnO/CdS interfaces by means of alterations to the classical SILAR procedure. The addition of a sequential annealing step improved the nanowire coverage leading to more conformal CdS layer formation.

1.2.1. Structural and Optical Properties of the ZnO/CdS Core/Shell Heterostructures (Modified SILAR)

Sequential annealing steps were performed on the ZnO/CdS samples after each 5 cycles at 100 °C for 30 seconds. Figure IV.8 shows SEM images of the ZnO/CdS core/shell

structures prepared by classical and modified SILAR procedure. The sequentially annealed CdS layer appears to be denser on the NW surface than that prepared by classical SILAR technique. In other wet chemical deposition methods, the increase of coverage of the ZnO NWs was observed at high temperature. This was attributed to a favored sulfur wetting of the ZnO NW surface due to the reduction of surface tension [113]. The same temperature effect could be expected in our case since the sequential annealing is carried out just after the rinsing process. Therefore the water layer seems beneficial (Figure IV.8b).

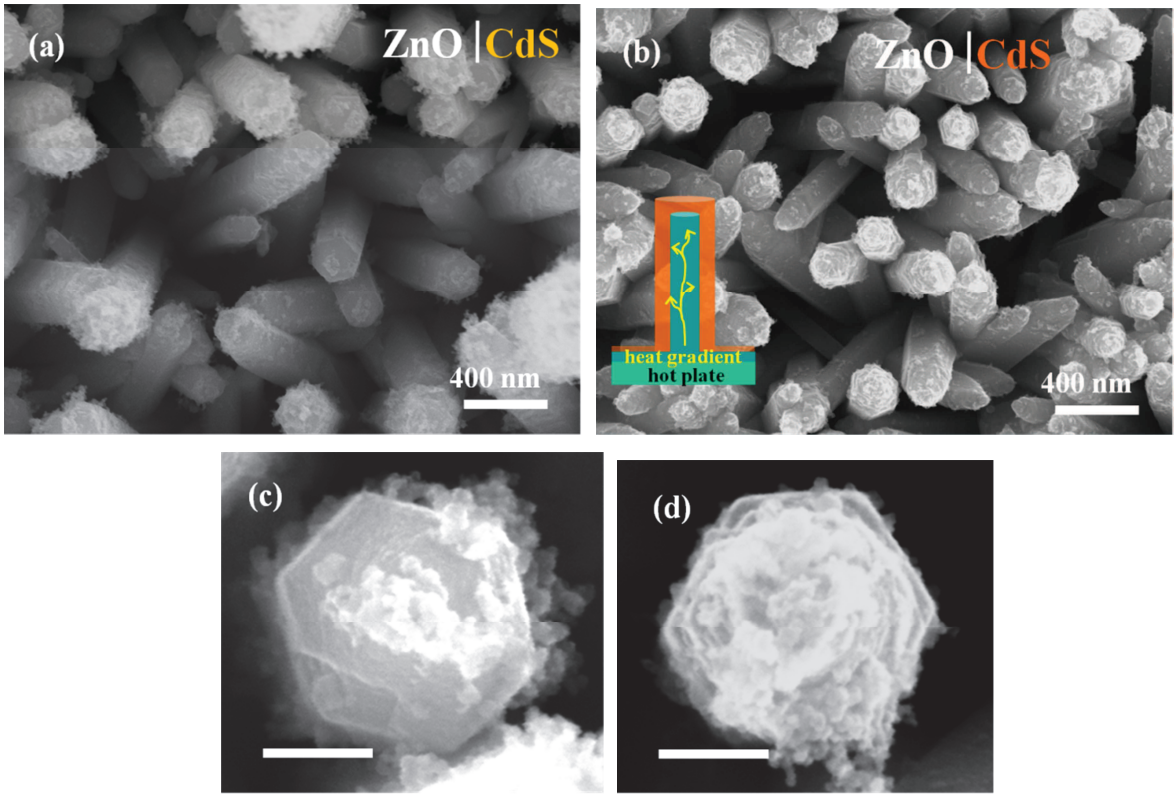

Figure IV.8. SEM images (top view) of CdS-coated ZnO nanowires after 40 SILAR cycles prepared by: (a) classical SILAR procedure. (b) Modified SILAR (inset is a schema of the heating effect. The heat distribution lines are indicated. The annealing step is performed on a hot plate at 100 °C for 30 seconds.in air). High-magnification images of a single ZnO/CdS heterostructures: (c) classical and (d) modified SILAR (Scale bars are 100 nm).

The introduction of an annealing step seems a reasonable approach since it is a simple procedure. The raise of the temperature from the ZnO core to the nanoparticle-formed CdS layer could be also advantageous. The early morphological changes occurring at the ZnO surfaces could improve the ZnO/CdS interface (Figure IV.8b inset).

Figure IV.9 shows SEM images of single ZnO/CdS heterostructures obtained after using classical and modified SILAR method. The dispersed CdS nanoparticles at the ZnO NW tip (Figure IV.9a) disappear when the modified SILAR procedure is used (Figure IV.9b). STEM analysis reveals differences in contrast within the layer deposited by classical SILAR (Figure IV.9c), suggesting that the layer is not dense and has an amorphous appearance. The reduced layer thickness in the case of the annealed nanostructure could be the result of both: the evaporation and/or the crystallization within the CdS shell (Figure IV.9b).

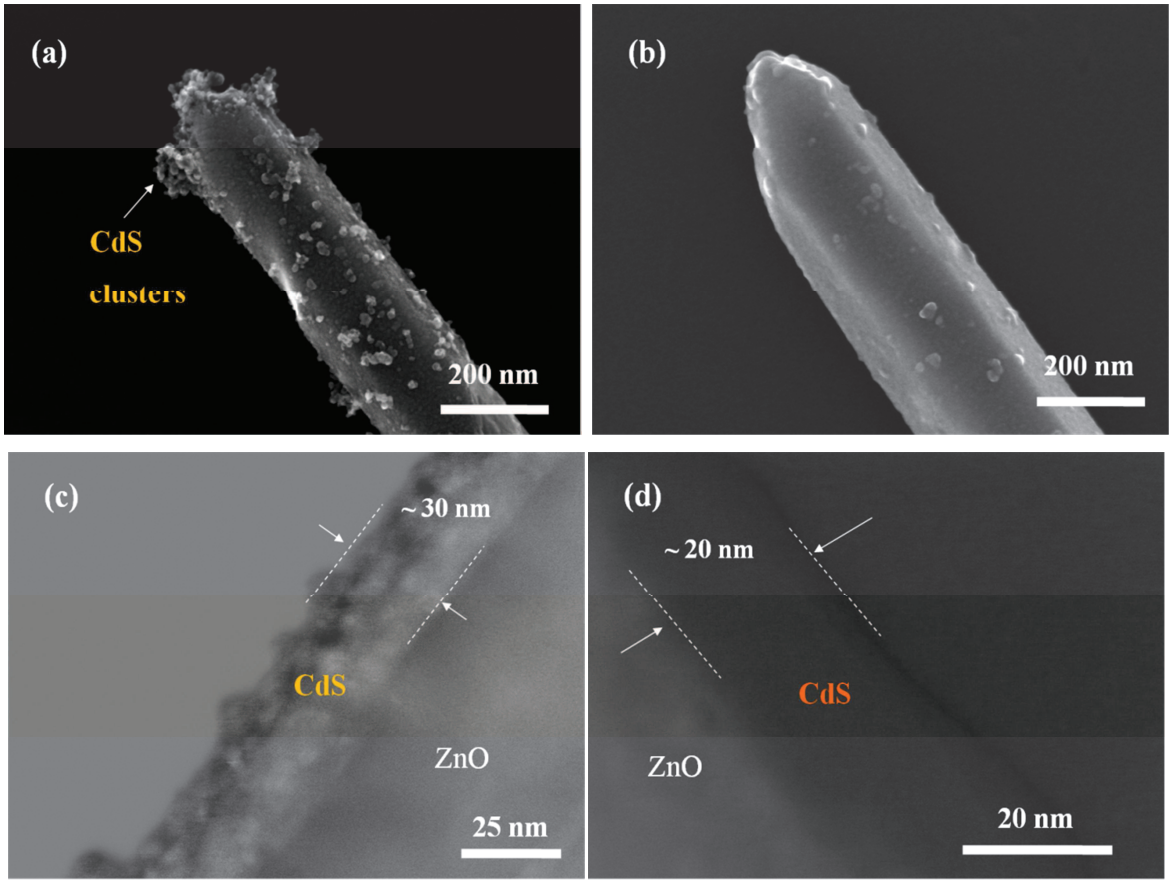

Figure IV.9. SEM images of a single ZnO/CdS core/shell heterostructure obtained after 40 cycles of CdS under (a) standard and (b) sequentially-annealed SILAR. (c) and (d) are Dark field (DF) STEM images of the samples in (a) and (b), respectively.

Optical Properties of the ZnO/CdS Core/Shell Heterostructures Prepared by Modified SILAR

Optical absorbance spectra (Figure IV.10a) show the effect of the sequential annealing treatment on the core/shell nanostructures. For the same number of deposition cycles the

sequentially-treated sample shows a decrease in the absorbance which could be result of partial evaporation of the CdS layer. A temperature of 100 °C and exposition time of 30 seconds seems to be optimal conditions for the layer quality improvement. The modified SILAR method seems a good possibility to further enhance the morphology, coverage and shell thickness.

Figure IV.10b shows the first derivative of the transmittance [183]. This approach has shown to be useful for the estimation of optical transitions when analyzing such extremely thin layers. The peaks corresponding to ZnO (~380 nm) are clearly observed for the bare and the CdS sensitized samples. On the other hand, the peak positions of the as deposited and annealed CdS layers are slightly shifted with respect to the value of bulk CdS (2.4 eV). The sharper peak for the modified CdS layer could be the result of improved material crystallinity despite that its thickness is lower (~ 20 nm).

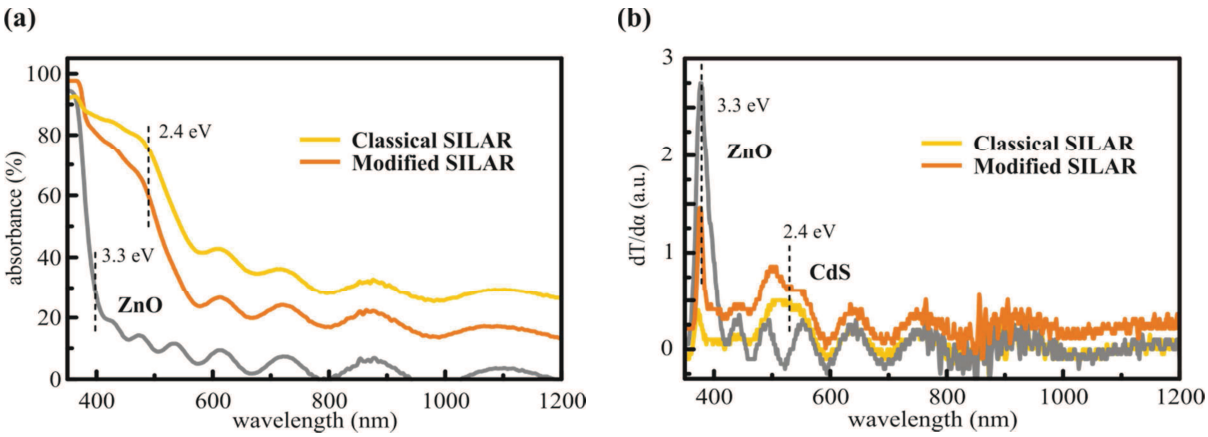

Figure IV.10. (a) UV-visible absorbance spectra of the CdS sensitized ZnO NWs arrays after 40 deposition cycles under standard and sequentially annealed SILAR. The annealing step was carried out on a hot plate at 100 °C for 30 seconds every 5 cycles. (b) First derivative of the transmittance, the bandgaps of bulk ZnO and CdS are indicated.

Briefly, the sensitization of ZnO NWs with extremely thin layers of CdS was demonstrated in this section. The SILAR technique appears to be a very suitable method for the conformal deposition of photosensitizing layers on complex nanostructures, allowing to control their thickness and absorbance with the number of the deposition cycles.

Modified SILAR process resulted in some changes in the properties of the sensitizing layer.

2 PREPARATION OF ZnO/CdSe CORE/SHELL HETEROSTRUCTURES

In this section, the photosensitization of ZnO NWs with CdSe thin film is introduced. The expertise which we gained in the synthesis of CdS by SILAR method here extended for the preparation of CdSe conformal layers.

New approaches for the improvement of layer crystalline quality and interfaces are proposed.

2.1. CdSe Layer Deposition by Classical SILAR Technique

Due to difficulties to prepare CdSe from aqueous solution (related to the instability of aqueous Se solution and using inflammable and toxic compounds), here we propose the sensitization of the ZnO NWs array in ethanol solvent at room temperature by classical SILAR method.

2.1.1. Structural and Optical Properties of the ZnO/CdSe Core/Shell Heterostructures (Classical SILAR)

Figure IV.11 shows SEM images of the ZnO NWs array after depositing 20 SILAR cycles of CdSe (20 seconds for both immersion and rinsing steps). The surface morphology of the ZnO NW walls before (Figure IV.11b) and after (Figure IV.11c) demonstrates the efficient formation of a continuous film of as has been previously observed in the case when CdS was deposited.

The preparation of CdSe from non-aqueous solution could be rather advantageous due to the fact that organic solvents, ethanol used in this work, are more chemically friendly towards ZnO. The amphoteric nature of ZnO is a factor that should be taken into account when using it in acidic or basic solutions [216]. The deposition of sensitizing materials by electrochemical or other wet chemical methods should be carried out at controlled pH (~7±2). In this regard, SILAR technique seems a more suitable deposition method due to the short immersion times. Even if acidic or basic solutions are used, the dissolution of the ZnO NWs could be prevented by careful control of immersion times.

Other effects regarding higher rate of drying and low polarity of the solvent might enhance the diffusion of reactants and better coverage could be achieved [117]. Figure IV.12 shows magnified SEM images of the ZnO NW surface after the deposition of CdS and CdSe layers. High roughness is clearly observed for the case of the CdS layer prepared from an aqueous solution (Figure IV.12a) and the more conformal CdSe layer obtained from ethanolic solution (Figure IV.12b). Since the films were prepared under same conditions, the high evaporation rate of the ethanol could be the reason for the absence of the nanoparticle agglomeration. The solvent polarity among other factors such as different chemical reactivity of S^{2-} and Se^{2-} ions might be also accounted for the observed morphology differences [217].

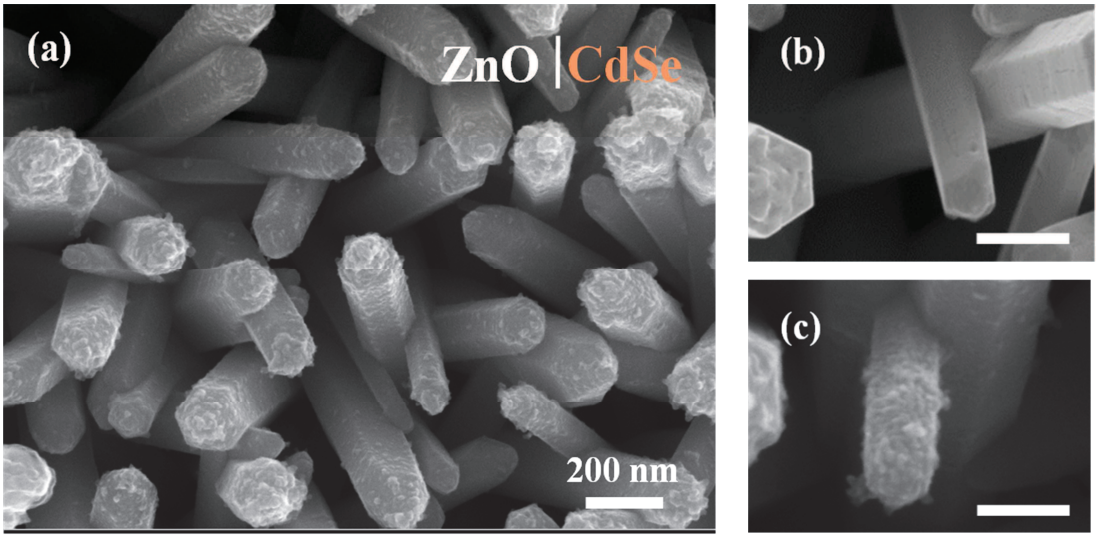

Figure IV.11. (a) SEM images (top view) of the ZnO/CdSe NW array. (b) Magnified SEM image of the as-prepared ZnO NWs, and (c) ZnO nanowire after CdSe deposition by standard SILAR procedure (20 cycles). Scale bars are 100 nm.

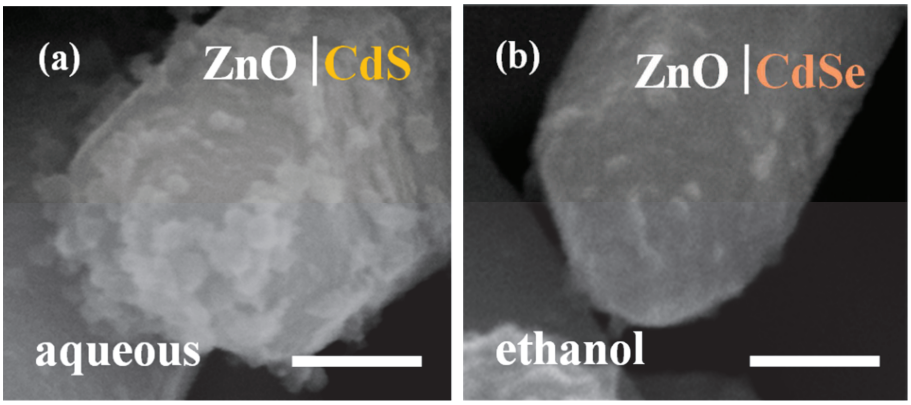

Figure IV.12. Magnified SEM images of (a) ZnO/CdS and (b) ZnO/CdSe single heterostructures obtained by SILAR in aqueous and ethanol solutions, respectively. The deposition conditions were the same: immersion time (20 seconds), 20 cycles, at room temperature. Scale bars are 100 nm.

Crystalline quality, surface coverage and optical properties of the as-deposited CdSe layer were studied. Figure IV.13 shows the XRD patters and UV-Vis absorbance of the ZnO/CdSe heterostructures. Regarding the CdSe layer crystallinity, the broad peak in the region corresponding to CdSe diffraction fingerprints indicates the formation of the desired material (Figure IV.13a). However, the wide bump around 25.5° reflects the poor crystalline quality or a layer composed of small nanoparticles. This broad peak might belong to Zinc Blende phase, since it is the phase usually obtained by other wet deposition methods such as CBD or electrodeposition [132, 218–220]. The wurtzite CdSe should not be ruled out since characteristic diffraction peaks occur also close to 25.5°.

Figure IV.13b shows the absorption spectra of the ZnO NWs array sensitized with CdSe. It can be clearly seen that the optical offset of the heterostructures is shifted to higher wavelengths (~700 nm) than in the case of ZnO/CdS prepared with same number of deposition cycles (20). The absorption edge is close to that of bulk CdSe (1.7 eV). However, the absorption transition is not very well defined.

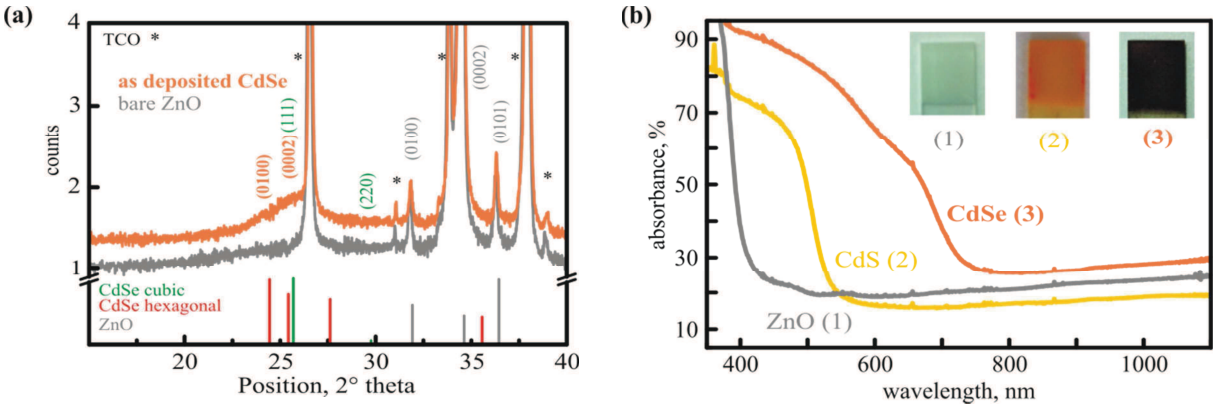

Figure IV.13. (a) XRD diffraction patterns of bare ZnO NWs and the ZnO/CdSe heterostructures with 20 SILAR cycles (reference patterns of wutrzite ZnO and CdSe are depicted). Stars (*) indicate diffraction peaks from the TCO (SnO_2:F) substrate. (b) Absorbance spectra of the core/shell ZnO/CdSe nanostructures (20 SILAR cycles). The color differences between sensitizing materials can be seen by naked eye from the pictures in the insets: (1) bare ZnO NWs, (2) ZnO/CdS and (3) ZnO/CdSe.

2.2. CdSe Layer Deposition by Modified SILAR Technique

Despite the encouraging results obtained when CdSe is prepared by the classical SILAR technique, the poor crystallinity and the absorption features indicate that the material quality should be improved.

What follows introduces the implementation of an annealing step and chemical treatment to the classical SILAR technique with the aim to improve the CdSe quality.

The ZnO/CdSe NW arrays were annealed at 100, 200 and 400 °C. For the chemical treatment, the heterostructure arrays were immersed for 30 seconds in saturated methanolic solution of $CdCl_2$ at 60 °C and annealed at 100, 200 and 400 °C. The experimental details can be found in the CHAPTER II.

2.2.1. Structural and Optical Properties of the ZnO/CdSe Core/Shell Heterostructures (Modified SILAR)

Figure IV.14 shows the changes in the morphology of the CdSe shell after annealing and $CdCl_2$ treatment. The CdSe layer exhibits no apparent change after the annealing step (Figure IV.14a and b). However, by comparing films annealed at the same temperature but one is chemically treated a morphology difference can be observed. The grains forming the chemically treated layer can be clearly distinguished rather than the amorphous-appearance of the as-deposited film (Figure IV.14c). This is clear evidence that the $CdCl_2$ activation process influences the CdSe crystalline quality. This procedure is usually used in the fabrication process of CdTe thin film solar cells; here we adapted it for CdSe.

Longer periods of $CdCl_2$ chemical treatment (> 30 seconds) resulted in the dissolution of the CdSe layer in the activating solution. The longer annealing times (> 5 minutes) and elevated temperatures (> 200 °C) provoke an agglomeration of particles transforming the continuous layer into spaced clusters thus leaving part of the NW surface uncovered. Figure IV.14d shows a single ZnO/CdSe heterostructure after $CdCl_2$ treatment and annealing at 400 °C for 3 minutes. It can be seen that the agglomeration of CdSe big particles onto the ZnO NW and the hexagonal facets of the NW can be distinguished (Figure IV.14d inset). From the SEM images, the grain size was estimated from few tens of nanometers up to 100 nm. The uncovered NW surface could affect the V_{oc} due to shunts [221, 222].

Regarding the $CdCl_2$ treatment, the diffusion of Cl through the CdTe layer has been shown to be an important factor for the enhancement of recrystallization of the treated thin films [223–225]. This effect, expected to be faster in grain boundaries than in bulk material, would continue with annealing time. Therefore, the coalescence of the neighboring grains and partial stripping of CdSe from the ZnO nanowires could be explained by the high density of grain boundaries in the as-deposited CdSe layer. These dramatic changes could be attributed to a decrease of the melting point with respect to the bulk material due to extremely low layers thickness and the surface free energy contribution [226–228]. Same effects have been previously reported for the case of CdS nanocrystals [226].

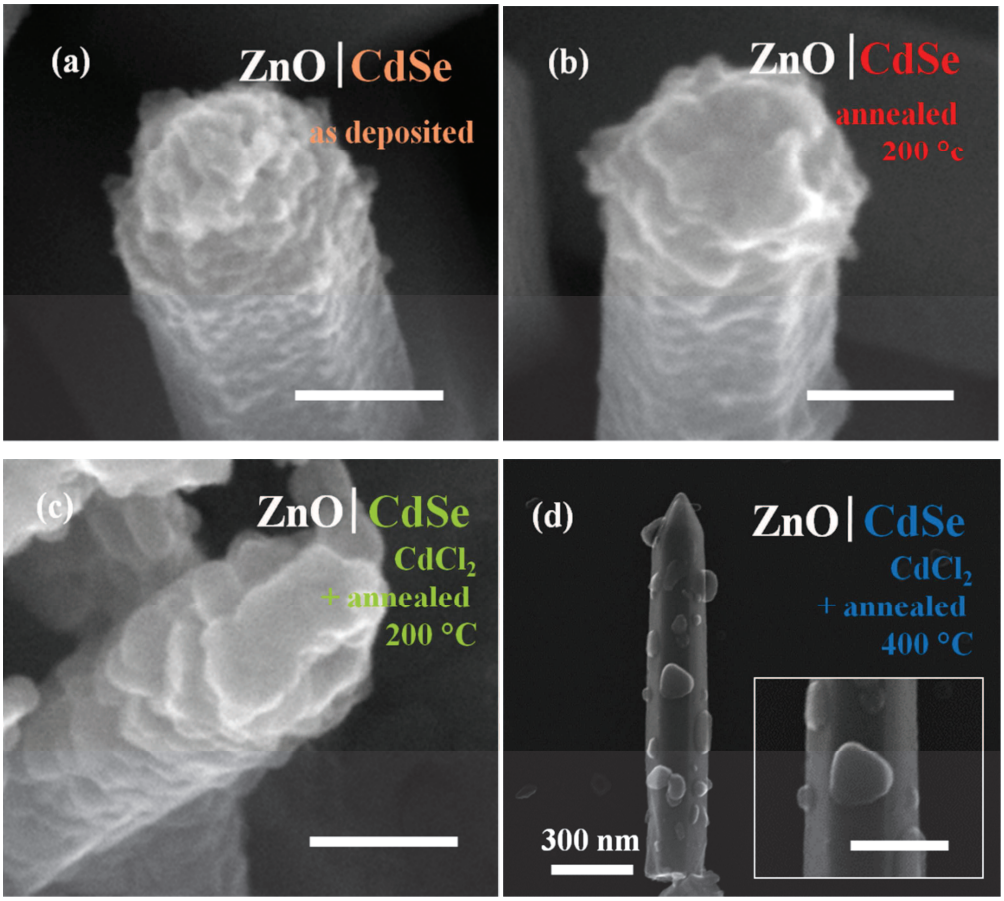

Figure IV.14. SEM images of single ZnO/CdSe nanostructure obtained after 20 SILAR deposition cycles: (a) as-deposited; (b) annealed at 200 °C; (c) $CdCl_2$ treated plus annealed at 200 °C and (d) $CdCl_2$ treated plus annealed at 400 °C. The annealing step was for 3 minutes and $CdCl_2$ treatment for 30 seconds at 60 °C. Scale bars in (a), (b) and (c) are 100 nm. Scale bar in the inset is 200 nm.

The EDX elemental mapping of the annealed ZnO/CdSe NW at 400 °C is shown in Figure IV.15. The images reveal the presence of *Zn* and *O* elements in the core part, and *Cd* and *Se* in the shell of the heterostructure. However, the shell layer does not cover

homogeneously the nanowire surface. The intensity signals belonging to *Cd* and *Se* elements are higher in the grains. The composition ratio of [*Se*]/[*Cd*] in the grains was hard to determine. Nevertheless, scans reveal a slightly higher content of *Cd*, which is result of the treatment with the highly concentrated $CdCl_2$ activating solution. *Cl* was barely detected.

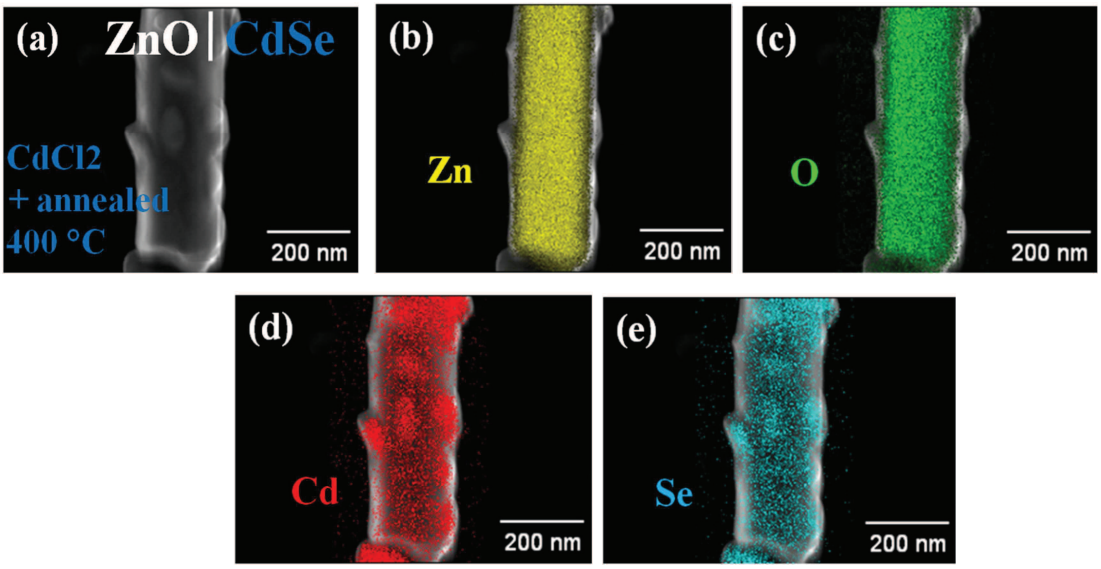

Figure IV.15. EDX elemental mapping of the ZnO/CdSe nanostructure chemically treated and annealed at 400°C for 3 minutes: (a) SEM image, (b) *Zn*, (c) *O*, (d) *Cd* and (e) *Se* elements.

XRD analysis confirms the evolution of the layer crystallinity after the annealing step and the chemical treatment (Figure IV.16). The characteristic (0100), (0002) and (0110) peaks of CdSe appear from the ZnO/CdSe heterostructures when treated at temperatures ≥ 200 °C. For the case of the only-annealed sample the two peaks of the hexagonal phase of CdSe are barely noticeable (Figure IV.17), nevertheless, they are more defined that the broad peak observed from the as-deposited sample (Figure IV.17). This demonstrates that the $CdCl_2$ treatment effectively promotes recrystallization of the CdSe layer. No variations of the peaks position from ZnO are observed after the chemical treatment, which confirms that the ZnO core is unaffected. The structural transition from zinc blende (possibly present in the as deposited sample) to the wurtzite phase (for the chemically treated and annealed layers) is in accordance with other reports where CdSe thin film was deposited by other method and annealed at 95 ± 5°C [229].

Calculated grain size and strain are summarized in Table IV.1. The values obtained for the CdSe layer treated and annealed at 400 °C (~114 nm) match with the determined particle size from SEM images (Figure IV.14d inset). The negative value of the strain for the layer

treated and annealed at 200 °C is an indication of the compressive stress in the grains forming the layer.

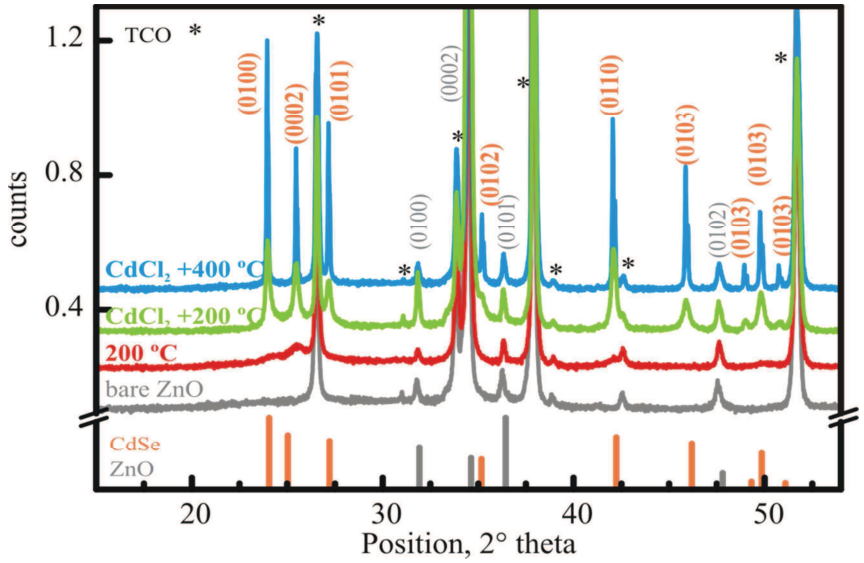

Figure IV.16. XRD diffraction patterns of bare ZnO NW array and ZnO/CdSe core/shell heterostructures prepared after 20 SILAR cycles. The curves correspond to the indicated chemical treatment and annealing temperatures. The annealing step was carried out after deposition for 3 minutes. Stars (*) indicate diffraction peaks from the TCO (SnO_2:F) substrate. The reference patterns of wurtzite ZnO and CdSe are indicated.

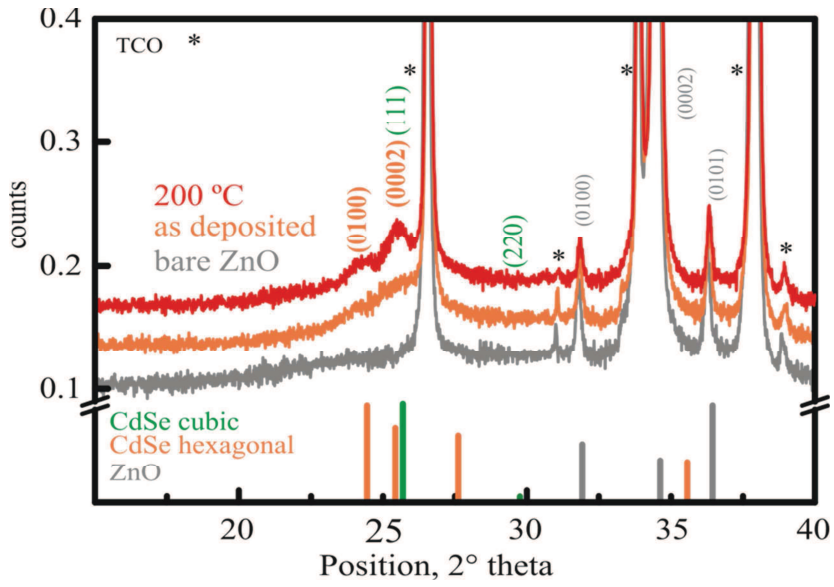

Figure IV.17. XRD diffraction patterns of bare ZnO NW array, ZnO/CdSe heterostructures after 20 SILAR cycles. The curves correspond to the as-deposited and annealed at 200 °C for 3 min samples. Stars (*) indicate diffraction peaks from the TCO (SnO_2:F) substrate. The reference patterns of wurtzite ZnO and CdSe are indicated.

Table IV.1. Calculated grain size and strain values of the CdSe shells prepared at different conditions.

Post deposition treatments	Grain size	Strain (ε)
Annealing at 200 ° (3 min)	11 nm	122.05 x10^{-5}
$CdCl_2$ + annealing 200 °C (3 min)	33 nm	-1.29 x10^{-5}
$CdCl_2$ + annealing 400 °C (3 min)	114 nm	1.45 x10^{-5}

The absorbance features of the ZnO/CdSe heterostructure arrays are shown in Figure IV.18. The photosensitization of ZnO NWs with CdSe extremely thin film leads to an extension of the absorption to the visible region of the solar spectrum. The as-deposited and annealed samples show a gradual absorption onset close to values characteristic of CdSe (1.7 eV). From the other hand, sharper optical transitions are observed when the photosensitizing layer was chemically treated. The reduced absorbance of the heterostructures annealed at 400 °C is due to the transformation of the CdSe layer into particle agglomeration and partial stripping from the ZnO NWs as discussed above. From these results, a modified SILAR procedure has been proposed to improve material quality and avoid the shell degradation: i) chemical treatment at 60 °C for 30 seconds and ii) annealing temperature (between 150 - 200 °C) for 3 minutes. From the absorbance spectra the calculated bandgaps using the Tauc relation match very well with bulk CdSe (1.7 eV, ~730 nm) material [214].

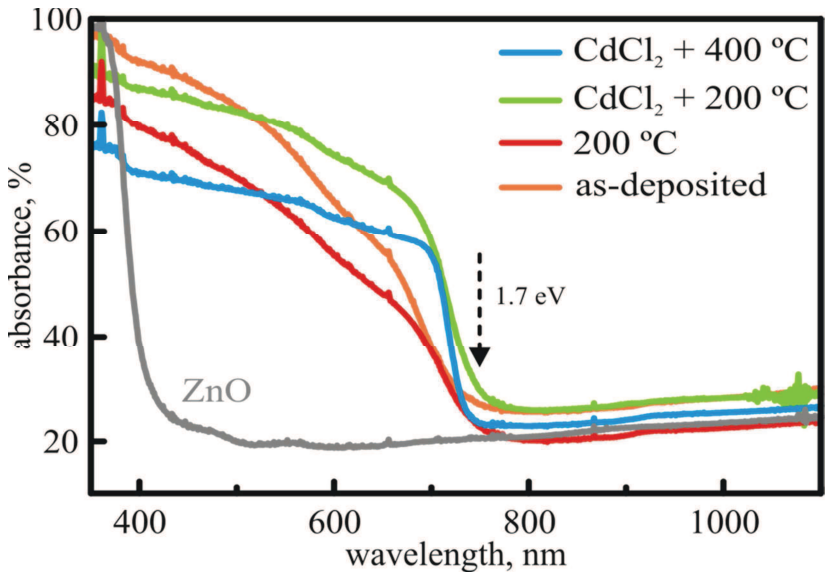

Figure IV.18. UV-visible absorbance spectra of the ZnO/CdSe core/shell heterostructures. Annealing time was 3 minutes. The bang gap of bulk CdSe is indicated.

In this section, the improvements of the physico-chemical properties of CdSe photosensitizing shells prepared by classical and modified SILAR technique was studied. The

usually used $CdCl_2$ chemical treatment in CdTe thin film solar cells was successfully applied to these extremely thin CdSe layers.

3 PREPARATION OF ZnO/CdTe CORE/SHELL HETEROSTRUCTURES

In the last part of this chapter, the photosensitization of ZnO NWs with CdTe is studied. CdTe thin layers are prepared by SILAR, CSS and QDs functionalization techniques. Advantages and drawbacks from each deposition method are highlighted.

3.1. CdTe Layer Deposition by Classical and Modified SILAR Technique

The attractive results which we obtained on the ZnO/CdSe heterostructures prepared by modified-SILAR method motivated us to prepare CdTe thin by the same technique. The CdTe layer was submitted to the same chemical treatment and annealing step as CdSe film.

The procedures for the preparation of the ionic solutions are similar to that for the deposition of CdSe. The shell thickness was also controlled by the number of SILAR cycles and the experimental details can be found in CHAPTER II.

3.1.1. Structural and Optical Properties of the ZnO/CdTe Core/Shell Heterostructures (SILAR)

In Figure IV.19 are shown the SEM images of the bare ZnO NWs and CdTe-covered after 20 SILAR cycles deposition for comparison. The smooth bare surface of the NWs (Figure IV.19a) became rough after the depositions of the sensitizing shell (Figure IV.19b). The changes in the layer morphology follow similar evolution as observed with CdSe. The chemically treated and annealed CdTe layer at 200 °C is composed of larger in size grains (Figure IV.19c and d), while the layer annealed at 400 °C is denser and even bigger grains are formed leaving some parts of the NWs uncovered (Figure IV.19e).

The full coverage and thickness of the as-deposited CdTe layer was confirmed by STEM analysis. The dark-field STEM image of a single ZnO/CdTe heterostructure shows the conformal layer formed on the entire NW surface (Figure IV.20) and the estimated thickness is about 12-15 nm. Additionally the STEM analysis helped us to confirm the efficient coverage of CdTe film till the bottom of the NWs (Figure IV.20c).

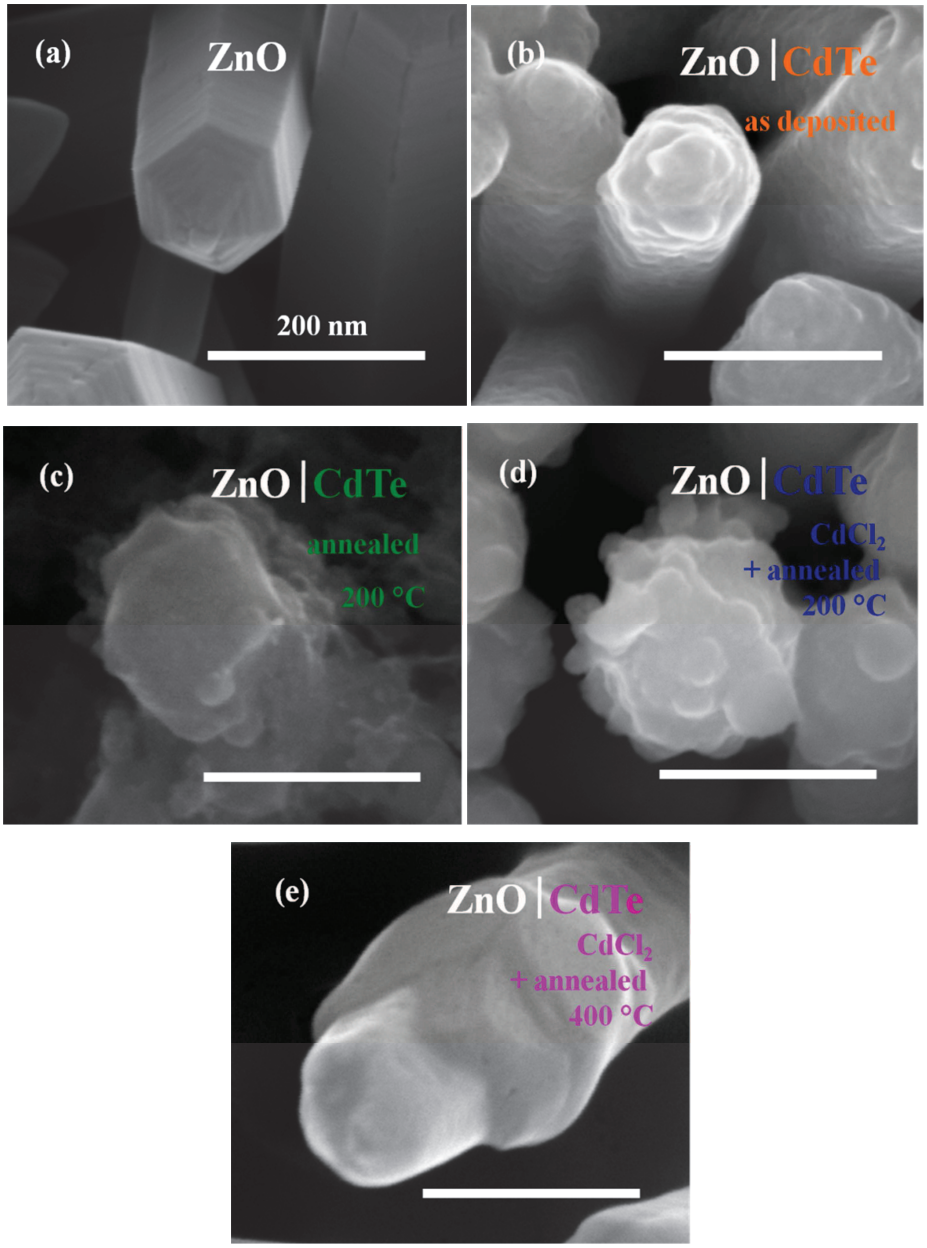

Figure IV.19. Magnified SEM images (top view) of (a) bare and (b) CdTe-covered ZnO NWs after 20 SILAR deposition cycles. Effect of chemical treatment and annealing step: (c) annealed sample at 200 °C, (d) *$CdCl_2$* treated plus annealed at 200 °C and (e) *$CdCl_2$* treated plus annealed at 400 °. The annealing was carried out for 3 minutes and the *$CdCl_2$* treatment for 30 seconds at 60 °C. Scale bars are 200 nm.

The structural and optical properties of the ZnO/CdTe core/shell NW arrays are presented in Figure IV.21 and 23. The obtained results once again (as with CdSe) confirm that the chemical activation with *$CdCl_2$* and annealing step are very efficient for the enhancement of the layer quality in such thickness (nm) (small FWHM of the diffraction peaks Figure IV.21). The observed changes could also be explained by the fact that *Cl^-* diffuses and smooths the surface at the grain boundaries. The crystallization is therefore promoted at high temperature and in the presence of *Cd* (furnished additionally by the chemical-activation

solution) [223–225]. In a nutshell, the chemical treatment promotes the coalescing of the grains, passivates grain boundaries, and thus improves the shell morphology. Such a layer would be with low probability for charge recombinations at the interfaces and would increase the carrier lifetime

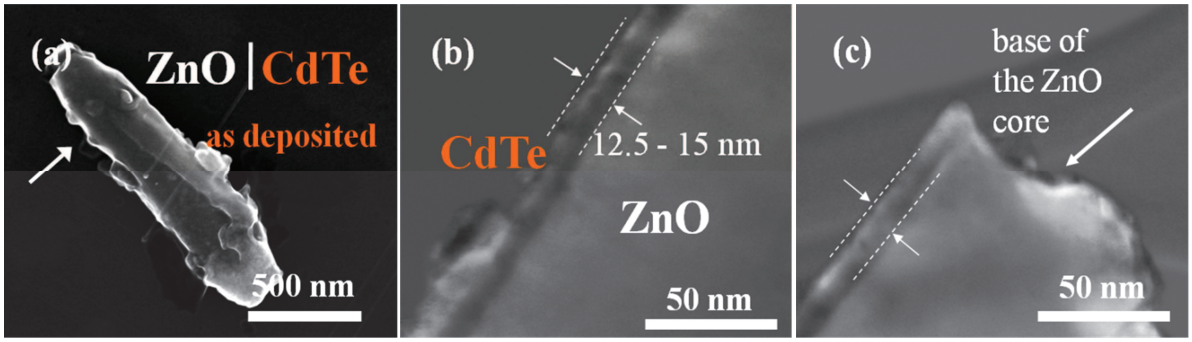

Figure IV.20. (a) SEM image of a single ZnO/CdTe core/shell heterostructure (as deposited) obtained after 20 SILAR cycles (the arrow points the tip to the nanostructure). (b) and (c) are dark field (DF) STEM images of the core/shell structure. The arrow in (c) indicates the bottom of the nanostructure (detached from the array during sample preparation).

The XRD spectra demonstrate the improvement in crystalline quality after the chemical activation treatment ($CdCl_2$) compared to the only annealed sample. The observed peaks match well the cubic zinc blende structure and no phase transitions are detected with the post deposition treatment. The different reactivity of Te^{2-} and Se^{2-} ions could explain the smaller calculated grain sizes for CdTe layer despite the use of ionic solutions with the same concentrations. Table IV.2 summarizes the evolution of the grain size and strain of the CdTe layers after the chemical treatment and annealing.

The optical absorbance spectra of the bare ZnO NWs and the core/shell ZnO/CdTe NW array are shown in Figure IV.22. The extension of the absorption to longer wavelengths is observed. The not well defined optical transition of the as-deposited CdTe layer could be result of its amorphous properties. The sharper optical transitions for annealed and $CdCl_2$ treated heterostructures prove the enhancement of the layer crystalline quality. Despite the good structural properties of the annealed sample at 400 °C, a small reduction of the absorbance compared to the sample annealed at 200 °C is noticed. The bandgaps of the as prepared layers are estimated from Tauc plots and they are very close to the value of bulk CdTe (1.5 eV, ~826 nm).

In this section, the photosensitizing of ZnO NWs by SILAR prepared CdTe was shortly introduced. It was clearly demonstrated that by this technique extremely thin layers with very good crystalline and optical quality could be prepared.

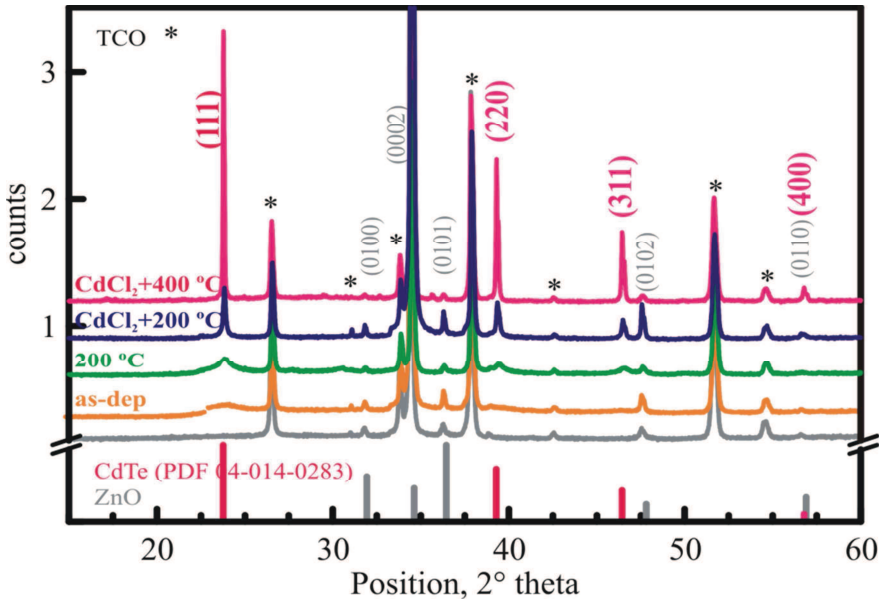

Figure IV.21. XRD diffraction patterns of bare ZnO NW array and ZnO/CdTe heterostructure array prepared with 20 SILAR cycles. The curves correspond to the indicated chemical treatment and annealing temperatures. The annealing step was carried out after deposition for 3 minutes. Stars (*) indicate diffraction peaks from the TCO (SnO_2:F) substrate. The reference patterns of wurtzite ZnO and CdTe are indicated.

Table IV.2. Calculated grain size and strain values of the CdTe shells prepared at different conditions.

Post deposition treatments	Grain size	Strain (ε)
As-deposited	4 nm*	
Annealing at 200 ° (3 min)	8 nm	$-262.05\ 10^{-5}$
$CdCl_2$ + annealing 200 °C (3 min)	53 nm	$3.59\ 10^{-5}$
$CdCl_2$ + annealing 400 °C (3 min)	83 nm	$25.11\ 10^{-5}$

* Result from Scherrer formula using the (111) peak at 23.7 (2theta °).

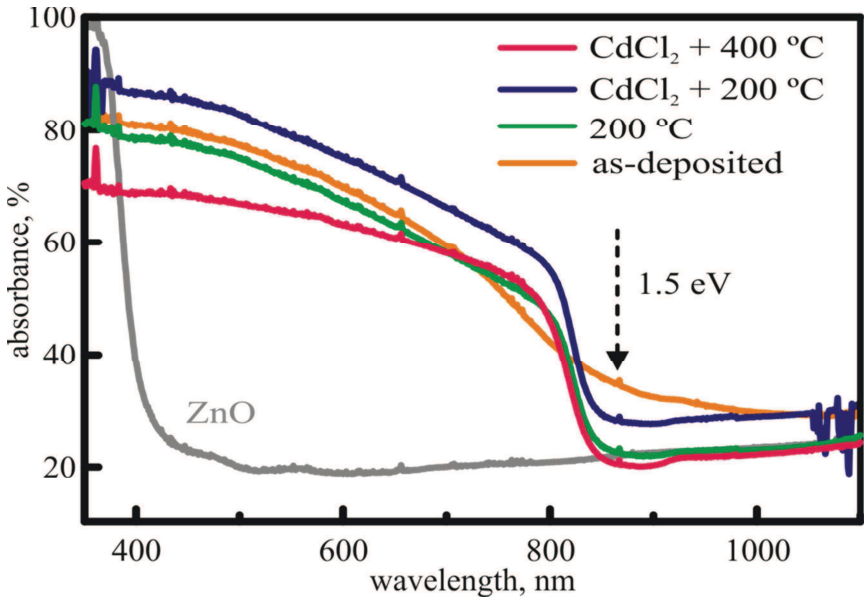

Figure IV.22. UV-visible absorbance spectra of the ZnO/CdTe core/shell heterostructures. Annealing time was 3 minutes. Bang gap of bulk CdTe is indicated.

3.2. CdTe Layer Deposition by Close Spaced Sublimation (CSS)

The second method which we explored for CdTe deposition is CSS. This technique is more suitable for thin film preparation on flat substrates and the goal of this study was to adapt it to nanostructured substrates based on electrodeposited ZnO NWs. the thickness of the CdTe layer was controlled by the deposition time.

3.2.1. Structural and Optical Properties of the ZnO/CdTe Core/Shell Heterostructures (CSS)

Planar and nanostructured ZnO/CdTe heterostructures were prepared by CSS. The preliminary experiments of CdTe deposition on planar substrates were performed with the aim to study the tolerance of the glass substrate and the electrodeposited ZnO at such elevated temperatures (580 °C). A ZnO 2D layer with a thickness of 150 nm (electrochemically deposited at 50 °C) and bare TCO (SnO_2:F) were used as substrates. Figure IV.23 shows SEM images of the CdTe thin film deposited on these substrates. It can be seen that the layer deposited on ZnO is more uniform than that on TCO. Although no epitaxial relation between the ZnO and CdTe is expected, due to the large growth rate of CdTe grains by CSS (~ 20 nm/min), the effect of ZnO layer on the CdTe film morphology is observed [230]. For the deposition time of 3.5 minutes, the thickness for the film is ~100 ± 10 nm.

CdTe growth by CSS has been previously investigated and the Volmer-Weber growth mechanism has been proposed [231, 232]. When CdTe is deposited on substrates with well-defined crystallographic orientation, the layer growth starts with a three dimensional nucleus formation which subsequently coalesce as deposition progresses. Therefore the CdTe deposition is considered to be governed by thermodynamic principles driven by the surface energy minimization.

In the present case, the ZnO layer is formed by small grains of about 40 nm in diameter (Figure IV.23b inset). The small surface on the ZnO grains is a prerequisite for the initial formation of small CdTe islands which explains the apparent smoother morphology of the CdTe film. This is not valid for the case of TCO substrate, which is formed of larger pyramidal grains (Figure IV.23a inset).

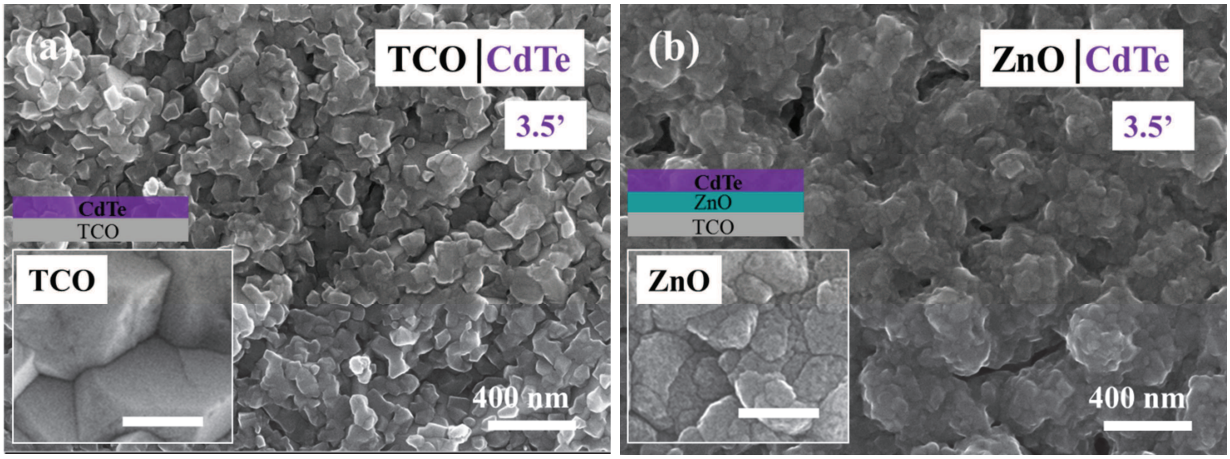

Figure IV.23. SEM images (top view) of the ZnO/CdTe planar heterostructures prepared with 3.5 minutes deposition time on: (a) TCO (SnO_2:F) and (b) ZnO 2D layer. Insets are the SEM images of the bare TCO and ZnO 2D layer (the scale bars are 200 nm).

For the case of the ZnO/CdTe core/shell nanostructures, the deposition time showed to be an important parameter to control the coverage and the thickness of the sensitizing layer. In Figure IV.24 are shown the ZnO/CdTe core/shell heterostructures after 3.5 and 7 minutes of CdTe deposition. It can be seen that for shorter deposition time, the ZnO NWs are not completely covered, whereas with longer deposition time the complete coverage was achieved. The further increase of the deposition time resulted in the filling of the space between NWs.

It is possible to see the pyramidal shape of separated CdTe nanoparticles formed on the NWs walls (Figure IV.24d) for 3.5 minutes deposition time. This observation confirms the Volmer-Weber growth mode of CdTe by CSS (Figure IV.24d inset), which is governed by a negative balance of the surface energy ($\Delta\gamma$) during overall deposition process according to Equation IV.1 (as discussed previously):

$$\Delta\gamma = \sigma_{ZnO} - (\sigma_{CdTe} + \gamma_{ZnO,CdTe}) \qquad \textbf{Equation IV.1}$$

Where σ_{ZnO} and σ_{CdTe} are the surface energies of ZnO and CdTe, respectively, and $\gamma_{ZnO,CdTe}$ is the solid–solid interfacial energy (related to the strain between the two lattices - mismatch).

Therefore, the island-like grain formation could be explained by the contributions of the surface energy of the foreign material, CdTe for this case (Table IV.3), and the significant lattice mismatch between CdTe and ZnO (high value of $\gamma_{ZnO,CdTe}$) [233]. Also, the surface

energy of CdTe {111} planes could explain the preferential growth along the <111> direction (Figure IV.24d inset) [231, 232].

Table IV.3. Calculated surface energies of CdTe surfaces [234].

Surface orientation	Surface energy (γ), J/m^2
(100)	0.85
(110)	0.18
(111)	0.58

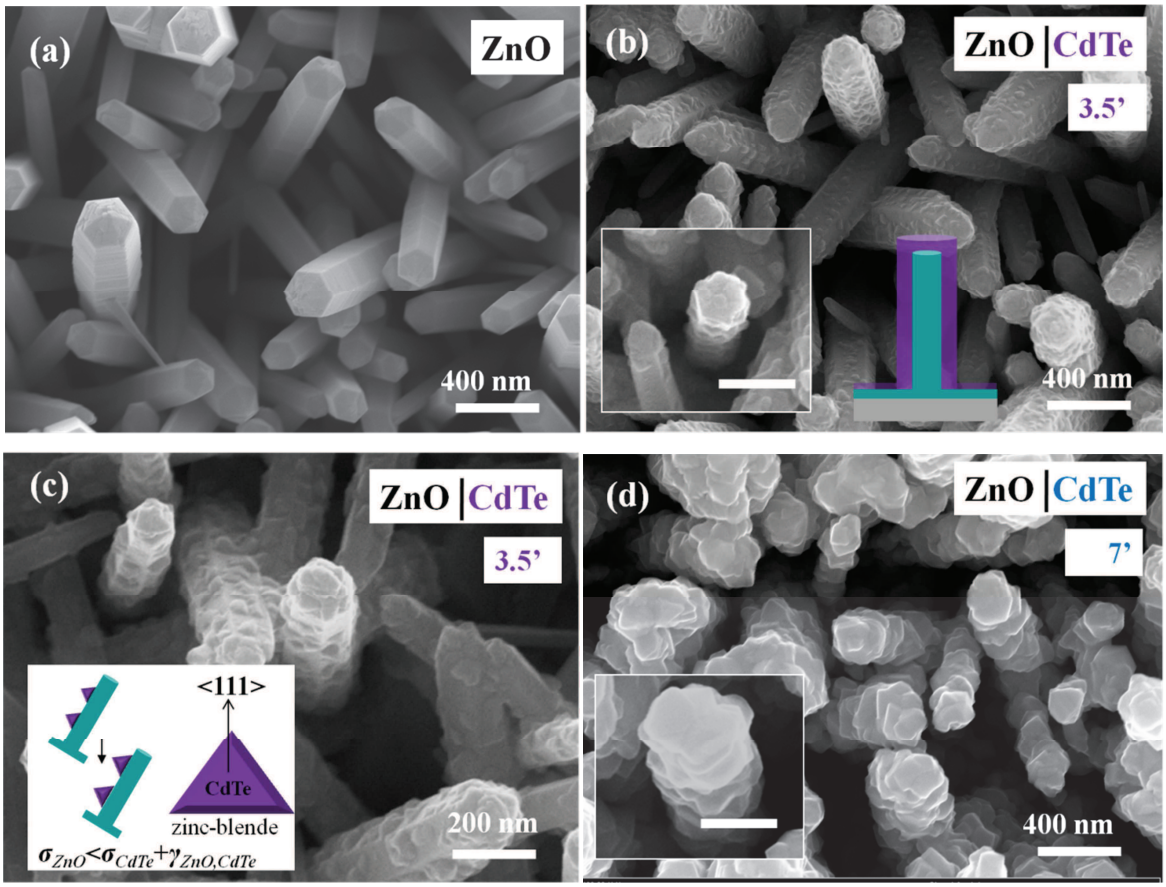

Figure IV.24. SEM images (top view) of the ZnO/CdTe core/shell arrays. (a) bare ZnO NWs, (b and c) ZnO/CdTe NWs after 3.5 minutes deposition by CSS, and (d) ZnO/CdTe NWs after 7 minutes deposition by CSS. Insets in (b) and (d) are magnified images of a single ZnO/CdTe NW (scale bars are 200 nm). Inset in (c) is the scheme of the Volmer-Weber growth mode and the preferred growth of the pyramidal CdTe grains.

XRD patterns of the ZnO/CdTe heterostructures confirm this hypothesis (Figure IV.25). The relative intensities and position of the diffraction peaks correspond to the zinc blende structure. However, an additional peak at 22.55 ° corresponding to the CdTe

hexagonal phase also appears. Similar results were previously reported and the same peak was assigned to the substrate [230]. In our case, comparing the XRD patterns of bare ZnO NW array and that of the ZnO/CdTe heterostructures (prepared by SILAR technique) allows us to assign the observed peak to the wurtzite phase of CdTe. This finding could indicate that the growth mechanism of the CdTe shell changes after the initial thin layer formation. After the first layers deposition, the consequent layers will grow on the CdTe substrate changing the surface energy ($\Delta\gamma$) and the interfacial energy would be reduced due to a lower lattice mismatch.

.

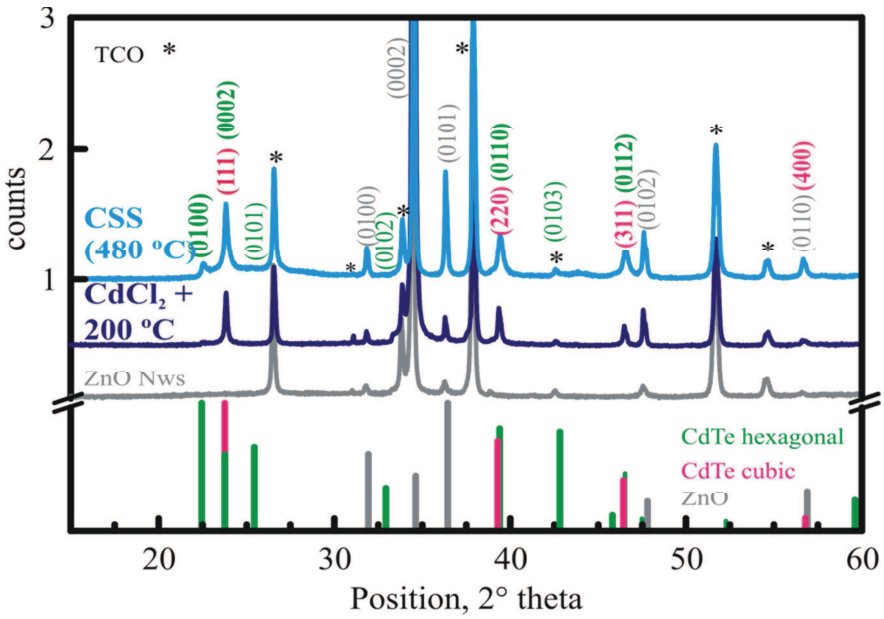

Figure IV.25. XRD patterns of bare ZnO NW and ZnO/CdTe core/shell heterostructures after 7 minutes of deposition by CSS. XRD pattern obtained from ZnO/CdTe heterostructures prepared by SILAR (treated at 200 °C) is also included for comparison. Stars (*) indicate diffraction peaks from the TCO (SnO_2:F) substrate. Reference peaks of bulk wurtzite ZnO (PDF4+ 04-013-7122), CdTe (PDF4+ 01-073-2870) and zinc blende CdTe (PDF4+ 04-014-0283) are displayed.

The thickness of the sensitizing shell was determined by STEM analysis. Figure IV.26 shows a single ZnO/CdTe NW. It is seen that the coverage and the thickness of the shell are not uniform and part of the bottom of the NW remains uncovered. The layer is formed by nanograins (calculated size about ~16 nm) and the thickness varies between 30-100 nm being thicker at tip of the NW. This accumulation of CdTe grains on the top of the NWs could provoke a shadowing effect which is reasonable for CSS deposition since it is a vapor-phase method. Figure IV.27 shows cross-sectional SEM images of the ZnO/CdTe NWs array where it is well seen that the diffusion of CdTe till the bottom of the NWs was impeded.

Figure IV.28 shows the absorbance spectra from nanostructured and planar ZnO/CdTe heterostructures. It is seen that when the CdTe film is prepared with the same deposition time, the planar heterostructure barely absorbs the incoming light (20 %). To overcome the poor absorbance, a thicker layer is required which is actually the case in thin film solar cells (at least 2 μm) [100, 235]. The nanostructured surface leads to higher absorbance which is more noticeable in the case of the sample after 7 minutes deposition time. For a NW density of 10^9 cm^{-2} (150-200 nm diameter and 1-1.5 μm height), the surface area of the NW array is estimated to be 10 times higher than the flat ZnO layer [32, 236]. The increased light absorbance of the CdTe coated ZnO NWs might stem from the light scattering by the nanostructures and/or the increase grain size at the tips of the NWs.

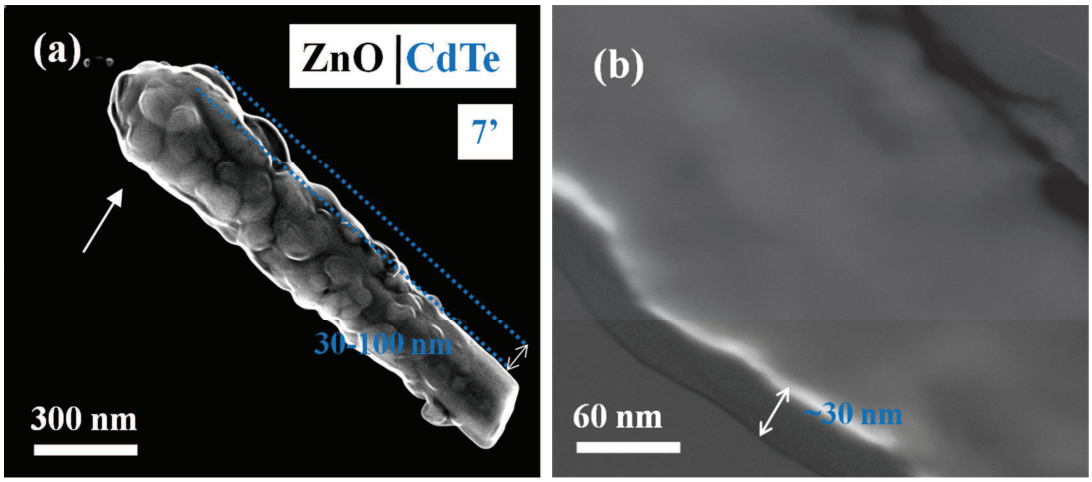

Figure IV.26. (a) SEM image of a single ZnO/CdTe core/shell heterostructure after 7 minutes CSS deposition (the arrow points the tip to the nanostructure). (b) Dark field (DF) STEM images of the same sample.

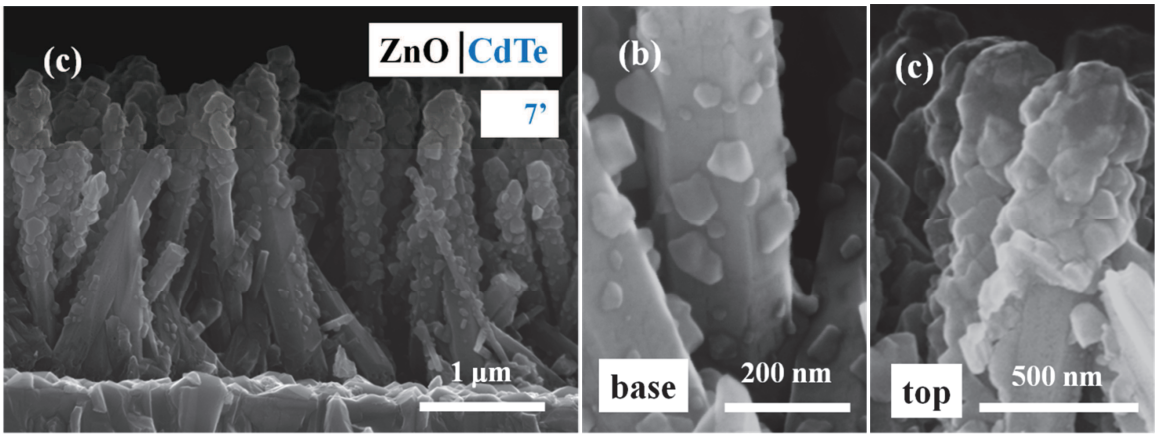

Figure IV.27. (a) Cross-sectional view of ZnO/CdTe core/shell heterostructure array obtained after 7 minutes CSS deposition (b) Magnified SEM images at the bottom and (c) top of the nanostructures.

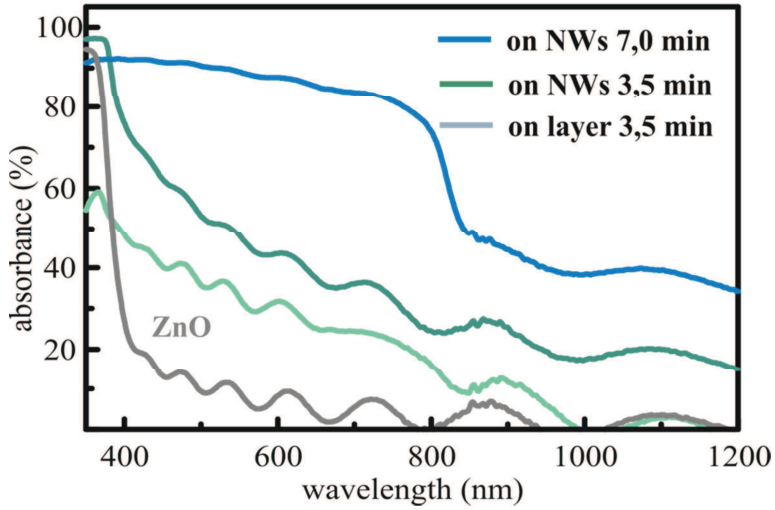

Figure IV.28. UV-Visible absorbance spectra of the ZnO/CdTe heterostructures deposited by CSS at indicated deposition times.

In brief, CSS technique was used to deposit thin layers of CdTe on ZnO NWs. The deposition time was the main parameter used to control the thickness of the layer. The structural and optical data confirm the presence of a CdTe sensitizing shell. However, uneven nanowire coverage was observed due to shadowing effects.

3.3. CdTe Layer Deposition by CdTe QDs Sensitization

In the last part of this section, CdTe thin films were prepared from pre-synthesized CdTe QDs. QDs synthesized by solvothermal route were deposited by a layer-by-layer (LbL) method. Chemical synthesis of QD allows better control of the size, shape and crystalline quality of the QDs. This is in particular attractive to tune light absorption properties to better match the solar spectrum.

3.3.1. Structural and Optical Properties of the ZnO/CdTe Core/Shell Heterostructures (QDs Sensitization)

The QDs sensitization was carried out using *PDDA* as a linker element. The deposition of the QDs was perceived with the change in color of the ZnO NW arrays. Figure IV.29 shows the CdTe QD sensitized ZnO NWs. Although the change in the surface morphology can be barely noticed, a conformal layer of QDs seems to be formed around the NW surface. Higher number of LbL cycles should be carried out for the deposition of thicker layers and to increase the light absorbance. For the present case where QDs of 1 nm in diameter were used for preparation of 10 LbL cycles, an extremely thin layer of CdTe could be distinguishable on a damaged heterostructure (produced while sample preparation) (Figure IV.29d).

STEM and EDX analysis confirm the presence of CdTe forming the shell (Figure IV.30). The thickness of the layer is estimated to be in the range of 6-10 nm. Taking into account that our QDs are of 1 nm, the determined thickness (10 nm) indicates that the LbL approach is close to deposit a single-layer of QDs per deposition cycle. The electrostatic interactions between the polyelectrolyte and the negatively-charged QDs appear to be strong enough to form the QD multilayers. The overlapping of elemental mappings (Figure IV.30b-c) shows that the shell is composed of CdTe, which is also confirmed by the line-scan (Figure IV.30d).

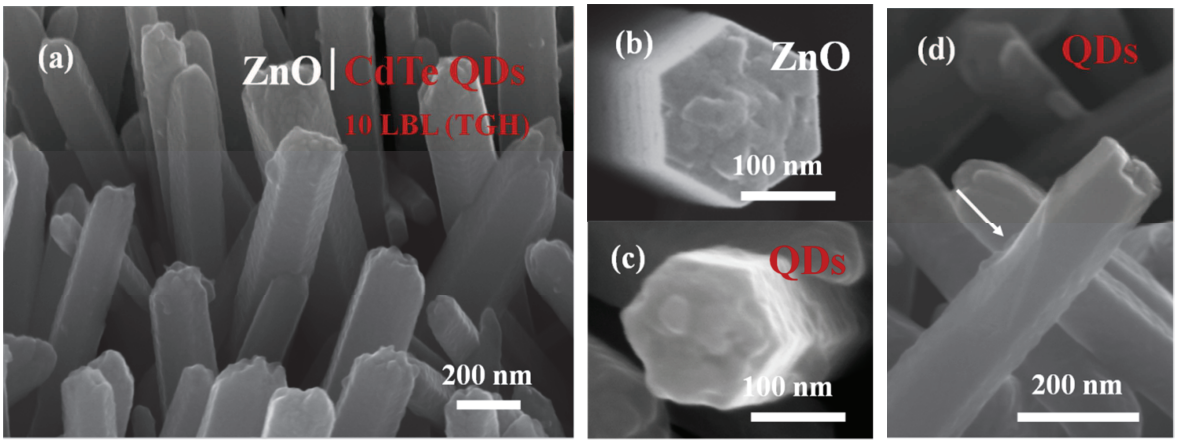

Figure IV.29. (a) SEM image of ZnO/CdTe heterostructures after 10 layer of QDs prepared by LbL deposition, (b) Magnified SEM image of a bare ZnO NW and (c-d) QD-sensitized NWs (the arrow in (d) shows the damaged QD-layer while sample preparation).

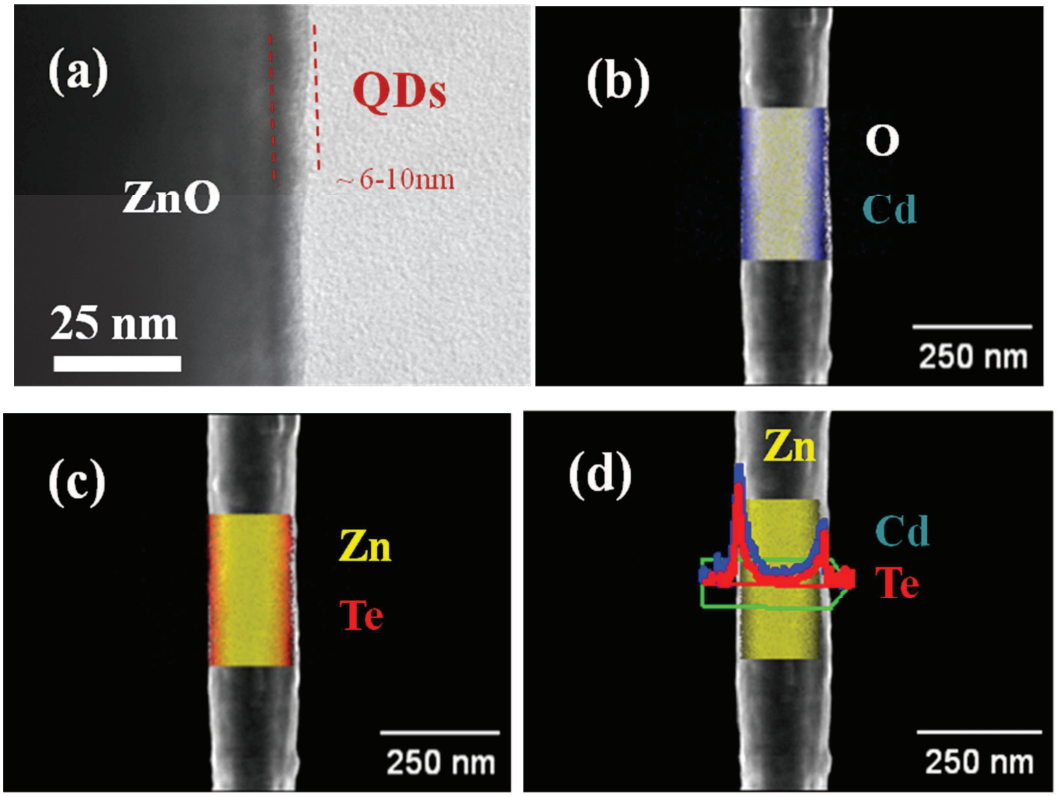

Figure IV.30. (a) Bright-Field STEM image of single ZnO/CdTe QDs nanostructure obtained after 10 LbL cycles and using 1 nm QD. EDX elemental mapping of the heterostructure showing: (b) *O* and *Cd* elements, (c) *Zn* and *Te* elements; and (d) horizontal line scan showing the relative intensities of *Zn*, *Cd* and *Te* elements.

We compared the absorbance of samples prepared with the same number of LbL cycles but with different size of CdTe QDs (1, 3, and 3.5 nm). The absorbance spectra show an increase of the absorbance with the QDs diameter (Figure IV.31). These samples are with

different colors (Figure IV.31a inset). The colors of the samples correspond to the color of the used QD solutions (Figure IV.31c).

Different capping agents were used for the stabilization of the CdTe QDs (*TGA*, *GSH*, *TGH* corresponding to 2.92, 3.39, and 1.04 nm QDs, respectively). The narrow PL emission confirms the stabilization of the QDs even after being deposited on the ZnO NW surface (Figure IV.31b). However, the peak positions do not match with dimensions of the QDs. The emission from the *TGA*-covered QDs is blue shifted with respect to the *GSH* and *TGH*-capped QDs. The PL emission from CdTe QDs colloidal solution has shown to depend on their size but also on the surface chemistry due to structural changes on the surface (removal of local traps) [237, 238]. Therefore, the observed blue-shift in the *TGA*-stabilized QDs could be result of surface effects provoked by the capping molecule. However, although hard to determine, charge transfer between CdTe QDs and ZnO NWs should not be discarded due to the fact that *TGA* is a relatively small molecule and the carboxylic group allows a stronger attachment to the polymeric linker (*PDDA*) or ZnO NW surface.

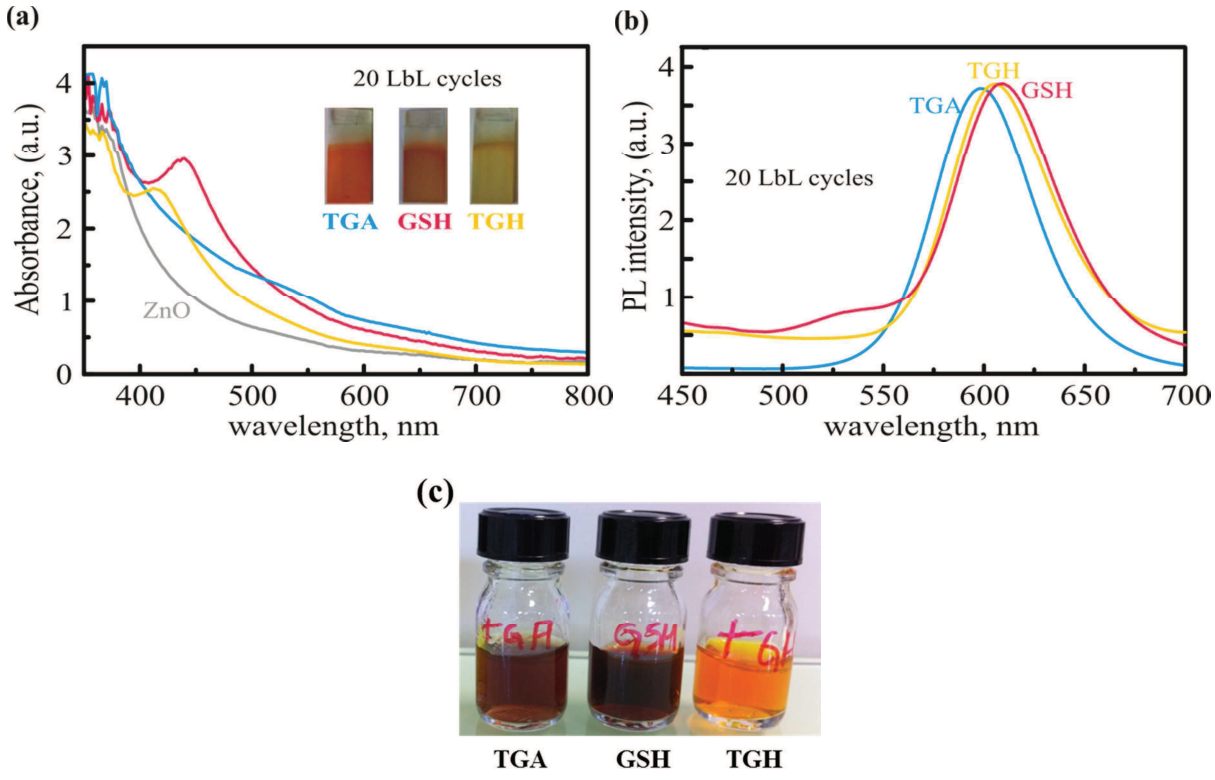

Figure IV.31. (a) Absorbance and (b) room-temperature PL spectra of the ZnO/CdTe QDs heterostructures prepared after 20 LbL cycles using different QDs (*TGA*, *GSH*, *TGH* corresponding to 2.92, 3.39, and 1.04 nm QDs, respectively) and (c) CdTe QDs colloidal solutions (pH 9) used in the deposition process.

Further increase of the deposition LbL cycles to 30 (using QDs of 2.9 nm) leads to enhancement of the absorbance (Figure IV.32)

The increased number of the deposition cycles produces a local increase of the photosensitizing CdTe layer and the subsequent loading of the QDs becomes more efficient. And that is exactly what can be seen on the Figure IV.32a, where the absorbance is doubled from 20 to 30 cycles.

The removal of the *PDDA* polymer is required in order to warrant the transfer of photogenerated carriers. However, high annealing temperatures could not only decompose the PDDA but also could promote the QDs coalescence. The last is not desired if the quantum effects are of the main interest when seeking energy harvesting. Annealing of the samples was performed at 180 °C. No change of the PL emission maximum with the increase of the QDs layers has been reported [147 239]. We have found that the PL emission peak from the deposited QDs on NW surface is shifted with 4 nm from that of the QDs in solution (Figure IV.32b) confirming that the QDs in the shell remain isolated and preserve their optoelectronic properties. However upon annealing the shift of the PL maximum is close to ~20 nm which could be related with an increase of the particle size [240].

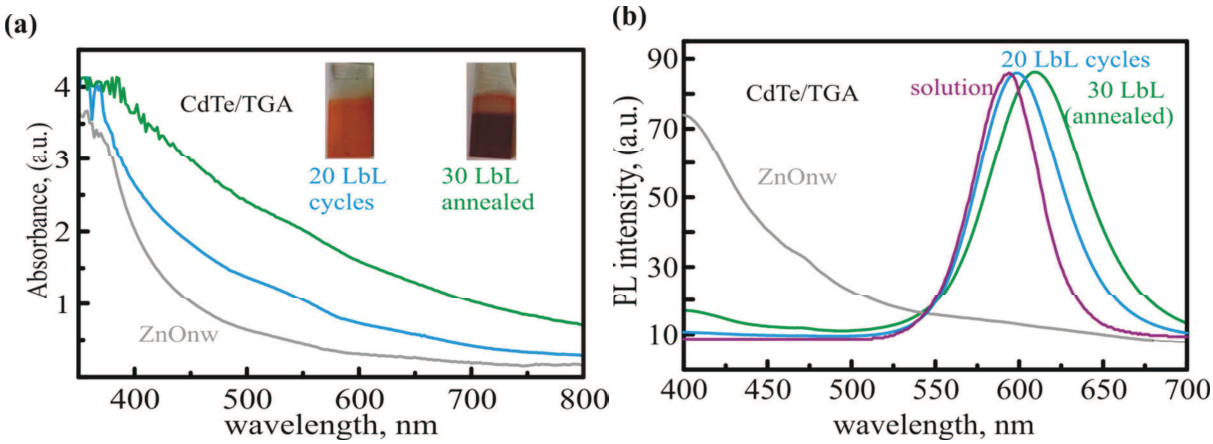

Figure IV.32. (a) Absorbance and (b) room-temperature PL spectra of the ZnO/CdTe QDs heterostructures prepared after 20 and 30 (annealed at 180 °C) LbL cycles. Insets in (a) are pictures of the ZnO/CdTe QDs samples.

In this section the ZnO NWs sensitization with CdTe QDs layers was demonstrated. Full coverage of the ZnO NWs was achieved using the LbL approach. The thickness of the sensitizing layer and the optical features of the ZnO NW-based heterostructures were controlled with the number of the deposition cycles. The annealing treatment carried out for the *PDDA* polymer removal produced an increase of the QD size.

4 CONCLUSION

In this chapter, the photosensitization of ZnO NW arrays with extremely thin layers of CdS, CdSe and CdTe was studied.

Classical SILAR deposition technique was used to prepare CdS, CdSe and CdTe layers. A modified-SILAR method consisting of sequential annealing steps resulted in more conformal and denser CdS layers. For the case of CdSe and CdTe layers, the additionally implemented chemical activating treatment considerably improved their crystalline and optical properties.

CdTe was also prepared by CSS and from QDs. Although CSS deposited CdTe exhibits good crystalline quality and optimal optical properties, shadowing effects and uneven coverage of the nanowires are limiting factors. For the case of the QDs the LbL approach allows to produce more conformal layers but problems related to the poor QD loading need to be further optimized.

The obtained results for SILAR and LbL-QDs sensitization represent versatile approaches for nanostructure photosensitization and open possibilities for large scalability.

CHAPTER V : Fabrication of the eta-Solar Cell

In this chapter, the preparation of complete eta-solar cell will be introduced. In the first part, *eta*-solar cells where CuSCN layer is prepared by electrochemical deposition (ECD), impregnation and SILAR methods are studied. In the second part, the photoelectrochemical *eta*-solar cell is used to study the interfaces and photosensitizing shell quality.

1 THE ALL INORGANIC eta-SOLAR CELL

In the previous chapters, the deposition of ZnO 2D layers and NWs and the preparation of core/shell nanostructures have been demonstrated. To complete the *eta*-solar cell, it is necessary to fill the free space between the heterostructures with a p-type semiconductor.

In this section, the deposition of the CuSCN (p-type) is studied. Three different preparation techniques have been explored. CuSCN layers prepared by electrochemical deposition (ECD), impregnation and SILAR methods are compared and their effects on the obtained solar cell efficiencies are discussed.

1.1. Deposition of the p-Type Semiconductor (CuSCN)

CuSCN have been prepared by different methods with the aim to find the more suitable technique for a good filling of the heterostructure arrays. ZnO/CdS NW arrays were filled with the hole conductor by the above proposed three preparation methods. The first experiments were performed using ZnO/CdS core/shell heterostructure arrays since the CdS preparation by SILAR is relatively easy and the layer presents good and stable physico-chemical properties.

Figure V.1a shows a cross sectional SEM image of the *eta*-solar cell (ZnO/CdS/CuSCN/Au contact), where the CuSCN was prepared by impregnation. The uniform in height of the ZnO/CdS NW array (1.5 μm) can be well distinguished. The thickness of the CuSCN film is not uniform and due to the high roughness in some areas it is about 2.5 μm above the core/shell heterostructures. It has been previously demonstrated by the group of Lévy-Clément that the thickness of this layer should not exceed 1.5 μm [173] (Equation II.5 from chapter II).The magnified SEM images (Figure V.1b-c) on the area of the ZnO/CdS core/shell heterostructure show that the voids are filled with big CuSCN crystals. It is also possible to distinguish the full coverage of ZnO NWs with the sensitizing layer and some areas of the bare ZnO NW surface that are produced while sample preparation for the cross sectional SEM observations.

In our group we studied the preparation of n-p junction of ZnO NWs-CuSCN prepared by ECD and SILAR methods for Light Emitting Diode applications. This experience has been

used also to complete the *eta*-solar cells. Both methods allow good control of the CuSCN layer thickness in the nanometer range. Although it is not directly related with *eta*-solar cells here it is worth to note that for the first time in our group CuSCN nanowires have been grown at room temperature by ECD [Appendix A].

Figure V.2 shows top view of complete eta-solar cells where CuSCN was deposited by the three studied techniques. It can be seen that the 100 nm thick layer of the evaporated Au contact follows the morphology of the CuSCN layer.

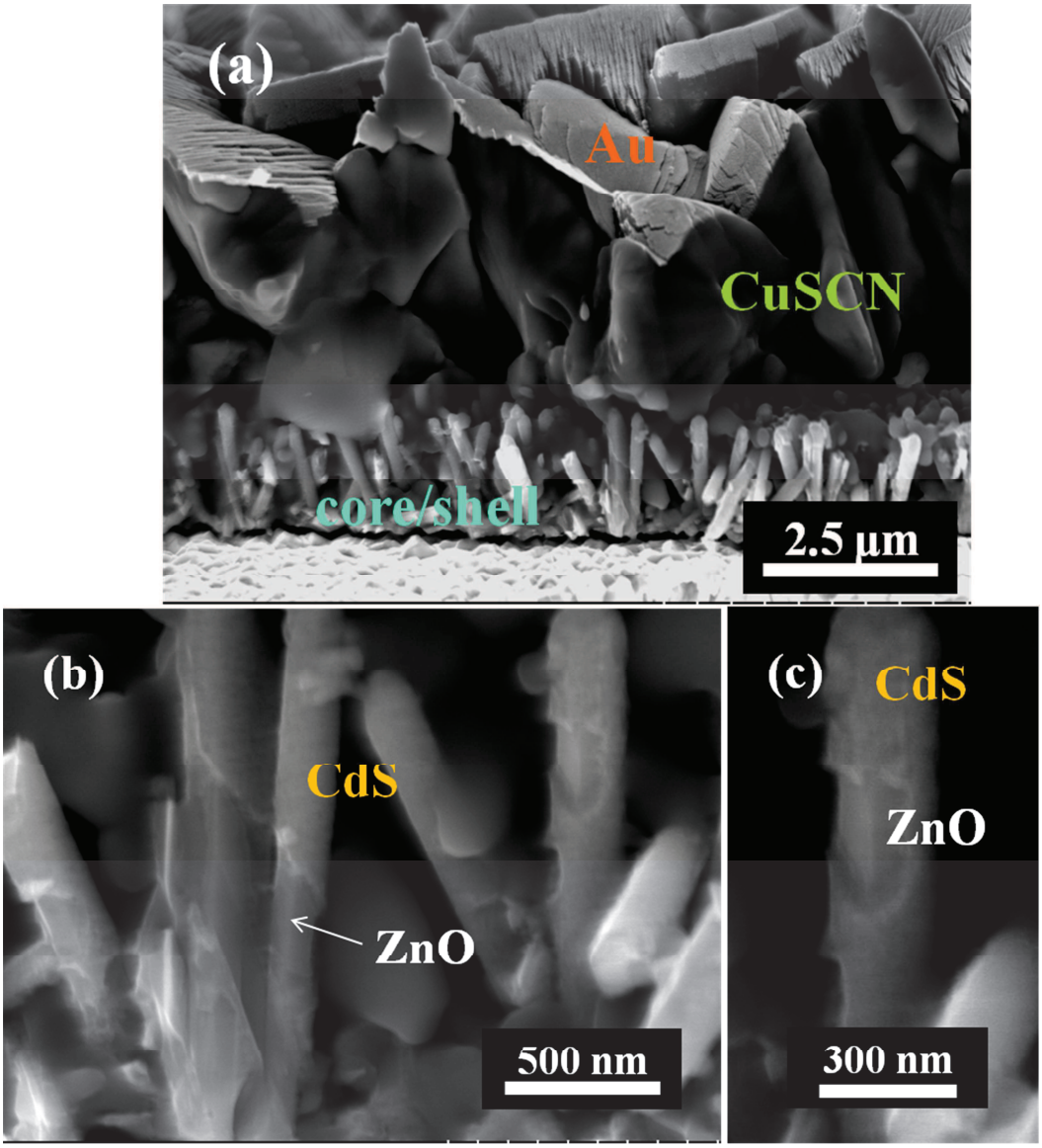

Figure V.1. (a) SEM image (cross-sectional view) of a complete *eta*-solar cell formed by ZnO/CdS/CuSCN/Au electrode (100 nm). (b) and (c) are magnified SEM images on the core/shell heterostructure array. The CuSCN was deposited by impregnation.

The layer deposited by impregnation is smoother and therefore the Au contact is continuously deposited. For the cases when CuSCN was prepared by ECD and SILAR the surface roughness is high and cracks in the Au layer are seen which could be the reason for poor electrical conduction.

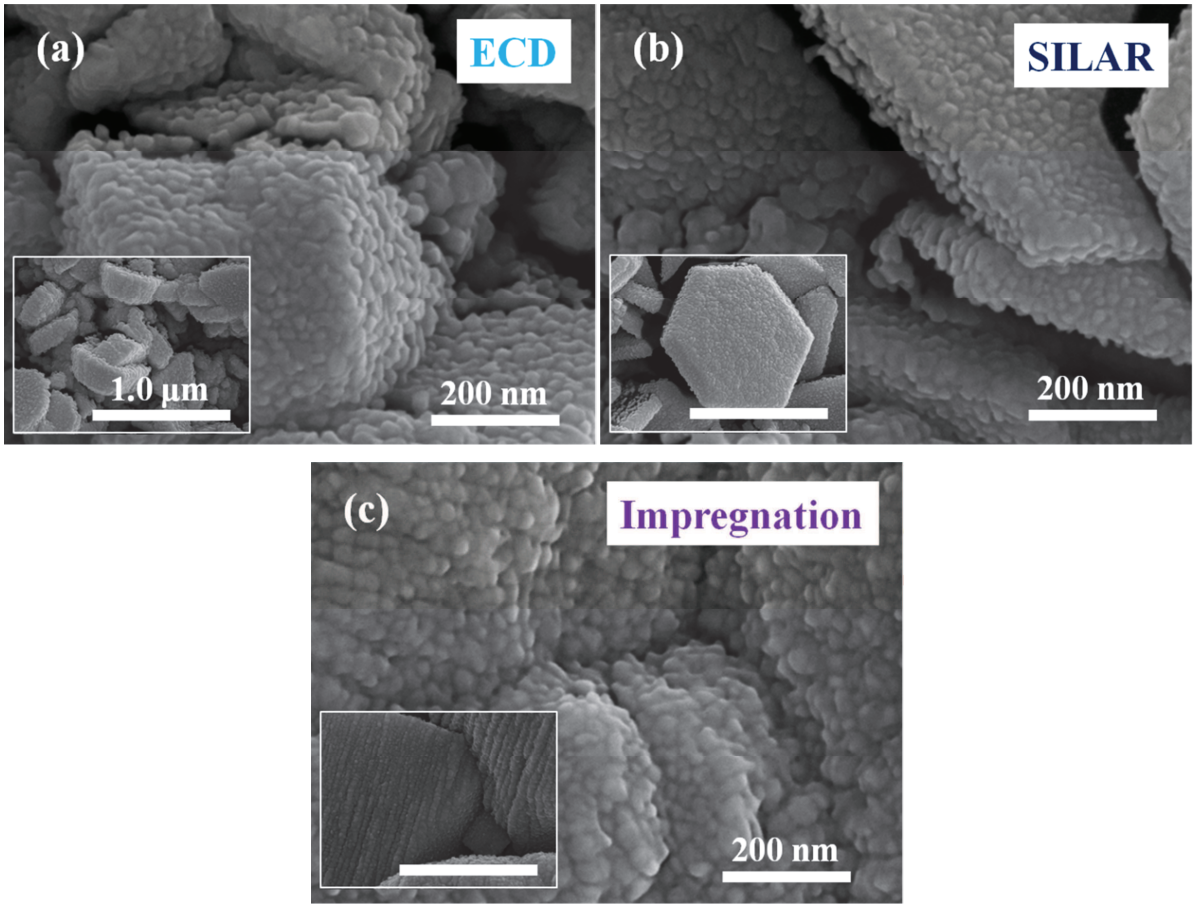

Figure V.2. SEM images (top view) of the ZnO/CdS/CuSCN/Au (100 nm), the CuSCN was deposited by: (a) ECD, (b) SILAR, and (c) Impregnation.

In terms of material quality, CuSCN layer deposited by the studied methods, present similar crystalline properties. Figure V.3 shows the XRD diffraction patterns of CuSCN prepared by the three studied methods. For all the cases the peaks corresponding to the rhombohedral β-phase of CuSCN were detected. It should be noted that for CuSCN deposited by SILAR other peaks assigned to $Cu(SCN)_2$ also appeared. Since the p-type character of CuSCN has been associated with Cu deficiency [241, 242], the possibility to control CuSCN composition when ECD and SILAR are used makes these techniques very attractive.

Optically, the CuSCN is a transparent semiconductor with a bandgap slightly wider than that of ZnO (Figure V.4). The high transparency of CuSCN could be used in the design of solar cells in the superstrate configuration.

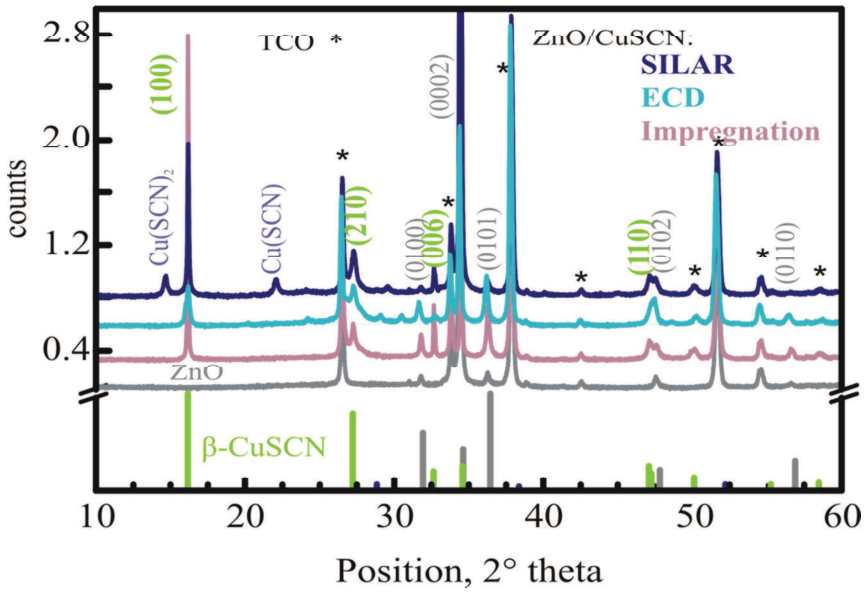

Figure V.3. XRD diffraction patterns of Zn NWs/CuSCN heterostructure where CuSCN was prepared by SILAR, ECD and Impregnation. The reference patterns of ZnO and the rhombohedral β- phase of CuSCN (PDF4+ 00-029-0581) are included.

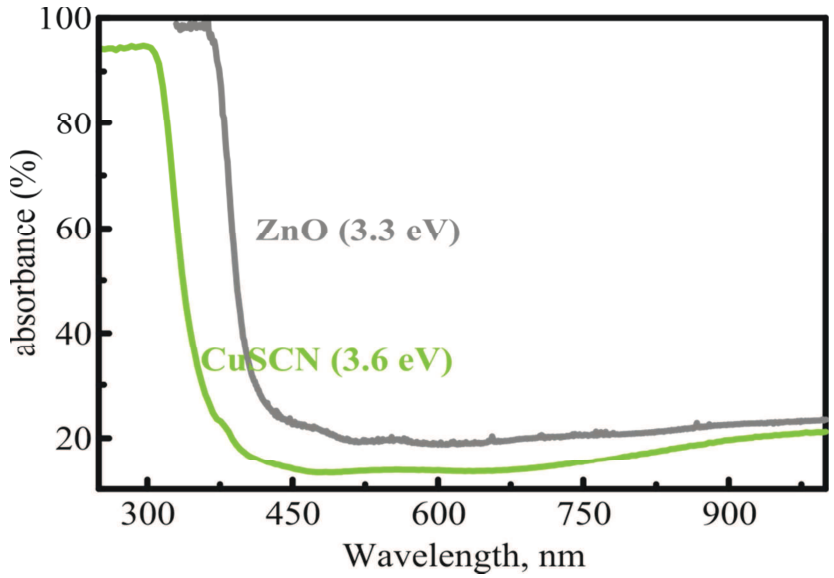

Figure V.4. UV-Vis absorbance spectra of ZnO NW array and a thin layer of CuSCN (400 nm thick) deposited by ECD (E = -0.4 V vs SCE). The bandgaps of bulk ZnO and CuSCN are given.

1.1.1. Eta-Solar Cell Characterization (Evaluation of the Method for CuSCN Preparation)

In Figure V.5 are shown the current density-voltage (J-V) curves for an eta-solar cell (ZnO/CdS/CuSCN/Au) where CuSCN layer was deposited by impregnation. This cell showed a weak rectifying behavior in the dark which is characteristic for poor junctions. Nevertheless under illumination the photovoltaic effect is observed and the following values for the solar cell parameters are measured: short-circuit photocurrent density (J_{sc} =-0.2167 mA cm^{-2}), open circuit voltage (V_{oc} = 17.21 mV), fill factor (FF = 0.2437), and conversion efficiency (η = 1.55 10^{-3} %).

Other eta-solar cell with same configuration (ZnO/CdS/CuSCN/Au) where CuSCN was prepared by the two other studied methods (ECD and SILAR) and their performance were measured under dark and illumination conditions. The Table V.1 summarizes the recorded of these *eta*-solar cells parameters. Although the obtained efficiencies are low, they permit to identify potential areas for optimization. The effect of the poor electrical contact is noticed. The *eta*-solar cell with the CuSCN deposited by impregnation and ECD showed the highest and lowest performances, respectively (η = 1.55 10^{-3} and η = 6.54 10^{-6} %). The difference of almost three orders of magnitude confirms the importance of the thickness of the hole conducting layer and the p-type/electrical contact interface.

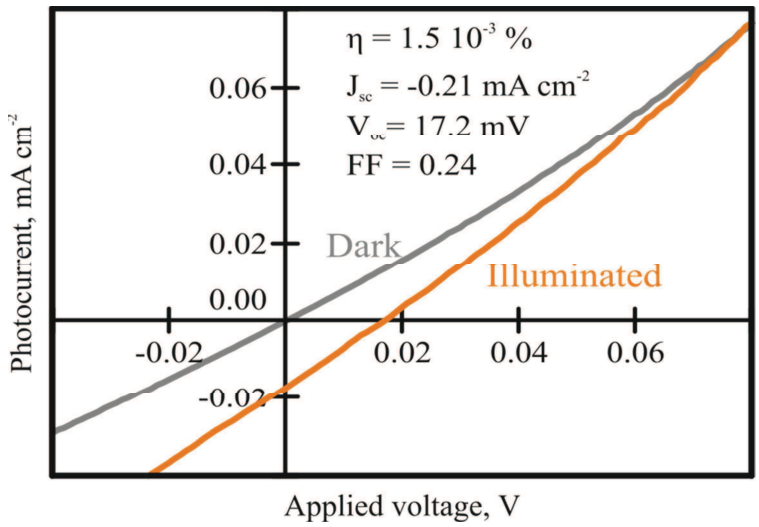

Figure V.5. J-V curves of an eta-solar cell (ZnO/CdS/CuSCN/Au) in the dark and under illumination with a 100 mW cm^{-2} power at 1.5 AM. The CuSCN hole transporting layer was deposited be impregnation.

Table V.1. *Eta-solar* cell (ZnO/CdS/CuSCN/Au) photovoltaic parameters where p-type CuSCN was prepared by ECD, SILAR and Impregnation. Testing conditions: 100 mW/cm2 AM 1.5, at room temperature and a cell surface of 0.25 cm^2.

Method	J_{sc} ($mA\ cm^{-2}$)	V_{oc} (mV)	FF	R series (Ohms)	R shunt (Ohms)	Efficiency η (%)
IMPREG	-0.21	17.21	0.24	1225.3	1989.6	**$1.5\ 10^{-3}$**
ECD	-0.06	0.19	0.32	75.1	89.6	**$6.5\ 10^{-6}$**
SILAR	-0.11	0.56	0.25	185568	7187	**$1.7\ 10^{-5}$**
SILAR *	-0.48	1.06	0.25	202.8	37.6	**$1.3\ 10^{-4}$**
ECD *	-0.08	0.22	0.31	60.0	82.3	**$9.7\ 10^{-6}$**

* Thin layer of CuSCN was deposited by impregnation over the already complete (ZnO/CdS/CuSCN) structures by the indicated methods to smooth the layer surface and improve the electrical contact.

A planarization of the CuSCN film surface prepared by SILAR and ECD, was achieved with the subsequent deposition of a thin film of CuSCN prepared by impregnation. The observed improvement is more noticeable for the SILAR-prepared CuSCN.

The significant decrease in the series and shunt resistances of the CuSCN deposited by SILAR after planarization shows that the planarization improves not only the electrical contact but also the interface with the Zn/CdS heterostructures. Moreover, if the infiltration of CuSCN by Impregnation method is considered to be ideal, the higher series and shunt resistances compared to the planarized SILAR could be an indication of difference in terms of material quality. The combination of both methods SILAR (good interface formation) and impregnation (use for planarization) seems a good alternative for the improvement of the cell performances.

The poor performances of ECD CuSCN film even after planarization are probably due to the fact that the electrodeposited film is very thick. Nevertheless, the prepared CuSCN by ECD exhibits good crystalline and optical properties (Figure V.3 and 5), this makes it a technique with potential for industrialization which should be further explored.

1.2. Characterization of Eta-Solar Cells with CdSe and CdTe Absorbers.

Eta-solar cells with the different absorber materials (ZnO/CdSe(Te)/CuSCN/Au) were fabricated and characterized in dark and under illumination. The obtained results for the cells prepared with the as-deposited materials by SILAR (CdSe and CdTe) and LbL (CdTe QDs) are summarized in Table V.2. The CuSCN was deposited by Impregnation. The recorded efficiencies remain low. The change of CdS for these two shorter bandgap absorbing materials shows no significance difference. The low performances could be due to both: i) poor heterojunction at the ZnO/Absorber/CuSCN interfaces and ii) low conductivity of CuSCN hole conductor.

Table V.2. E*ta*-solar cells (ZnO/CdSe(Te)/CuSCN/Au) photovoltaic parameters. The as-deposited materials by SILAR (CdSe and CdTe after 20 SILAR cylces) and LbL (CdTe QDs after 20 LbL cycles). The p-type CuSCN was deposited by Impregnation. Testing conditions: 100 mW/cm2 AM 1.5, at room temperature and a cell surface of 0.25 cm^2.

Absorber Material	J_{sc} (mA cm^{-2})	V_{oc} (mV)	FF	R series (Ohms)	R shunt (Ohms)	Efficiency η (%)
CdSe SILAR	-0.0002	7.0	0.24	-0.02	9754.2	**$5.0\ 10^{-6}$**
CdTe SILAR	-0.0220	6.6	0.24	-0.078	176.6	**$1.3\ 10^{-4}$**
CdTe QDs (20 Layers)	-0.0788	6.6	0.24	176.68	292.2	**$1.2\ 10^{-4}$**

2 THE PHOTOELECTROCHEMICAL eta-SOLAR CELL (Effects of ZnO/Absorber Interfaces)

Three different methods for the preparation of the hole conducting layer (CuSCN) were introduced in the first part of this chapter. The CuSCN deposited by Impregnation showed better electrical contact with the Au electrode. However, the contribution from the p-type conductor (CuSCN layer) to the observed low performances is hard to determine. Reproducibility effects related to the filling and material quality have been reported [243].

Here, the effects of the core/shell heterostructure interface (ZnO/absorber) were studied in a photoelectrochemical cell using the $3I^-/I^-_3$ redox electrolyte as in a standard DSSC (Figure V.6a) [244]. The effects of the chemical treatment and annealing step of the photosensitizing shell are studied. ZnO/CdS and ZnO/CdSe heterostructure arrays were prepared by SILAR method. The results for CdTe shells are not included due to the corrosive nature of the electrolyte towards CdTe.

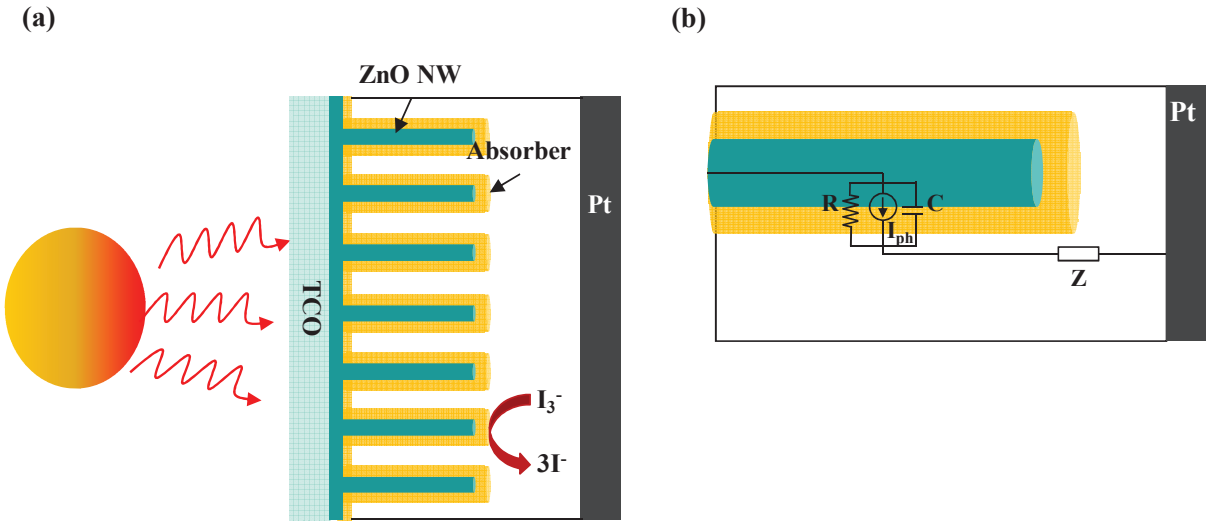

Figure V.6. (a) Scheme of the photoelectrochemical *eta*-solar cell (core/shell ZnO/absorber heterostructure array) with the iodide/tri-iodide electrolyte. (b) Equivalent circuit of a single heterostructure describing the response of the system [55].

2.1. ZnO/CdS Heterostructures

Figure V.7 shows the current-voltage curves of the photoelectrochemical cell using ZnO/CdS heterojunctions under 1 sun illumination and Table V.3 summarizes the recorded photovoltaic performances. The following observations depending on the CdS photosensitizing layer preparation are noticed:

i) A too thin layer (CdS layer deposited with 10 SILAR cycles) produces low photocurrent due to poor light absorption.

ii) A too thick layer (CdS layer deposited with 80 SILAR cycles) also shows low photocurrents despite the almost 90% absorbance of these structures. This could be due to high resistances at the interface and increase of recombination within the layer, which is translated into a higher V_{oc} [221, 222].

iii) A layer with an intermediate thickness (CdS layer deposited with 40 SILAR cycles) shows a good performance. A balance between sufficient light absorption and shell thickness might be favourable for charge collection.

iv) The annealed (at 200 °C) heterostructure shows better performances. However, the irregular J-V curve (under illumination) could be an indication of the non-uniform shell thickness or pin-holes produced upon annealing, which are related to low FF.

v) And finally, for the ZnO/CdS heterostructure array prepared by modified-SILAR method, the highest performance is obtained. Although the J_{sc} is lower than in the only-annealed sample, the sequential improvement of the ZnO/CdS interface could be the reason for the higher FF. It is worth to say that the sequentially-annealed shell (20 nm thick) absorbs roughly 60 % of available light compared to 90 % by the as deposited CdS layer (30 nm thick) with the same 40 SILAR cycles. In this regard, further enhancement of the solar cell efficiency could be achieved by increasing the shell thickness.

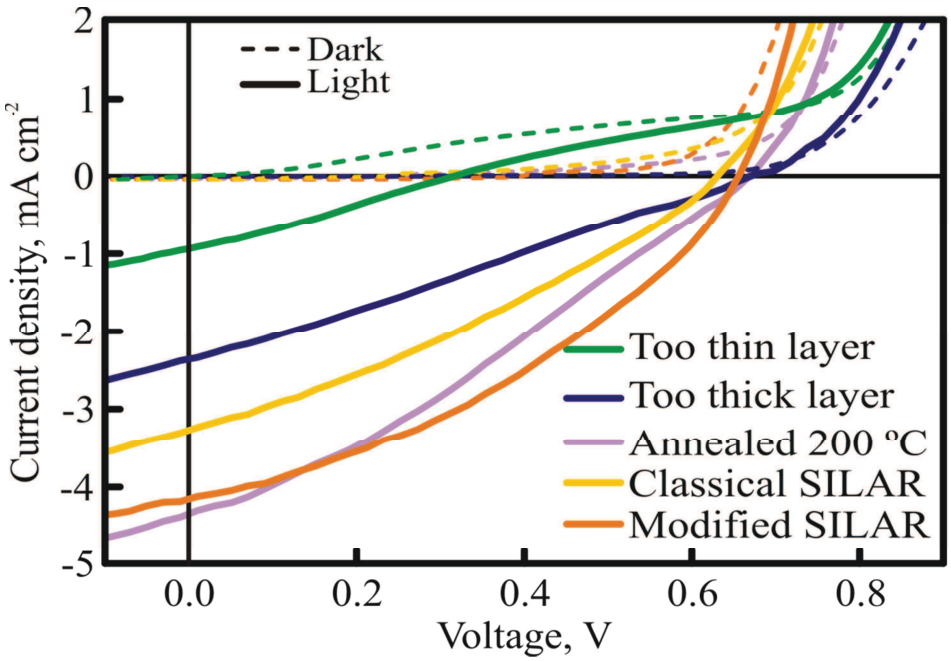

Figure V.7. J–V curves of ZnO/CdS photoelectrochemical *eta*-solar cell in the dark and under 1 sun illumination (100 mW cm^{-2}AM 1.5). The curves correspond to ZnO/CdS heterostructure arrays prepared under different conditions: thin layer (10 SILAR cycles), thick layer (80 SILAR cycles), by classical SILAR (40 cycles), annealed (40 cycles, annealing at 200 °C for 3 minutes), and by modified SILAR (40 cycles; sequential annealing after every 5 cycles at 100 °C).

Table V.3. ZnO/CdS photoelectrochemical *eta*-solar cell photovoltaic parameters determined from the J-V curves (Figure V.7).

CdS absorber	J_{sc} (mA cm^{-2})	V_{oc} (V)	FF	Efficiency η (%)
Classical (40 cycles)	3.30	0.63	0.30	**0.64**
Too thin layer (10 cycles)	0.93	0.32	0.27	**0.08**
Too thick layer (80 cycles)	2.60	0.67	0.25	**0.44**
Annealed (200 °C) *	4.38	0.67	0.29	**0.86**
Modified (40 cycles) **	4.18	0.65	0.36	**1.01**

* annealing was carried out for 3 minutes on a hot plate after 40 SILAR cycles.
** annealing steps were done after every 5 cycles for 30 seconds on a hot plate.

In order to explain the observed results, the core/shell ZnO/absorber interfaces could be approximated as an equivalent electrical circuit depicted in Figure V.6b. In the proposed model [55, 245]:

- **C** represents the chemical capacitance of the semiconductor absorber (C = c_μ x L, where L is the shell thickness and c_μ is the chemical capacitance that relates a variation of the carrier density to a displacement of the Fermi level).
- **R** is the charge transfer resistance at the ZnO/absorber/hole conductor heterostructure. (R = r x L, where L is the shell thickness and r is related to recombination of electrons within the shell and at the interfaces)
- $\mathbf{I_{ph}}$ represent the photogenerated current upon light excitation.

The series resistance accounting for the transport of carriers in the ZnO NWs and the impedance (Z) related to the hole transporter (electrolyte) are assumed to be stable [241, 243]. Moreover, low series resistance can be expected for the case of the electrodeposited ZnO NWs due to high intrinsic doping and single-crystal character [198, 246].

From the J-V curves the following observation can be drawn:

- The observed current onsets (around ~0.65 V) could indicate similar layer quality and thickness (for the same number of SILAR cycles). In the other two cases, a thicker (large L) and thinner shell (small L) influence the **C** value, shifting the current onset to a higher and lower applied voltages, respectively. Moreover, for the case of the thin layer, the J-V curve in the dark exhibits weak rectification and leakage currents can be seen at high applied voltages. In this case, tunnelling currents should be also taken into account.

  The effect of the resistance **R** is more noticeable in the case of the thicker layer. High recombination of photogenerated carriers within the layer and poor charge separation could be responsible for the relatively low photocurrent.

  And the improved ZnO/CdS interfaces prepared by the modified-SILAR technique might significantly reduce the transfer resistance increasing the photocurrent.
- Higher photogenerated current ($\mathbf{I_{ph}}$) is measured when the CdS shell is annealed or prepared by the modified-SILAR method. The improved layer crystalline quality warrants higher current generation upon illumination.

2.2. ZnO/CdSe Heterostructures

The other studied core/shell heterostructure is ZnO/CdSe. Extremely thin layers of CdSe were prepared by SILAR on the ZnO NW arrays and photoelectrochemical *eta*-solar cells were characterized. The absorber layer properties showed to influence the photovoltaic performances. The enhanced crystalline and optical properties of the layer improved the solar cells efficiencies.

Figure V.8 shows the J-V curves of the photoelectrochemical cell using ZnO/CdSe heterostructures under 1 sun illumination and Table V.3 summarizes the recorded photovoltaic performances.

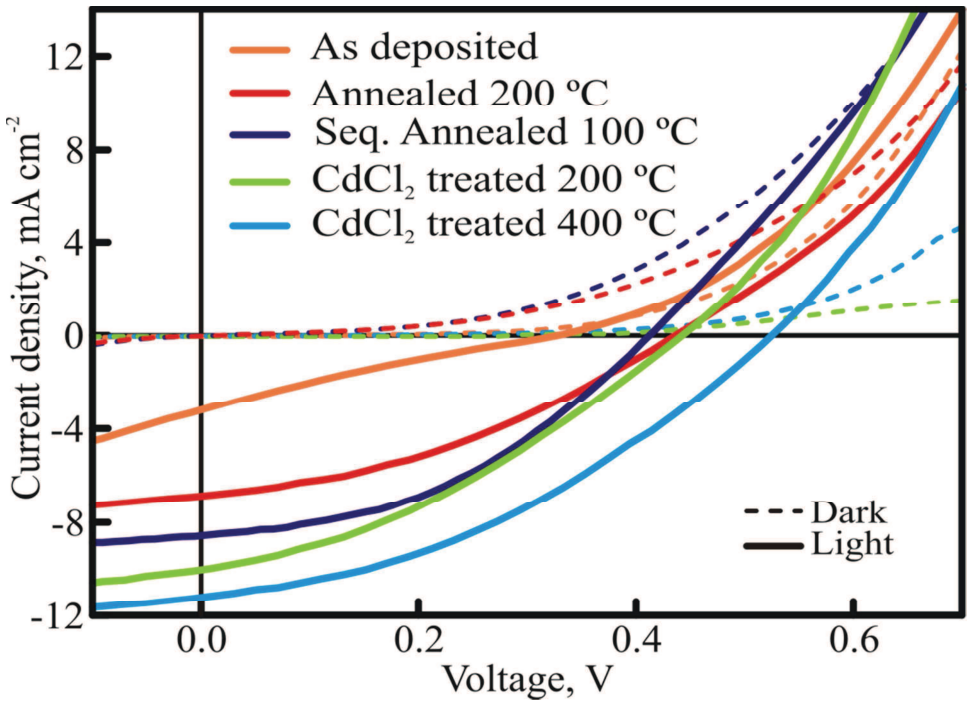

Figure V.8. J–V curves of the ZnO/CdSe photoelectrochemical *eta*-solar cells in the dark and under 1 sun illumination (100 mW cm^{-2}AM 1.5). The curves correspond to the heterostructures prepared by SILAR (20 cycles). The results include: the as-deposited CdSe layer, and under indicated annealing and chemical treatments. The sequential annealing was carried out after every 5 SILAR cycles at 100 °C for 30 seconds.

Comparing CdS and CdSe as photosensitizing materials, the following differences can be readily perceived:

- The V_{oc} using the CdSe shells are lower than those with CdS. In the photoelectrochemical cell the V_{oc} corresponds to the difference between the redox potential of the $3I^-/I_3$ electrolyte and the Fermi level of the nanocrystalline shell.

As discussed in CHAPTER I, the conduction band of CdSe is 0.11 eV below that one of the CdS, therefore lower V_{oc} values are expected.

- Higher photocurrents are measured in the case of CdSe. Despite the small layer thickness (~15 nm) compared to that of CdS (~30 nm) shell, the absorption extension to longer wavelengths in the visible spectrum seems to contribute to the photocurrent as envisaged.

Table V.4. ZnO/CdSe photoelectrochemical *eta*-solar cell photovoltaic parameters determined from the J-V curves (Figure V.8).

CdSe absorber	J_{sc} (mA cm^{-2})	V_{oc} (V)	FF	Efficiency η (%)
Classical SILAR	3.33	0.33	0.19	**0.22**
Annealed (200 °C)*	6.88	0.43	0.36	**1.10**
Seq. annealed (100 °C)	8.59	0.41	0.40	**1.45**
***$CdCl_2$* treated (200 °C)**	10.08	0.45	0.33	**1.52**
***$CdCl_2$* treated (400 °C)**	11.25	0.53	0.36	**2.19**

* annealing steps were carried out for 3 minutes on a hot plate at the indicated temperatures.
** the sequential annealing steps were carried out every 5 cycles for 30 seconds on a hot plate.

The effect of annealing step

Improvement of the sensitizing layer quality upon annealing is directly translated in higher photocurrents. The efficiency increases four times compared to the as-deposited CdSe layer. This is an indication that the SILAR method is suitable to prepare conformal sensitizing layers on nanostructures but approaches to improve the material quality should be implemented.

The effect of sequential annealing procedure

The sequential annealing procedure performed on the ZnO/CdSe heterostructures enhances the photovoltaic performance and higher efficiency than the only-annealed heterostructure is measured. This procedure introduced in CHAPTER IV appears to be appealing due to the required low temperatures and the demonstrated good cell performances. Even more interesting, the determined FF for the sequentially-annealed heterostructures (using CdS or CdSe layers) is higher even than those for the chemically treated and annealed at higher temperatures (200 and 400 °C). These effects could be due to the fact that pin-holes and shell stripping from the NW surface are avoided at this relatively low temperature (100

°C). Moreover, in case of morphological defects or crack of the shell, the subsequent deposition of the material would replenish and repair the layer.

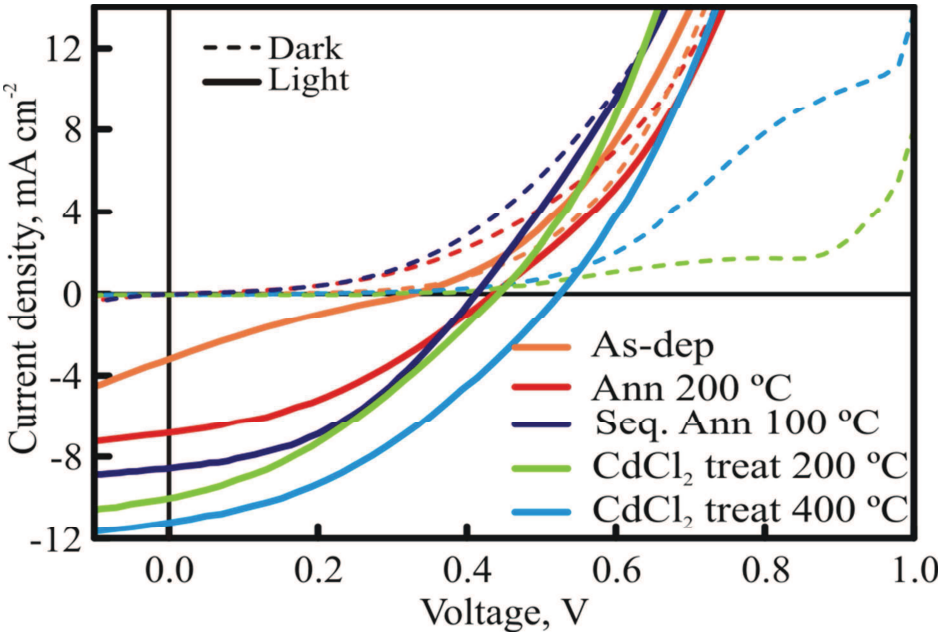

Figure V.9. J–V curves of the ZnO/CdSe photoelectrochemical *eta*-solar cells in the dark and under 1 sun illumination (100 mW cm^{-2}AM 1.5). The curves correspond to the heterostructures prepared by SILAR (20 cycles). The results include: the as-deposited CdSe layer, and under indicated annealing and chemical treatments. The sequential annealing was carried out after every 5 SILAR cycles at 100 °C for 30 seconds.

The effect of the chemical activating treatment ($CdCl_2$)

The $CdCl_2$-chemically-treated ZnO/CdSe heterostructures show remarkable improvement of the photoelectrochemical *eta*-solar cell performance compared to that when as-deposited heterostructure is used. The efficiency of 0.21% for the as-deposited case is raised up to 2 % when a chemical treatment is performed. These results are explained by the dramatic improvement of the material quality as discussed in chapter IV.

Despite of the existence of partially uncovered parts of the ZnO NW surface, the annealed at 400 °C CdSe layer shows higher performance than the one annealed at 200 °C. More interestingly, the J-V curves in the dark (Figure V.9) of both $CdCl_2$-treated samples show current onsets at far higher applied voltages (0.8 V) compared to the untreated heterostructures (0.45 V), which could be the result of improved ZnO/CdSe interfaces or the formation of thin ZnCdSe layer [247] The higher leakage current measured for the 400 °C annealed heterostructure could be related to damaged shell (partially uncovered ZnO surface).

3 CONCLUSION

In this chapter, we have presented the fabrication and characterization of the *eta*-solar cell in the all-inorganic and photoelectrochemical versions.

The first case allows to find the more suitable method for the deposition of the solid-state hole conductor (CuSCN). The *eta*-solar cell with CuSCN prepared by Impregnation technique showed higher efficiency ($\eta = 1.55\ 10^{-3}$ with a sensitizing layer of CdS) than the other methods.

The photoelectrochemical version of the *eta*-solar cell was used to study the effects of the photosensitizing layer quality and the ZnO/absorber interfaces on the photovoltaic performances. The efficiency of the as deposited CdSe layer, for example, was increased from $\eta = 0.2$ to $\eta = 2$ % when the heterostructure (ZnO/CdSe) was chemically treated and annealed at 400 °C for 3 minutes. In this case high J_{sc} was measured.

These results allow us to say that the efficiencies could be further raised if the shell thickness is increased or the nanostructured surface area is more developed. Moreover, they are useful for the optimization of the eta-solar cell.

The present study proves that the ZnO NW-based heterostructures prepared by low cost deposition methods (ECD and SILAR) exhibit good properties for the development of highly efficient solid state photovoltaic devices.

Conclusions

The development of semiconducting materials for the eta-solar cell using cheap and scalable methods was the main objectives of this work.

High quality ZnO layers and nanowires were prepared by electrochemical deposition. The obtained results on thin film and nanowires preparation using galvanostatic mode is a step forward towards industrial applications.

The tailoring of ZnO nanowire dimensions was achieved by using ZnO seed layer with different morphology and thickness. Additionally, the deposition parameters: current density, electrolyte concentration, and total passed charge could be used to further control the nanowire dimensions. Novel nanostructures (nanowalls) were also grown by simply manipulating the deposition configuration when using polar ZnO substrates.

The ZnO NW arrays were photosensitized with CdS, CdSe and CdTe conformal layers. The as-prepared absorbers by classical-SILAR technique showed good material properties and their thicknesses were easily controlled by the number of SILAR cycles.

A modified-SILAR approach consisting of sequential annealing steps or chemical treatment ($CdCl_2$) was proposed. The quality of the sensitizing shells was significantly improved with the implementation the modified-SILAR: annealing step (100, 200 and 400 °C were tested) and a chemical treatment ($CdCl_2$).

ZnO/CdTe heterostructure arrays were also prepared by two other methods: Close Spaced Sublimation or QDs functionalization. The first technique presents limitations related to the full coverage of the NWs due to shadowing effects, whereas the second one produced highly conformal layers on the entire NW surface. The ZnO/CdTe QDs heterostructures showed poor optical features.

The eta solar cell was completed with the hole conducting CuSCN layer prepared by: Impregnation, Electrochemical deposition (ECD) and SILAR techniques. SEM observations revealed that the CuSCN layers deposited by SILAR or ECD present high surface roughness which could be the reason for poor electrical conduction. Improvement of the cell performance was achieved for the case of SILAR prepared CuSCN when a relatively thin layer from the same material was spread over by Impregnation. The combination of the

preparation methods seems promising since ECD and SILAR might permit the doping of CuSCN in a more easy and controllable way.

Also, while experimenting with the preparation of CuSCN by ECD, the growth of CuSCN nanowires was discovered. The nanowire dimensions are easily controlled by the deposition parameters: applied charge density, deposition potential, electrolyte concentration, total passed charge density and substrate morphology. This represents a significant achievement in technology since few wide bandgap p-type nanowires are reported.

Finally the testing of the ZnO/absorber core/shell heterostructures in a photoelectrochemical cell revealed that:

i) the as-prepared ZnO/absorber interface is with good quality;

ii) the implementation of annealing and chemical treatments further improve the material and interface quality which is translated into higher photoresponse (efficiencies up to 2% were achieved).

As future work, it is necessary to gain a better understanding on the properties and preparation methods for CuSCN as hole conducting layer. Further experiments are ongoing and full inorganic eta-solar cells are under investigation.

The knowledge gained throughout this thesis could contribute to the development of more efficient *eta*-solar cells. The obtained results also open the possibility to explore other light absorbing materials, that due to their unfit properties, haven not been used in thin film solar cells such as FeS_2. The practicality of the proposed deposition methods and the obtained good materials quality was demonstrated.

It is our pleasure to contribute to the Renascence of the SILAR technique since it was invented 30 years ago in our Institute (LETI). In this work its extension for the preparation of other materials like CdSe and CdTe was nicely demonstrated.

References

[1] "European Photovoltaic Industry Association (EPIA) - Home." [Online]. Available: http://www.epia.org/. [Accessed: 31-Aug-2012].

[2] "Photovoltaic publications : Global Market Outlook, Solar Generation." [Online]. Available: http://www.epia.org/index.php?id=18. [Accessed: 31-Aug-2012].

[3] W. Shockley and H. J. Queisser, "Detailed Balance Limit of Efficiency of p-n Junction Solar Cells," *Journal of Applied Physics*, vol. 32, no. 3, pp. 510–519, Mar. 1961.

[4] "NREL: Learning - Solar Photovoltaic Technology Basics." [Online]. Available: http://www.nrel.gov/learning/re_photovoltaics.html. [Accessed: 31-Aug-2012].

[5] G. f. Brown and J. Wu, "Third generation photovoltaics," *Laser & Photonics Reviews*, vol. 3, no. 4, pp. 394–405, 2009.

[6] G. Conibeer, "Third-generation photovoltaics," *Materials Today*, vol. 10, no. 11, pp. 42–50, Nov. 2007.

[7] J. Nelson, *The Physics of Solar Cells*, 1st ed. Imperial College Press, 2003.

[8] M. A. Green, K. Emery, Y. Hishikawa, W. Warta, and E. D. Dunlop, "Solar cell efficiency tables (version 39)," *Progress in Photovoltaics: Research and Applications*, vol. 20, no. 1, pp. 12–20, 2012.

[9] M. A. Green, *Third Generation Photovoltaics: Advanced Solar Energy Conversion*. Springer, 2003.

[10] A. J. Nozik, "Exciton Multiplication and Relaxation Dynamics in Quantum Dots: Applications to Ultrahigh-Efficiency Solar Photon Conversion†," *Inorg. Chem.*, vol. 44, no. 20, pp. 6893–6899, Oct. 2005.

[11] R. D. Schaller and V. I. Klimov, "High Efficiency Carrier Multiplication in PbSe Nanocrystals: Implications for Solar Energy Conversion," *Phys. Rev. Lett.*, vol. 92, no. 18, p. 186601, mai 2004.

[12] R. J. Ellingson, M. C. Beard, J. C. Johnson, P. Yu, O. I. Micic, A. J. Nozik, A. Shabaev, and A. L. Efros, "Highly Efficient Multiple Exciton Generation in Colloidal PbSe and PbS Quantum Dots," *Nano Lett.*, vol. 5, no. 5, pp. 865–871, mai 2005.

[13] M. C. Hanna and A. J. Nozik, "Solar conversion efficiency of photovoltaic and photoelectrolysis cells with carrier multiplication absorbers," *Journal of Applied Physics*, vol. 100, no. 7, pp. 074510–074510–8, Oct. 2006.

[14] A. Luque and A. Martí, "Increasing the Efficiency of Ideal Solar Cells by Photon Induced Transitions at Intermediate Levels," *Phys. Rev. Lett.*, vol. 78, no. 26, pp. 5014–5017, juin 1997.

[15] B. O'Regan and M. Grätzel, "A low-cost, high-efficiency solar cell based on dye-sensitized colloidal TiO_2 films," *, Published online: 24 October 1991; | doi:10.1038/353737a0*, vol. 353, no. 6346, pp. 737–740, Oct. 1991.

[16] A. Polizzotti, J. Schual-Berke, E. Falsgraf, and M. Johal, "Investigating New Materials and Architectures for Grätzel Cells," in *Third Generation Photovoltaics*, V. Fthenakis, Ed. InTech, 2012.

[17] A. G. Pattantyus-Abraham, I. J. Kramer, A. R. Barkhouse, X. Wang, G. Konstantatos, R. Debnath, L. Levina, I. Raabe, M. K. Nazeeruddin, M. Grätzel, and E. H. Sargent, "Depleted-Heterojunction Colloidal Quantum Dot Solar Cells," *ACS Nano*, vol. 4, no. 6, pp. 3374–3380, juin 2010.

[18] T. Dittrich, A. Belaidi, and A. Ennaoui, “Concepts of inorganic solid-state nanostructured solar cells,” *Solar Energy Materials and Solar Cells*, vol. 95, no. 6, pp. 1527–1536, juin 2011.
[19] G. Boschloo, T. Edvinsson, and A. Hagfeldt, “Chapter 8 - Dye-Sensitized Nanostructured ZnO Electrodes for Solar Cell Applications,” in *Nanostructured Materials for Solar Energy Conversion*, Amsterdam: Elsevier, 2006, pp. 227–254.
[20] Q. Zhang, C. S. Dandeneau, X. Zhou, and G. Cao, “ZnO Nanostructures for Dye-Sensitized Solar Cells,” *Advanced Materials*, vol. 21, no. 41, pp. 4087–4108, 2009.
[21] I. Gonzalez-Valls and M. Lira-Cantu, “Vertically-aligned nanostructures of ZnO for excitonic solar cells: a review,” *Energy & Environmental Science*, vol. 2, no. 1, p. 19, 2009.
[22] X. Pan, C. Chen, K. Zhu, and Z. Fan, “TiO_2 nanotubes infiltrated with nanoparticles for dye sensitized solar cells,” *Nanotechnology*, vol. 22, no. 23, p. 235402, Jun. 2011.
[23] C. Lévy-Clément, “Chapter 14 - Nanostructured ETA-Solar Cells,” in *Nanostructured Materials for Solar Energy Conversion*, Amsterdam: Elsevier, 2006, pp. 447–484.
[24] R. Könenkamp, P. Hoyer, and A. Wahi, “Heterojunctions and devices of colloidal semiconductor films and quantum dots,” *Journal of Applied Physics*, vol. 79, no. 9, pp. 7029–7035, May 1996.
[25] S. Siebentritt, K. Ernst, C.-H. Fischer, R. Könenkamp, and M. C. Lux-Steiner, “CdTe and CdS as extremely thin absorber materials in an eta solar cell,” *Conference Proceedings of the 14th EPS, Barcelona*, Barcelona, p. 1823, 1997.
[26] K. Tennakone, G. R. R. A. Kumara, I. R. M. Kottegoda, V. P. S. Perera, and G. M. L. P. Aponsu, “Nanoporous n-/selenium/p-CuCNS photovoltaic cell,” *Journal of Physics D: Applied Physics*, vol. 31, no. 18, pp. 2326–2330, Sep. 1998.
[27] I. Kaiser, K. Ernst, C.-H. Fischer, R. Könenkamp, C. Rost, I. Sieber, and M. C. Lux-Steiner, “The eta-solar cell with $CuInS_2$: A photovoltaic cell concept using an extremely thin absorber (eta),” in *Solar energy materials and solar cells*, vol. 67, pp. 89–96.
[28] K. Ernst, R. Engelhardt, K. Ellmer, C. Kelch, H.-J. Muffler, M.-C. Lux-Steiner, and R. Könenkamp, “Contacts to a solar cell with extremely thin CdTe absorber,” in *Thin solid films*, vol. 387, pp. 26–28.
[29] C. Lévy-Clément, R. Tena-Zaera, M. A. Ryan, A. Katty, and G. Hodes, “CdSe-Sensitized p-CuSCN/Nanowire n-ZnO Heterojunctions,” *Advanced Materials*, vol. 17, no. 12, pp. 1512–1515, 2005.
[30] R. Tena-Zaera, A. Katty, S. Bastide, and C. Lévy-Clément, “Annealing Effects on the Physical Properties of Electrodeposited ZnO/CdSe Core−Shell Nanowire Arrays,” *Chem. Mater.*, vol. 19, no. 7, pp. 1626–1632, avril 2007.
[31] F. Lenzmann, B. O’Regan, J. Wienke, C. Huisman, L. Reijnen, and A. Goossens, “Surface photovoltage measurements: a useful tool for the detection of electron injection processes in extremely thin absorber (ETA) solar cells,” *Physica E: Low-dimensional Systems and Nanostructures*, vol. 14, no. 1–2, pp. 233–236, avril 2002.
[32] R. Tena-Zaera, A. Katty, S. Bastide, C. Lévy-Clément, B. O’Regan, and V. Muñoz-Sanjosé, “ZnO/CdTe/CuSCN, a promising heterostructure to act as inorganic eta-solar cell,” *Thin Solid Films*, vol. 483, no. 1–2, pp. 372–377, juillet 2005.
[33] G. Hodes and D. Cahen, “All-Solid-State, Semiconductor-Sensitized Nanoporous Solar Cells,” *Acc. Chem. Res.*, vol. 45, no. 5, pp. 705–713, mai 2012.
[34] M. Nanu, J. Schoonman, and A. Goossens, “Inorganic Nanocomposites of n- and p-Type Semiconductors: A New Type of Three-Dimensional Solar Cell,” *Advanced Materials*, vol. 16, no. 5, pp. 453–456, 2004.

[35] M. Nanu, J. Schoonman, and A. Goossens, "Nanocomposite Three-Dimensional Solar Cells Obtained by Chemical Spray Deposition," *Nano Lett.*, vol. 5, no. 9, pp. 1716–1719, Sep. 2005.
[36] R. Bayón, R. Musembi, A. Belaidi, M. Bär, T. Guminskaya, C. H. Fischer, M. C. Lux-Steiner, and T. Dittrich, "Highly structured TiO_2/In(OH)xSy/PbS/PEDOT:PSS to be used in photovoltaic applications," *Comptes Rendus Chimie*, vol. 9, no. 5–6, pp. 730–734, mai 2006.
[37] B. Tian, X. Zheng, T. J. Kempa, Y. Fang, N. Yu, G. Yu, J. Huang, and C. M. Lieber, "Coaxial silicon nanowires as solar cells and nanoelectronic power sources," *Nature*, vol. 449, no. 7164, pp. 885–889, Oct. 2007.
[38] A. Belaidi, T. Dittrich, D. Kieven, J. Tornow, K. Schwarzburg, M. Kunst, N. Allsop, M.-C. Lux-Steiner, and S. Gavrilov, "ZnO-nanorod arrays for solar cells with extremely thin sulfidic absorber," *Solar Energy Materials and Solar Cells*, vol. 93, no. 6–7, pp. 1033–1036, juin 2009.
[39] Y. Itzhaik, O. Niitsoo, M. Page, and G. Hodes, "Sb_2S_3-Sensitized Nanoporous TiO_2 Solar Cells," *J. Phys. Chem. C*, vol. 113, no. 11, pp. 4254–4256, Mar. 2009.
[40] C. Colombo, M. Heiβ, M. Grätzel, and A. Fontcuberta i Morral, "Gallium arsenide p-i-n radial structures for photovoltaic applications," *Applied Physics Letters*, vol. 94, no. 17, pp. 173108–173108–3, Apr. 2009.
[41] M. Krunks, E. Kärber, A. Katerski, K. Otto, I. Oja Acik, T. Dedova, and A. Mere, "Extremely thin absorber layer solar cells on zinc oxide nanorods by chemical spray," *Solar Energy Materials and Solar Cells*, vol. 94, no. 7, pp. 1191–1195, juillet 2010.
[42] E. Garnett and P. Yang, "Light Trapping in Silicon Nanowire Solar Cells," *Nano Lett.*, vol. 10, no. 3, pp. 1082–1087, Mar. 2010.
[43] X. Wang, R. Li, and D. Fan, "Nanostructured Al-ZnO/CdSe/Cu_2O ETA solar cells on Al-ZnO film/quartz glass templates," *Nanoscale Research Letters*, vol. 6, no. 1, p. 614, Dec. 2011.
[44] C. Gutsche, A. Lysov, D. Braam, I. Regolin, G. Keller, Z.-A. Li, M. Geller, M. Spasova, W. Prost, and F.-J. Tegude, "n-GaAs/InGaP/p-GaAs Core-Multishell Nanowire Diodes for Efficient Light-to-Current Conversion," *Advanced Functional Materials*, vol. 22, no. 5, pp. 929–936, 2012.
[45] C. Lévy-Clément, A. Katty, S. Bastide, F. Zenia, I. Mora, and V. Munoz-Sanjose, "A new CdTe/ZnO columnar composite film for Eta-solar cells," *Physica E: Low-dimensional Systems and Nanostructures*, vol. 14, no. 1–2, pp. 229–232, avril 2002.
[46] R. Tena-Zaera, M. A. Ryan, A. Katty, G. Hodes, S. Bastide, and C. Lévy-Clément, "Fabrication and characterization of ZnO nanowires/CdSe/CuSCN eta-solar cell," *Comptes Rendus Chimie*, vol. 9, no. 5–6, pp. 717–729, May 2006.
[47] K. Taretto and U. Rau, "Modeling extremely thin absorber solar cells for optimized design," *Progress in Photovoltaics: Research and Applications*, vol. 12, no. 8, pp. 573–591, 2004.
[48] V. I. Klimov, "Detailed-balance power conversion limits of nanocrystal-quantum-dot solar cells in the presence of carrier multiplication," *Applied Physics Letters*, vol. 89, no. 12, pp. 123118–123118–3, Sep. 2006.
[49] A. Ennaoui, S. Fiechter, C. Pettenkofer, N. Alonso-Vante, K. Büker, M. Bronold, C. Höpfner, and H. Tributsch, "Iron disulfide for solar energy conversion," *Solar Energy Materials and Solar Cells*, vol. 29, no. 4, pp. 289–370, mai 1993.
[50] N. Cai, S.-J. Moon, L. Cevey-Ha, T. Moehl, R. Humphry-Baker, P. Wang, S. M. Zakeeruddin, and M. Grätzel, "An Organic D-π-A Dye for Record Efficiency Solid-State Sensitized Heterojunction Solar Cells," *Nano Lett.*, vol. 11, no. 4, pp. 1452–1456, avril 2011.

[51] S.-J. Moon, Y. Itzhaik, J.-H. Yum, S. M. Zakeeruddin, G. Hodes, and M. Grätzel, "Sb_2S_3-Based Mesoscopic Solar Cell using an Organic Hole Conductor," *J. Phys. Chem. Lett.*, vol. 1, no. 10, pp. 1524–1527, mai 2010.
[52] J. A. Chang, J. H. Rhee, S. H. Im, Y. H. Lee, H. Kim, S. I. Seok, M. K. Nazeeruddin, and M. Gratzel, "High-Performance Nanostructured Inorganic−Organic Heterojunction Solar Cells," *Nano Lett.*, vol. 10, no. 7, pp. 2609–2612, juillet 2010.
[53] F. Zenia, C. Lévy-Clément, R. Triboulet, R. Könenkamp, K. Ernst, M. Saad, and M. C. Lux-Steiner, "Electrochemical texturization of ZnTe surfaces," *Applied Physics Letters*, vol. 75, no. 4, pp. 531–533, Jul. 1999.
[54] P. P. Boix, G. Larramona, A. Jacob, B. Delatouche, I. Mora-Seró, and J. Bisquert, "Hole Transport and Recombination in All-Solid Sb_2S_3-Sensitized TiO_2 Solar Cells Using CuSCN As Hole Transporter," *J. Phys. Chem. C*, vol. 116, no. 1, pp. 1579–1587, Jan. 2012.
[55] I. Mora-Seró, S. Giménez, F. Fabregat-Santiago, E. Azaceta, R. Tena-Zaera, and J. Bisquert, "Modeling and characterization of extremely thin absorber (eta) solar cells based on ZnO nanowires," *Phys. Chem. Chem. Phys.*, vol. 13, no. 15, pp. 7162–7169, Mar. 2011.
[56] J. Cui, "Zinc oxide nanowires," *Materials Characterization*, vol. 64, pp. 43–52, février 2012.
[57] P. Yang, H. Yan, S. Mao, R. Russo, J. Johnson, R. Saykally, N. Morris, J. Pham, R. He, and H.-J. Choi, "Controlled Growth of ZnO Nanowires and Their Optical Properties," *Advanced Functional Materials*, vol. 12, no. 5, pp. 323–331, 2002.
[58] J. Jie, G. Wang, Y. Chen, X. Han, Q. Wang, B. Xu, and J. G. Hou, "Synthesis and optical properties of well-aligned ZnO nanorod array on an undoped ZnO film," *Applied Physics Letters*, vol. 86, no. 3, pp. 031909–031909–3, Jan. 2005.
[59] Z. W. Pan, Z. R. Dai, and Z. L. Wang, "Nanobelts of Semiconducting Oxides," *Science*, vol. 291, no. 5510, pp. 1947–1949, Mar. 2001.
[60] M. Kirkham, X. Wang, Z. L. Wang, and R. L. Snyder, "Solid Au nanoparticles as a catalyst for growing aligned ZnO nanowires: a new understanding of the vapour–liquid–solid process," *Nanotechnology*, vol. 18, no. 36, p. 365304, Sep. 2007.
[61] W. Lee, M.-C. Jeong, and J.-M. Myoung, "Fabrication and application potential of ZnO nanowires grown on GaAs(002) substrates by metal–organic chemical vapour deposition," *Nanotechnology*, vol. 15, no. 3, pp. 254–259, Mar. 2004.
[62] M. Kawakami, A. B. Hartanto, Y. Nakata, and T. Okada, "Synthesis of ZnO Nanorods by Nanoparticle Assisted Pulsed-Laser Deposition," *Japanese Journal of Applied Physics*, vol. 42, no. Part 2, No. 1A/B, pp. L33–L35, 2003.
[63] L. Vayssieres, K. Keis, S.-E. Lindquist, and A. Hagfeldt, "Purpose-Built Anisotropic Metal Oxide Material: 3D Highly Oriented Microrod Array of ZnO," *J. Phys. Chem. B*, vol. 105, no. 17, pp. 3350–3352, mai 2001.
[64] Z. Wang, X. Qian, J. Yin, and Z. Zhu, "Large-Scale Fabrication of Tower-like, Flower-like, and Tube-like ZnO Arrays by a Simple Chemical Solution Route," *Langmuir*, vol. 20, no. 8, pp. 3441–3448, avril 2004.
[65] S. Peulon and D. Lincot, "Cathodic electrodeposition from aqueous solution of dense or open-structured zinc oxide films," *Advanced Materials*, vol. 8, no. 2, pp. 166–170, 1996.
[66] Z. Liu, Z. Jin, J. Qiu, X. Liu, W. Wu, and W. Li, "Preparation and characteristics of ordered porous ZnO films by a electrodeposition method using PS array templates," *Semiconductor Science and Technology*, vol. 21, no. 1, pp. 60–66, Jan. 2006.
[67] J. Elias, C. Lévy-Clément, M. Bechelany, J. Michler, G.-Y. Wang, Z. Wang, and L. Philippe, "Hollow Urchin-like ZnO thin Films by Electrochemical Deposition," *Advanced Materials*, vol. 22, no. 14, pp. 1607–1612, 2010.

[68] H. Xu, H. Wang, Y. Zhang, W. He, M. Zhu, B. Wang, and H. Yan, “Hydrothermal synthesis of zinc oxide powders with controllable morphology,” *Ceramics International*, vol. 30, no. 1, pp. 93–97, 2004.
[69] K. Krunks, O. Bijakina, V. Mikli, T. Varema, and E. Mellikov, “Zinc Oxide Thin Films by Spray Pyrolysis Method,” *Physica Scripta*, vol. T79, no. 1, p. 209, 1999.
[70] S. Chu, G. Wang, W. Zhou, Y. Lin, L. Chernyak, J. Zhao, J. Kong, L. Li, J. Ren, and J. Liu, “Electrically pumped waveguide lasing from ZnO nanowires,” *Nature Nanotechnology*, vol. 6, no. 8, pp. 506–510, 2011.
[71] X. Yang, A. Wolcott, G. Wang, A. Sobo, R. C. Fitzmorris, F. Qian, J. Z. Zhang, and Y. Li, “Nitrogen-Doped ZnO Nanowire Arrays for Photoelectrochemical Water Splitting,” *Nano Lett.*, vol. 9, no. 6, pp. 2331–2336, juin 2009.
[72] A. M. C. Ng, Y. Y. Xi, Y. F. Hsu, A. B. Djurišić, W. K. Chan, S. Gwo, H. L. Tam, K. W. Cheah, P. W. K. Fong, H. F. Lui, and C. Surya, “GaN/ZnO nanorod light emitting diodes with different emission spectra,” *Nanotechnology*, vol. 20, no. 44, p. 445201, Nov. 2009.
[73] C. Soci, A. Zhang, B. Xiang, S. A. Dayeh, D. P. R. Aplin, J. Park, X. Y. Bao, Y. H. Lo, and D. Wang, “ZnO Nanowire UV Photodetectors with High Internal Gain,” *Nano Lett.*, vol. 7, no. 4, pp. 1003–1009, avril 2007.
[74] P. J. Pauzauskie and P. Yang, “Nanowire photonics,” *Materials Today*, vol. 9, no. 10, pp. 36–45, Oct. 2006.
[75] Y. W. Heo, L. C. Tien, D. P. Norton, B. S. Kang, F. Ren, B. P. Gila, and S. J. Pearton, “Electrical transport properties of single ZnO nanorods,” *Applied Physics Letters*, vol. 85, no. 11, pp. 2002–2004, Sep. 2004.
[76] Q. H. Li, Q. Wan, Y. X. Liang, and T. H. Wanga, "Electronic transport through individual ZnO nanowires", Applied Physics Letters, vol. 84, no. 22, pp. 4556-4558, May 2004.
[77] P.-C. Chang, Z. Fan, D. Wang, W.-Y. Tseng, W.-A. Chiou, J. Hong, and J. G. Lu, “ZnO Nanowires Synthesized by Vapor Trapping CVD Method,” *Chem. Mater.*, vol. 16, no. 24, pp. 5133–5137, Nov. 2004.
[78] Z. Fan, D. Wang, P.-C. Chang, W.-Y. Tseng, and J. G. Lu, “ZnO nanowire field-effect transistor and oxygen sensing property,” *Applied Physics Letters*, vol. 85, no. 24, pp. 5923 –5925, Dec. 2004.
[79] I. Mora-Sero, F. Fabregat-Santiago, B. Denier, J. Bisquert, R. Tena-Zaera, J. Elias, and C. Levy-Clement, “Determination of carrier density of ZnO nanowires by electrochemical techniques,” *Applied Physics Letters*, vol. 89, no. 20, pp. 203117 – 203117–3, Nov. 2006.
[80] F. Bernardini, V. Fiorentini, and D. Vanderbilt, “Spontaneous polarization and piezoelectric constants of III-V nitrides,” *Phys. Rev. B*, vol. 56, no. 16, pp. R10024–R10027, Oct. 1997.
[81] Z. L. Wang, X. Y. Kong, Y. Ding, P. Gao, W. L. Hughes, R. Yang, and Y. Zhang, “Semiconducting and Piezoelectric Oxide Nanostructures Induced by Polar Surfaces,” *Advanced Functional Materials*, vol. 14, no. 10, pp. 943–956, 2004.
[82] Z. L. Wang and J. Song, “Piezoelectric Nanogenerators Based on Zinc Oxide Nanowire Arrays,” *Science*, vol. 312, no. 5771, pp. 242–246, Apr. 2006.
[83] M. Paunovic and M. Schlesinger, *Fundamentals of Electrochemical Deposition*, 2nd ed. Wiley-Interscience, 2006.
[84] M. Izaki and T. Omi, “Transparent zinc oxide films prepared by electrochemical reaction,” *Applied Physics Letters*, vol. 68, no. 17, pp. 2439–2440, Apr. 1996.
[85] M. Izaki and T. Omi, “Electrolyte Optimization for Cathodic Growth of Zinc Oxide Films,” *J. Electrochem. Soc.*, vol. 143, no. 3, pp. L53–L55, Mar. 1996.

[86] B. N. Illy, A. C. Cruickshank, S. Schumann, R. D. Campo, T. S. Jones, S. Heutz, M. A. McLachlan, D. W. McComb, D. J. Riley, and M. P. Ryan, "Electrodeposition of ZnO layers for photovoltaic applications: controlling film thickness and orientation," *J. Mater. Chem.*, vol. 21, no. 34, pp. 12949–12957, Aug. 2011.
[87] S. Peulon and D. Lincot, "Mechanistic Study of Cathodic Electrodeposition of Zinc Oxide and Zinc Hydroxychloride Films from Oxygenated Aqueous Zinc Chloride Solutions," *J. Electrochem. Soc.*, vol. 145, no. 3, pp. 864–874, Mar. 1998.
[88] T. Pauporté, E. Jouanno, F. Pellé, B. Viana, and P. Aschehoug, "Key Growth Parameters for the Electrodeposition of ZnO Films with an Intense UV-Light Emission at Room Temperature," *J. Phys. Chem. C*, vol. 113, no. 24, pp. 10422–10431, juin 2009.
[89] J. Elias, R. Tena-Zaera, and C. Lévy-Clément, "Electrodeposition of ZnO nanowires with controlled dimensions for photovoltaic applications: Role of buffer layer," *Thin Solid Films*, vol. 515, no. 24, pp. 8553–8557, Oct. 2007.
[90] A. Goux, T. Pauporté, J. Chivot, and D. Lincot, "Temperature effects on ZnO electrodeposition," *Electrochimica Acta*, vol. 50, no. 11, pp. 2239–2248, avril 2005.
[91] T. Pauporté and D. Lincot, "Heteroepitaxial electrodeposition of zinc oxide films on gallium nitride," *Applied Physics Letters*, vol. 75, no. 24, pp. 3817–3819, Dec. 1999.
[92] T. Pauporté, R. Cortès, M. Froment, B. Beaumont, and D. Lincot, "Electrocrystallization of Epitaxial Zinc Oxide onto Gallium Nitride," *Chem. Mater.*, vol. 14, no. 11, pp. 4702–4708, Nov. 2002.
[93] A. Goux, T. Pauporté, and D. Lincot, "Oxygen reduction reaction on electrodeposited zinc oxide electrodes in KCl solution at 70 °C," *Electrochimica Acta*, vol. 51, no. 15, pp. 3168–3172, avril 2006.
[94] T. Pauporté and D. Lincot, "Hydrogen Peroxide Oxygen Precursor for Zinc Oxide Electrodeposition I. Deposition in Perchlorate Medium," *J. Electrochem. Soc.*, vol. 148, no. 4, pp. C310–C314, Apr. 2001.
[95] T. Pauporté and D. Lincot, "Hydrogen peroxide oxygen precursor for zinc oxide electrodeposition II—Mechanistic aspects," *Journal of Electroanalytical Chemistry*, vol. 517, no. 1–2, pp. 54–62, décembre 2001.
[96] R. Könenkamp, K. Boedecker, M. C. Lux-Steiner, M. Poschenrieder, F. Zenia, C. Levy-Clement, and S. Wagner, "Thin film semiconductor deposition on free-standing ZnO columns," *Applied Physics Letters*, vol. 77, no. 16, pp. 2575–2577, Oct. 2000.
[97] J. Elias, R. Tena-Zaera, and C. Lévy-Clément, "Electrochemical deposition of ZnO nanowire arrays with tailored dimensions," *Journal of Electroanalytical Chemistry*, vol. 621, no. 2, pp. 171–177, Sep. 2008.
[98] W. E. Mustain and J. Prakash, "A Model for the Electroreduction of Molecular Oxygen," *Journal of The Electrochemical Society*, vol. 154, no. 7, p. A668, 2007.
[99] I. Repins, M. A. Contreras, B. Egaas, C. DeHart, J. Scharf, C. L. Perkins, B. To, and R. Noufi, "19·9%-efficient ZnO/CdS/CuInGaSe2 solar cell with 81·2% fill factor," *Progress in Photovoltaics: Research and Applications*, vol. 16, no. 3, pp. 235–239, 2008.
[100] X. Wu, "High-efficiency polycrystalline CdTe thin-film solar cells," *Solar Energy*, vol. 77, no. 6, pp. 803–814, décembre 2004.
[101] C. Wadia, A. P. Alivisatos, and D. M. Kammen, "Materials Availability Expands the Opportunity for Large-Scale Photovoltaics Deployment," *Environ. Sci. Technol.*, vol. 43, no. 6, pp. 2072–2077, Mar. 2009.
[102] T. K. Todorov, K. B. Reuter, and D. B. Mitzi, "High-Efficiency Solar Cell with Earth-Abundant Liquid-Processed Absorber," *Advanced Materials*, vol. 22, no. 20, pp. E156–E159, 2010.

[103] H.-J. Muffler, C.-H. Fischer, K. Diesner, and M. . Lux-Steiner, "ILGAR – A novel thin-film technology for sulfides," *Solar Energy Materials and Solar Cells*, vol. 67, no. 1–4, pp. 121–127, Mar. 2001.
[104] R. R. Prabhakar, S. S. Pramana, K. R. G. Karthik, C. H. Sow, and K. B. Jinesh, "Ultra-thin conformal deposition of $CuInS_2$ on ZnO nanowires by chemical spray pyrolysis," *Journal of Materials Chemistry*, vol. 22, no. 28, p. 13965, 2012.
[105] C. G. V. de Walle and J. Neugebauer, "Universal alignment of hydrogen levels in semiconductors, insulators and solutions," *Nature*, vol. 423, no. 6940, pp. 626–628, Jun. 2003.
[106] N. Du, H. Zhang, B. Chen, J. Wu, and D. Yang, "Low-temperature chemical solution route for ZnO based sulfide coaxial nanocables: general synthesis and gas sensor application," *Nanotechnology*, vol. 18, no. 11, p. 115619, Mar. 2007.
[107] T. Gao, Q. Li, and T. Wang, "Sonochemical Synthesis, Optical Properties, and Electrical Properties of Core/Shell-Type ZnO Nanorod/CdS Nanoparticle Composites," *Chem. Mater.*, vol. 17, no. 4, pp. 887–892, février 2005.
[108] L. M. Caicedo, L. C. Moreno, J. W. Sandino, and G. Gordillo, "Deposition, optical and structural characterization of SnO_2:F/CdS and ZnO/CdS structures used as optical windows in solar cells," *Surface Review and Letters*, vol. 09, no. 05n06, pp. 1693–1696, Oct. 2002.
[109] S. Saito, Y. Hashimoto, and K. Ito, "Efficient ZnO/CdS/InP heterojunction solar cell," in *IEEE Photovoltaic Specialists Conference - 1994, 1994 IEEE First World Conference on Photovoltaic Energy Conversion, 1994., Conference Record of the Twenty Fourth*, 1994, vol. 2, pp. 1867 –1870 vol.2.
[110] Z. Fan, H. Razavi, J. Do, A. Moriwaki, O. Ergen, Y.-L. Chueh, P. W. Leu, J. C. Ho, T. Takahashi, L. A. Reichertz, S. Neale, K. Yu, M. Wu, J. W. Ager, and A. Javey, "Three-dimensional nanopillar-array photovoltaics on low-cost and flexible substrates," *Nature Materials*, vol. 8, no. 8, pp. 648–653, 2009.
[111] T. Zhai, X. Fang, L. Li, Y. Bando, and D. Golberg, "One-dimensional CdS nanostructures: synthesis, properties, and applications," *Nanoscale*, vol. 2, no. 2, p. 168, 2010.
[112] F. Fang, D. X. Zhao, B. H. Li, Z. Z. Zhang, J. Y. Zhang, and D. Z. Shen, "The enhancement of ZnO nanowalls photoconductivity induced by CdS nanoparticle modification," *Applied Physics Letters*, vol. 93, no. 23, pp. 233115–233115–3, Dec. 2008.
[113] Y. Luo, "Hydrothermal Synthesis of One-Dimensional ZnO/CdS Core/Shell Nanocomposites," *Colloid journal*, vol. 71, no. 3, pp. 370–374.
[114] X. Q. Meng, D. X. Zhao, J. Y. Zhang, D. Z. Shen, Y. M. Lu, X. W. Fan, and X. H. Wang, "Photoluminescence properties of single crystalline ZnO/CdS core/shell one-dimensional nanostructures," *Materials letters*, vol. 61, no. 16, pp. 3535–3538.
[115] Y. Tak, S. J. Hong, J. S. Lee, and K. Yong, "Fabrication of ZnO/CdS core/shell nanowire arrays for efficient solar energy conversion," *Journal of Materials Chemistry*, vol. 19, no. 33, p. 5945, 2009.
[116] Y. Tak, S. J. Hong, J. S. Lee, and K. Yong, "Solution-Based Synthesis of a CdS Nanoparticle/ZnO Nanowire Heterostructure Array," *Crystal Growth & Design*, vol. 9, no. 6, pp. 2627–2632, juin 2009.
[117] J. Joo, D. Kim, D.-J. Yun, H. Jun, S.-W. Rhee, J. S. Lee, K. Yong, S. Kim, and S. Jeon, "The fabrication of highly uniform ZnO/CdS core/shell structures using a spin-coating-based successive ion layer adsorption and reaction method," *Nanotechnology*, vol. 21, no. 32, p. 325604, Aug. 2010.

[118] E. D. Spoerke, M. T. Lloyd, Y. Lee, T. N. Lambert, B. B. McKenzie, Y.-B. Jiang, D. C. Olson, T. L. Sounart, J. W. P. Hsu, and J. A. Voigt, "Nanocrystal Layer Deposition: Surface-Mediated Templating of Cadmium Sulfide Nanocrystals on Zinc Oxide Architectures," *J. Phys. Chem. C*, vol. 113, no. 37, pp. 16329–16336, Sep. 2009.
[119] Y. Tak, H. Kim, D. Lee, and K. Yong, "Type-II CdS nanoparticle–ZnO nanowire heterostructure arrays fabricated by a solution process: enhanced photocatalytic activity," *Chem. Commun.*, no. 38, pp. 4585–4587, Sep. 2008.
[120] Y. F. Nicolau, "Solution deposition of thin solid compound films by a successive ionic-layer adsorption and reaction process," *Applications of Surface Science*, vol. 22–23, Part 2, pp. 1061–1074, mai 1985.
[121] Y. F. Nicolau and J. C. Menard, "Procedure for solution growth of ZnS, CdS and Zn1?x Cd x S thin films by successive ionic-layer adsorptions and reactions," *Journal of Applied Electrochemistry*, vol. 20, no. 6, pp. 1063–1066, Nov. 1990.
[122] Y. F. Nicolau and J. C. Menard, "Solution growth of ZnS, CdS and Zn1-xCdxS thin films by the successive ionic-layer adsorption and reaction process; growth mechanism," *Journal of Crystal Growth*, vol. 92, no. 1–2, pp. 128–142, Oct. 1988.
[123] Y. F. Nicolau, M. Dupuy, and M. Brunel, "ZnS, CdS, and Zn1-xCdxS thin films deposited by the successive ionic layer adsorption and reaction process," *Journal of the Electrochemical Society*, vol. 137, no. 9, pp. 2915–2924.
[124] Y. . Nicolau and J. . Menard, "An electrokinetic study of ZnS and CdS surface chemistry," *Journal of Colloid and Interface Science*, vol. 148, no. 2, pp. 551–570, février 1992.
[125] Y. F. Nicolau, U.S. Patent 4 675 207.
[126] Wikipedia contributors, "Cadmium sulfide," *Wikipedia, the free encyclopedia*. Wikimedia Foundation, Inc., 05-Sep-2012.
[127] P. Sudhagar, S. Chandramohan, R. S. Kumar, R. Sathyamoorthy, C.-H. Hong, and Y. S. Kang, "Fabrication and charge-transfer characteristics of CdS QDs sensitized vertically grown flower-like ZnO solar cells with CdSe cosensitizers," *physica status solidi (a)*, vol. 208, no. 2, pp. 474–479, 2011.
[128] X. W. Sun, J. Chen, J. L. Song, D. W. Zhao, W. Q. Deng, and W. Lei, "Ligand capping effect for dye solar cells with a CdSe quantum dot sensitized ZnO nanorod photoanode," *Opt. Express*, vol. 18, no. 2, pp. 1296–1301, Jan. 2010.
[129] K. Žídek, K. Zheng, C. S. Ponseca, M. E. Messing, L. R. Wallenberg, P. Chábera, M. Abdellah, V. Sundström, and T. Pullerits, "Electron Transfer in Quantum-Dot-Sensitized ZnO Nanowires: Ultrafast Time-Resolved Absorption and Terahertz Study," *J. Am. Chem. Soc.*, vol. 134, no. 29, pp. 12110–12117, juillet 2012.
[130] K. Zidek, K. Zheng, P. Chabera, M. Abdellah, and T. Pullerits, "Quantum dot photodegradation due to CdSe-ZnO charge transfer: Transient absorption study," *Applied Physics Letters*, vol. 100, no. 24, pp. 243111 –243111–4, Jun. 2012.
[131] H. Wang, T. Wang, X. Wang, R. Liu, B. Wang, H. Wang, Y. Xu, J. Zhang, and J. Duan, "Double-shelled ZnO/CdSe/CdTe nanocable arrays for photovoltaic applications: microstructure evolution and interfacial energy alignment," *Journal of Materials Chemistry*, vol. 22, no. 25, p. 12532, 2012.
[132] H. Majidi and J. B. Baxter, "Electrodeposition of CdSe coatings on ZnO nanowire arrays for extremely thin absorber solar cells," *Electrochimica Acta*, vol. 56, no. 6, pp. 2703–2711, février 2011.
[133] M. Seol, H. Kim, Y. Tak, and K. Yong, "Novel nanowire array based highly efficient quantum dot sensitized solar cell," *Chemical Communications*, vol. 46, no. 30, p. 5521, 2010.

[134] Y. Hao, J. Pei, Y. Wei, Y. Cao, S. Jiao, F. Zhu, J. Li, and D. Xu, "Efficient Semiconductor-Sensitized Solar Cells Based on Poly(3-hexylthiophene)/CdSe/ZnO Core−Shell Nanorod Arrays," *J. Phys. Chem. C*, vol. 114, no. 18, pp. 8622–8625, mai 2010.
[135] M. Seol, H. Kim, W. Kim, and K. Yong, "Highly efficient photoelectrochemical hydrogen generation using a ZnO nanowire array and a CdSe/CdS co-sensitizer," *Electrochemistry Communications*, vol. 12, no. 10, pp. 1416–1418, Oct. 2010.
[136] Wikipedia contributors, "Cadmium selenide," *Wikipedia, the free encyclopedia*. Wikimedia Foundation, Inc., 06-Sep-2012.
[137] C. Ma, Y. Ding, D. Moore, X. Wang, and Z. L. Wang, "Single-Crystal CdSe Nanosaws," *J. Am. Chem. Soc.*, vol. 126, no. 3, pp. 708–709, Jan. 2004.
[138] M. Califano, A. Zunger, and A. Franceschetti, "Direct carrier multiplication due to inverse Auger scattering in CdSe quantum dots," *Applied Physics Letters*, vol. 84, no. 13, pp. 2409–2411, Mar. 2004.
[139] R. D. Schaller, M. A. Petruska, and V. I. Klimov, "Effect of electronic structure on carrier multiplication efficiency: Comparative study of PbSe and CdSe nanocrystals," *Applied Physics Letters*, vol. 87, no. 25, pp. 253102–253102–3, Dec. 2005.
[140] E. Hendry, M. Koeberg, F. Wang, H. Zhang, C. de Mello Donegá, D. Vanmaekelbergh, and M. Bonn, "Direct Observation of Electron-to-Hole Energy Transfer in CdSe Quantum Dots," *Phys. Rev. Lett.*, vol. 96, no. 5, p. 057408, février 2006.
[141] H. Lee, M. Wang, P. Chen, D. R. Gamelin, S. M. Zakeeruddin, M. Grätzel, and M. K. Nazeeruddin, "Efficient CdSe Quantum Dot-Sensitized Solar Cells Prepared by an Improved Successive Ionic Layer Adsorption and Reaction Process," *Nano Lett.*, vol. 9, no. 12, pp. 4221–4227, décembre 2009.
[142] Y.-L. Lee, B.-M. Huang, and H.-T. Chien, "Highly Efficient CdSe-Sensitized TiO_2 Photoelectrode for Quantum-Dot-Sensitized Solar Cell Applications," *Chem. Mater.*, vol. 20, no. 22, pp. 6903–6905, Nov. 2008.
[143] X. Wang, H. Zhu, Y. Xu, H. Wang, Y. Tao, S. Hark, X. Xiao, and Q. Li, "Aligned ZnO/CdTe Core−Shell Nanocable Arrays on Indium Tin Oxide: Synthesis and Photoelectrochemical Properties," *ACS Nano*, vol. 4, no. 6, pp. 3302–3308, juin 2010.
[144] T. Surek, "Crystal growth and materials research in photovoltaics: progress and challenges," *Journal of Crystal Growth*, vol. 275, no. 1–2, pp. 292–304, février 2005.
[145] A. J. Kothari and T. K. Chaudhuri, "Enhanced light harvesting in photovoltaics with ZnO nanorod arrays," *AIP Conference Proceedings*, vol. 1447, no. 1, pp. 361–362, Jun. 2012.
[146] T. C. Kaspar, T. Droubay, and J. E. Jaffe, "ZnO/Sn:In2O3 and ZnO/CdTe band offsets for extremely thin absorber photovoltaics," *Applied Physics Letters*, vol. 99, no. 26, pp. 263504–263504–3, Dec. 2011.
[147] J. Briscoe, D. E. Gallardo, and S. Dunn, "Layer-by-layer CdTe Nanoparticle Absorbers for ZnO Nanorod Solar Cells - The Influence of Annealing on Cell Performance," *MRS Online Proceedings Library*, vol. 1260, p. null, 2010.
[148] J. Briscoe, D. E. Gallardo, S. Hatch, V. Lesnyak, N. Gaponik, and S. Dunn, "Enhanced quantum dot deposition on ZnO nanorods for photovoltaics through layer-by-layer processing," *Journal of Materials Chemistry*, vol. 21, no. 8, p. 2517, 2011.
[149] Wikipedia contributors, "Cadmium telluride," *Wikipedia, the free encyclopedia*. Wikimedia Foundation, Inc., 07-Sep-2012.
[150] B. E. McCandless and J. R. Sites, "Cadmium Telluride Solar Cells," in *Handbook of Photovoltaic Science and Engineering*, A. Luque and S. Hegedus, Eds. John Wiley & Sons, Ltd, 2011, pp. 600–641.

[151] K. Tennakone and W. M. Ariyasingha, “Ionic Conductivity in cuprous thiocynate,” *Electrochimica Acta*, vol. 25, no. 5, p. 731, mai 1980.
[152] H. J. Snaith and L. Schmidt-Mende, “Advances in Liquid-Electrolyte and Solid-State Dye-Sensitized Solar Cells,” *Advanced Materials*, vol. 19, no. 20, pp. 3187–3200, 2007.
[153] B. O’Regan, D. T. Schwartz, S. M. Zakeeruddin, and M. Grätzel, “Electrodeposited Nanocomposite n–p Heterojunctions for Solid-State Dye-Sensitized Photovoltaics,” *Advanced Materials*, vol. 12, no. 17, pp. 1263–1267, 2000.
[154] B. O’Regan and D. T. Schwartz, “Efficient Photo-Hole Injection from Adsorbed Cyanine Dyes into Electrodeposited Copper(I) Thiocyanate Thin Films,” *Chem. Mater.*, vol. 7, no. 7, pp. 1349–1354, juillet 1995.
[155] B. O’Regan, F. Lenzmann, R. Muis, and J. Wienke, “A Solid-State Dye-Sensitized Solar Cell Fabricated with Pressure-Treated P25−TiO_2 and CuSCN: Analysis of Pore Filling and IV Characteristics,” *Chem. Mater.*, vol. 14, no. 12, pp. 5023–5029, décembre 2002.
[156] C. Rost, I. Sieber, S. Siebentritt, M. C. Lux-Steiner, and R. Könenkamp, “Spatially distributed p-n heterojunction based on nanoporous TiO_2 and CuSCN,” *Applied Physics Letters*, vol. 75, no. 5, pp. 692–694, Aug. 1999.
[157] T. Dittrich, D. Kieven, A. Belaidi, M. Rusu, J. Tornow, K. Schwarzburg, and M. C. Lux-Steiner, “Formation of the charge selective contact in solar cells with extremely thin absorber based on ZnO-nanorod/In_2S_3/CuSCN,” *Journal of Applied Physics*, vol. 105, no. 3, pp. 034509–034509–6, Feb. 2009.
[158] V. P. S. Perera, M. K. I. Senevirathna, P. K. D. D. P. Pitigala, and K. Tennakone, “Doping CuSCN films for enhancement of conductivity: Application in dye-sensitized solid-state solar cells,” *Solar energy materials and solar cells*, vol. 86, no. 3, pp. 443–450.
[159] K. Tennakone, A. H. Jayatissa, C. a. N. Fernando, S. Wickramanayake, S. Punchihewa, L. K. Weerasena, and W. D. R. Premasiri, “Semiconducting and Photoelectrochemical Properties of n- and p-Type β-CuCNS,” *physica status solidi (a)*, vol. 103, no. 2, pp. 491–497, 1987.
[160] D. L. Smith and V. I. Saunders, “Preparation and structure refinement of the 2H polytype of β-copper(I) thiocyanate,” *Acta Crystallographica Section B Structural Crystallography and Crystal Chemistry*, vol. 38, no. 3, pp. 907–909, Mar. 1982.
[161] D. L. Smith and V. I. Saunders, “The structure and polytypism of the β modification of copper(I) thiocyanate,” *Acta Crystallographica Section B Structural Crystallography and Crystal Chemistry*, vol. 37, no. 10, pp. 1807–1812, Oct. 1981.
[162] J. A. Dobado, R. Uggla, M. R. Sundberg, and J. Molina, “On the bonding isomerism in three-co-ordinated copper(I) thiocyanates,” *J. Chem. Soc., Dalton Trans.*, no. 3, pp. 489–496, Jan. 1999.
[163] G. R. R. . Kumara, A. Konno, G. K. . Senadeera, P. V. . Jayaweera, D. B. R. . De Silva, and K. Tennakone, “Dye-sensitized solar cell with the hole collector p-CuSCN deposited from a solution in n-propyl sulphide,” *Solar Energy Materials and Solar Cells*, vol. 69, no. 2, pp. 195–199, Sep. 2001.
[164] X.-D. Gao, X.-M. Li, W.-D. Yu, J.-J. Qiu, and X.-Y. Gan, “Room-temperature deposition of nanocrystalline CuSCN film by the modified successive ionic layer adsorption and reaction method,” *Thin solid films*, vol. 517, no. 2, pp. 554–559.
[165] Q. Zhang, H. Guo, Z. Feng, L. Lin, J. Zhou, and Z. Lin, “n-ZnO nanorods/p-CuSCN heterojunction light-emitting diodes fabricated by electrochemical method,” *Electrochimica Acta*, vol. 55, no. 17, pp. 4889–4894, juillet 2010.
[166] R. Salazar, C. Lévy-Clément, and V. Ivanova, “Galvanostatic deposition of ZnO thin films,” *Electrochimica Acta*, vol. 78, pp. 547–556, Sep. 2012.

[167] C. Chappaz-Gillot, R. Salazar, S. Berson, and V. Ivanova, “Room temperature template-free electrodeposition of CuSCN nanowires,” *Electrochemistry Communications*, vol. 24, pp. 1–4, Oct. 2012.
[168] Q. Zeng, X. Kong, Y. Sun, Y. Zhang, L. Tu, J. Zhao, and H. Zhang, “Synthesis and Optical Properties of Type II CdTe/CdS Core/Shell Quantum Dots in Aqueous Solution via Successive Ion Layer Adsorption and Reaction,” *J. Phys. Chem. C*, vol. 112, no. 23, pp. 8587–8593, juin 2008.
[169] B. R. Sankapal, E. Goncalves, A. Ennaoui, and M. C. Lux-Steiner, “Wide band gap p-type windows by CBD and SILAR methods,” *Thin Solid Films*, vol. 451–452, pp. 128–132, Mar. 2004.
[170] X.-D. Gao, X.-M. Li, W.-D. Yu, J.-J. Qiu, and X.-Y. Gan, “Room-temperature deposition of nanocrystalline CuSCN film by the modified successive ionic layer adsorption and reaction method,” *Thin Solid Films*, vol. 517, no. 2, pp. 554–559, Nov. 2008.
[171] W. A. Pinheiro, V. D. Falcão, L. R. de O. Cruz, and C. L. Ferreira, “Comparative study of CdTe sources used for deposition of CdTe thin films by close spaced sublimation technique,” *Materials Research*, vol. 9, no. 1, pp. 47–49, Mar. 2006.
[172] B. O’Regan and D. T. Schwartz, “Efficient dye-sensitized charge separation in a wide-band-gap p-n heterojunction,” *Journal of Applied Physics*, vol. 80, no. 8, p. 4749, 1996.
[173] J. Elias, “Réseaux de nanofils et de nanotubes d’oxyde de zinc de dimensions contrôlées obtenus par voie électrochimique. Application aux cellules solaires nanostructurées,” PhD thesis, Université Paris XII, Val de Marne, France, 2008.
[174] M. Grätzel, “Photoelectrochemical cells,” *Nature*, vol. 414, no. 6861, pp. 338–344, Nov. 2001.
[175] Wikipedia contributors, “Scanning electron microscope,” *Wikipedia, the free encyclopedia*. Wikimedia Foundation, Inc., 08-Sep-2012.
[176] R. E. Lee, *Scanning electron microscopy and x-ray microanalysis*. PTR Prentice Hall, 1993.
[177] Wikipedia contributors, “Scanning transmission electron microscopy,” *Wikipedia, the free encyclopedia*. Wikimedia Foundation, Inc., 05-Sep-2012.
[178] H. P. Klug and L. E. Alexander, “X-Ray Diffraction Procedures: For Polycrystalline and Amorphous Materials, 2nd Edition,” *X-Ray Diffraction Procedures: For Polycrystalline and Amorphous Materials, 2nd Edition, by Harold P. Klug, Leroy E. Alexander, pp. 992. ISBN 0-471-49369-4. Wiley-VCH , May 1974.*, vol. -1, May 1974.
[179] “Introduction to X-ray Diffraction (XRD) | PANalytical.” [Online]. Available: http://www.panalytical.com/index.cfm?pid=135. [Accessed: 09-Sep-2012].
[180] “ICDD Support - Product References and Information.” [Online]. Available: http://www.icdd.com/support/references/default.htm. [Accessed: 09-Sep-2012].
[181] J. I. Langford and A. J. C. Wilson, “Scherrer after sixty years: A survey and some new results in the determination of crystallite size,” *Journal of Applied Crystallography*, vol. 11, no. 2, pp. 102–113, Apr. 1978.
[182] J. P. Enríquez and X. Mathew, “Influence of the thickness on structural, optical and electrical properties of chemical bath deposited CdS thin films,” *Solar Energy Materials and Solar Cells*, vol. 76, no. 3, pp. 313–322, Mar. 2003.
[183] R. E. Marotti, D. N. Guerra, C. Bello, G. Machado, and E. A. Dalchiele, “Bandgap energy tuning of electrochemically grown ZnO thin films by thickness and electrodeposition potential,” *Solar Energy Materials and Solar Cells*, vol. 82, no. 1–2, pp. 85–103, mai 2004.

[184] Wikipedia contributors, “Ultraviolet–visible spectroscopy,” *Wikipedia, the free encyclopedia*. Wikimedia Foundation, Inc., 06-Sep-2012.
[185] Z. Feng, J. Zhou, Y. Xi, B. Lan, H. Guo, H. Chen, Q. Zhang, and Z. Lin, “Solid-state hybrid photovoltaic cells with a novel redox polymer and nanostructured inorganic semiconductors,” *Journal of Power Sources*, vol. 194, no. 2, pp. 1142–1149, décembre 2009.
[186] J. Tauc, *Amorphous and liquid semiconductors*. Plenum, 1974.
[187] Wikipedia contributors, “Semiconductor characterization techniques,” *Wikipedia, the free encyclopedia*. Wikimedia Foundation, Inc., 06-Aug-2012.
[188] T. H. Gfroerer, “Photoluminescence in Analysis of Surfaces and Interfaces,” in *Encyclopedia of Analytical Chemistry*, John Wiley & Sons, Ltd, 2006.
[189] K. A. Emery and C. R. Osterwald, “Solar cell efficiency measurements,” *Solar Cells*, vol. 17, no. 2–3, pp. 253–274, avril 1986.
[190] “Measurement of Solar Cell Efficiency.” [Online]. Available: http://www.pveducation.org/pvcdrom/characterisation/measurement-of-solar-cell-efficiency. [Accessed: 09-Sep-2012].
[191] M. L. Hitchman, *Measurement of Dissolved Oxygen*. Krieger Publishing Company, 1988.
[192] S. Sanchez, R. Salazar, C. Lévy-Clément, and V. Ivanova, “ZnO Buffer Layers and Nanowires Electrodeposition for Extremely Thin Absorber Solar Cells,” *ECS Trans.*, vol. 33, no. 17, pp. 183–190, Mar. 2011.
[193] J. Rousset, E. Saucedo, and D. Lincot, “Extrinsic Doping of Electrodeposited Zinc Oxide Films by Chlorine for Transparent Conductive Oxide Applications,” *Chem. Mater.*, vol. 21, no. 3, pp. 534–540, février 2009.
[194] B. Cao, W. Cai, H. Zeng, and G. Duan, “Morphology evolution and photoluminescence properties of ZnO films electrochemically deposited on conductive glass substrates,” *Journal of Applied Physics*, vol. 99, no. 7, pp. 073516–073516–6, Apr. 2006.
[195] R. Tena-Zaera, J. Elias, and C. Lévy-Clément, “ZnO nanowire arrays: Optical scattering and sensitization to solar light,” *Applied Physics Letters*, vol. 93, no. 23, pp. 233119–233119–3, Dec. 2008.
[196] J. Elias, R. Tena-Zaera, and C. Levy-Clement, “Effect of the Chemical Nature of the Anions on the Electrodeposition of ZnO Nanowire Arrays,” *J. Phys. Chem. C*, vol. 112, no. 15, pp. 5736–5741, avril 2008.
[197] T. Pauporté and D. Lincot, “Electrodeposition of semiconductors for optoelectronic devices: results on zinc oxide,” *Electrochimica Acta*, vol. 45, no. 20, pp. 3345–3353, juin 2000.
[198] R. Tena-Zaera, J. Elias, G. Wang, and C. Lévy-Clément, “Role of Chloride Ions on Electrochemical Deposition of ZnO Nanowire Arrays from O_2 Reduction,” *J. Phys. Chem. C*, vol. 111, no. 45, pp. 16706–16711, Nov. 2007.
[199] L. Xu, Y. Guo, Q. Liao, J. Zhang, and D. Xu, “Morphological Control of ZnO Nanostructures by Electrodeposition,” *J. Phys. Chem. B*, vol. 109, no. 28, pp. 13519–13522, juillet 2005.
[200] B. Meyer and D. Marx, “Density-functional study of the structure and stability of ZnO surfaces,” *Phys. Rev. B*, vol. 67, no. 3, p. 035403, Jan. 2003.
[201] S.-H. Na and C.-H. Park, “First-Principles Study of the Surface of Wurtzite ZnO and ZnS : Implications for Nanostructure Formation,” *Journal of the Korean Physical Society*, vol. 54, no. 2, pp. 867–872.
[202] U. Diebold, L. V. Koplitz, and O. Dulub, “Atomic-scale properties of low-index ZnO surfaces,” *Applied Surface Science*, vol. 237, no. 1–4, pp. 336–342, Oct. 2004.

[203] M. W. Allen, D. Y. Zemlyanov, G. I. N. Waterhouse, J. B. Metson, T. D. Veal, C. F. McConville, and S. M. Durbin, "Polarity effects in the x-ray photoemission of ZnO and other wurtzite semiconductors," *Applied Physics Letters*, vol. 98, no. 10, pp. 101906–101906–3, Mar. 2011.

[204] M. Kubo, Y. Oumi, H. Takaba, A. Chatterjee, A. Miyamoto, M. Kawasaki, M. Yoshimoto, and H. Koinuma, "Homoepitaxial growth mechanism of ZnO(0001): Molecular-dynamics simulations," *Physical Review B*, vol. 61, no. 23, pp. 16187–16192, Jun. 2000.

[205] H. Xu, K. Ohtani, M. Yamao, and H. Ohno, "Surface morphologies of homoepitaxial ZnO on Zn- and O-polar substrates by plasma assisted molecular beam epitaxy," *Applied Physics Letters*, vol. 89, no. 7, pp. 071918–071918–3, Aug. 2006.

[206] X. Y. Kong and Z. L. Wang, "Spontaneous Polarization-Induced Nanohelixes, Nanosprings, and Nanorings of Piezoelectric Nanobelts," *Nano Lett.*, vol. 3, no. 12, pp. 1625–1631, décembre 2003.

[207] G. Loget and A. Kuhn, "Electric field-induced chemical locomotion of conducting objects," *Nature Communications*, vol. 2, p. 535, Nov. 2011.

[208] E. P. Warekois, M. C. Lavine, A. N. Mariano, and H. C. Gatos, "Crystallographic Polarity in the II-VI Compounds," *Journal of Applied Physics*, vol. 33, no. 2, pp. 690–696, Feb. 1962.

[209] Z. Liu, R. Zhu, and G. Zhang, "Electric-field-assisted growth and alignment of ZnO nanowires in device fabrication," *Journal of Physics D: Applied Physics*, vol. 43, no. 15, p. 155402, Apr. 2010.

[210] A. N. Mariano and R. E. Hanneman, "Crystallographic Polarity of ZnO Crystals," *Journal of Applied Physics*, vol. 34, no. 2, p. 384, 1963.

[211] S. H. Lee, T. Minegishi, J.-S. Ha, J. Park, H.-J. Lee, H. J. Lee, H. Shiku, T. Matsue, S.-K. Hong, H. Jeon, and T. Yao, "Lateral arrays of vertical ZnO nanowalls on a periodically polarity-inverted ZnO template," *Nanotechnology*, vol. 20, no. 23, p. 235304, Jun. 2009.

[212] A. Cortes, H. Gómez, R. E. Marotti, G. Riveros, and E. A. Dalchiele, "Grain size dependence of the bandgap in chemical bath deposited CdS thin films," *Solar Energy Materials and Solar Cells*, vol. 82, no. 1–2, pp. 21–34, mai 2004.

[213] R. Vogel, P. Hoyer, and H. Weller, "Quantum-Sized PbS, CdS, Ag_2S, Sb_2S_3, and Bi2S3 Particles as Sensitizers for Various Nanoporous Wide-Bandgap Semiconductors," *J. Phys. Chem.*, vol. 98, no. 12, pp. 3183–3188, Mar. 1994.

[214] R. Bhargava, *Properties of Wide Bandgap Ii-VI Semiconductors*. INSPEC, Institute of Electrical Engineers, 1997.

[215] X. Peng, M. C. Schlamp, A. V. Kadavanich, and A. P. Alivisatos, "Epitaxial Growth of Highly Luminescent CdSe/CdS Core/Shell Nanocrystals with Photostability and Electronic Accessibility," *J. Am. Chem. Soc.*, vol. 119, no. 30, pp. 7019–7029, juillet 1997.

[216] M. Willander, P. Klason, L. L. Yang, S. M. Al-Hilli, Q. X. Zhao, and O. Nur, "ZnO nanowires: chemical growth, electrodeposition, and application to intracellular nano-sensors," *physica status solidi (c)*, vol. 5, no. 9, pp. 3076–3083, 2008.

[217] S. Gorer and G. Hodes, "Quantum size effects in the study of chemical solution deposition mechanisms of semiconductor films," *J. Phys. Chem.*, vol. 98, no. 20, pp. 5338–5346, mai 1994.

[218] G. Hodes, A. Albu-Yaron, F. Decker, and P. Motisuke, "Three-dimensional quantum-size effect in chemically deposited cadmium selenide films," *Phys. Rev. B*, vol. 36, no. 8, pp. 4215–4221, Sep. 1987.

[219] H. Cachet, H. Essaaidi, M. Froment, and G. Maurin, “Chemical bath deposition of CdSe layers from Cd(II)-selenosulfite solutions,” *Journal of Electroanalytical Chemistry*, vol. 396, no. 1–2, pp. 175–182, Oct. 1995.
[220] M. C. A. Fantini, J. R. Moro, and F. Decker, “Electrodeposition of CdSe films on SnO_2:F coated glass,” *Solar Energy Materials*, vol. 17, no. 4, pp. 247–255, juin 1988.
[221] A. Belaidi, T. Dittrich, D. Kieven, J. Tornow, K. Schwarzburg, and M. Lux-Steiner, “Influence of the local absorber layer thickness on the performance of ZnO nanorod solar cells,” *physica status solidi (RRL) - Rapid Research Letters*, vol. 2, no. 4, pp. 172–174, Aug. 2008.
[222] C. Herzog, A. Belaidi, A. Ogacho, and T. Dittrich, “Inorganic solid state solar cell with ultra-thin nanocomposite absorber based on nanoporous TiO_2 and In_2S_3,” *Energy & Environmental Science*, vol. 2, no. 9, p. 962, 2009.
[223] A. Romeo, D. . Bätzner, H. Zogg, and A. . Tiwari, “Recrystallization in CdTe/CdS,” *Thin Solid Films*, vol. 361–362, pp. 420–425, février 2000.
[224] Z. Bai, L. Wan, Z. Hou, and D. Wang, “Effect of $CdCl_2$ annealing treatment on CdS thin films and CdTe/CdS thin film solar cells,” *physica status solidi (c)*, vol. 8, no. 2, pp. 628–630, 2011.
[225] V. Komin, B. Tetali, V. Viswanathan, S. Yu, D. L. Morel, and C. S. Ferekides, “The effect of the $CdCl_2$ treatment on CdTe/CdS thin film solar cells studied using deep level transient spectroscopy,” *Thin Solid Films*, vol. 431–432, pp. 143–147, mai 2003.
[226] A. N. Goldstein, C. M. Echer, and A. P. Alivisatos, “Melting in Semiconductor Nanocrystals,” *Science*, vol. 256, no. 5062, pp. 1425–1427, Jun. 1992.
[227] A. P. Alivisatos, “Perspectives on the Physical Chemistry of Semiconductor Nanocrystals,” *J. Phys. Chem.*, vol. 100, no. 31, pp. 13226–13239, Jan. 1996.
[228] Q. Jiang, H. X. Shi, and M. Zhao, “Melting thermodynamics of organic nanocrystals,” *The Journal of Chemical Physics*, vol. 111, no. 5, pp. 2176–2180, Aug. 1999.
[229] V. A. Fedorov, V. A. Ganshin, and Y. N. Korkishko, “Determination of the Point of the Zincblende-to-Wurtzite Structural Phase Transition in Cadmium Selenide Crystals,” *physica status solidi (a)*, vol. 126, no. 1, pp. K5–K7, 1991.
[230] V. Consonni, G. Rey, J. Bonaimé, N. Karst, B. Doisneau, H. Roussel, S. Renet, and D. Bellet, “Synthesis and physical properties of ZnO/CdTe core shell nanowires grown by low-cost deposition methods,” *Applied Physics Letters*, vol. 98, no. 11, pp. 111906–111906–3, Mar. 2011.
[231] V. Consonni, G. Feuillet, and P. Gergaud, “Plasticity induced texture development in thick polycrystalline CdTe: Experiments and modeling,” *Journal of Applied Physics*, vol. 103, no. 6, pp. 063529–063529–8, Mar. 2008.
[232] C. V. Thompson, “Secondary grain growth in thin films of semiconductors: Theoretical aspects,” *Journal of Applied Physics*, vol. 58, no. 2, pp. 763–772, Jul. 1985.
[233] M. Casavola, R. Buonsanti, G. Caputo, and P. D. Cozzoli, “Colloidal Strategies for Preparing Oxide-Based Hybrid Nanocrystals,” *European Journal of Inorganic Chemistry*, vol. 2008, no. 6, pp. 837–854, 2008.
[234] M. A. Berding, S. Krishnamurthy, A. Sher, and A.-B. Chen, “Cleavage energies in semiconductors,” *Journal of Applied Physics*, vol. 67, no. 10, pp. 6175–6178, May 1990.
[235] D. H. Rose, F. S. Hasoon, R. G. Dhere, D. S. Albin, R. M. Ribelin, X. S. Li, Y. Mahathongdy, T. A. Gessert, and P. Sheldon, “Fabrication procedures and process sensitivities for CdS/CdTe solar cells,” *Progress in Photovoltaics: Research and Applications*, vol. 7, no. 5, pp. 331–340, 1999.
[236] D. Kieven, T. Dittrich, A. Belaidi, J. Tornow, K. Schwarzburg, N. Allsop, and M. Lux-Steiner, “Effect of internal surface area on the performance of ZnO/In_2S_3/CuSCN

solar cells with extremely thin absorber," *Applied Physics Letters*, vol. 92, no. 15, p. 153107, 2008.
[237] M. A. Hines and P. Guyot-Sionnest, "Synthesis and Characterization of Strongly Luminescing ZnS-Capped CdSe Nanocrystals," *J. Phys. Chem.*, vol. 100, no. 2, pp. 468–471, Jan. 1996.
[238] M. Gao, S. Kirstein, H. Möhwald, A. L. Rogach, A. Kornowski, A. Eychmüller, and H. Weller, "Strongly Photoluminescent CdTe Nanocrystals by Proper Surface Modification," *J. Phys. Chem. B*, vol. 102, no. 43, pp. 8360–8363, Oct. 1998.
[239] H. C. Gardner, D. E. Gallardo, S. Dunn, N. Gaponik, and A. Eychmüller, "A photoluminescence study of film structure in CdTe nanoparticle thin films," *J Nanosci Nanotechnol*, vol. 8, no. 5, pp. 2578–2581, May 2008.
[240] J. Briscoe, D. E. Gallardo, V. Lesnyak, and S. Dunn, "Influence of Annealing on Composition and Optical Properties of CdTe Nanoparticle Layer-by-Layer Films," *Journal of Nanoscience and Nanotechnology*, vol. 11, no. 6, pp. 5270–5273, 2011.
[241] I. Mora-Seró, S. Giménez, F. Fabregat-Santiago, R. Gómez, Q. Shen, T. Toyoda, and J. Bisquert, "Recombination in Quantum Dot Sensitized Solar Cells," *Acc. Chem. Res.*, vol. 42, no. 11, pp. 1848–1857, Nov. 2009.
[242] J. E. Jaffe, T. C. Kaspar, T. C. Droubay, T. Varga, M. E. Bowden, and G. J. Exarhos, "Electronic and Defect Structures of CuSCN," *J. Phys. Chem. C*, vol. 114, no. 19, pp. 9111–9117, mai 2010.
[243] V. González-Pedro, X. Xu, I. Mora-Seró, and J. Bisquert, "Modeling High-Efficiency Quantum Dot Sensitized Solar Cells," *ACS Nano*, vol. 4, no. 10, pp. 5783–5790, Oct. 2010.
[244] M. Grätzel, "Dye-sensitized solar cells," *Journal of photochemistry and photobiology. C, Photochemistry reviews*, vol. 4, no. 2, pp. 145–153.
[245] J. Bisquert, "Chemical capacitance of nanostructured semiconductors: its origin and significance for nanocomposite solar cells," *Physical Chemistry Chemical Physics*, vol. 5, no. 24, p. 5360, 2003.
[246] R. Tena-Zaera, J. Elias, C. Lévy-Clément, C. Bekeny, T. Voss, I. Mora-Seró, and J. Bisquert, "Influence of the Potassium Chloride Concentration on the Physical Properties of Electrodeposited ZnO Nanowire Arrays," *J. Phys. Chem. C*, vol. 112, no. 42, pp. 16318–16323, Oct. 2008.
[247] Y. Myung, J. H. Kang, J. W. Choi, D. M. Jang, and J. Park, "Polytypic ZnCdSe shell layer on a ZnO nanowire array for enhanced solar cell efficiency," *Journal of Materials Chemistry*, vol. 22, no. 5, p. 2157, 2012.

Publications

- ZnO Buffer Layers and Nanowires Electrodeposition for Extremely Thin Absrober Solar Cell. S. Sanchez, R. Salazar, C. Lévy-Clément, V. Ivanova. ECS Transaction, Vol. 33, Photovoltaics for the 21st Century 6, p. 183, 2011.
- ZnO/CdTe and ZnO/CdS core-shell nanowire arrays for extremely thin absorber solar cells, R. Salazar, A. Delamoreanu, C. Lévy-Clément, V. Ivanova, Energy Procedia, Vol 10, p. 122, 2011.
- ZnO Nanowire Arrays Sensitized with Different Absorber Materials for Fabrication of Nanostructured Solar Cells, R. Salazar, S. Sanchez, A. Delamoreanu, C. Lévy-Clément, V. Ivanova. ECS Transactions 41, p. 119, 2011.
- Galvanostatic deposition of ZnO Thin Films, Raul Salazar, Claude Lévy-Clément, Valentina Ivanova, Elchem. Acta 78, p. 547-556, 2012.
- Room Temperature Template-free Electrodeposition of CuSCN Nanowires, Cyril Chappaz-Gillot, Raul Salazar, Solenn Berson, Valentina Ivanova, Electrochemistry Communications 24, 1–4, 2012.
- Sylvia Sanchez, Cyril Chappaz-Gillot, Raul Salazar, Hervé Muguerra, Edrisse Arbaoui, Solenn Berson, Claude Lévy-Clément and Valentina Ivanova, Comparative study of semiconducting nanowires electrodeposition on different substrates, Journal of Solid State Electrochemistry, (2012), Accepted.

Patents

- Valentina Ivanova-Hristova, Cyril Chappaz-Gillot, Solenn Berson, Raul Salazar, Une nouvelle méthode de fabrication des nanofils de CuSCN par voie électrochimique, N° CEA DD13429CV, 2012 (Brevet français).

Presentations

- Journées de la Matière Condensée (JMC12)- Troyes, France, August 23-27, 2010 (poster).
- 61st annual meeting of ISE, Nice, France, September 26 – October 1st, 2010 (poster)

- 218th The Electrochemical Society Meeting, Las Vegas, USA, October 10-15, 2010 (oral).
- E-MRS Warsaw, Poland, September 13-17, 2010 (oral).
- Second International Workshop on Advanced, nano- and Biomaterials and Their Applications (*nabm*), French-Romanian Topical Meeting on Nano and Biomaterials, Sibiu, Romania, September 15-19, 2010 (invited).
- Solar Fuels / Photochemistry conference, Puerto, Morelos Mexico, December 1-4, 2010 (oral).
- 219th The Electrochemical Society Meeting, Montreal, QC, Canada, May 1-6, 2011 (oral).
- E-MRS spring, Nice, France, May 9-13, 2011 (oral).
- Journées d'Electrochimie, Grenoble, France, July 4-8, 2011 (oral).
- 220th ECS Meeting and Electrochemical Energy Summit, Boston, MA, USA, October 9-14, 2011 (oral).
- 2nd International Conference on Semiconductor Sensitized Solar Cells, Mallorca, Spain, September 18-20, 2011 (oral).
- E-MRS 2012 Spring Meeting, Strasbourg, France, May 15-17, 2012 (poster).
- PVTC Conference, Aix-en-Provence, France. 22-24 May 2012 (poster).
- 63rd Annual Meeting of the International Electrochemical Society, Prague 18-24 August 2012 (invited).
- 2012 International Semiconductor Conference Dresden-Grenoble (2012 ISCDG), Grenoble September 24 to 26, 2012 (invited).
- 222nd The Electrochemical Society Meeting, PRiME 2012, Honolulu, Hawaii, USA, October 7-12 October 2012 (oral).

Appendix A

Electrochemistry Communications 24 (2012) 1–4

Contents lists available at SciVerse ScienceDirect

Electrochemistry Communications

journal homepage: www.elsevier.com/locate/elecom

Room temperature template-free electrodeposition of CuSCN nanowires

Cyril Chappaz-Gillot [a,b], Raul Salazar [a], Solenn Berson [b], Valentina Ivanova [a,*]

[a] CEA, LETI, MINATEC Campus, 17 rue des Martyrs, 38054 Grenoble, France
[b] CEA-INES, Savoie Technolac BP 332, 50 Avenue du Lac Léman, 73377 Le Bourget-du-Lac, France

ARTICLE INFO

Article history:
Received 10 July 2012
Received in revised form 30 July 2012
Accepted 31 July 2012
Available online 10 August 2012

Keywords:
Copper thiocyanate
p-Type semiconductor
Electrodeposition
Nanowires

ABSTRACT

Here for the first time electrochemical deposition of copper thiocyanate (CuSCN) nanowires (NWs) from an aqueous electrolyte at room temperature is reported. The formation of CuSCN in an aqueous solution is a two-step reaction, where in the first step Cu^{2+} is reduced to Cu^{+} and in the second step Cu^{+} chemically precipitates with SCN^{-} to form CuSCN. CuSCN preparation in the form of nanowires depends on the chelating agent in the electrolyte and could be precisely controlled by the applied potential or the applied current density. Additionally the CuSCN NWs dimensions could be tailored by the electrolyte composition and the passed charge density. The electrodeposited CuSCN NWs exhibit high crystalline quality and are c-axis oriented. We believe that this easy way of preparing CuSCN NWs could open several avenues for their application in the domain of photovoltaics, sensors and optical displays.

1. Introduction

The electrochemical deposition is a versatile technique for the preparation of nanostructured materials due to its simplicity, the low temperature preparation and the possibility for easy and large scale processing. The wideband gap semiconductors are very attractive materials, being transparent in the visible region of the electromagnetic spectrum and absorbing ultraviolet radiations. The most studied electrochemical preparation of a wideband gap material is that of ZnO. Since the first reports on its electrochemical deposition [1] nowadays ZnO nanowires (NWs) with controlled dimensions on different substrates could be grown [2,3]. A less investigated process is the direct electrochemical deposition of p-type semiconducting nanowires. Among the various transparent materials copper thiocyanate (CuSCN) received attention as one of the promising hole transporting solid electrolytes in extremely thin absorber [4] and dye-sensitized solar cells [5] because of its energy gap (3.7 eV) and valence band edge position. It was also used for preparation of resistive memory devices due to the reversible electrical bistability of the system Cu/CuSCN [6]. CuSCN thin films have been prepared by electrochemical deposition [7–11], successive ionic layer adsorption and reaction (SILAR) [12,13] and chemical bath deposition [14]. In the early works the electrodeposition of CuSCN was carried out in organic solvents [5,7] and only recently it was performed in aqueous electrolytes containing chelating agents [8,9,11]. The group of Könenkamp electrodeposited CuSCN NWs into templates with cylindrical holes from ethanolic solutions [15,16]. The obtained nanowires are polycrystalline after the template removal and a post annealing treatment was applied to improve the material quality.

Here we report template-free CuSCN nanowire direct electrodeposition from an aqueous electrolyte containing chelating agent. The appropriate choice of the chelating agent is crucial for CuSCN NWs formation. To the best of our knowledge this is the first time when CuSCN nanowire template-free fabrication is reported.

2. Experimental

$CuSO_4 \cdot 5H_2O$ (purity > 99.9%, Sigma-Aldrich), ethylenediaminetetraacetic acid (EDTA, purity ≥ 99.0%, Fluka), 1,2-diaminocyclohexanetetraacetic acid (CDTA, purity ≥ 98.5%, Fluka), and KSCN (purity ≥ 99%, Sigma-Aldrich) were used as received for electrolyte preparation.

Aqueous solutions containing between 5 and 120 mM $CuSO_4 \cdot 5H_2O$ and 0.25 to 2.0 M equivalents of KSCN were prepared. EDTA or CDTA were used as chelating agents and their amount in the solution was kept equal to $CuSO_4 \cdot 5H_2O$ in 1:1 M ratio. Thus the molar ratio in the electrolyte between $CuSO_4 \cdot 5H_2O$, EDTA (or CDTA) and KSCN was varied from 1:1:0.25 to 1:1:2. All electrolytes were prepared with electronic grade deionized water.

The electrodeposition was performed in a standard three-electrode electrochemical cell at room temperature. The working electrode (with 1.7 cm^2 active surface area) was glass covered with transparent conducting oxide (which was either ITO or fluorine doped tin oxide (FTO), R = 10 to 15 $\Omega\,sq^{-1}$), polyethylene terephthalate (PET) covered with ITO (R = 15 $\Omega\,sq^{-1}$) or gold substrate (Si wafer with thermally grown SiO_2 covered with 100 nm Au film, prepared by chemical vapor deposition). A platinum wire was used as a counter electrode and a saturated calomel electrode as the reference electrode. The potentials

* Corresponding author. Tel.: +33 4 38786504; fax: +33 4 38781628.
E-mail address: valentina.ivanova@cea.fr (V. Ivanova).

1388-2481/$ – see front matter © 2012 Elsevier B.V. All rights reserved.
http://dx.doi.org/10.1016/j.elecom.2012.07.030

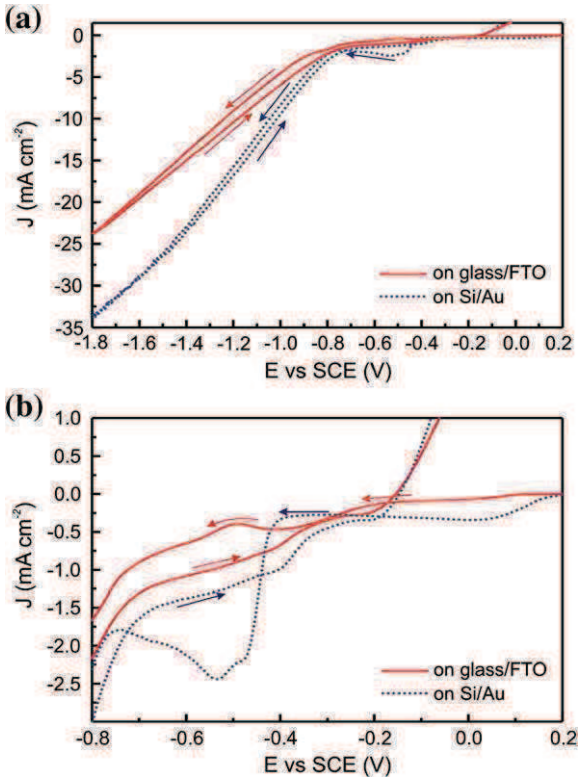

Fig. 1. (a) Cyclic voltammograms of glass/FTO and Si/SiO_2/Au electrode in an electrolyte containing 12 mM Cu^{2+} (Cu^{2+}/EDTA/SCN^- = 1:1:0.25); (b) a zoomed view of the potential window 0.2 to −0.8 V. Scan rate 20 mV s^{-1}. The arrows are showing the scan directions.

mentioned in this article are given versus SCE. All electrochemical measurements were performed with Princeton Applied Research potentiostat/galvanostat system (PARSTAT 2273).

Scanning electron microscopy (SEM, Hitachi S-4100 or FEI Nova NanoSEM) was used for the surface morphology characterizations. The crystal structure and orientation of the deposits were determined by X-ray diffractometry (XRD, PANalytical X'Pert MPD), using a cobalt anticathode (Co, Kα1, λ = 1.7889 Å).

3. Results and discussion

With the aim to find an appropriate inorganic hole transporting layer for nanostructured solar cells, we have studied the CuSCN electrodeposition from aqueous solutions in the presence of two kinds of chelating compounds. Continuous CuSCN 2D layers were prepared at room temperature from stable aqueous electrolytes containing triethanolamine [9]. When the chelating agent was replaced by EDTA, and by applying the same deposition conditions as for the 2D layer deposition surprisingly CuSCN nanowires were grown. This result motivated us to perform additional experiments with the aim to find the reason for CuSCN nanowire formation and to propose a reproducible and simple way for their preparation. Firstly a cyclic voltammetry study on different substrates from an electrolyte containing Cu^{2+}, EDTA and SCN^- with a molar ratio of 1:1:0.25 was performed. For simplicity in Fig. 1 the cyclic voltammograms in this electrolyte are depicted only for the glass/FTO and gold substrates. On the cyclic voltammograms (Fig. 1b) one can observe an increase of the cathodic current starting at around −0.1 V for the glass/FTO substrate and at 0.2 V for the gold one and after passing through the maximum it slightly decreases and increases again at −0.55 and −0.4 V for the glass/FTO and gold substrates, respectively. At

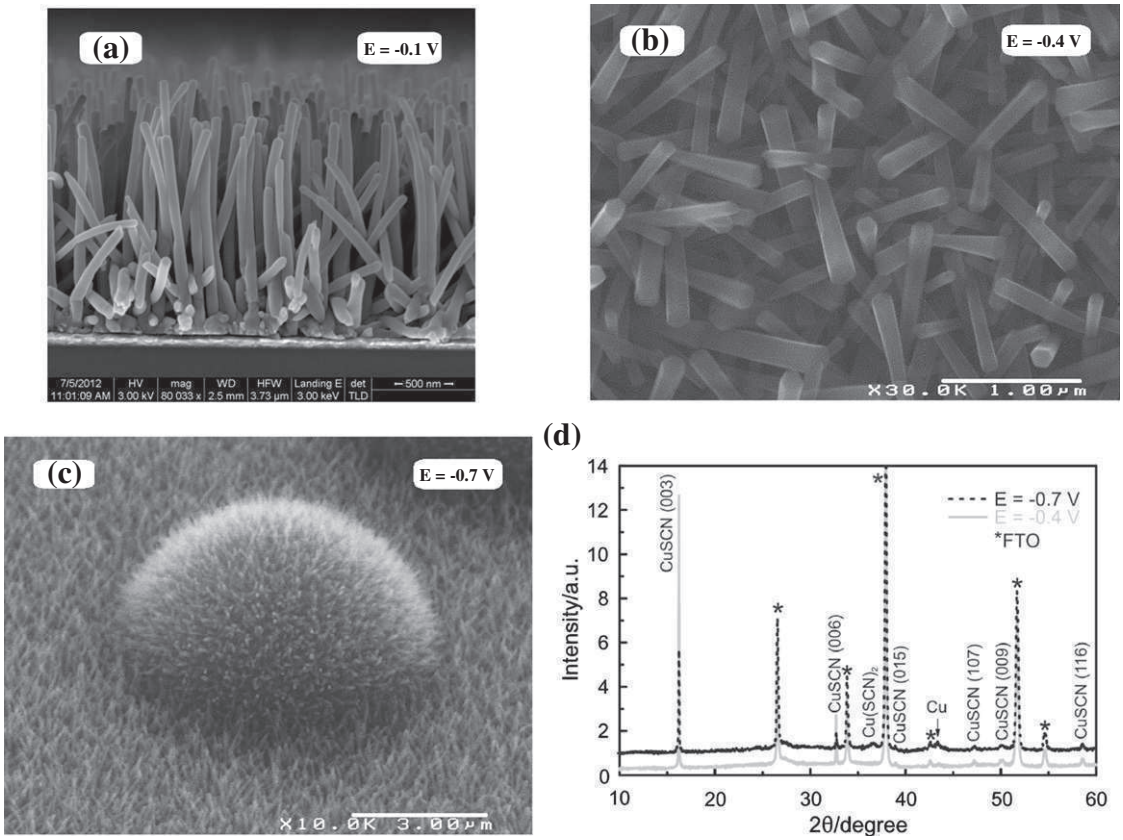

Fig. 2. SEM images of electrodeposited CuSCN NWs from an electrolyte containing 12 mM Cu^{2+} (Cu^{2+}/EDTA/SCN^- = 1:1:0.25) on: (a) Si/SiO_2/Au substrate (E = −0.1 V, Q = 150 mC cm^{-2}), cross section; (b) glass/ITO substrate (E = −0.4 V, Q = 50 mC cm^{-2}), top view; (c) glass/ITO substrate (E = −0.7 V, Q = 50 mC cm^{-2}), top view. (d) XRD spectra of CuSCN NWs deposited on glass/FTO substrates at −0.4 and −0.7 V, Q = 200 mC cm^{-2}. The diffraction peaks of FTO substrate are marked with stars (*).

more negative potentials (around −1.0 V) the cathodic reaction of hydrogen (H^+) reduction to form H_2 in aqueous solutions starts. The first increase of the cathodic current is assigned to the reduction of the chelated Cu^{2+} to Cu^+ whereas the second one is to the reduction of Cu^{2+} to Cu^0 (metallic copper). In the first potential region the CuSCN electrodeposition takes place, which is a two-step reaction: the first is electrochemical (Eq. (1)) and the second one is the chemical precipitation of Cu^+ with SCN^- (Eq. (2)) [9,17]:

$$Cu^{2+} + e^- \rightarrow Cu^+ \quad E^\circ = +0.159\ V\ (NHE) \tag{1}$$

$$Cu^+ + SCN^- \rightarrow CuSCN. \tag{2}$$

The electrochemical deposition of CuSCN from aqueous solutions is less investigated due to the poor stability of $Cu^{2+}$and SCN^- in water, which rapidly react and precipitate as $Cu(SCN)_2$. To avoid this problem the electrodeposition is mostly carried out in organic solvents or in an aqueous electrolyte containing a strong ligand of Cu^{2+}. The deposition of CuSCN 2D layers from stable aqueous electrolytes containing triethanolamine, sodium lactate or EDTA disodium salt as chelating agents, was investigated [8,9,11]. Replacing these ligands by a diamino-tetraacetic acid compound H_4Y (EDTA or CDTA) changes the electrolyte pH from basic to acidic (pH<2). We consider that the formed complexes between $Cu^{2+}$and H_4Y and the pH are responsible for the formation of the CuSCN 1D nanostructure. The pH value of the as-prepared electrolyte is below 2 and in it the tetradentate $Cu(H_2Y)$ complex is the prevailing species [18]. At higher pH values, other complexes like the pentadentate $Cu(HY)^-$ or the hexadentate $CuY^{2-}$are predominant and the utilization of such electrolytes leads to the CuSCN 2D layer or to the direct metallic copper deposition [18]. From cyclic voltammograms different potentials in the region between −0.05 and −0.5 V (for glass/FTO) were chosen to perform the depositions. CuSCN NWs have been obtained for all studied potentials (Fig. 2a and b). They could be deposited in quite a large potential window (about 400 mV), which for the metallic substrate is shifted to more positive potentials (from 0.15 to −0.25 V, in the case of Au). CuSCN NWs can be also prepared galvanostatically. For example, for the glass/FTO substrate the applied current density should be between −50 and −100 μA cm^{-2}. One should be aware that the applied potential and current density values depend on the electrode substrate. In Fig. 2a it is seen that the CuSCN nanowire array (deposited at −0.1 V) is with preferential longitudinal growth perpendicular to the substrate, with high density (10^5 to 10^6 nanowires cm^{-2}) and uniform in height. When the deposition is realized at more negative potentials (−0.7 V) urchin-like structures on the surface are observed (Fig. 2c).

The structural XRD analysis confirmed the fact that the electrodeposited CuSCN nanowires exhibit high crystalline quality in agreement with the rhombohedral β−CuSCN (PDF4 00-029-0581) phase (Fig. 2d). The nanowire XRD spectrum consists of a very intense (003) peak, together with smaller (006), (009), (116), (015) and (107) peaks. The extremely high intensity of the (003) peak in comparison with that of the others indicates that the nanowires are preferentially oriented along the c-axis, in a direction orthogonal to the substrate (in accordance with the SEM images). Fig. 2d also depicts the XRD patterns of the film deposited at −0.7 V. It consists not only of CuSCN but also some traces of $Cu(SCN)_2$ and metallic copper, which should be responsible for the urchin structure formation.

The CuSCN morphology is influenced by the Cu^{2+} concentration in the electrolyte and the bath temperature. In the concentration ranges between 5 and 90 mM, CuSCN nanowires are grown, whereas from an electrolyte containing 100 mM Cu^{2+}, the nanowires are transformed into a fennel-shape (Fig. 3a). The further increase of Cu^{2+} concentration leads to a mixture between a fennel-shape and a compact film. The experiments performed at different temperatures showed that above 50 °C, between CuSCN NWs some prism-shaped nanocrystals are formed (Fig. 3b).

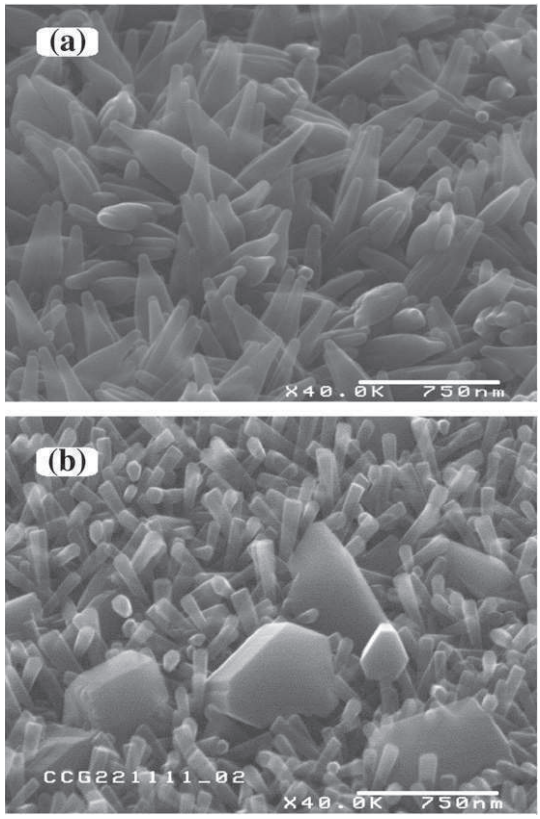

Fig. 3. SEM images (45°) of CuSCN NWS deposited from an electrolyte containing Cu^{2+}, EDTA and KSCN with a molar ratio of 1:1:0.25 on: (a) PET/ITO substrate where $[Cu^{2+}]$=100 mM, E=−0.3 V, Q=50 mC cm^{-2} and (b) glass/ITO substrate where $[Cu^{2+}]$=60 mM, E=−0.3 V, Q=50 mC cm^{-2}, at 50 °C.

The nanowire dimensions could be controlled by: i) the total passed charge density during the deposition (Q), ii) the applied potential (E) and iii) the molar ratio SCN^-/Cu^{2+} in the electrolyte. The first parameter plays a role on the nanowire length, while the last two influence their diameter (Fig. 4). For charge densities from 1.5 to 30 mC cm^{-2}, the nanowire length increases from 40 to 400 nm, whereas for longer deposition times it reaches several micrometers (Fig. 4a). NWs with desired lengths could be grown in the order of several seconds to a few minutes. We have found that the NWs deposited at more positive potentials are larger in diameter than those prepared at more negative potentials (Fig. 4b). Their diameter varies by 50 nm for a change of 100 mV in the applied potential. At more negative potentials higher nucleus densities are responsible for the smaller diameter of NWs. Another parameter influencing the CuSCN NWs dimensions is the concentration of SCN^- in the solution. The tuning of the molar ratio SCN^-/Cu^{2+} in the electrolyte leads to an increase in the diameter of the nanowires from 80 to 180 nm (Fig. 4c). The increased SCN^- concentration probably changes the stoichiometric proportion of SCN/Cu in the deposit, which consequently results in an increase of NWs diameter.

4. Conclusion

CuSCN nanowire arrays with high crystalline quality and a preferred orientation normal to the plane were prepared for the first time by direct electrodeposition from an aqueous solution at room temperature. The use of diamino-tetraacetic acid compounds as chelating agents is crucial for the deposition of CuSCN in form of nanowires. The NWs dimensions could be controlled by the applied

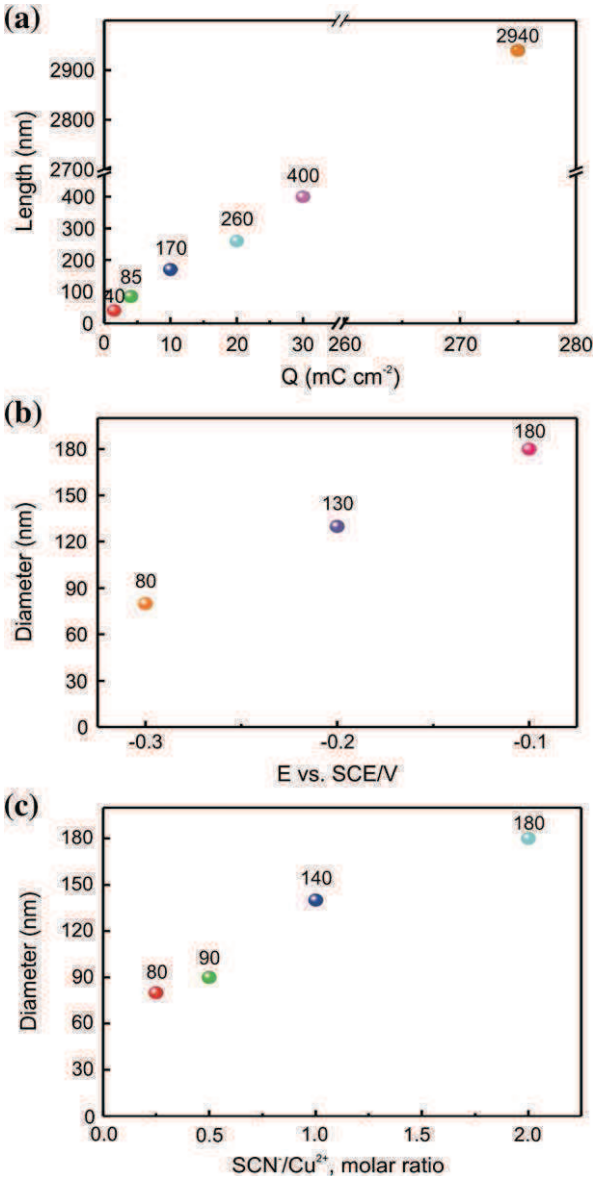

Fig. 4. (a) NWs length evolution with the passed charge density (Cu^{2+}/EDTA/SCN^{-} = 1:1:0.25, E = −0.3 V); (b) NWs diameter change with applied potential (Cu^{2+}/EDTA/SCN^{-} = 1:1:0.25, Q = 15 mC cm^{-2}) and (c) NWs diameter dependence on the molar ratio SCN^{-}/Cu^{2+} in the electrolyte (E = −0.3 V, Q = 15 mC cm^{-2}). CuSCN nanowires are deposited on PET/ITO substrate from electrolytes containing 12 mM Cu^{2+}.

potential, the molar ratio SCN^{-}/Cu^{2+} in the electrolyte and the passed charge density during the deposition. This finding could open numerous new applications for CuSCN NWs in the domain of photovoltaic and optoelectronic devices. Once again it is demonstrated that electrochemical deposition is a well suited technique used to prepare high quality nanostructured materials with controlled dimensions.

Acknowledgments

Cyril Chappaz-Gillot acknowledges the CEA program “NTE” for his post-doctoral fellowship. Raul Salazar gratefully acknowledges the Nanosciences Foundation of Grenoble for his PhD funding as well as the support from CONACYT Mexico. The authors thank Guillaume Rodriguez from CEA-Leti for the Au substrate preparation.

References

[1] S. Peulon, D. Lincot, Advanced Materials 8 (1996) 166.
[2] J. Elias, R. Tena-Zaera, C. Lévy-Clément, Thin Solid Films 515 (2007) 8553.
[3] Th. Pauporté, G. Bataille, L. Joulaud, F.J. Vermersch, Journal of Physical Chemistry C 114 (2010) 194.
[4] C. Lévy-Clément, R. Tena-Zaera, M.A. Ryan, A. Katty, G. Hodes, Advanced Materials 17 (2005) 1512.
[5] B. O'Regan, D.T. Schwartz, S.M. Zakeeruddin, M. Grätzel, Advanced Materials 12 (2000) 1263.
[6] Y.-W. Dong, X. Ji, W. Xu, J.-Q. Tang, P. Guo, Electrochemical and Solid-State Letters 12 (2009) H54.
[7] K. Tennakone, A.R. Kumarasinghe, P.M. Sirimanne, G.R.R.A. Kumara, Thin Solid Films 261 (1995) 307.
[8] W. Wu, Z. Jin, Z. Hua, Y. Fu, J. Qiu, Electrochimica Acta 50 (2005) 2343.
[9] Y. Ni, Z. Jin, Y. Fu, Journal of the American Ceramic Society 90 (2007) 2966.
[10] Y. Selk, T. Yoshida, T. Oekermann, Thin Solid Films 516 (2008) 7120.
[11] K. Kamiya, K. Hashimoto, S. Nakanishi, Chemical Physics Letters 530 (2012) 77.
[12] B.R. Sankapal, E. Goncalves, A. Ennaoui, M.C. Lux-Steiner, Thin Solid Films 451–452 (2004) 128.
[13] X.-D. Gao, X.-M. Li, W.-D. Yu, J.-J. Qiu, X.-Y. Gan, Thin Solid Films 517 (2008) 554–559.
[14] P.B. Ahirrao, S.R. Gosavi, Sanjay S. Sonawane, R.S. Patil, Archives of Physics Research 2 (2011) 29.
[15] R. Engelhardt, R. Könenkamp, Journal of Applied Physics 90 (2001) 4287.
[16] J. Chen, R. Könenkamp, Applied Physics Letters 82 (2003) 4782.
[17] A.J. Bard, L.R. Faulkner, Electrochemical Methods: Fundamentals and Applications, second ed. John Wiley & Sons, Inc., Hoboken, 2001. Appendix C.
[18] S. Aksu, F.M. Doyle, in: R. Woods, F.M. Doyle (Eds.), Proceedings of the International Symposium on Electrochemistry in Mineral and Metal Processing V, The Electrochemical Society Proceedings Series, Volume 2000–14, 2000, p. 258, The Electrochemical Society, Pennington, NJ.

Extremely thin absorber "eta" solar cell with nanostructured II-VI absorber

The development of semiconducting materials for the extremely thin absorber (*eta*) solar cell using cheap and scalable methods was the main objective of this work. The *eta*-solar cell is composed of all inorganic materials consisting of an extremely thin layer of absorbing material (1.1 <Eg< 1.8 eV) sandwiched between nanostructured transparent electron and hole conductors (Eg ≥ 3.3 eV). Compact and defect free ZnO thin film and nanowires (NWs) were prepared galvanostatically. The ZnO nanowire dimensions were controlled with the ZnO seed layer or the applied current density. The photosensitization of the ZnO nanowires with conformal layers of CdS, CdSe and CdTe prepared by Successive Ionic Layer Adsorption and Reaction (SILAR) was studied. The improvement of the absorber structural and optical properties by annealing and chemical treatment was achieved. The Close Spaced Sublimation (CSS) and Quantum Dot (QD) sensitization were also used for CdTe thin shell deposition, while the first method produced poor coverage, the second resulted in better coverage but with poor optical features. The ZnO NW/absorber heterostructure was completed with a hole conducting CuSCN layer. The influence of the CuSCN layer (prepared by three methods) morphology on the *eta*-solar cell performance is discussed. Electrodeposited and SILAR prepared films exhibited rougher surfaces than that by the Impregnation technique (which affects the electrical conductivity). The ZnO/absorber core/shell heterostructures were also tested in a photoelectrochemical cell. The recorded efficiencies (up to 2 %) for the case of CdS and CdSe photosensitizers demonstrated an improvement of the ZnO/absorber interfaces and the material quality achieved by the modified-SILAR technique. These results let us to consider that today a Renascence of the SILAR method is happening.

Cellules solaires avec un absorbeur II-VI nanostructuré

L'objectif de ce travail est d'élaborer des méthodes peu chères pour produire des matériaux semi-conducteurs pouvant entrer dans la fabrication de cellules solaires de type "*eta*" (extremely thin absorber). Ces cellules sont constituées d'une couche extrêmement fine d'un adsorbeur inorganique dont la bande interdite est situé entre 1.1 et 1.8 eV placée entre deux nanostructures transparentes l'une de type n et l'autre de type p et dont les bandes interdites doivent être supérieurs à 3.3 eV. Une couche compacte et des nanofils de ZnO ont été préparés en mode galvanostatique. Les dimensions des nanofils ont été contrôlées à l'aide de la couche compacte et de la densité du courant appliqué. La photosensibilisation des nanofils par des couches uniformes de CdS, CdSe et CdTe préparée par la méthode SILAR (Successive Ionic Layer Adsorption and Reaction) a été étudiée. Les propriétés de ces couches ont été améliorées par recuit et traitement chimique. En ce qui concerne les fines coquilles de CdTe deux autres méthodes de sensibilisation ont été également étudiées : la CSS (Close Spaced Sublimation) et les QDs (Quantum Dots). La première méthode conduit à un faible recouvrement alors que la seconde produit un matériau mal défini optiquement. Les hétérostructures formées sur les nanofils ont été complétées par une couche de CuSCN, un semi-conducteur de type p, préparée par trois méthodes différentes. L'influence de la morphologie de ces couches sur les propriétés des cellules *eta* a été étudiée. Les films préparés par électrodéposition et SILAR sont plus rugueux que ceux obtenus par imprégnation et leur conductivité est moins bonne. Les hétérostructures (avec CdS et CdSe comme absorbeurs) ont été testées dans une cellule photoélectrochimique et les rendements obtenus (jusque 2%) montrent une amélioration certaine des propriétés de ces matériaux préparée par SILAR-modifiée ainsi que des interfaces ZnO/absorbeur. La qualité des matériaux obtenus par SILAR montre qu'aujourd'hui on peut s'attendre à une Renaissance de cette technique.